Methods and Systems for Rapid, Noninvasive Ablation of Large Tissue-Targets Using Histotripsy

by

Jonathan E. Lundt

A dissertation submitted in partial fulfillment
of the requirements for the degree of
Doctor of Philosophy
(Biomedical Engineering)
in The University of Michigan
2019

Doctoral Committee:

Associate Professor Zhen Xu, Chair
Professor Clifford S. Cho
Professor Cheri Deng
Professor J. Brian Fowlkes
Associate Research Scientist Timothy L. Hall

they who bettered life through discovered arts
and they who won remembrance by merit

Virgil, *Aeneid* 6.663-664

Jonathan E. Lundt

lundt@umich.edu

ORCID iD: 0000-0002-1614-6464

Acknowledgements

First and foremost, I would like to express my deep gratitude to Dr. Zhen Xu for serving as my advisor over the past four and a half years. I consider myself fortunate to have conducted my doctoral studies in a world-class laboratory led by a gifted and accomplished investigator. I benefitted greatly from the abundant resources that Zhen provides for her students – things like quick and insightful feedback, talented peers, and ample funding to name just a few. I would like to thank Drs. Tim Hall and Brian Fowlkes for their unwavering support and guidance throughout my time at the University of Michigan. It was truly a pleasure to have both of you as mentors and to share in your clear passion for science and engineering. I would like to thank Drs. Cheri Deng and Cliff Cho for serving on my dissertation committee and for the fruitful and enjoyable conversations we have had. I would also like to thank Dr. Charles Cain for the insightful conversations we had during my time in the lab.

In addition to the members of my committee, I would also to thank all the members of the Histotripsy Lab, past and present, who overlapped with my time here: Drs. Kim Ives, Will Roberts, Ryan Miller, Yohan Kim, Alex Duryea, Eli Vlaisavljevich, Steven Allen, Aiwei Shi, Youhan Sunny, Hedieh Tamaddoni, Yige Li, and Jonathan Sukovich as well as Tyler Gerhardson, Sang Won Choi, Greyson Stocker, Jonathan Macoskey, Tejaswi Workliar, Zhijie Dong, Ellen Yeats,

Ning Lu, Ryan Hubbard, Akshay Rao, Thai-Son Nguyen, Chad Wilson, Varsha Kumar, Albert Cai, and Robert Macdonald. I feel that a great deal of the lab's success can be traced to its culture of hard work and spirit of collaboration.

Thank you to the professors within the Department of Biomedical Engineering and beyond who were mentors and collaborators: Drs. Joan Greve, Joe Bull, Uli Scheven, Oliver Kripfgans, Gabe Owens, Tom Wenisch, Mario Fabiilli, Doug Noll, Ariella Shikanov, and Jan Stegemann. Thank you for sharing your time, laboratories, and wisdom with me on projects both within and outside the scope of my dissertation research.

Thank you to the administrative staff within the BME department who supported our research from behind the scenes: Kathy McCrumb, Maria Steele, Rebecca Green, Pat Metzler, Dana Jackson, and Chuck Nicholas in particular. Thank you for your patience and dedication.

Thank you to everyone at the Zell Lurie Institute at the University of Michigan's Ross School of Business and particularly Prof. Erik Gordon, Josh Botkin, Mike Johnson, Anne Perigo, Sarika Gupta, and all of my colleagues, past and present, on Wolverine Venture Fund. Serving on WVF for over three years was a transformative experience. It not only cultivated my capacity to think like an early-stage investor, it enhanced my ability to make decisions as a scientist-engineer which take into account consequential elements of the broader ecosystem in which research and product development reside. Prof. Gordon has been a wonderful and keenly insightful mentor throughout this journey and I am eternally grateful for the opportunity to serve as a doctoral student advisor on WVF. Participating in business plan competitions with my teammates Jon Macoskey and Nikita Jambulingam was also a lot of fun and a great learning experience. I owe a huge thanks to Anne, Josh, and Mike for the countless hours they put into

mentoring us. It was an honor to represent the University of Michigan under your guidance. I would also like to thank Joe Cabral from the Zell Lurie Commercialization Fund for the many enjoyable conversations we had about the intersection of science and entrepreneurship.

Thank you to everyone at Arboretum Ventures for the opportunity to join you as an intern this spring. This is a wonderful way to continue what I started on WVF and to begin what I hope will be a fruitful career in entrepreneurial science and engineering.

Thank you to the all of my academic and professional mentors who helped prepare me to conduct doctoral research at UM, many of whom continue to lend their ongoing support. An exhaustive list would be far too long to fit here but some of those who had the biggest impact on me were Beverly Williams, Jim Gillison, Randy York, Matt Stergios, and Drs. Tyrone Porter, Andrew Brayman, and Tom Matula. Working under the guidance of Tom and Andy at the Center for Industrial and Medical Ultrasound at the University of Washington was a big part of what made me want to make applied science a central facet of my life. Dr. Porter has a gift for scientific communication in addition to being an excellent researcher. I grew a great deal as an engineer under his mentorship and I have been grateful for his ongoing support. I am also thankful to have received invaluable guidance from Drs. Larry Crum, Ron Roy, Robin Cleveland, Allan Pierce, Paul Barbone, Hong Chen, Peter Kaczkowski, Barry Friemel, Jackie Stilwell, Bill Dietze, and Kyle Johnston.

Thank you to the friends I've made here in Ann Arbor and to those in Seattle, Missoula, and elsewhere who have been in touch since I struck out for the heartland. Thank you to my cousin Greta and her family here in Michigan for the warm welcome. Thank you especially to my father, Dr. John C. Lundt and my mother Pamela Lundt for their love and support and for always

patiently listening to me ramble about the minutiae and vicissitudes of my research. The engineering-based hobbies I pursued as a boy, with your support and encouragement, were the foundation for every subsequent accomplishment.

Table of Contents

List of Figures

List of Tables

Abstract

Percutaneous local ablation techniques including radiofrequency and microwave ablation are increasingly supplanting surgical resection as the standard of care for solid-tumor intervention due to lower risk of complications, lower costs, and shorter associated hospital stays. However, these techniques present several risks associated with device insertion and traditionally struggle to treat tumors greater than 3 cm in diameter. Thermally-based high intensity focused ultrasound and stereotactic body radiation are noninvasive but may damage healthy surrounding tissue and require long treatment times. Thus, there is an unmet need for a noninvasive ablation technique capable of treating large tumors rapidly and safely.

Histotripsy is a completely extracorporeal, non-thermal ablation technique which uses high-amplitude, short-duration, focused acoustic pulses at low duty cycle to homogenize target-tissue into an acellular slurry by means of finely-controlled acoustic cavitation. This dissertation investigated methods and systems toward the clinical translation of histotripsy for the treatment of large-volume tissue-targets. Hepatocellular carcinoma (HCC) was selected as a test-case to frame development efforts.

In the first part of this dissertation, strategies for accelerating treatment based on electronic focal steering of a phased array histotripsy transducer were investigated. Research was centered around the management and manipulation of residual cavitation nuclei, hundreds of

which are dispersed throughout the focus following collapse of the cavitation bubble cloud produced by each histotripsy pulse and perturb subsequent *de novo* cavitation at the intended focus. A novel method in which low-gain regions of the therapy beam were utilized to drive the coalescence of residual nuclei via the secondary Bjerknes force was developed and validated. Results demonstrated 99.9% complete ablation of a 27-mL volume (equivalent to a sphere 3.7 cm in diameter) within 30 s.

In the second part of this dissertation, compensation methods for respiratory motion of abdominal organs during histotripsy treatment were investigated. This part of the dissertation reviewed existing methods for respiratory motion compensation, explored the feasibility of integrating these methods with histotripsy therapy, and presented a novel cavitation-based motion tracking technique. Using this technique, residual cavitation nuclei were coalesced into a small bubble-system and used as an *in situ* fiducial marker which was tracked throughout a predefined trajectory by a histotripsy therapy system capable of receiving acoustic backscatter signals. Results demonstrated the feasibility of receiving acoustic signals from this fiducial cavitation bubble cloud throughout a 16-cm trajectory with a mean error of 0.7 ± 0.3 mm.

In the final part of the dissertation, novel design and fabrication techniques were developed for a phased array histotripsy transducer for ablation in the liver. The design implemented algorithms which analyzed human CT data to define the geometry of the array's aperture, divided the aperture into discrete, nesting elements, and simulated the electronic focal steering range of this aperture as a function of the number of elements. The resulting design yielded an array with 50% greater packing density than previous designs. Simulation shows that this array

is capable of electronically steering over a range sufficient to treat tissue-targets up to 3.6 cm in diameter in porcine or human subjects.

Chapter 1

Introduction

This dissertation focuses on the research and development of histotripsy for rapid ablation of large-volume tissue-targets toward the goal of eventual clinical translation. The work is presented in three primary sections: 1) feasibility of using the electronic focal steering functionality of a phased array histotripsy transducer to ablate a large volume of tissue rapidly, based primarily on the management and manipulation of residual cavitation nuclei, 2) the development of methods to compensate for respiratory motion, and 3) the design of a highly steerable histotripsy therapy phased array for the treatment of abdominal organs in human and porcine subjects.

1.1 Current Treatment Options for Large Tumors

Surgical resection has long been considered the gold-standard for solid-tumor intervention [1]–[3]. However, minimally invasive local ablation techniques are increasingly indicated as first-

option treatments for select cases due to lower cost, shorter associated hospital stays, and lower risk of complications [4]–[7]. Further motivating this transition, surgery is often feasible for only a small fraction of patients (9-27% of those presenting with hepatocellular carcinoma for example) due to the presence of various complicating factors including compromised organ function, tumor location and morphology, and patient frailty [5], [8]. Despite these advantages, current minimally invasive techniques including radio frequency ablation (RFA), microwave ablation (MWA), laser ablation, and cryo-therapy have traditionally struggled to treat tumors greater than 3 cm in diameter and those with more than 3 nodules [7], [9], [10].

Other contemporary clinical alternatives to surgical resection for larger tumors and those with multiple tumor nodules include stereotactic body radiation (SBRT), transcatheter arterial chemoembolization (TACE), and high intensity focused ultrasound (HIFU). SBRT, a technique that uses multiple overlapping radiation beams, can treat moderately sized tumors. However, for tumors >3 cm in diameter, its efficacy diminishes and the risk of damaging healthy tissue increases due to the toxicity associated with radiation [11], [12]. TACE has produced a significant tumor response in 17-62% of patients with large tumors, but the rate of complete tumor ablation is very low (0-5% in hepatocellular carcinoma, for example) [5]. Thus, TACE is generally used as a palliative or adjuvant therapy. HIFU has been used noninvasively to treat very large tumors (>10 cm) [13], [14] but is hampered by generally long treatment times which average approximately 5.5 hours for tumors roughly 8 cm in diameter, presenting a major obstacle to widespread clinical application [13]–[16]. Several studies have demonstrated i*n vivo* HIFU ablation rates of ≥ 2 mL/min for targets ≤ 8 mL (equivalent to a sphere with 2.5 cm diameter) using optimized electronic focal steering sequences [17], [18]. However, this

technique does not appear scalable to larger tissue targets while maintaining a high ablation rate due to concerns for damaging surrounding tissue structures. For thermal therapies like RFA, MWA, laser therapy, cyrotherapy, and HIFU, perfusion-mediated convection (due to blood flow and commonly referred to as the *heat sink effect*) presents a major challenge for achieving homogeneous coagulative necrosis in highly vascularized tissues like the liver, resulting in incomplete ablation and often requiring repeated treatment [3], [4], [19]. Despite early performance similar to RFA, the most recent generation of MWA devices have demonstrated high efficacy for select cases of HCC up to 5 cm [10] but retain the risk of serious complications associated with percutaneous device insertion [9], [20], [21]. MWA is also constrained to producing roughly spherical zones of ablation and requires margins of approximately 1 cm after which a gradient of thermal damage is observed [22], [23].

Fundamentally, contemporary clinical ablation techniques rely on the deposition of heat, radiation, or chemicals with only moderate localization to the tumor. Each modality is thereby constrained by confounding dosage limits after which larger tumors either go undertreated or patients are put at risk for serious collateral damage to healthy tissue. Thus, the unmet clinical need for a noninvasive technique capable of effectively treating large-volume tissues is unlikely to be met by further advances in existing clinical techniques.

1.2 Hepatocellular Carcinoma as a First Indication and Test-Case

Hepatocellular carcinoma (HCC) is the fastest growing cause of cancer deaths in the United States, having nearly tripled since the 1980s [24]–[26] with incidence expected to increase over

the next decade [27] and showing dismal survival rates of 0-10% among cases detected at a symptomatic stage [24]. In the third world, incidence is markedly higher and inevitably fatal [28]. Studies have found HCC > 3 cm in 76% of patients [29], HCC > 5 cm in 32-71% of patients [29]–[32], and HCC >10 cm in 13-40% of patients [30], [31], [33], [34]. Large size does not preclude the possibility of a successful intervention. Though still somewhat controversial for large HCC, surgical intervention – the only potentially curative treatment option currently available – has demonstrated a significant survival advantage over palliative care [35], [36]. Furthermore, several studies have shown that survival is not significantly different after the resection of large HCC compared to similar resections for HCC <5 cm when surgical candidates and techniques are carefully chosen [32], [37], [38]. These results suggest that the "nihilistic approach to [patients with very large HCC] among several surgeons and institutions" [35] may be unfounded [34]. However, among patients who undergo large HCC intervention, there remains significant morbidity due to complications during or shortly following surgery [32], [34] underscoring the unmet clinical need for a non-invasive technique capable of addressing large HCC.

The research described in this dissertation supports the feasibility of using histotripsy as a non-invasive, non-thermal, and highly localized technique for ablating large-volume tumors. Though HCC was selected as a test case, the overarching goal is to develop histotripsy as a generalizable platform technology for the treatment of large-volume tumors, an area of unmet clinical need. HCC was selected because it is a common malignancy worldwide with up to 76% of patients presenting with tumors greater than 3 cm in diameter [9], [29] and 31% presenting with multiple tumor nodules [29]. As a platform technology, histotripsy has the potential to

treat liver tumors as well as targets in the brain, prostate, breast, heart, kidney, and other tissues.

1.3 Histotripsy for Tumor Ablation

Histotripsy is a noninvasive, non-thermal tissue ablation technique which uses extremely high-amplitude (peak rarefactional pressure amplitudes >10 MPa), short-duration (as few as ~1.5 cycles) focused acoustic pulses at low duty cycle (typically <1%) to ablate soft tissue, generating an acellular, liquid-like homogenate. Histotripsy renders this function in a purely mechanical fashion by means of finely-controlled acoustic cavitation [39]–[47]. *In vivo* studies have demonstrated the potential use of histotripsy for several clinical applications where tissue-ablation is desired including cancer [48]–[52], thrombosis [53]–[56], benign prostate hyperplasia [57]–[59], congenital heart disease [60]–[62], renal calculi [63]–[65], and several applications in the brain [66] including intracerebral hemorrhage [67].

Histotripsy's therapeutic cavitation effect is predicated on exceeding a precise rarefactional acoustic pressure threshold [68], [69]. The effect is restricted to a well-defined focal region where time-averaged, macroscopic heating is minimal and does not rely upon (nor typically produce) coagulative necrosis. Because the mechanism of tissue-ablation (inertial cavitation) is purely mechanical, histotripsy is largely insensitive to overtreatment and pulses can be applied with an extremely flexible timing sequence. In a previous study, heating of overlying and surrounding tissues was shown to be negligible even during very long exposures when a thermal steady-state was reached [70]. Previous studies have also demonstrated several other unique advantages of histotripsy over existing ablative techniques: 1) the ability to generate an

acellular homogenate [71] while sparing vessels and other critical structures which may reside within the treatment zone [72], [73], 2) a moderate treatment rate of 1 mL/min by mechanically scanning the transducer's focus [73] with the potential to dramatically increase this rate using electronic focal steering, 3) aberration correction is not strictly necessary for robust targeting [70], [74], 4) the ability to accommodate real-time ultrasound imaging guidance and dosimetry feedback readily [75], [76], and 5) sharp treatment boundaries [57], [77]. Building upon these studies to advance histotripsy further toward clinical applicability will require pioneering techniques for improving treatment efficiency, compensating for breathing motion, and designing and fabricating highly specialized transducers for validation studies. By addressing these challenges, the research presented in this dissertation bolsters the feasibility of histotripsy as a transformative large-volume ablation therapy.

1.4 Current Treatment-Rate Limitations of Histotripsy

The ultimate treatment-rate limit of histotripsy is dictated by the deposition of heat at high PRF and by a phenomenon known as the *cavitation memory effect*. While histotripsy tissue-ablation does not *rely* on temperature elevation, some incidental heat is nevertheless deposited to tissues along the acoustic propagation path and at and near the focus. At moderate PRF (e.g., 200 Hz) the temperature elevation within intervening and surrounding tissue structures is modest [78]. However, in order to achieve the ablation of large tissue-volumes (>30 mL) in a clinically practical time-frame (<20 min), a high PRF (on the order of 1 kHz) is expected to be necessary. A full heating model encompassing the parameters which may

contribute to tissue-heating *in vivo* (transducer geometry, acoustic pulse design, nonlinear acoustic effects, acoustic coupling methods, tissue composition and vascularization, etc.) is outside the scope of this dissertation and has not been attempted herein.

Following the collapse of a cavitation bubble cloud, residual microbubbles can persist for up to seconds and function as nuclei for subsequent cavitation events. The presence of such residual microbubbles within the focal zone or along the intervening acoustic propagation path can result in attenuation [79]–[81] and scattering of the therapy pulse [68], [82] as well as distortion [83], [84] of the intended focal zone in a phenomenon referred to as the *cavitation memory effect*. Previous studies have shown that the cavitation memory effect can hinder fractionation efficiency and homogeneity during histotripsy treatment [77], [83], [85], [86].

Strategies for mitigating the cavitation memory effect can be broadly categorized as passive or active. In the passive approach, sufficient time is provided between pulses such that residual nuclei dissolve under the Laplace pressure and at rates dependent on the dissolved gas concentration in the host medium [87], [88]. Because the time required for passive dissolution may be >1 s for microbubbles of the size remaining after histotripsy cavitation collapse, the practical implementation of a passive approach for therapeutic applications necessitates electronically steering the therapy focus of a phased array transducer to other locations within an ablation zone defined by a grid of numerous overlapping foci during the off-time for a given focus [86].

An active strategy, termed *bubble coalescence* (BC), follows each high-amplitude therapy pulse with a moderately long (tens to thousands of cycles), lower-amplitude (~1 MPa) BC pulse which drives residual nuclei together within several milliseconds by means of the secondary

Bjerknes force [89]–[96]. Previous studies have demonstrated that histotripsy with BC can significantly increase ablation speed [93]–[97] by allowing a relatively high pulse repetition frequency (PRF) for histotripsy (e.g., PRF = 100 Hz for a single focus) while maintaining treatment homogeneity. In these studies, separate acoustic sequences for histotripsy and BC were transmitted. The BC sequences found to be optimal in the studies by Duryea et al. and Shi et al. deposited approximately 30% additional acoustic energy (relative to the histotripsy therapy pulses) within the -6 dB region of the therapy focus [95], [97]. The ablation of large tissue volumes may require a high PRF in order to achieve a clinically practical total treatment time. For such an application, the additional acoustic energy associated with a separate BC sequence may pose a risk of tissue heating or prolong treatment times. Thus, careful consideration must be given to accounting for the cavitation memory effect in the design of effective electronic focal steering sequences for the treatment of large-volume tissue structures.

1.5 Respiratory Motion

Like radiation therapy and several imaging modalities, histotripsy is sensitive to the periodic respiratory motion of abdominal organs, which typically oscillate at approximately 0.2-0.3 Hz [98], [99], with 0.5-4 cm peak-to-trough amplitude [100]–[107], and at up to 1.5-3 cm/s [107]–[112] during normal respiration. Without compensation for respiratory motion there is an elevated risk of under-treating target-tissue, damaging adjacent healthy tissues [108], [113], and prolonging treatment times. Several existing methods for compensation would likely be amenable to integration with histotripsy therapy. Respiratory gating is a simple solution

commonly used in radiation therapies [105], [107], [114]–[117] and one likely to be particularly amenable to histotripsy therapy.

Previous studies have demonstrated the ability of phased array therapy transducers to perform motion tracking using tissue speckle and prominent features like blood vessels as reference markers [118]–[121]. Feature tracking is the more robust of the two methods [122] but requires the proximity of a prominent feature to the target. If this condition is not met, the deformable nature of organs like the liver [122]–[124] may introduce targeting errors when no proximal feature is available for tracking. The clinical translation of histotripsy would benefit from a robust method for addressing respiratory motion.

1.6 Structure of this Dissertation

This dissertation is presented in six chapters which document the research and development of histotripsy for the ablation of large tissue-targets toward the goal of eventual clinical translation. The present section briefly summarizes each chapter.

Chapter 1 provides motivation for undertaking this research and introduces background information on topics to be discussed subsequently.

Chapter 2 characterizes the formation and dissolution behavior of residual cavitation nuclei formed during the growth and collapse of histotripsy cavitation bubble clouds as these phenomena pertain to the cavitation memory effect. It then uses insights derived from this analysis to devise a basic electronic focal steering strategy which is used to demonstrate proof of principle regarding the use of intrinsic-threshold histotripsy with electronic focal steering (EFS) for the noninvasive homogenization of a large-volume tissue-target.

Chapter 3 introduces a novel method for performing bubble coalescence which uses low-gain regions of the histotripsy therapy beam rather than separate acoustic sequences as demonstrated in previous studies. Proof of principle is established using a single, isolated focus. A series of experiments using two isolated foci is performed in which separation distance and pulse-timing are varied to serve as the basis for the design of strategic EFS sequences. Theoretical and practical design considerations of EFS sequences are described and the sequences are tested in tissue-mimicking gel phantoms.

Chapter 4 first reviews compensation methods for respiratory motion during ablative therapies and explores the feasibility of integrating existing techniques with histotripsy. The chapter then introduces a novel cavitation-based motion tracking technique in which residual cavitation nuclei are used as a fiducial marker and tracked throughout a predefined trajectory by a histotripsy therapy system capable of receiving acoustic backscatter signals.

Chapter 5 describes novel design and fabrication techniques for a histotripsy phased array transducer with elements which are arbitrarily shaped, densely packed, and easily replaceable. The design starts with the selection of basic geometric dimensions which are guided by an analysis of a set of human CT scans. Details of the material-selection process are presented. The development of MATLAB scripts which are used to select the number of elements and predict the EFS range is discussed. The design of specialized element modules, a mounting scaffold, and fabrication fixtures are also presented. Finally, several array elements, the remainder of which needed to fully populate the array are still under construction at the time of this writing, are calibrated and used to guide an acoustic simulation of the array's performance.

Chapter 6 summarizes the work of this dissertation and suggests several possible avenues for ongoing research based on its findings.

Chapter 2

Electronic Focal Steering for Large-Volume Ablation: Proof of Principle

This chapter demonstrates proof of principle regarding the use of intrinsic-threshold histotripsy with electronic focal steering (EFS) for the noninvasive ablation of a large-volume tissue-target. Because the focal zone of the transducer used in this study was much smaller than the desired total treatment zone, as is commonly the case, it was necessary to deliver pulses throughout a grid composed of numerous overlapping foci which together populate the larger total volume. The primary motivation for using EFS is its ability to translate the focus from one grid position to the next nearly instantaneously (on the order of 10 microseconds if so desired) while the histotripsy array remains stationary, thereby allowing scanning rates much faster than mechanical steering. We hypothesize that a strategic EFS sequence enabled by the ability to steer the focus rapidly will have the capacity to mitigate the perturbation of histotripsy's therapeutic effect caused by persistent residual cavitation nuclei. This hypothesis was tested by characterizing residual nuclei and their impact on the efficiency and homogeneity

of lesion-formation in tissue-mimicking gel phantoms where a lesion was generated at a single electronic focal steering position using different pulse repetition frequencies (PRFs). By varying PRF, residual nuclei dissolved passively to varying degrees between pulses. Treatment parameters derived from these simplified experiments were then applied to large-volume ablation experiments performed in *ex vivo* bovine hepatic tissue where the treatment-volume was defined by a grid comprised of numerous overlapping electronic focal steering positions and where residual nuclei were assumed to dissolve in a similarly passive manner.

*Note: portions of this chapter were published as listed below.

1. **Jonathan E. Lundt**, Steven P Allen, Jiaqi Shi, Timothy L. Hall, Charles A. Cain, Zhen Xu. Noninvasive, Rapid Ablation of Tissue Volume Using Histotripsy. *Ultrasound in Medicine and Biology,* Volume 43, Issue 12, December 2017, Pages 2834-2847.
2. **Jonathan Lundt,** Timothy Hall, Akshay Rao, Charles Cain, Zhen Xu. Coalescence of Residual Histotripsy Cavitation Nuclei Using Low-Gain Regions of the Therapy Beam During Electronic Focal Steering. *Physics in Medicine and Biology*, 2018. Accepted manuscript online 24 Oct. 2018.
3. **J.E. Lundt**, S.P. Allen, J. Shi, F.T. Lee Jr, C.S. Cho, T.L. Hall, C.A. Cain, Z. Xu. Noninvasive, Non-Thermal, Rapid Ablation of Tissue Using Histotripsy. World Conference on Interventional Oncology, Boston, MA, June 7-10, 2018.
4. **J.E. Lundt**, S.P. Allen, J. Shi, J.R. Sukovich, T.L. Hall, C.A. Cain, Z. Xu. Rapid Ablation of Large Tissue Volume Using Histotripsy with Electronic Focal Steering. Institute of Electrical and Electronics Engineers – International Ultrasonics Symposium, Tours, France, September 18-21, 2016.
5. **J.E. Lundt**, S.P. Allen, J.R. Sukovich, T.L. Hall, C.A. Cain, Z. Xu. Noninvasive, Rapid Ablation of Large Tissue Volume Using Histotripsy. International Symposium on Therapeutic Ultrasound, Tel Aviv, Israel, May 14-16, 2016.

2.1 Introduction

2.1.1 Generation of Residual Microbubbles and the Cavitation Memory Effect

During the expansion phase of *de novo* histotripsy cavitation, gas diffuses into endogenous nanoscale nuclei from the host medium, increasing gas content by what Bader and Bollen

estimate to be more than five orders of magnitude [125]. The inertial collapse of an acoustic cavitation bubble or bubble cloud is commonly followed by several rebounds of diminishing amplitude [126]–[130]. Following the final cavitation collapse, the focal zone can be littered with tens [131] to hundreds [132] of residual microbubbles with radii ranging from less than one micron to tens of microns [127], [131], [133], [134]. Micron-scale bubbles may then persist for up to seconds even in degassed media before completely dissolving [87]. Sources of residual nuclei described in the literature include the primary cavitation bubble itself, incomplete fusion of individual bubbles during the expansion of the cloud, particularly at the periphery of the cloud [135], and fission of the primary bubble during collapse [132]. If a subsequent pulse arrives before residual bubbles have sufficient time to dissolve, they can function as cavitation nuclei for subsequent pulses in a phenomenon known as the *cavitation memory effect* [83], [95], [131], [136]–[139]. The presence of such pre-existing microbubbles within the focal zone or along the intervening acoustic propagation path can result in attenuation [79]–[81] and scattering of the therapy pulse [68], [82] as well as distortion [83], [84] of the intended focal zone. Previous studies have shown that this preferential, repeated nucleation of bubbles at specific positions within the focus can hinder fractionation efficiency and homogeneity during histotripsy treatment [77], [83], [85], [86].

Strategies for mitigating the cavitation memory effect can be broadly categorized as passive or active. In the passive approach, which is addressed in this chapter, sufficient time must be provided between pulses such that residual nuclei dissolve passively, driven by the Laplace pressure and undersaturation of dissolved gas in the host medium [87], [88]. Alternatively, an active strategy for mitigating the cavitation memory effect which has been termed *bubble*

coalescence, follows each high-amplitude therapy pulse with a moderately long (tens to thousands of cycles), lower-amplitude (~1 MPa) pulse which drives residual nuclei together within several milliseconds by means of the secondary Bjerknes force [89]–[93], [95]. A novel approach to driving bubble coalescence using a low-gain feature of the therapy beam and EFS is presented in Chapter 3.

Because the time required for passive dissolution may be >1 s for microbubbles of the size remaining after histotripsy cavitation collapse, the practical implementation of an EFS strategy based on passive dissolution of residual nuclei necessitates steering the therapy focus to other locations within an ablation zone defined by a grid of numerous overlapping foci during the off-time for a given focus [86]. Histotripsy with EFS can steer to thousands of overlapping focal locations (which together fully populate the larger volume) during this off-time period and thereby afford an opportunity for residual nuclei to dissolve unperturbed at a given focus. In this manner, the treatment-time for a large target-volume can be shortened while maintaining high per-pulse homogenization efficiency. We hypothesize that histotripsy combined with EFS performed using a phased array transducer can achieve rapid, complete ablation of a large target-volume.

In this study, we test this hypothesis using a 256-element phased array transducer. First, the size and dissolution behavior of residual cavitation nuclei were characterized in tissue-mimicking gel phantoms. Second, a lesion was generated at a single focal site in a tissue-mimicking phantom and monitored to establish acoustic parameters (PRF, dose and focal spacing). Finally, acoustic parameters derived from phantom experiments were applied to large-volume homogenization experiments using 1000 EFS positions and performed in *ex vivo*

bovine liver samples. Lesion-size and the completeness of tissue ablation were assessed with magnetic resonance imaging (MRI) and histology.

2.1.2 Rapid Ablation of a Large Ex Vivo Tissue Volume

Histotripsy using shock scattering and boiling mechanisms have demonstrated ablation of tissue targets in the 20-60 mL range at a rate of approximately 1 mL/min [73], [140]. These techniques generate a bubble cloud larger than the region of the therapy focus where P- exceeds the intrinsic threshold by taking advantage of the reflection and inversion of high-amplitude compressional excursions in the incident focal waveform at the surface of relatively small cavitation bubbles formed by the first few rarefactional excursions [68] or at the surface of boiling bubbles [141]. In contrast, the method using the intrinsic threshold mechanism, also referred to as *microtrpsy* [142], generates cavitation using a focal waveform with ~1.5 cycles where the principle rarefactional excursion exceeds the intrinsic cavitation threshold of the host medium. The intrinsic threshold mechanism presents several advantages with respect to heat deposition: 1) it relies on fewer cycles per pulse (the development of “monopolar” pulses could further improve upon this advantage [143]), 2) it does not rely on high-amplitude shocks which promote unwanted heating, and 3) it does not require any form of maintenance pulses [144]. The work in this dissertation addresses concerns for the intrinsic threshold mechanism though it remains unclear which technique will ultimately prove to be best-suited for clinical practice at the time of this writing.

Previous studies have demonstrated that shock scattering histotripsy with mechanical focal steering is capable of moderate ablation rates. Khoklova *et al.* showed that histotripsy is capable of lysing large hemotomas (20 mL) *in vitro* at a rate of 1.3 mL/min using mechanical focal steering [140]. Vlaisavljevich *et al.* demonstrated the ability to generate a 60 mL lesion within 60 minutes in an *in* vivo porcine model by mechanically steering the therapy focus of a transducer that used the shock scattering mechanism with multi-cycle (≥3 cycles) pulses to generate and maintain a cavitation bubble cloud [68].

Electronic focal steering has been used with therapeutic ultrasound for tissue volume ablation, particularly with thermal HIFU [145]–[148]. Previous studies have demonstrated that cavitation-induced tissue homogenization can be achieved by electronically steering the therapy focus while the transducer remains in a fixed position [149], [150]. In these early proof-of-principle studies where a high treatment rate was not the primary objective, the ablation rate was a fairly modest 0.05 mL/min. In our group, Zhang *et al.* demonstrated that histotripsy with electronic focal steering can be combined with mechanical focal steering, resulting in higher efficiency for thrombolysis applications than when mechanical steering is used alone; however, the steering range used for this application was small (± 1 mm) [55].

The cavitation memory effect necessitates moving the focus throughout a volume-treatment grid on a per-pulse basis rather than dwelling in one grid-position and then moving to the next position. This requirement makes EFS much more attractive than mechanical steering. The principle advantage of electronic focal steering is its ability to scan the focus from one position to the next nearly instantaneously (on the order of 10 microseconds if so desired) while the histotripsy array remains stationary. Mechanical steering of an array with a fixed focus requires

moving the entire therapy array within the coupling liquid and in close proximity to an easily deformable viscoelastic target (the patient), introducing a host of potentially confounding challenges. EFS allows the system to scan a large number of overlapping foci, which together comprise a treatment grid, rapidly enough that the time required for residual nuclei to dissolve at a given focus can be used to treat thousands of other foci within the treatment grid. In this section, acoustic and steering parameters derived from phantom experiments described in the previous section were applied to volume-ablation experiments using electronic focal steering performed in *ex vivo* bovine liver samples. Lesion size and the completeness of tissue ablation were assessed with MRI and histology.

2.2 Methods

2.2.1 Characterization of Residual Microbubbles and the Cavitation Memory Effect

2.2.1.1 Experimental Setup

The transducer used for this study, as previously described [86], was a hemispherical phased array with 256 individually addressable elements. It had a center frequency of 250 kHz, a 30 cm aperture, and a 15 cm focal distance. It was controlled by a field programmable gate array (FPGA) digital circuit and generated acoustic pulses approximately 1.5-cycles in duration as shown in figure 2.3. Histotripsy pulses in this study generated cavitation by the intrinsic

threshold mechanism (also termed *microtripsy*) [151]. Experiments were performed in tissue-mimicking agarose hydrogel phantoms measuring 127 mm x 70 mm x 13 mm and secured using a 3D printed holder designed such that no part of the holder blocked the ultrasound propagation path to the focus [86]. The center of the therapy focus was always positioned at least 20 mm from the holder where pressure was ~26 dB down from the peak pressure, such that scattered pressure at the focus would be expected to be negligible. Agarose gel was prepared by adding low-melting-point agarose powder (DSA20070, Dot Scientific, Burton, MI) at 1 g per 100 mL to deionized water and bringing the mixture to a boil. A previous study in our lab found the elastic modulus of gels prepared with this agarose concentration to be 21.7 ± 1.0 kPa which is on the order of physiological values of soft tissue [152]. The hot gel was then vacuum filtered to 0.2 μm (12-566-218, Thermo Scientific, Waltham, MA) to remove dust and debris, poured into a mold with the gel holder, and allowed to cool to room temperature. Photographs of the mold and gel holders appear in fig. 1. Prior to use, phantoms were placed in a room temperature water bath held at either ≤ approximately 20% or approximately 100% dissolved gas concentration with respect to saturation, depending on the experiment to be performed and allowed to equilibrate [153] for ≥ 12 hours prior to use.

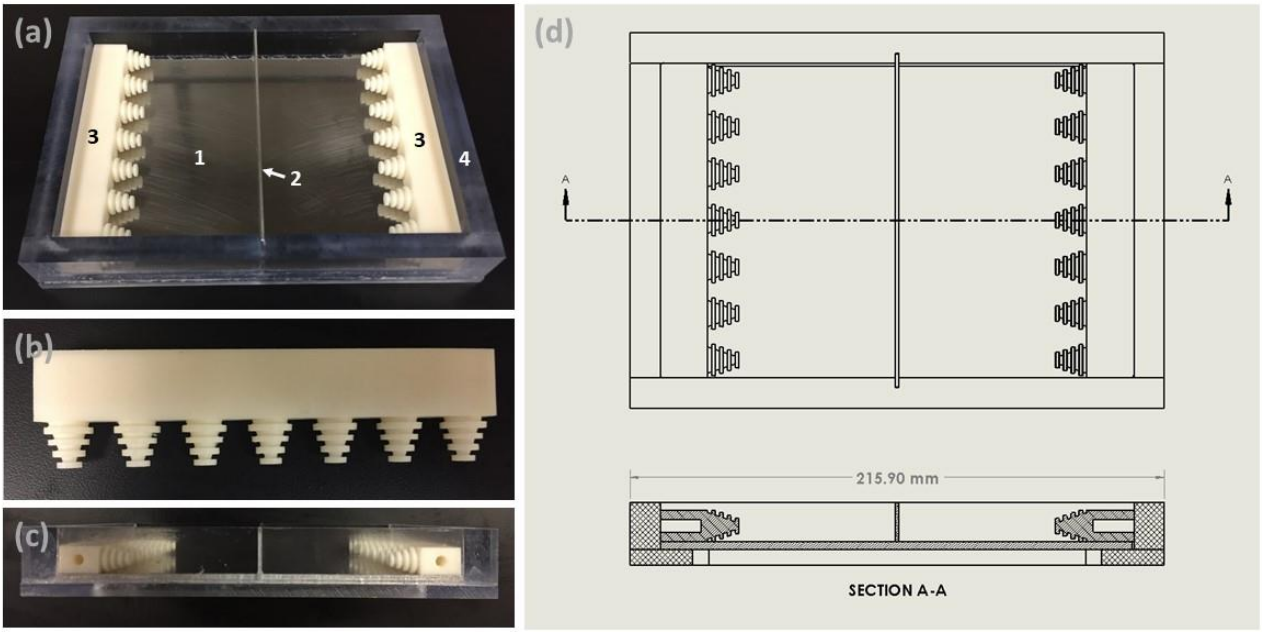

Figure 2. 1. Photographs and drawings of tissue mimicking gel phantom mold and gel-holders. a) Angled view of mold with gel-holders prior to addition of gel. 1 indicates stainless steel bottom plate. 2 indicates aluminum divider which allows two phantoms to be made simultaneously in the same mold. 3 indicates gel-holder which is later used in experimentation. 4 indicates polycarbonate frame. Bottom plate and frame are temporarily bonded using high vacuum grease and can be easily separated once the gel has set. b) Gel-holder in isolation. Cone-shaped protrusions with ribbed features serve as anchors to suspend the gel phantom vertically. c) Side view of mold and gel-holders. d) Computer aided design (CAD) drawing of mold and gel holders. Upper sketch is a top-down view. Lower sketch is a cross sectional view. Once the gel was set, the phantoms were extracted from the mold by lifting the stainless steel plate.

These gas concentrations were selected in an attempt to represent two distinct aspects of cavitation activity *in vivo*. First, for a given host medium, the acoustic pressure threshold for the heterogeneous nucleation of inertial cavitation is influenced by the size and number-density of endogenous stabilized nuclei [154]–[157]. In an *in vivo* setting, endogenous nuclei are believed to be relatively small and sparse [66], [158], [159], due to physiological filtration and cleaning mechanisms [160]. Agarose gel, in contrast has been described as “hyper-nucleated,” containing relatively large nuclei at high number-density [161]. Previous studies have suggested that cavitation nucleation behavior *in vivo* can be approximated in agarose gel by degassing phantoms during preparation [162], [163]. Second, the dissolution-time of a microbubble is dramatically shorter in a degassed medium than one near gas-saturation [87], [88], [164].

Literature values for the gas concentration in living mammalian tissues are approximately 90-95% relative to saturation in water [134], [165]. Thus, one group of samples was prepared with ≤ approximately 20% gas concentration to mimic the nucleation behavior of endogenous nuclei *in vivo* [83], [144], [166], while a second group of samples was prepared with approximately 100% gas concentration to mimic the dissolution behavior of residual nuclei *in vivo*. Gas concentration was measured by a dissolved oxygen probe (Orion Star A323, Thermo Scientific, Waltham, MA) with relative accuracy of ± 2% within the range measured in this study (manufacturer's claim).

The transducer was oriented facing upward and the gel phantom was affixed to a 3D positioning system as shown in figure 2.2. The activity of residual nuclei at a single focus located at (0 mm, 3 mm, 0 mm) was monitored by an optical camera. Subsequent references to coordinate positions omit the unit (mm) unless otherwise indicated. This position, slightly offset from the geometric focus (0, 0, 0), was selected to reduce the impact of cavitation expansion and collapse signals on residual nuclei, having been reflected and refocused by the surface of the transducer [42]. It was observed that the reflection of cavitation signals originating at a position (x, y, z), were refocused to a mirrored position (-x, -y, -z).

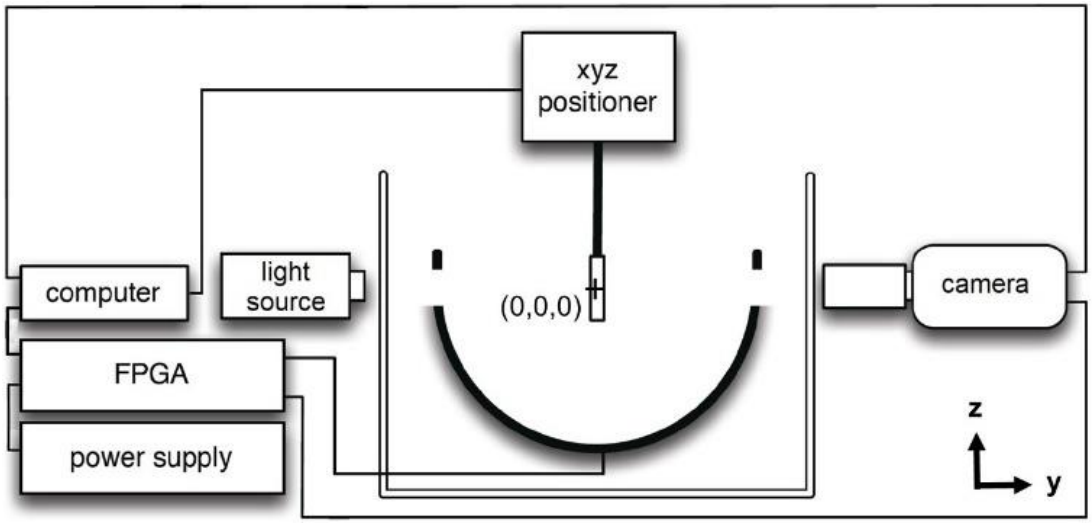

Figure 2. 2. Diagram of experimental setup. Geometric focus is labeled (0, 0, 0).

The ultrasound pressure waveform at (0, 3, 0) was characterized using a hydrophone with robust directivity-response (HGL-0085, Onda, Sunnyvale, CA). At the acoustic pressure used for experimentation, cavitation was generated instantaneously. Thus, direct measurement was not possible. For the calibration procedure, each of the array's modules was driven individually at the voltage used for experimentation. Individual waveforms were then summed in a linear fashion to estimate the therapy waveform. The peak rarefactional pressure amplitude (P-) at (0, 3, 0) was estimated to be approximately 52 MPa. While underestimation of nonlinear effects is a drawback of this approach, several factors limited the extent of error from nonlinear effects. The transducer's f-number was very low (0.5) and the ratio of active area to the aperture's total surface area was modest (0.57). Thus, waveforms from individual modules interacted minimally until near the focus [167]. The center frequency (250 kHz) was also fairly low [168], [169]. Additionally, nonlinear acoustic propagation impacts the compressional phase to a greater

extent than the rarefactional phase [170], [171], which is of primary interest for histotripsy therapy in the absence of shock scattering [68].

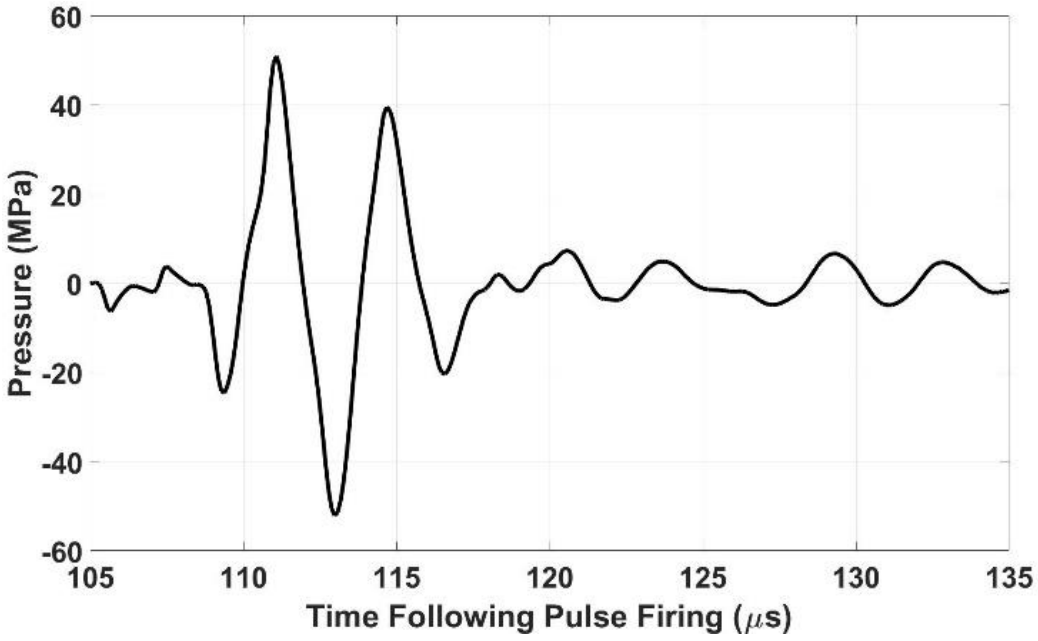

Figure 2. 3. Acoustic waveform at EFS position (0, 3, 0) estimated by the linear summation of hydrophone measurements from individual elements. t=0 corresponds to the time at which the pulse was fired.

2.2.1.2 Investigation of the Generation of Residual Cavitation Nuclei

The time-course of cavitation activity was monitored by a high speed optical camera (Phantom v2012, Vision Research, Wayne, NJ) equipped with a telephoto lens (1922, Nikkor AF 28 mm f/2.8D, Nikon Corporation, Minato, Tokyo, Japan) and teleconverter (MC 2X N-AF DGII, Bower, Long Island City, NY) backlit with an LED light source (CLU550-3626C1-40AL7G4-B24, Citizen Electronics, Fujiyoshida, Japan) operated in continuous mode. Images had resolution of

128 pixels x 96 pixels and covered a field of view measuring 18 mm x 13.5 mm at the focal plane. Frames were captured at a rate of 500,000 s^{-1} with an exposure of 285 ns. Frame-capture was initiated at approximately 8 microseconds prior to the arrival of the acoustic pulse at the focus and continued for a duration of 800 microseconds. 200 pulses were delivered to a clear gel phantom with a pulse repetition period of 5 s to provide sufficient time for residual nuclei to dissolve. A total of 10 samples were treated in this manner in which separate lesions were generated, each at an untreated location in the gel phantom.

Images were post-processed in MATLAB (R2017a, The Mathworks, Natick, MA) by first converting images to binary using the *imbinarize* function with the threshold set to 0.5 and then masking the periphery of the image such that only the focus plus an approximately 2 mm margin was retained. This prevented the inclusion of peripheral bubbles arising from weak nuclei [82] as part of the primary cloud. Images were then processed by the *imfill* function to remove optical reflections from the surface of large bubbles which otherwise might be counted as “holes” within the interior of the projected bubble’s area. These data provided a statistical perspective on the complete expansion, collapse, and rebound cycle of individual cavitation clouds and were used to guide subsequent higher-resolution imaging experiments in which only a single frame could be captured per cavitation event.

Previous studies cite fission of the bubble cloud upon collapse as the primary mechanism for the generation of residual nuclei [128], [131], [132], [172]. Pishchalnikov et al. showed that bubbles at the periphery of a bubble cloud may remain isolated, fail to fuse with bubbles near the center of the cloud, and undergo collapse well before the primary, coalesced bubble [135]. This phenomenon, however, has not been discussed (in any literature that the author of this

study is aware of) as a mechanism for the generation of residual cavitation nuclei. In the present study, I hypothesize that peripheral microbubbles generated during the initial cloud expansion are the primary source of residual nuclei which persist after violent cavitation activity has ceased.

The formation of residual nuclei was investigated using an optical camera (FL3-U3-120S3C-C, FLIR Integrated Imaging Solutions, Richmond, BC, Canada) equipped with a telephoto lens (107-306, Sigma Corporation, Ronkonkoma, NY). In this configuration, images had a resolution of approximately 3 μm/pixel. Bubble clouds were backlit by a custom-built strobe light emitting flashes 5 μs in duration as measured by a photodetector (DET02AFC, Thorlabs, Newton, NJ). The histotripsy focus was electronically steered to (0, 3, 0) and pulses with approximately 52 MPa P- were fired at 5 s pulse repetition period (PRP). One frame per pulse was captured over the course of 200 pulses. The timing of frame-capture was incremented by 5 μs for each pulse starting at 10 μs prior to the arrival of the pulse at the focus. In this manner, a series of images tracking the evolution of typical cavitation growth, collapse, and rebound and well as the activity of residual nuclei was reconstructed, covering a 1-ms span beginning slightly before the arrival of the histotripsy pulse at position (0, 3, 0). Following each pulse, the image was saved in *.tif* format to the personal computer (PC) used to run the experiment. The principle limitation of this composite approach is that it fails to account for the inter-pulse variation in cavitation dynamics (i.e., collapse time). Images were post-processed in MATLAB to reorient the images, crop, and adjust contrast to make fine features more easily discernable.

2.2.1.3 Enumeration of Residual Cavitation Nuclei

The number of residual nuclei was quantified as a function of the number of pulses delivered using the same imaging setup as the previous section with the exception that every frame was captured at 210 microseconds following the arrival of the therapy pulse at the focus. It was observed that this time-point corresponded to the arrival at the focus of the reflection of the cavitation expansion signal from the surface of the array. The reflected signal was detectable by hydrophone (CA-1148-2, Dynasen, Goleta, CA) only when cavitation was generated at the therapy focus and was on the order of approximately 2 MPa peak-to-peak. This pressure-amplitude was sufficient to excite weak nuclei in the periphery of the expanded cavitation bubble cloud but not sufficient to generate cavitation *de novo* in filtered, degassed aqueous media [152], [163], [173]. In this manner, the reflected signal served as probe-pulse for interrogating these microbubbles which would otherwise be too small for the camera to resolve. 2000 pulses were applied to a single, untreated location in a gel phantom and a single frame was recorded for each.

Images were post-processed in MATLAB by a script that segmented and enumerated peripheral bubbles. Segmentation was performed through a series of thresholding, filtering, morphological, and masking operations. An adaptive thresholding method described by Bradley and Roth [174] and available for download as *bradley.m* online (https://www.mathworks.com/matlabcentral/fileexchange/40854-bradley-local-image-thresholding) was particularly helpful. A limitation of this segmentation protocol is the ability to resolve very small bubbles those that appear closely adjacent in the image. Better sensitivity and specificity are likely possible by employing more advanced image processing techniques

like k-means or perhaps machine learning, albeit at the expense of additional algorithm development and processing time.

The total number of peripheral bubbles was estimated by multiplying the number peripheral bubbles visible in the image by a correction factor to account for those not detectable by the camera due to the presence of the dense primary cavitation bubble cloud [132]. As shown in figure 2.4, this correction factor was derived by constructing a CAD model (Solidworks 2017, Dassault Systèmes, Vélizy-Villacoublay, France) based on an imported image using the *Sketch Picture* function. The correction factor was set to 2.13.

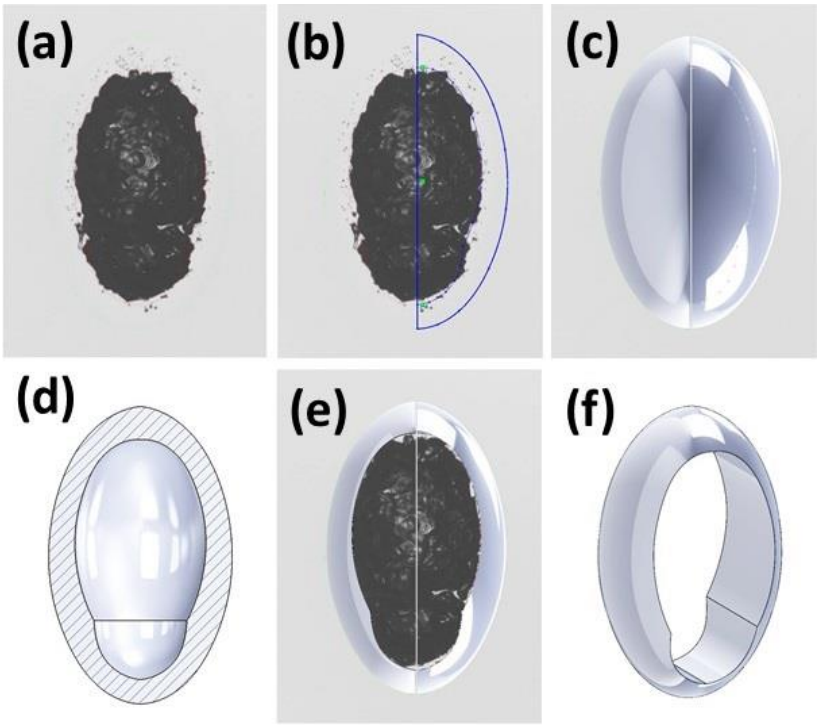

Figure 2. 4. Diagram detailing construction of a CAD model representing the shell of peripheral bubbles surrounding the primary cavitation cloud. a) Image of bubble cloud formed by 250th pulse. Sparse shell of peripheral bubbles is visible surrounding dense primary bubble cloud. b) Solidworks sketch using bubble cloud image as a guide. c) Three-dimensional solid model of full shell formed from sketch. d) Cross-sectional view of shell model. e) Solid model of region of the shell in which peripheral bubbles were detectable by the camera. View is along the axis of the camera. Bubble image is shown. f) Angled view of partial shell. Direction of ultrasound propagation is from bottom to top of image.

2.2.1.4 Passive Dissolution of Residual Cavitation Nuclei

To provide a reference for subsequent lesion-formation experiments described later in this chapter and bubble coalescence experiments described in Chapter 3, the passive dissolution behavior of residual nuclei in gel phantoms with 20% and 100% gas concentration was monitored by optical imaging employing the same setup as the previous two sections. For phantoms with 20% gas concentration, histotripsy pulses were fired at PRP of 5 s and 50 frames were captured at 100-ms intervals with the first frame captured at 10 ms following each initial cavitation expansion. For phantoms with 100% gas concentration, histotripsy pulses were fired at 800 s PRP. Here, one frame was collected every 5 s for 800 s starting at 100 ms following each initial cavitation expansion. These PRP values were selected to provide sufficient time for the dissolution of residual bubbles between pulses.

Images were post-processed in MATLAB using a script that segmented and sized residual nuclei. To summarize the functionality of this script briefly, it adjusted contrast, subtracted the background using the final image in the sequence which contained no bubbles, performed initial segmentation using an adaptive thresholding method [174], filled in “holes” formed by optical reflections within bubbles using the *imclose* and *imfill* functions, smoothed the image using *imgaussfilt*, and finally applied the *imbinarize* function. The area of objects in the resulting image were characterized using the *regionprops* function from which bubble radii were calculated. The script was calibrated by imaging opaque polystyrene beads 25 µm in diameter (Stock No. 42730, Alfa Aesar, Ward Hill, MA) placed in a disposable hemocytometer (C-Chip, SKC, Inc., Covington, GA) and submerged at the focal position (0, 3, 0). 25 µm beads were

selected because this was observed to be the approximate initial size of the residual nuclei of interest.

The passive dissolution of a single bubble was also modeled using the differential equation of Epstein and Plesset which appears below. Please see ref. [87], Eq. (34) and ref. [164], Eq. (3) for more detail.

$$\frac{da}{dt} = -D\frac{C_s}{\rho_a}\frac{1-\gamma+\frac{\tau}{\rho_a a}}{1+\frac{2}{3}\frac{\tau}{\rho_a a}}\left[\frac{1}{a}+\frac{1}{\sqrt{\pi D t}}\right], \tag{2.1}$$

where

$$\tau = \frac{2M\sigma}{BT}, \tag{2.2}$$

$$\gamma = \frac{C_0}{C_s}, \tag{2.3}$$

D = 2.4 m·s^{-2} is the diffusion constant of air in water [175], C_s = 0.024 kg·m^{-3} is the concentration of air in saturated distilled water, C_0 is the concentration of air in the host medium, ρ_a = 1.196 kg/m^3 is the density of air at 1 atm and 22° C, M = 0.02897 kg·mol^{-1} is the molecular weight of air, σ = 0.072 N·m^{-1} is the surface tension of the air-water interface, B = 8.31447 J·mol^{-1}·K^{-1}, T = 295.15 K is the temperature of the host medium, a is the radius of the bubble in meters, and t is time in seconds. For the case where gas concentration was ≤ ~20%, initial values of a were set to 8, 12, and 16 microns. For the case of where gas concentration was ~100%, the initial values of a were set to 16, 25, and 36 microns. These values were selected after a cursory examination of the experimental data and intended to bracket the range of initial radii observed. Huen's

method was used to solve this equation in MATLAB (see pages 266-267 of ref. [176]) in a manner similar to the approach taken by Kapodistrias and Dahl [164].

It is expected that the constants associated with bubble dissolution in water would be nearly identical to those for agarose gel due to water comprising the vast majority of the medium. Bhunia et al. found that values of oxygen diffusivity differed by approximately 9% between water and 1% agar [153]. In tissue, however, organic materials, present in varying degrees of homogenization, will likely accumulate at the gas-liquid interface of the bubble and prolong its dissolution time. This phenomenon has been thoroughly documented in the literature and is the basic principle behind the design of ultrasound contrast agents [154], [177]–[179].

2.2.1.5 Single Lesion Formation in RBC Phantoms

To monitor progression of lesion formation resulting from histotripsy cavitation activity, a second group of phantoms with identical dimensions was prepared with a layer 0.5 mm thick containing red blood cells (RBCs) at 5% concentration and positioned in the middle of the phantom. RBC phantoms allowed cavitation and resulting damage to be directly visualized on a per-pulse basis [162]. This experiment served to establish treatment parameters including PRF, the number of pulses to deliver (dose) for a given electronic focal steering site, and the spacing between adjacent electronic focal steering sites in subsequent volume-ablation experiments. Because tissue was de-gassed during preparation, only one group of phantoms with 20% gas concentration was prepared.

Bovine blood was obtained from a local slaughterhouse (Dunbar Meat Packing Company, Milan, MI) where it was mixed with citrate-phosphate-dextrose solution at 10:1 ratio (C7165, Sigma-Aldrich Corporation, St. Louis, MO). Blood was stored at 4 ^{o}C and used for experimentation within 14 days. All procedures involving animal tissue were performed in accordance with guidelines established by the University of Michigan's Committee on Use and Care of Animals. RBC phantoms were prepared in a manner similar to that previously described [162] and measured 127 mm x 70 mm x 13 mm as shown in figure 2.5. During experimentation RBC phantoms were submerged and centered in a clear, 33 µm thick polyethylene bag (McMaster-Carr, Elmhurst, IL) containing approximately 2 L of degassed phosphate buffered saline (PBS) to prevent osmotic lysis, thereby maintaining consistent optical contrast. Acoustic attenuation through the polyethylene bag containing PBS was measured using a needle hydrophone and found to be -0.3 dB (3.6%) relative to P- in the free field.

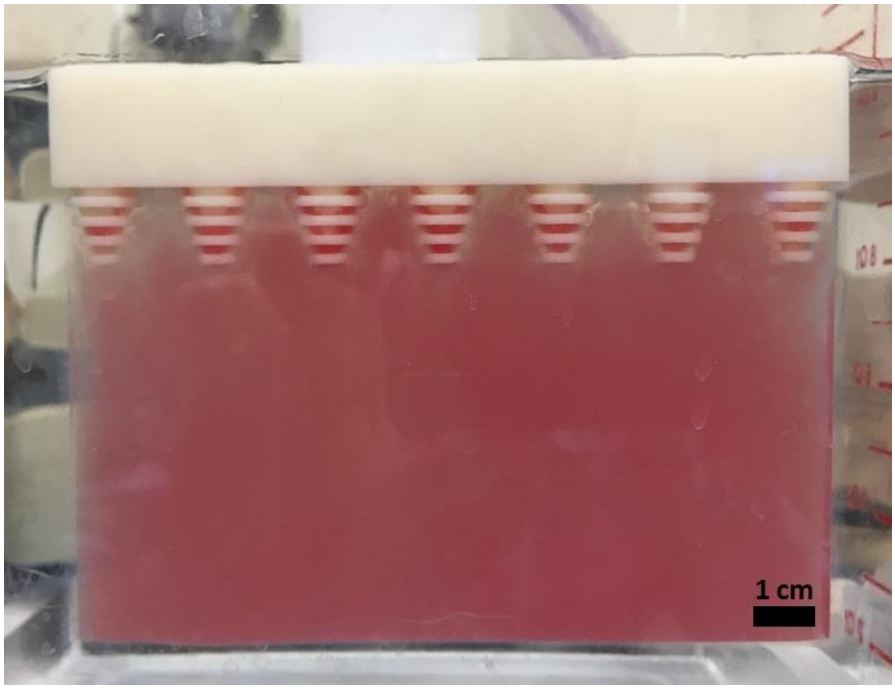

Figure 2. 5. Tissue-mimicking phantom consisting of a thin layer of red blood cells (RBCs) and agarose gel sandwiched between two layers of transparent agarose gel. Gel holder was buoyant in water and phosphate buffered saline.

The setup for the RBC phantom experiments is shown in figure 2.2. Optical monitoring was performed by positioning a high-speed digital camera (Phantom v210, Vision Research Inc., Wayne, NJ) with a telephoto lens (PN 1979, AF Nikkor 70-210 mm f/4-5.6, Nikon Corporation, Minato, Tokyo, Japan) facing the broad side of the phantom and centered on the transducer's geometric focus. Images had resolution of approximately 46 microns/pixel. Continuous-wave (CW) illumination was provided by a film projector (Carousel 4400, Kodak Company, Rochester, NY) positioned on the opposite side of the water tank from the camera. During experimentation the FPGA supplied a trigger signal at 50 ms after the arrival of the histotripsy pulse. The timing of the trigger was set such that the camera would capture an image of the cavitation damage sustained by the phantom after visible cavitation activity had ceased. Commands were sent to the FPGA, camera, and 3D positioner from a PC running a control script written in MATLAB. The script directed the FPGA to fire 200 histotripsy pulses at the geometric focus at a given PRF, during which time the camera would record images. The script then directed the 3D positioner to move the RBC phantom to a new position where the process would repeat with the next PRF to be tested. Focal sites were spaced 15 mm apart in the lateral direction and 19 mm in the axial direction. PRFs tested ranged from 0.1 Hz to 1.2 Hz, each of which was used once per phantom (N = 7). P- was set to 50 MPa for all RBC phantom experiments detailed here as this was the estimated minimum *in situ* P- used for subsequent experiments in *ex vivo* tissue.

Optical images of phantom ablation were post-processed using a MATLAB script based on techniques previously described [83], [142], [162]. Each image was converted to two separate

binary images. The first defined regions of fractionation and the second, through a series of morphological operations, defined a smooth region inset approximately 0.5 mm from the jagged lesion boundary. The extent of fractionation was then defined as the ratio of the number of bright pixels within the smoothed, inset region to the number of total pixels comprising this region. This procedure is detailed in figure 2.6.

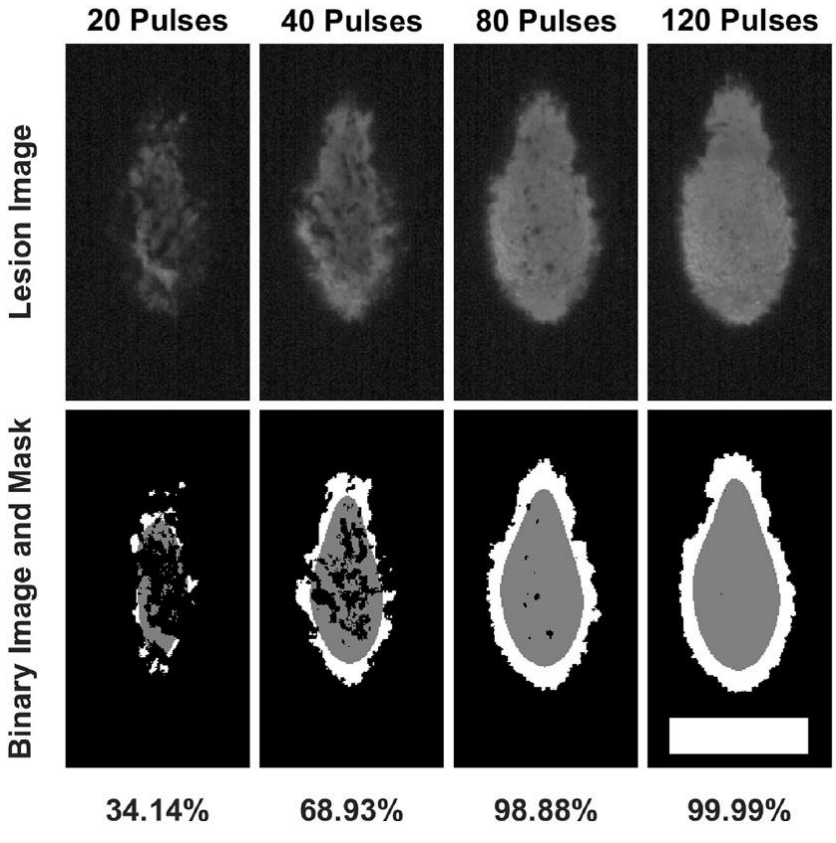

Fig

Figure 2. 6. First row: lesions generated in a red blood cell phantom by successive pulses. Second row: segmented images. Extent of fractionation is defined as (grey pixels)/(total pixels enclosed by grey region). Scale bar = 5 mm.

2.2.2 Preparation and Analysis of Large-Volume *Ex Vivo* Tissue Samples

A total of 5 whole bovine livers were obtained from a local slaughterhouse (Dunbar Meat Packing Company, Milan, MI) and used for experimentation within 8 hours after harvest. Each sample was cut into sections measuring approximately 8 cm x 8 cm x 10 cm. These sectioned samples were then submerged for 5 hours in a vacuum desiccation chamber (model F42025-0000, Bel-Art, SP Industries, Inc., Wayne, NJ) partially filled with degassed PBS. Samples were then secured in exposure fixtures fabricated from polycarbonate film approximately 125 microns thick (McMaster-Carr, Elmhurst, IL) using degassed porcine skin gelatin (50 g : 1 L PBS). Acoustic attenuation through the fixture was measured to be approximately 0.2 dB (5%).

Each sample was secured to a 3D motion system and aligned with the transducer using low-power lasers such that the geometric focus was centered within the sample in the lateral directions and 5.7 cm from the sample's bottom face along the acoustic axis as displayed in figure 2.7b. Results from RBC phantom experiments were used to guide treatment parameters including PRF, dose, and the spacing of electronic focal steering sites for volume tissue ablation experiments in *ex vivo* bovine liver. Tissue-samples were treated by electronically scanning the therapy focus at 200 Hz over 1000 sites (or 0.2 Hz per focal site). Focal sites were arranged in a modified hexagonal close-packed structure with 2.5 mm center-center spacing in the lateral plane and 4.1 mm plane-plane spacing in the axial direction. It was estimated that the total volume of the lesion would be 34 mL based on a CAD model of the electronic focal steering grid shown in figure 2.7a. Three doses were tested, 120 pulses, 250 pulses, and 500 pulses (N=6 for each dose). Total treatment times were 10 min, 21 min, and 42 min, respectively.

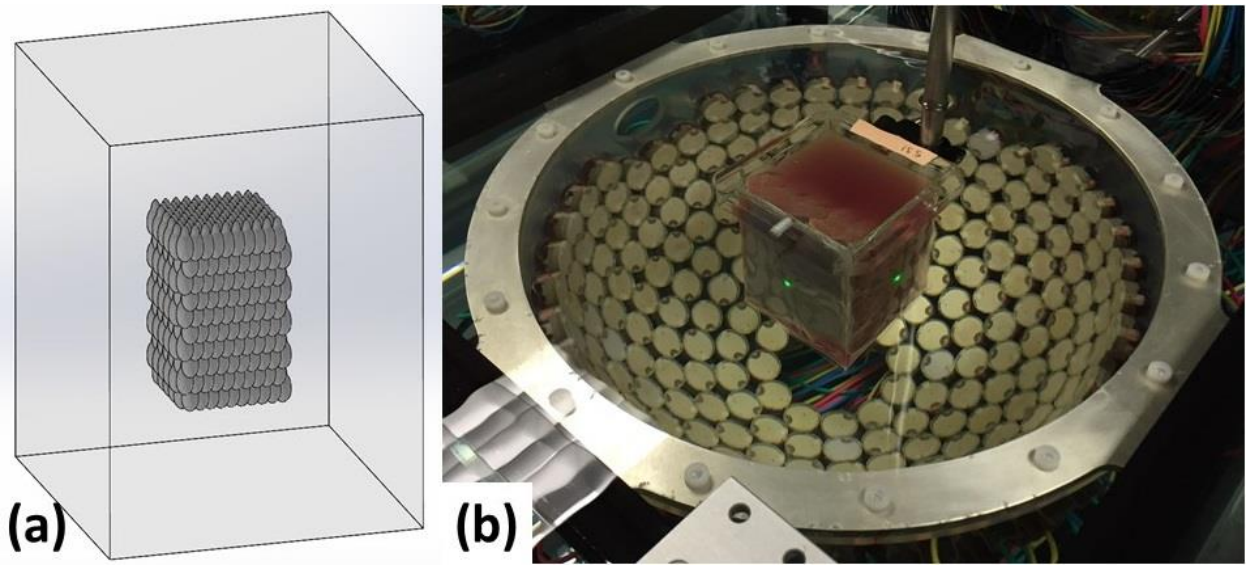

Figure 2. 7. (a) CAD rendering of liver sample (shown in wireframe outline) and packed treatment foci. (b) photograph of transducer and tissue sample.

Tavakkoli et al. suggested that like thermal HIFU treatment, cavitation-induced tissue ablation using electronic focal steering could be made more efficient by employing a randomized electronic focal steering pattern [149]. Though the rationale for this hypothesis was not explicitly stated, the authors may have been alluding to the treatment rate limitation imposed by the cavitation memory effect [180]. Previous experience in our lab supports this idea; randomly ordering the temporal sequence of focal sites in a volume-ablation treatment has been found to ablate tissue more effectively than using a raster scan. Thus, the electronic focal steering scanning sequence, initially generated as a raster pattern, was randomized by applying the MATLAB function *randperm* and this pattern was then repeated during treatment.

Magnetic resonance imaging (MRI) was used to estimate the treatment volume [181]. Following treatment, samples were stored at 4 degrees C and scanned by MRI within 48 hours.

Scans were performed with the sample still in its fixture using a 7-Tesla, small bore, Magnetic Resonance Imaging scanner (Agilent Technologies, Walnut Creek, CA) using a T2*-weighted, gradient-echo sequence. Scanning the samples while still mounted in the fixtures used for treatment was believed to minimize their deformation and promote the fidelity of volumetric measurements. The imaging parameters were TR: 2 s, TE: 10 ms, Matrix: 180 x 180 x 50, FOV: 9 x 9 x 10 cm, Resolution: 0.05 x 0.05 x 0.2 cm, sampling rate: 50 kHz, flip angle: 90 degrees, and slice gap: 0 cm. The resulting series of images represented rectangular volumes encapsulating the lesion within each sample. MR images were reconstructed from the MR acquisition data using the *ifft2* function in MATLAB. Images were then normalized and segmented to isolate the region of ablation using a threshold midway between the respective mean pixel intensities of regions of untreated and treated tissue. For each set of MR images, the image-slice located closest to the center of the lesion was used to establish the pixel intensity threshold for segmenting the entire image stack. Several images were segmented by hand using the *imfreehand* function due to the presence of vasculature or other structures intersecting the lesion boundary with pixel intensity similar to the lesion. To estimate the total volume of the lesion, the sum of the lesion areas from each image was multiplied by the distance separating each imaging plane.

Routine hematoxylin and eosin (H&E) staining was performed for histological evaluation of tissue fractionation extent and to validate the MRI segmentation procedure by assessing the tissue histology and completeness of homogenization throughout the sectioned plane after formalin-fixed paraffin-embedded (FFPE) tissue specimens were processed according to standard protocols. Sectioning planes bisected the lesion along the axis of acoustic propagation.

H&E slides were scanned and digitized into *.svs* format at 400x total optical magnification using a digital whole slide scanner (AT2, Leica Biosystems, Wetzlar, Germany).

A pathologist examined each digital slide and demarcated the boundary between necrotic and viable tissue using digital pathology software (ImageScope, Leica Biosystems, Wetzlar, Germany). Tissue was deemed completely necrotic if there was confluent cell death (≥95%) with cell loss and only residual cellular debris. Since the treatment was done after blood supply to the tissue had ceased, there was no inflammatory response to the necrosis in the tissue. Regions classified as viable were those containing morphologically viable tissue and cells with intact architecture and cytology.

The extent of tissue-ablation within the lesion boundary was assessed for each sample by randomly selecting 32 square regions measuring approximately 250 microns per side within the lesion boundary and counting the number of intact hepatocyte nuclei, intact hepatocytes, and hepatocyte clusters within each region based on visual inspection by a single pathologist. Those regions which encompassed large cracks in the tissue or were located within 1 mm of the lesion boundary were excluded and a substitute was selected at a different location. Three control regions were selected within untreated tissue far from the lesion boundary. Intact cell nuclei were defined as those with smooth and complete nuclear membrane and visible chromatin pattern or nucleoli with or without intact cytoplasm or cell membrane. Nuclei with irregular or incomplete nuclear membrane or appear to be smudgy or fragmented were excluded from the count. Hepatocytes were considered intact if they contained an intact nucleus, cytoplasm, and cell membrane. Clusters were defined as two or more adjacent, intact hepatocytes. Previous studies in our lab have demonstrated that the nucleus is the cell structure most resistant to

histotripsy damage and that the area-density of healthy-appearing nuclei, which appear prominently in H&E sections, can be used as a proxy for the extent of histotripsy tissue fractionation in *ex vivo* tissue [71], [77]. The authors acknowledge that using only one observer to evaluate histological data introduces an element of subjectivity into the analysis and is a limitation of this study.

2.3 Results

2.3.1 Residual Microbubbles and the Cavitation Memory Effect

2.3.1.1 Timescale of Cavitation Expansion, Collapse, and Rebound

The time-course of cavitation activity initiated by the transmitted pulse is displayed in figure 2.8. Images captured the projected area of the cavitation bubble cloud. Frame sequences collected for pulses 45:55 across 10 samples (110 total sequences) were used to construct an area-time curve which displays growth, collapse, and rebound behavior typical of primary cavitation activity in this study. This pulse-range was selected because the cavitation-collapse time increases with pulse number and saturates after approximately 30 pulses in 1% agarose gel [182]. The resolution, exposure, and frame rate of the optical setup used in this experiment were not sufficient to interrogate the earliest stages of cavitation expansion or the final stages of collapse. Previous studies have observed shock emission upon the expansion and collapse of cavitation bubbles with shock-velocities ranging from 1.5-7 km/s and shock amplitudes on the

order of 10-100 MPa [183]–[187], suggesting fluid motion of similar velocity during these very brief phases. By comparison, the detonation velocity of high explosives in air is commonly 2.5-9.5 km/s [188]–[190]. The histotripsy clouds represented in figure 2.7 reached a maximum volume at approximately 141 ± 16 microseconds after the initial expansion and collapsed 378 ± 6 microseconds. Two rebounds were commonly observed.

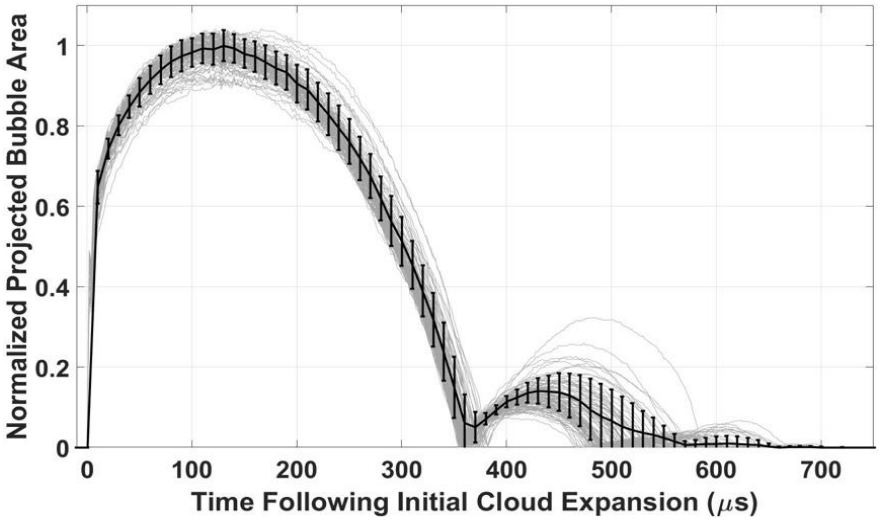

Figure 2. 8. Projected bubble area as a function of time. Data from frame sequences captured for pulses 45:55 of 200 are shown here (N=10 lesions, 110 pulses total). Each grey line represents a single area-time curve for a single pulse. The black line represents the averaged area. Error bars represent ± the standard deviation with every 5th frame displayed to reduce clutter.

2.3.1.2 Generation of Residual Cavitation Nuclei

The expansion and collapse sequence of the cavitation cloud generated by a histotripsy pulse was recorded by an optical imaging setup that allowed fine resolution of small bubbles. Images collected at selected time-points are displayed in figure 2.9. The first frame (t=0) corresponds to the arrival of the primary rarefactional excursion (see figure 2.3) of the acoustic pulse at the

focus. At this time-point, the cavitation cloud expanded rapidly via the intrinsic threshold mechanism [151]. Frames captured at 0, 10, and 30 μs show heterogeneous bubble size, spatial density, and extent of fusion behavior. Pishchalnikov *et al.* suggested that bubble clouds appearing to undergo coalescence may in fact retain a thin layer of fluid separating some bubbles [135], [191]. The frame captured at 210 μs displays a sparse layer of small microbubbles (~5-50 μm in radius) surrounding the primary cavitation bubble as shown in figure 2.9, frame at 210 microseconds. The timing of the appearance of these microbubbles is consistent with the reflection and refocusing of the cavitation expansion shockwave by the surface of the therapy array. The wall-velocity of the bubble cloud was approximately 2.4 ± 0.5 m/s (N = 110) at this time-point and is not expected to have made an acoustic contribution to peripheral bubble formation. This frame also shows the ragged surface of the primary bubble cloud which may promote fission upon collapse. In the frame captured at 550 μs, distinct fission of the cavitation bubble cloud following collapse is observed. The frame captured at 570 μs displays what is likely re-excitement of the residual microbubble population by the primary cavitation collapse signal, reflected by the surface of the therapy array. This assertion is based on the estimated amplitude of these reflected signals being only approximately 2 MPa peak-to-peak which is insufficient to nucleate such cavitation *de novo* in filtered, degassed aqueous media [152], [163], [173]. The presence of peripheral microbubbles in large numbers prior to cavitation collapse suggests that this mechanism may contribute significantly to the population of residual nuclei persisting after collapse.

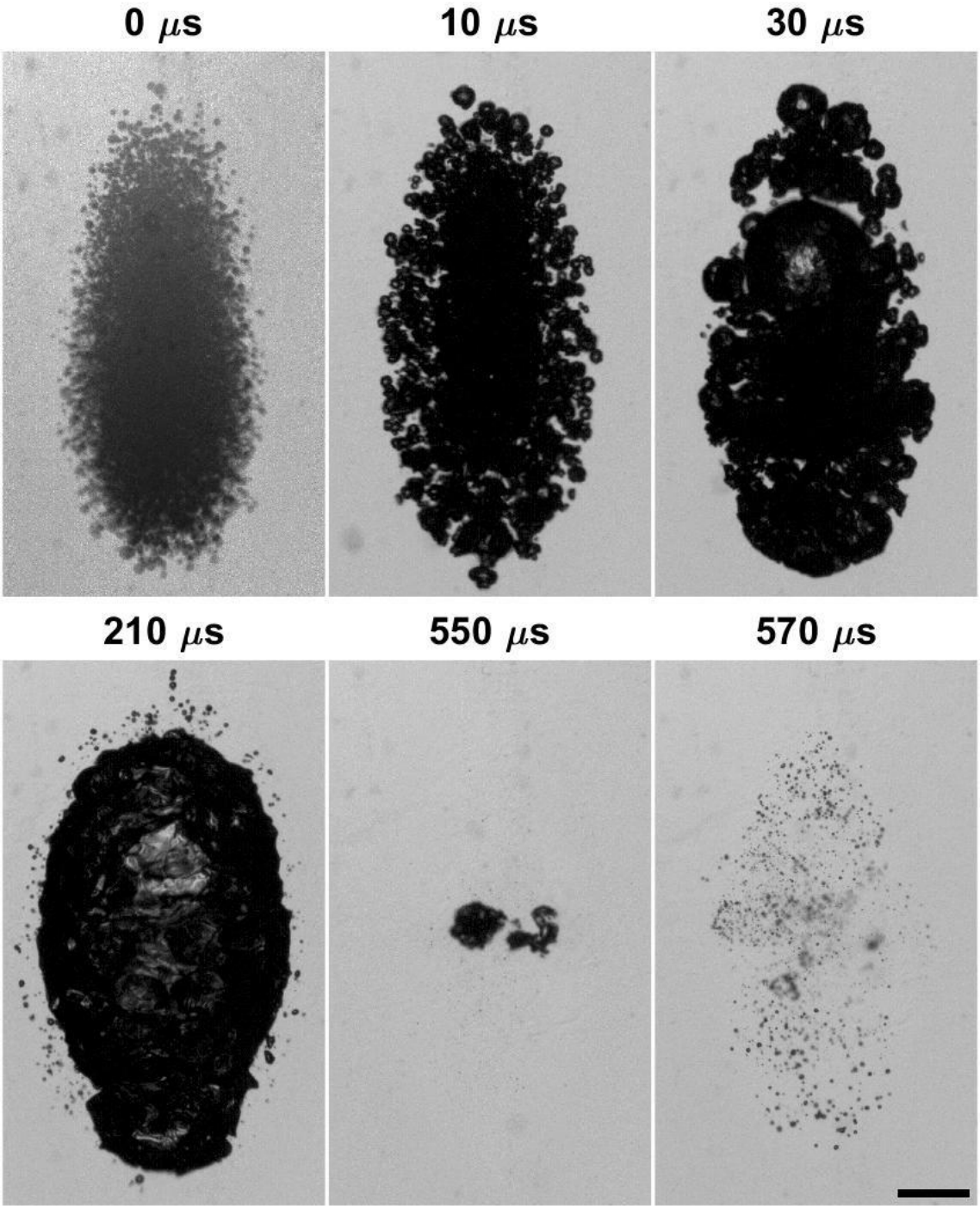

Figure 2. 9. Cavitation bubble cloud images. Each frame displays a unique cloud generated by a separate pulse captured at a different time-point. Collectively, the full image sequence displays the progression of cavitation growth, collapse, and rebounds. Time of frame-capture relative to the arrival of the pulse at the focus appears above each frame. Frames captured at 0, 10, and 30 μs show individual bubbles with heterogeneous size and spatial density throughout the focus. Frames captured between 200-225 μs (only frame captured at 210 μs is presented) display a thin layer of small bubbles surrounding the primary cloud. In the frame captured at 550 μs, after the cloud has undergone at least one collapse, the primary bubble has undergone fission. The frame captured at 570 μs likely shows the population of residual nuclei, likely numbering around 1000, re-excited by the cavitation collapse signal reflected at the transducer surface (see text for explanation). Direction of ultrasound propagation was from bottom to top. Scale bar = 1 mm.

2.3.1.3 Enumeration of Residual Cavitation Nuclei

The number of peripheral microbubbles surrounding the primary cavitation cloud at 210 microseconds after initial cavitation expansion was found to decrease as a function of pulse number, approaching a steady state value after approximately 750 pulses as shown in figure 2.10. A possible explanation for this trend is two-fold. First, the extent and collapse-time of the primary cloud grow as a function of time [182] while the outer dimensions of the peripheral microbubble population, interestingly, remain fairly constant. Thus, for the first few (~5-10) pulses, the reflected cavitation expansion signal encounters an appreciably smaller primary cloud and a larger zone containing peripheral microbubbles. Second, repeated cavitation events may destroy motes or stabilized nuclei [177], [192]–[195] which may account for the statistical variation in the probability of nucleating heterogeneous cavitation as P- approaches the intrinsic threshold [163], [173] and which likely seed peripheral bubbles.

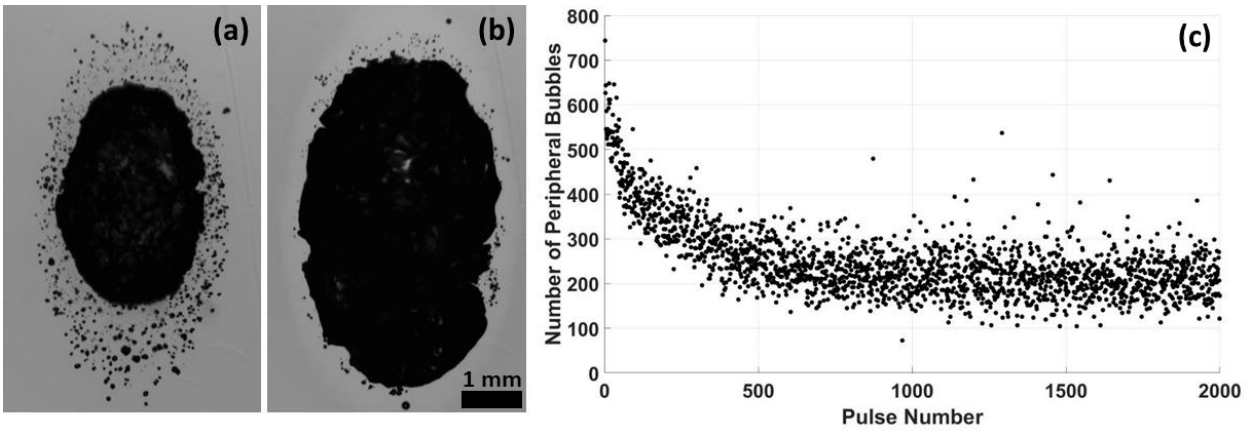

Figure 2. 10. Peripheral microbubbles which failed to fuse with primary cavitation cloud during initial expansion. a) Characteristic image of peripheral microbubble cloud at first pulse. b) Characteristic image of peripheral microbubble population at 1000th pulse. Frames captured at 210 microseconds after initial cloud expansion. c) Number of peripheral bubbles a as a function of pulse number. Each datum represents a single pulse from one treatment. Direction of ultrasound propagation was from bottom to top of images.

The outer boundary of the peripheral bubble cloud consistently approximated the isobaric focal contour roughly corresponding to the intrinsic threshold (~24 MPa at 250 kHz), while the maximum extent of the dense, primary cavitation cloud grew and reached a steady state after approximately 10 pulses. The disparity in size between the two clouds during the first pulse helps illuminate the source of residual cavitation nuclei and may also provide some insight into the dynamics of cloud formation upon the first pulse. The presence of hundreds of peripheral microbubbles occupying the region between the perimeter of the focus and the dense primary cloud prior to collapse provides strong support for the hypothesis that of the roughly 1000 residual microbubbles present immediately after cavitation collapse (see figure 2.9, frame at 570 microseconds), the majority were formed by incomplete fusion with the primary cloud rather than fission upon collapse. The author acknowledges that interrogating residual and peripheral bubbles with acoustic pulses of a prescribed amplitude and timing rather than by reflected shock waves would be a superior technique if further investigation is warranted.

2.3.1.4 Passive Dissolution of Residual Cavitation Nuclei

The passive dissolution behavior of residual microbubbles was monitored optically starting 10 ms following the arrival of the pulse at the focus to allow sufficient time for the cessation of violent cavitation activity and damping of large local oscillations of the host medium [196]. At 10 ms following the arrival of the pulse at the focus, the mean and maximum radii of residual microbubbles generated in phantoms degassed to ≤ 20% saturation were found to be 4.4 ± 0.4 and 11.2 ± 1.4 μm, respectively. It should be noted that the detection limit of the camera was

approximately 3 µm. In gas-saturated phantoms, the mean radius was 10.2 ± 0.9 µm and the radius of the largest bubble per pulse was 23.2 ± 4.8 µm. The largest residual microbubble generated by each pulse persisted for 1.0 ± 0.4 s in gel at approximately 20% gas-saturation and 170 ± 110 s gel at 100% gas-saturation before dissolving below the camera's resolution limit of 3 µm. Figure 2.11 displays the experimentally observed dissolution behavior of the largest residual bubble of the population created by each pulse (grey lines). This figure also displays simulation data derived from solving the Epstein-Plesset model (blue lines). The model shows good agreement with the experimental data for the case of 20% gas concentration but poor agreement for the case of 100% gas concentration.

A limitation of this study was the ability to set the gas concentration to a precisely defined value and the ability to measure gas concentration accurately. While 20% was the targeted set point for degassing pumps, measured values commonly fell within the range of 12-20%. Additionally, successive measurements of the same sample with the dissolved oxygen probe produced a range of readings that exceeded the ± 2% precision claimed by the manufacturer. For degassed samples, the impact of these sources of error was minimal. To illustrate this point, solving eq. 2.1 with a = 16 microns and γ = 0.1, 0.2, and 0.3 (gas concentrations 10%, 20%, and 30%) gives predicted dissolution times of t_D = 2.34, 2.61, and 2.94 s, respectively. A 50% deviation in γ from the target value of 0.2 only results in a 10-13% change in predicted dissolution time. However, near saturation, dissolution time is sensitive to even small variations in gas concentration. For instance, solving eq. 2.1 with a = 16 microns and γ = 0.97, 1, and 1.03 gives predicted dissolution times of t_D = 15.70, 19.84, and 27.08 s, respectively. In this case, a 3% change in γ results in 21% and 36% changes in t_D, respectively. For bubbles with larger radii,

the sensitivity is further magnified. Solving eq. 2.1 with a = 36 microns and γ = 0.97, 1, and 1.03 gives t_D = 142.90, 224.61, 589.05 s, respectively. Here, a 3% change in γ results in 36% and 162.25% changes in t_D, respectively.

Though ostensibly at saturation, the water-preparation method may have elevated the gas concentration slightly above saturation. Preparation of water for this experiment involved first degassing the DI water used for experimentation then bubbling it with a jet of water directed at the surface to bring it to saturation. However, bubbles below a certain size would be expected to dissolve even in water at 100% concentration under the Laplace pressure. This mechanism likely made the steady-state gas concentration slightly higher than 100% saturation while the jet was active. This step was performed to rectify the super-saturation of non-oxygen species due to plumbing-pressure and preferential sequestration of oxygen by carbon filters in the DI system. DI water measured directly from the tap typically had ~50% oxygen concentration while the concentration of other gaseous species in solution (N_2, CO_2, etc.) was likely >100% saturation at atmospheric pressure due to overpressure in the plumbing. Solving eq. 2.1 with γ = 1.03 (103% gas concentration relative to saturation) results in good agreement with experimental data for 36-micron bubbles (error < 1%) and moderate agreement for 16-micron bubbles (error of ~35%). These data are displayed as dotted red lines in fig. 2.11b.

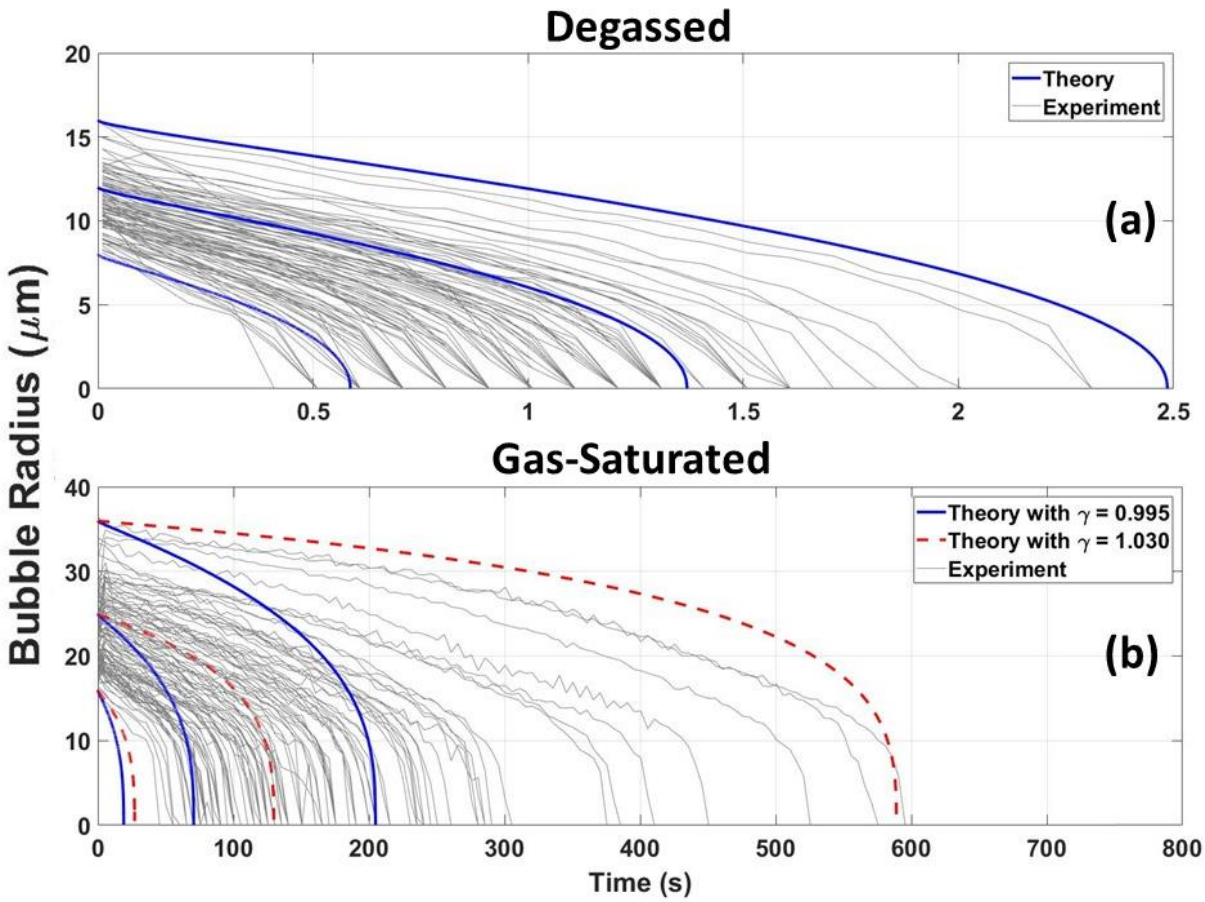

Figure 2. 11. Passive dissolution behavior of residual nuclei. Theoretical (blue and red) and experimentally observed (grey) dissolution curves. Experimental data represent the radius of the largest residual nucleus for each pulse (N=100). a) Degassed gel phantom. Experimentally measured gas concentration was 15.7% (stable). Simulation γ-value set to .157. b) Gas-Saturated phantom. Experimentally measured gas concentrations were 98.8%, 99.1%, and 99.5% collected consecutively. Simulation γ-values set to 0.995 (blue curves) and 1.030 (dotted red curves).

2.3.1.5 Single Lesion Formation in RBC Phantoms

A total of 49 single-focus lesions were formed in RBC phantoms at PRFs ranging from 0.1 to 1.2 Hz (N=7 for each PRF). The extent of fractionation within the lesion boundary (defined as the number of bright pixels within a binarized, smoothed, and inset boundary region to the number of total pixels comprising this smoothed region) decreased with increasing PRF for a

given therapy dose. Figure 2.12 shows representative images for lesions generated with 120 pulses and at various PRFs. It was found that for 0.1 Hz and 0.2 Hz, at approximately 95 and 120 pulses, respectively, fractionation approached saturation (>99%). However, among PRFs tested, those > 0.2 Hz required greater than 200 pulses in order to achieve a comparable level of fractionation. The PRF-dependence observed is believed to result from the cavitation memory effect described previously [83]. Based on the results from RBC phantom experiments, 0.2 Hz PRF was chosen as the per-point treatment PRF for subsequent *ex vivo* tissue experiments with electrical focal steering. From figure 2.12 it can be seen that the extent of fractionation achieved by 0.2 Hz PRF after 100 pulses is approximately equal to that of 0.4 Hz after 200 pulses. In an effort to minimize potential heating with future *in vivo* studies in mind, the emphasis was placed on per-pulse fractionation efficiency, rather than gains which may have been possible with respect to time-efficiency. Because previous experiments in our lab have shown that tissue is more resistant to fractionation than RBC phantoms [197], 120, 250, and 500 pulses were chosen as the doses to test for *ex vivo* experiments.

The profile of the lesion was analyzed across 7 RBC phantoms by averaging the images from each sample corresponding to 120 pulses delivered at 0.2 Hz to form a composite profile. The mean extent of the 7 lesions was 4.1 ± 0.2 mm in the lateral direction and 8.6 ± 0.7 mm in the axial direction. The profile and mean dimensions were used to establish the spacing of the electronic focal steering grid used for subsequent *ex vivo* tissue experiments. The doses selected for *ex vivo* tissue experiments were 120, 250, and 500 pulses per location with the expectation that the number of pulses required to fully treat tissue would be greater than or equal to the dose sufficient to achieve complete ablation in tissue mimicking gel.

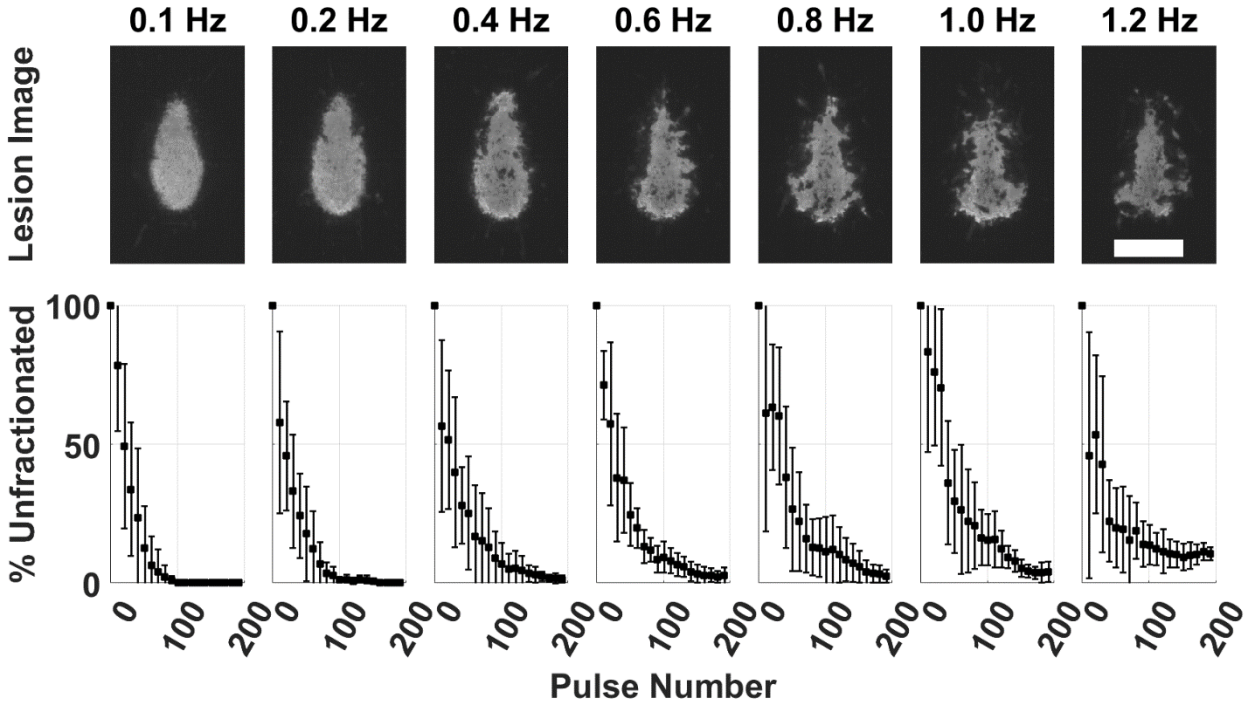

Figure 2. 12. Top row: Representative images of lesions in an RBC phantom after sustaining 120 pulses at various PRFs. Bottom row: Percent of material unfractionated within a region inset approximately 0.5 mm from the lesion boundary. Error bars represent ± standard deviation. N=7 for each PRF tested. Scale bar = 5 mm.

2.3.2 Rapid Ablation of a Large *Ex Vivo* Tissue Volume

2.3.2.1 MRI Volume Measurements

To validate histotripsy with EFS, a total of 18 lesions were generated in *ex vivo* bovine liver samples using doses of 120, 250, and 500 pulses (N=6 for each dose). MR imaging was used to estimate lesion volume for all samples. Representative images appear in figure 2.13. The volume of each individual sample was calculated as the mean of values derived from axial and coronal image stacks. The lesion volumes for each dose group (mean ± SD) were found to be

34.1 ± 1.1 mL for 120 pulses, 32.1 ± 1.5 mL for 250 pulses, and 40.7 ± 3.1 mL for 500 pulses. 1-way ANOVA comparing these data found p-values of 0.02, 6.5×10^{-4}, and 1.2×10^{-4} for 120 vs. 250, 120 vs. 500, and 250 vs. 500 pulses, respectively. The larger lesion-volume observed in the group treated with 500 pulses may be due to the breakdown of supporting tissue structures, allowing the homogenate to behave more like a single-phase fluid and permitting expansion of cavitation activity at the tissue-fluid boundary. Remaining structures, possibly blood vessels or bile ducts, appeared faint but slightly more prominent in MR images of lesions treated with 120 and 250 pulses than those treated with 500 pulses.

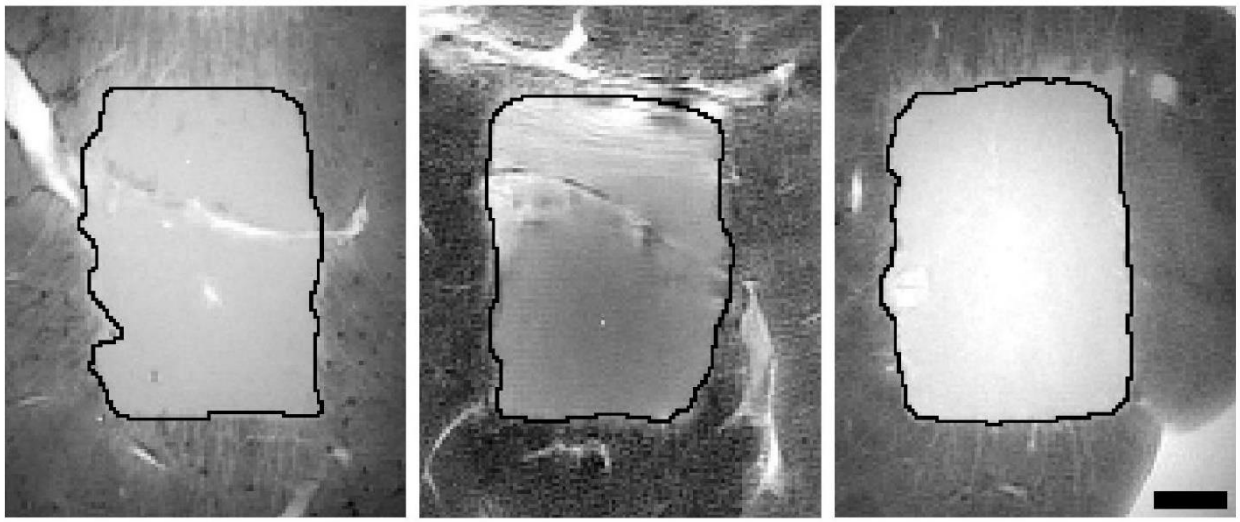

Figure 2. 13. MR images of ex vivo tissue treated with 120, 250, and 500 pulses. Scans were performed with the sample still in its fixture using a 7-Tesla, small bore, Magnetic Resonance Imaging scanner (Agilent Technologies, Walnut Creek, CA) using a T2*-weighted, gradient-echo sequence. The imaging parameters were TR: 2 s, TE: 10 ms, Matrix: 180 x 180 x 50, FOV: 9 x 9 x 10 cm, Resolution: 0.05 x 0.05 x 0.2 cm, sampling rate: 50 kHz, flip angle: 90 degrees, and slice gap: 0 cm. Image slices shown were near the center of the lesion. Lesion segmentation boundary appears in black. Ultrasound propagation direction: bottom to top of images. Scale bar: 1 cm.

2.3.2.2 Histology

To assess the extent of fractionation achieved by histotripsy with electric focal steering, samples treated were analyzed microscopically using H&E staining. Digitized H&E slides were examined by a pathologist (JS) and a region of confluent tissue necrosis (≥95% cell death) was demarcated. Thirty-two randomly selected regions within the lesion boundary of each digital slide were examined for the presence of intact nuclei, hepatocytes, and viable hepatocyte clusters.

In all samples, a distinct lesion consisting of tissue necrosis grossly similar to respective MR images was observed. The area within the lesion-boundary consisted primarily of necrotic tissue homogenate with sparsely scattered nuclear debris. Rare intact nuclei, hepatocytes, or hepatocyte clusters were present and were found almost exclusively around vessels or near the lesion margins. Occasionally, residual vessels were observed in the lesion as well. The higher resilience of vascular structures to histotripsy damage [72] likely afforded nearby hepatocytes a degree of protection from cavitation activity. The presence of residual intact nuclei, hepatocytes, and vessels present in the lesion was found to be inversely correlated with dose. Viable hepatocytes in untreated tissue were arranged in cords and were typically polygonal with abundant eosinophilic cytoplasm and round nuclei with prominent nucleoli. Representative images appear in figure 2.14.

The average percent remaining of intact-appearing cells relative to untreated tissue was 1.4 ± 1.1 %, 0.13 ± 0.2%, and 0.05 ± 0.06% for 120, 250, 500 pulses, respectively (see figure 2.15). Even though sparse intact-appearing cells were found within the necrotic homogenate in

treated areas for all samples but one from the 500-pulses group, the pathologist's analysis suggested that these cells are most likely not viable due to lack of blood supply and would eventually be lysed and cleaned up by inflammatory cells together with the necrotic debris if the treatment were applied *in vivo*. Since we only looked at a fixed time point post-treatment in an *ex vivo* organ model, it is impossible to predict the fate of these cells in a live animal accurately. However, judging from their appearance and environment in the tissue, it is reasonable to anticipate their death within a short period of time. Furthermore, it is likely that intact material originated at the periphery of the lesion and was carried to the center late in the treatment as this phenomenon was observed in RBC phantoms. In a clinical setting such material would be part of the treatment margin consisting of healthy parenchyma.

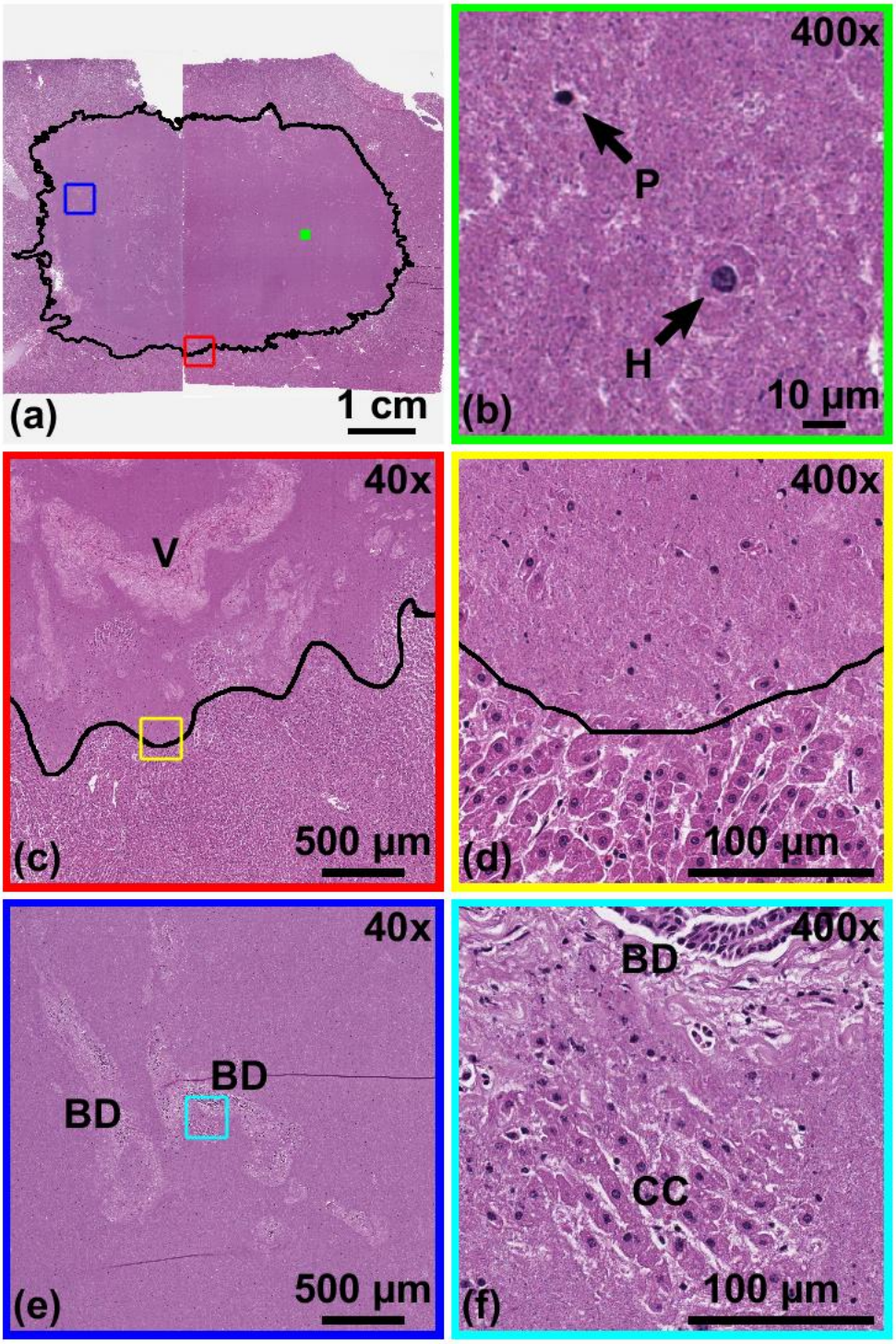

Figure 2. 14. Representative H&E staining of tissue sample treated with 250 pulses. Magnification power is specified in terms of total original optical magnification (objective lens power x eyepiece or camera lens). (a) Low power view of lesion and surrounding tissue. The lesion margin was demarcated by the black line for (a), (c), and (d). The color of each border in magnified views (b-f) corresponds to a highlighted square region in views (a), (c), and (e). (b) 400x view of the center of the lesion showing one healthy-appearing, intact cell nucleus (H) and one pyknotic nucleus (P) surrounded by homogenate. (c), 40x & (d), 400x views of lesion margin showing a sharp demarcation between viable-appearing hepatocytes and necrotic cells. A few residual vessels (V), intact cells, nuclei can be seen in the necrotic tissue near the lesion margin. (e), 40x & (f), 400x views. Residual cell clusters (CC) were occasionally found within the necrotic lesion, often around residual vessels or bile ducts (BD).

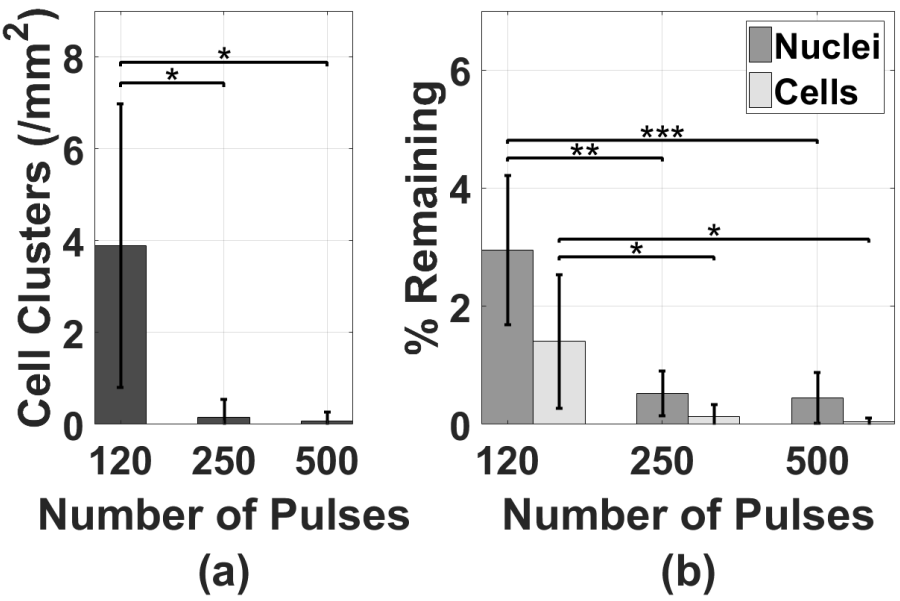

Figure 2. 15. (a) Area-density of remaining cell clusters within the lesion. (b) Percentages of intact cells and cell nuclei remaining within the lesion after treatment relative to untreated tissue. Significance at *p ≤ 0.05, **p ≤ 0.01 and ***p ≤ 0.001.

2.3.2.3 Peripheral Damage and Boundary Expansion

MR images and histology revealed isolated regions of tissue damage outside the predicted lesion perimeter. This damage manifests in two patterns highlighted in Figure 2.16. In all samples, small irregular elongated areas of tissue damage outside the lesion margin were observed in MR images and histology. Peripheral damage was densest in post-focal tissue immediately adjacent to the distal margin of the lesion and took the form of elongated, streak-like necrotic zones running parallel to the acoustic axis. These features are indicative of a phenomenon known as *bubble tunneling* in which a cavitation bubble carves out a path through a viscoelastic host medium (like gel or tissue) as it translates under the influence of the primary radiation force and pressure gradients in the sound field [162], [198], [199]. Features with similar morphology appeared pre-focally in tissue that lay between the transducer and the

proximal margin of the lesion but were more sparsely distributed. Streak-like features are similarly observed in RBC phantom experiments in this and previous studies [74], [82], [162] and are believed to correspond to the cavitation and translation of pre-existing, initially sub-micron gas pockets in the sample. Peripheral damage was also occasionally noted near the lateral margins of the lesion and tended to be less elongated, sometimes roughly spherical. This form of peripheral damage is expected to be less pronounced in an *in vivo* animal model where the impurities introduced to *ex vivo* tissue samples during preparation, and which may function as cavitation nuclei, would be absent.

A slight expansion of the lesion perimeter was observed in all directions when >250 pulses were applied. 1-way ANOVA shows no significant difference between the volume of lesions generated with 120 and 250 pulses (p=0.82). However, the analysis did find a significant difference between the volume of lesions generated with 120 and 500 pulses (p=6x10^{-5}) as well as 250 and 500 pulses (p=3x10^{-5}). A possible explanation is that after the complete destruction of tissue components which lend structural support, the necrotic homogenate may behave more like a single-phase fluid and thus permit expansion of cavitation activity at the tissue-fluid boundary, resulting in a slight expansion of the lesion boundary. Further, it was noted in MR images of several samples treated with 500 pulses, that along the lesion boundary there exists a region of intermediate pixel intensity (figure 2.16a). Corresponding regions on H&E slides do not appear noticeably different that other regions of homogenate. The scalloped pattern of the boundary corresponds to the dimensions of individual foci appearing at the intervals prescribed by the electronic focal steering grid.

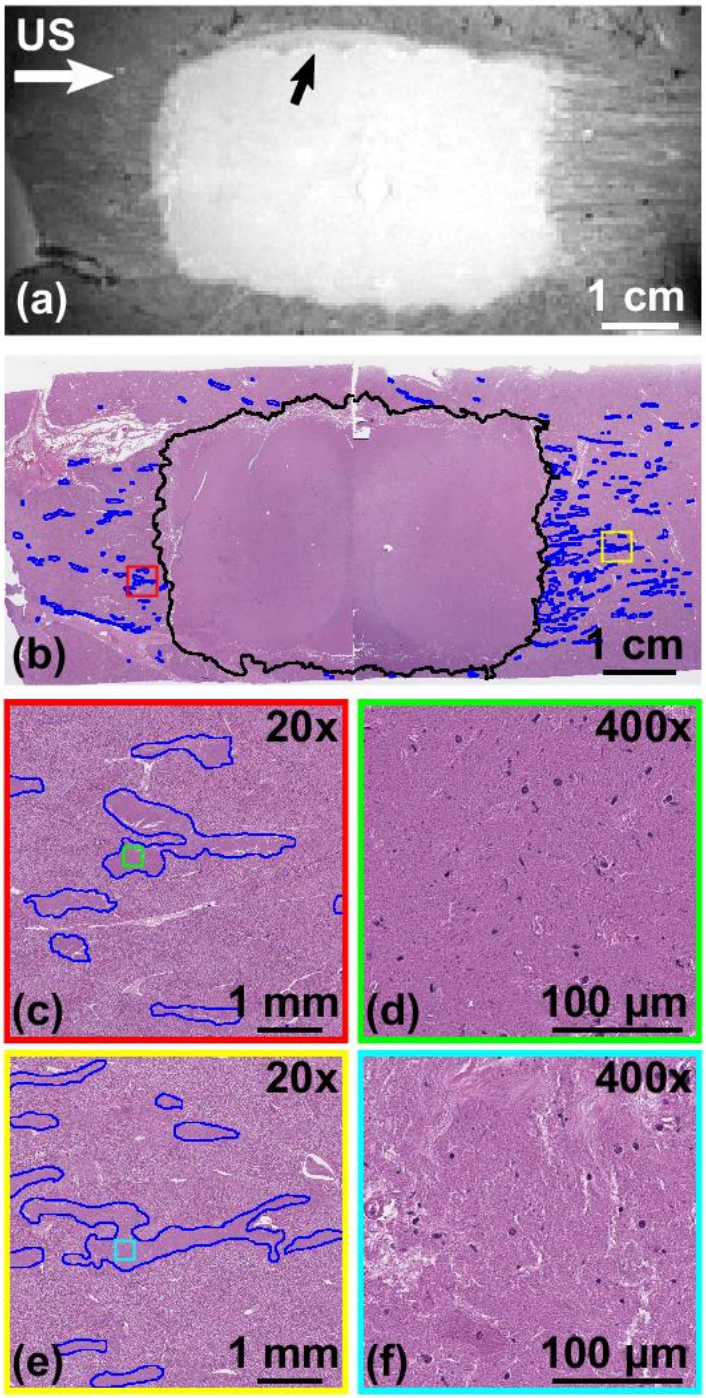

Figure 2. 16. MR image (a) and H&E staining (b-f) of sample treated with 500 pulses. Magnification power is specified in terms of total original optical magnification (objective lens power x eyepiece or camera lens). Ultrasound propagation direction is indicated by a white arrow (US) in (a). The color of each border in magnified views (c-f) corresponds to a highlighted square region in views (b), (c), and (e). (a) Border expansion and scalloped edge feature is indicated by a black arrow. Border expansion is also observed on contralateral and proximal margins but is not annotated. Streak-like features indicative of bubble tunneling can be observed in pre and post-focal tissue. (b) Low power view of lesion and surrounding tissue. Lesion margin is delineated by black line. Regions of peripheral tissue necrosis are highlighted in blue. (c) 20x view of pre-focal peripheral tissue necrosis in red square in (b). (d) 400x view of region of necrotic debris in pre-focal tissue. (e) 20x view of post-focal peripheral tissue damage. (f) 400x view of region of necrotic debris in post-focal tissue.

2.4 Discussion

2.4.1 Residual Cavitation Nuclei and the Cavitation Memory Effect

In this study, strong support was provided for the hypothesis that residual nuclei are primarily generated by the incomplete fusion of individual microbubbles with the primary cavitation cloud. This observation may have implications for the design of histotripsy pulsing sequences and further investigation of preconditioning pulses [82], [200]. Additionally, these findings suggest that there may be interesting differences in the cloud nucleation behavior in untreated vs. treated media. In the case of untreated gel, the pulse appears to nucleate a dense cloud at the center of the focus, whereas in a gel where numerous previous pulses have been delivered, nucleation has been shown to progress from the proximal to the distal end of the focus, tracking with the propagation of the rarefactional excursion of the therapy pulse [201].

Experiments in which bubble dissolution time was directly monitored in clear agarose gel suggest that ~2.5 s is sufficient for residual nuclei to dissolve fully. However, single-lesion experiments in RBC phantoms show less efficient fractionation at 0.4 Hz (2.5 s PRP) than at 0.2 Hz (5 s PRP). This discrepancy may be due to the resolution limit of the optical camera in detecting very small residual nuclei. A bubble with a 3-micron radius would be expected to dissolve within < 10 ms, suggesting that perhaps that some very small bubbles were stabilized or slowed in dissolution to some extent by the presence of organic impurities introduced by ruptured RBCs or organic materials found in the blood. RBCs were isolated by centrifugation but not washed to eliminate plasma proteins. Previous studies have described at length the impact of organic materials including impurities in stabilizing small bubbles, thereby slowing or

preventing their complete dissolution [154], [177]–[179]. In human blood, plasma proteins are very large (tens of thousands to millions of Daltons) and constitute 7% of the plasma's mass [202]. Components of disrupted cells' bilipid membranes may also contribute.

2.4.2 Large-Volume Ablation

This study demonstrates the feasibility of using histotripsy with EFS to ablate a target-volume of *ex vivo* tissue rapidly. By electronically steering the focus of a phased array histotripsy transducer, it was possible to excite cavitation events rapidly throughout a large ensemble of overlapping foci such that while remnant nuclei at a given focus were dissolving, the other focal locations in the ensemble could be treated before returning to the given focus. This approach helped to mitigate the rate-limitation imposed by the cavitation memory effect.

The cavitation memory effect imposes both temporal and spatial constraints on the design of an effective EFS sequence. The temporal constraint can be seen in the single lesion RBC phantom experiments. When the local pulse repetition period (PRP) for a given electronic focal steering site is too short, residual cavitation nuclei lack sufficient time to dissolve before the arrival of subsequent pulses. Upon the arrival of subsequent pulses, residual nuclei are preferentially re-excited. Acoustic energy directed at the intended focus is then scattered and attenuated. Additionally, under these conditions in a host medium like tissue or gel that does not readily permit chaotic fluid mixing during and after cavitation bubble-cloud collapse, clouds from one pulse to the next share highly correlated spatial distributions. However, when the

local PRP is sufficiently long, residual nuclei have time to dissolve and subsequent clouds nucleate from a more randomized spatial distribution of individual sites within the intended focal region. A previous study in our lab showed that greater randomization of individual bubbles within the cloud resulted in more complete and efficient fractionation of the target [83]. The spatial constraint of the cavitation memory effect in the context of EFS arises due to the proximity or overlap of electronic focal steering sites. If a region of the sound field with high enough gain (i.e. a side lobe or the shoulder of the main lobe) is incident on a population of residual nuclei from a previous pulse, they can be re-excited in a manner that compromises the formation of a robust bubble cloud at the intended, current focus. Furthermore, this re-excitement of residual nuclei is expected to prolong the time required for their dissolution. Thus, a minimum separation distance is required for adjacent pulses as well as minimum time-period for which this condition must be maintained. This explains why an EFS following a raster pattern, for example, would yield low tissue fractionation efficiency.

In this study, a very low local PRF (0.2 Hz) was applied to each focus individually to address the temporal constraint of the cavitation memory effect. EFS sites were ordered in a temporally random sequence to reduce the impact of interactions between spatially proximal foci, thereby addressing the spatial constraint of the memory effect. The following chapter addresses the design of structured steering sequences to mitigate further the impact of the cavitation memory effect and thereby improve treatment efficiency. These sequences impose minimum spatial limits on proximal foci such that after a given electronic focal steering location has been pulsed, immediately subsequent pulses will be directed at locations separated from the given location for a certain time-period.

A limitation of this study is the simplifying assumption that the dissolution behavior of residual nuclei at a given focus is independent of further acoustic activity in the sequence. While the focal gain of the transducer and short pulse duration restrict the spatial region of extreme pressure (>24 MPa), the remainder of the sound field experiences peak-to-peak sound pressure amplitudes on the order of hundreds of kPa to several MPa (more than sufficient to elicit a dramatic response from bubbles with static radii on the order of several to tens of microns) from the transmitted pulse. Additionally, cavitation expansion and collapse events can produce shocks with amplitudes on the order of 100 MPa [185], [203] and can cause other nuclei to cavitate violently [204]. Chapter 3 explores EFS strategies incorporating the effects of secondary fields driven by these interactions – that is, acoustic fields emitted by oscillating bubbles which in turn cause mutual interactions within bubble populations, the basis for the secondary Bjerknes force [89]–[93], [95].

The hemispherical transducer used in this study was designed for transcranial brain applications. Geometrical constrains for treatment of abdominal organs, such as the liver, pancreas, and kidney will require a smaller aperture and higher f-number which may result in greater focal heating due to nonlinear acoustic propagation. However, nonlinear effects are expected to take place only in regions of high focal gain at or near the focus [170], [205].

In this *ex vivo* study, heating was not measured. In a previous study in our lab, where a higher frequency (750kHz) transducer (f-number= 0.8) was used to treat the *in vivo* porcine liver at 200 Hz PRF through full rib coverage without using aberration correction, a temperature increase of 4.1 ± 1.8 °C in the ribcage was observed [74]. For the driving electronics used in the current study, additional signal conditioning may retain the high amplitude peak negative phase

to ensure cavitation generation while reducing high frequency components which contribute to heating.

The size of the target-lesion in this study was limited by the number of EFS locations that could be stored in the FPGA's memory (1024) rather than the electronic focal steering range. With a greater number of available electronic focal steering locations, the global PRF and treatment rate could be increased as long as steering range and thermal constraints are not exceeded. Future iterations of the system will include an expanded memory capacity. Used in conjunction with mechanical focal steering, it will be feasible to treat a tissue volume of arbitrary size.

When it is necessary to ablate a region that exceeds the electronic focal steering range, it is possible to combine electrical and mechanical focal steering in a manner similar to that developed by Zhang et al. [55] to cover the entire volume while maintaining a high ablation rate. This approach will likely prove useful for *in vivo* settings like abdominal targets which require a higher f-number than that used in the current study, resulting in a diminished maximum steering angle. Additionally, the use of single crystal materials which generate higher surface pressure as well as soft tissue aberration correction techniques may help to offset *in vivo* pressure losses.

The center frequency of the transducer used for this study was 250 kHz, the lowest our lab has used for a histotripsy study. This frequency was selected to take advantage of the lower attenuation, large focal zone, and large electronic focal steering range associated with lower frequencies. However, as the center frequency decreases, the probability of cavitating regions outside the targeted focus increases since these regions experience P- on the order of several

MPa [173]. Furthermore, the cavitation memory effect is expected to be more pronounced at lower frequency due to the formation of larger, longer-lived bubble clouds and longer dissolution times for residual nuclei [87], [206]. Peripheral damage and bubble tunneling may be reduced in future systems by using a transducer with higher center frequency [152].

This study demonstrates that histotripsy with electronic focal steering is capable of noninvasively ablating a large tissue volume rapidly and uniformly in an *ex vivo* bovine hepatic tissue model by mitigating the impact of the cavitation memory effect. This technique is highly repeatable and fairly resilient to overtreatment. Histotripsy with electronic focal steering has the potential to achieve rapid, complete necrosis of a large tissue volume at a rate exceeding any current ablation treatment for large-volume targets.

Chapter 3

Electronic Focal Steering Strategies Incorporating Bubble Coalescence Driven by Low-Gain Regions of the Therapy-Beam

In the previous chapter, the dissolution behavior of residual cavitation nuclei generated at a given electronic focal steering position, within an ensemble comprised of many of foci, was approximated by the dissolution behavior of an isolated single focus. In this simplified model, only interactions between the high-gain focus of the therapy beam and residual nuclei were considered. Acoustic signals from low-gain regions of the therapy beam and secondary acoustic signals [89], [207] were ignored. This chapter explores the impact of low-gain regions of the transmitted sound field and secondary acoustic fields on residual nuclei and how resulting interactions can be exploited to achieve faster treatment rates.

*Note: portions of this chapter were published as listed below.

1. **Jonathan Lundt,** Timothy Hall, Akshay Rao, Charles Cain, Zhen Xu. Coalescence of Residual Histotripsy Cavitation Nuclei Using Low-Gain Regions of the Therapy Beam During Electronic Focal Steering. *Physics in Medicine and Biology*, 2018. Accepted manuscript online 24 Oct. 2018.
2. **J.E. Lundt**, A. Rao, T.L. Hall, J.J. Macoskey, C.A. Cain, Z. Xu. Volume Ablation Using Histotripsy with Electronic Focal Steering: Utilization of Low-Gain Regions of the Therapy Beam to Drive Bubble Coalescence. International Symposium on Therapeutic Ultrasound, Kobe, Japan, Oct. 22-25, 2018.
3. **J.E. Lundt**, T.L. Hall, A. Rao, J.J. Macoskey, C.A. Cain, Z. Xu. Coalescence and Extinction of Residual Cavitation Nuclei by Means of the Secondary Acoustic Field while Performing Histotripsy with Electronic Focal Steering. International Symposium on Therapeutic Ultrasound, Nashville, TN, May 14-17, 2018.
4. **J.E. Lundt**, S.P. Allen, J. Shi, J.R. Sukovich, T.L. Hall, C.A. Cain, Z. Xu. Rapid Ablation of Large Tissue Volume Using Histotripsy with Electronic Focal Steering. Institute of Electrical and Electronics Engineers – International Ultrasonics Symposium, Tours, France, September 18-21, 2016.

3.1 Introduction

3.1.1 Separate Acoustic Sequences for Driving Bubble Coalescence

Bubble coalescence (BC) is an active strategy for manipulating residual cavitation nuclei which follows each high-amplitude therapy pulse with a moderately long (tens to thousands of cycles), lower-amplitude (~1 MPa) BC pulse. BC pulses can drive residual nuclei to translate in aggregate by means of the primary Bjerknes force [91], [177], [208]–[211] or to cluster by means of the secondary Bjerknes force [89]–[93], [95], [177], [207] following the application of a modest number of BC pulses. Previous studies have demonstrated that histotripsy with BC can significantly increase ablation speed [93]–[97] by allowing a relatively high pulse repetition frequency (PRF) for histotripsy (e.g., PRF = 100 Hz for a single focus) while maintaining high treatment homogeneity. In these studies, separate acoustic sequences for histotripsy therapy and BC were transmitted. The BC sequences found to be optimal in the studies by Duryea et al. and Shi et al. deposited approximately 30% additional acoustic energy (relative to the

histotripsy therapy pulses) within the -6 dB region of the therapy focus [95], [97]. The ablation of large tissue volumes is expected to require a high PRF in order to achieve a clinically practical total treatment time. For this application, the additional acoustic energy associated with a separate BC sequence may pose a risk of tissue heating or require extending the duration of treatment in order to accommodate the dissipation of additional heat.

3.1.2 Low-Gain Regions of the Therapy Beam as a Driver of Bubble Coalescence

While electronically steering the histotripsy therapy beam and in the absence of any separate acoustic sequence for BC, regions outside the high-gain therapy focus experience an acoustic pressure field from the transmitted pulse similar in amplitude to sequences used for BC. This effect was simulated in the acoustic modeling software FOCUS [212]–[214] and is displayed in figure 3.1. This figure features acoustic simulation data for the 250 kHz hemispherical phased array described in Chapter 2 and used for experimentation in the present chapter. If an electronic focal steering (EFS) sequence were arranged appropriately, populations of nascent residual nuclei would experience a series of short, low-amplitude acoustic pulses. In this manner, each therapy pulse would have the potential to serve the dual-purpose of exciting cavitation at the current EFS focus and driving BC at the foci which recently preceded it. This strategy for manipulating residual nuclei would not require a separate BC sequence. In this study, we hypothesize that while electronically steering the histotripsy therapy focus, low-gain regions of the therapy beam can be used to drive BC. Low-gain regions of the transmitted

sound field are defined here to be those approximately 20 dB or more down from the peak pressure.

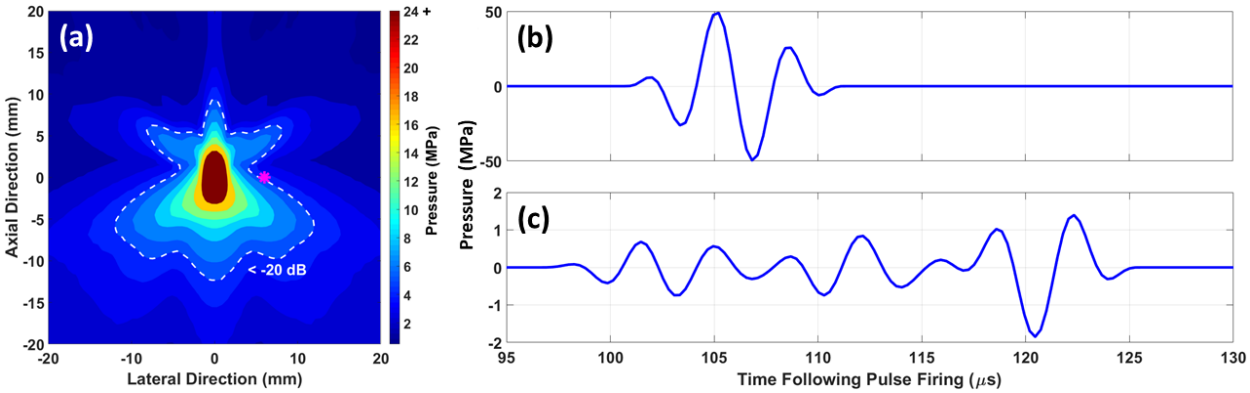

Figure 3. 1. Acoustic simulation data generated in FOCUS highlighting low-gain regions of the pressure field. (a) Peak rarefactional acoustic pressure (P-) distribution in the x-z plane, centered about the transducer's geometric focus. The dark red region in the center corresponds to P- > 24 MPa. The white dotted line demarcates the -20 dB isobaric contour. Pink asterisk indicates position (6, 0, 0), one wavelength away from the center of the geometric focus. (b) Simulated waveform at the geometric focus with P- = 50 MPa. (c) Simulated waveform at (6, 0, 0) with mean peak-to-peak amplitude of approximately 2 MPa and containing approximately 8 cycles.

We investigated the feasibility of this approach and examined the behavior of a population of residual nuclei under the influence of low-gain regions of the therapy beam while executing specially-designed EFS sequences. One important application of EFS-BC is to enable rapid and homogenous ablation of a large volume target, such as tumors in the liver, kidney, and pancreas.

3.2 Methods

3.2.1 Proof of Principle Using a Single, Isolated Focus

3.2.1.1 Specialized Electronic Focal Steering Sequence

In this experiment, a specially-designed 50-foci EFS sequence was constructed in which the first EFS position lay at (0, 3 mm, 0) and positions 2:50 lay in the plane z=12 mm (2λ away) with a minimum of 5 mm of center-center spacing between these positions as shown in figure 3.2. In subsequent references to (x, y, z) positions within the sound field, the unit (mm) is omitted. This configuration was selected to investigate the behavior of residual nuclei under the influence of low-gain regions of the therapy beam at EFS position 1 with this position in relative isolation. The criteria for achieving BC was defined as the consolidation of residual nuclei into a single bubble or dense cluster of bubbles no greater than 1 mm in greatest dimension as visualized during expansion by the low-gain regions of EFS-BC pulses which also served as acoustic probe pulses. This value was chosen empirically as residual bubbles were observed to coalesce to a central locus with a steady-state expanded size approximately 0.75 mm in greatest extent. The transducer, a hemispherical phased array with a center frequency of 250 kHz, and experimental setup was identical to that described in Chapter 2.

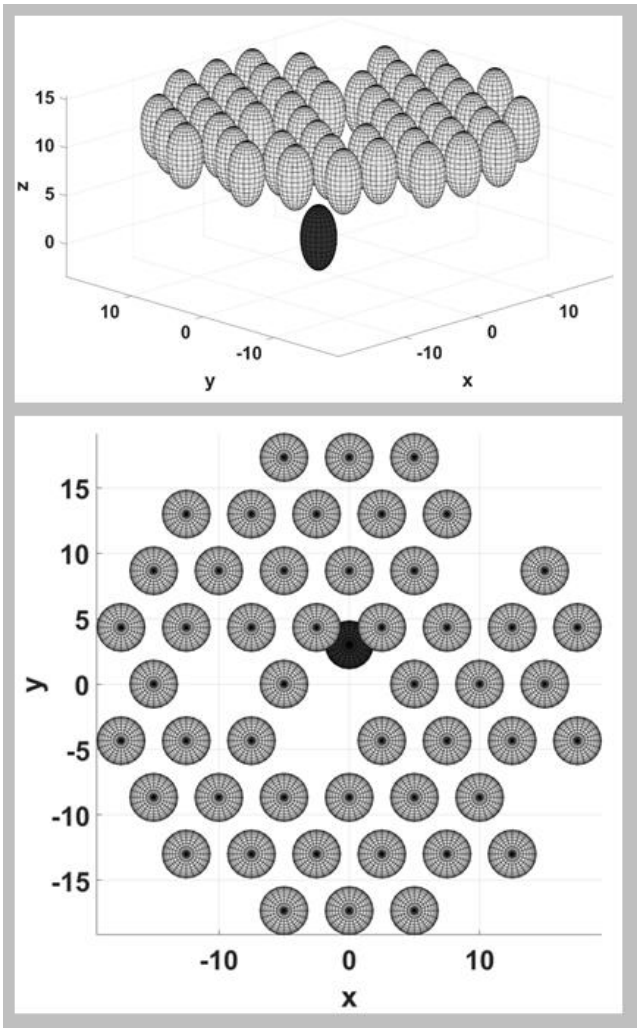

Figure 3. 2. Diagrams of EFS positions for investigation of BC behavior at an isolated focus. Monitored focus, EFS position 1, appears in dark grey. EFS positions 2:50, appear in light grey. The optical camera was oriented along the y-axis. Units are millimeters. Ultrasound propagation was in the positive z-direction. Top: angled view. Bottom: top-down view, looking in the direction of the transducer. Units are in mm.

3.2.1.2 Characterization of Low-Gain Regions of the Therapy Beams

Low-gain regions of the therapy beams incident upon the monitored focus were characterized in the free field using a hydrophone (HGL-0085, Onda, Sunnyvale, CA). Its tip was positioned at (0, 3, 0) facing the array and with its axis oriented vertically, similar to the

configuration displayed in figure 2.2. The therapy beam was then steered throughout EFS positions 2:50. Because the driving voltage used for experimentation generated acoustic pressures which exceeded the operating range of the hydrophone, these measurements were collected with the driving voltage set to 20% of the value used for experimentation and linearly extrapolated. Waveforms were captured and averaged by an oscilloscope and transferred to a PC. Throughout EFS positions 2:50, the mean ± standard deviation of peak compressional and rarefactional pressure amplitudes were 3.5 ± 0.7 MPa and 2.7 ± 0.6 MPa, respectively. These waveforms contained approximately 3-7 cycles with the first cycle having the highest amplitude. A typical low-gain waveform appears in figure 3.3.

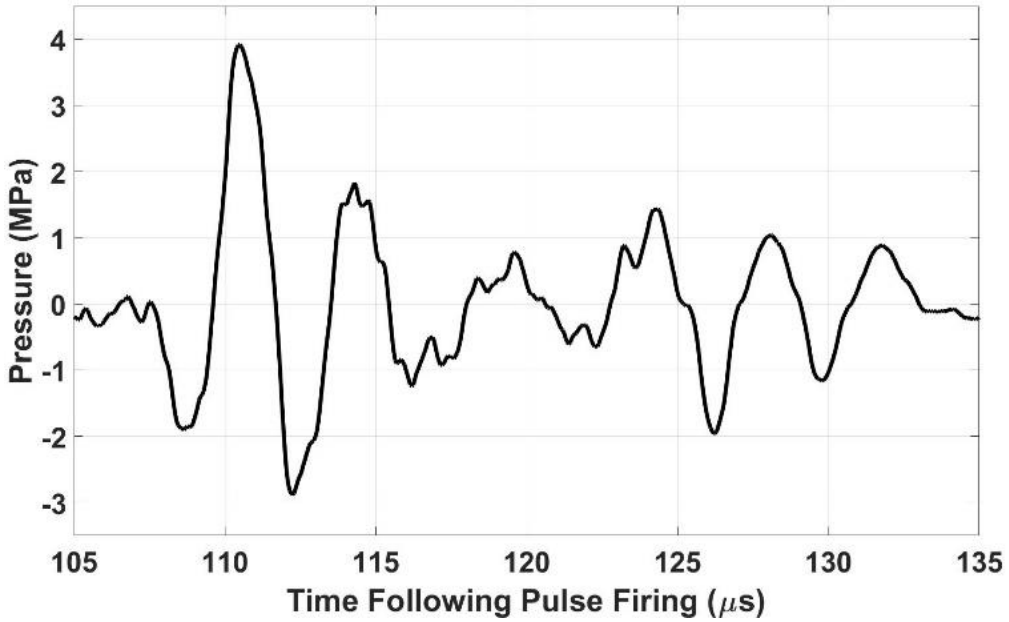

Figure 3. 3. Linearly extrapolated waveform at (0, 3, 0) while electronically steering the therapy focus to (-10, 8.7, 12).

3.2.1.3 Characterization of Coalescence Behavior of Residual Nuclei During EFS

The coalescence behavior of residual nuclei during EFS was characterized in a tissue-mimicking agarose hydrogel phantom measuring 127 mm × 70 mm × 13 mm prepared as described in Chapter 2 and in ref. [215]. We hypothesize that using the low-gain fields generated at EFS position 1, when the focus is steered to EFS positions 2:50, will induce BC at EFS position 1. The phantom was positioned such that EFS position 1, (0, 3, 0), was centered within the phantom, and EFS positions 2:50 were at least 10 mm from the gel holder. The PRF within EFS bursts through positions 1:50 was varied from 50 Hz to 5 kHz (N=10 for each PRF). The burst repetition frequency for the overall EFS burst was 0.2 Hz for all tests. For each dataset, the gel phantom was repositioned such that the EFS position 1 lay within an untreated region of gel. EFS position 1, (0, 3, 0), was monitored by a high speed optical camera (Phantom V2012, Vision Research, Wayne, NJ) equipped with a telephoto lens (107-306, Sigma Corporation, Ronkonkoma, NY) and two teleconverters (MC 2X N-AF DGII, Bower, Long Island City, NY) and backlit with an LED light source (CLU550-3626C1-40AL7G4-B24, Citizen Electronics, Fujiyoshida, Japan) operated in continuous mode. Frames covered a region measuring 4.21 mm x 6.57 mm at the focal plane and had a resolution of approximately 8 μm/pixel. The camera was set up to capture one frame with a 10-μs exposure per EFS pulse. The timing of frame-capture was set to 113 μs following firing the earliest phased array element such that the midpoint of the exposure was approximately synchronized with the maximum radii of residual nuclei, having been re-excited by the low-gain regions of the therapy beam. In addition to driving BC, low-gain regions of the therapy beam also functioned as a probe for optical monitoring, expanding residual nuclei to facilitate their visualization. Control data were

acquired for both gas concentrations (approximately 20% and 100%, respectively) by generating a cavitation bubble cloud at EFS position 1, waiting 1-50 ms, and then delivering a single pulse to EFS position 2 which functioned as a probe to re-excite residual nuclei at EFS position 1. These data serve as a reference for the spatial distribution of residual nuclei under passive conditions.

The collection of data was automated by a MATLAB script which supplied commands to the transducer array's field programmable gate array (FPGA) driving circuit. The camera, operating in *continuous record* mode, received a trigger to initiate a new recording for each position in the gel. The camera was set up to record 5220 frames and save them as a single *.cine* file with the timestamp as the file name to the PC for each position. The FPGA synchronized frame-capture by supplying triggers to the camera's *fsync* and *memgate* inputs. The script also saved a *.mat* file for each gel position containing the experimental parameters and with a timestamp similar to that of the *.cine* file. A 3-axis linear motion system was used to reposition the gel for each new position to be treated.

Data were processed in MATLAB where images were read from the camera's native *.cine* format using a modified version of the script *ReadCineFileImage.m* supplied by the manufacturer. The modified version of the script, *ReadCineFileImageNoHandle.m* (see appendix), reconciled an issue in which the function would attempt to create a new object handle each time it accessed an image, allocating ~5 MB of memory in the process, and causing MATLAB to crash when a *.cine* file with a large number of frames was processed. The modified script created a single handle for the entire processing loop. This modification prevented the script from crashing and executed the load operation ~5X faster. Image processing functions

are briefly summarized in the following steps. Images were high-pass filtered to remove out-of-focus cavitation bubbles which were observed to traverse the field of view commonly at high PRF and/or high gas concentration. Images were converted to binary using a locally adaptive thresholding method [174]. Images were manipulated through a series of morphological operations which served to segment residual microbubbles. The vertical and horizontal spatial extent of the residual microbubble population was recorded for each frame.

3.2.2 Two-Foci Experiments

As noted in section 2.2.4, the primary concerns for the design of an effective EFS sequence are the distance and time-interval separating neighboring foci in the firing order. To investigate the impact of a proximal population of residual nuclei on the dynamics of *de novo* bubble cloud formation, a series of experiments was conceived in which the therapy focus was steered to two focal positions in succession. The first bubble cloud was generated at position (x/2, 0, 0), referred to as *focus 1*. Then, a second cloud was formed at position (-x/2, 0, 0), referred to as *focus 2*. This configuration is displayed in figure 3.5a. A 5-s pause then followed before this two-pulse burst was repeated. Spacing was varied from x = 1 to 10 mm and PRP within a single burst was varied from 500 microseconds to 5 s. The first set of experiments was performed in clear gel phantoms and RBC phantoms (0.5 mm, 1% RBC layer) measuring 127 mm x 70 mm x 13 mm and prepared as described in sections 2.2.1.1. This set of experiments sought to investigate *de novo* cloud formation in proximity to a population of nascent residual nuclei and

served to inform the minimum separation distance of directly sequential foci in an EFS sequence. Only gel phantoms degassed to approximately 20% were used for this experiment due to the long period (several minutes) required for residual nuclei to dissolve in gas-saturated gel. Additionally, for PRP of a few milliseconds (similar value for volume-ablation), the extent of dissolution in degassed gel would be minimal upon the arrival of the second pulse. This also allowed the 5-s PRP dataset to serve as a control.

For RBC phantom experiments, a high-speed camera (Phantom v210, Vision Research Inc., Wayne, NJ) with a telephoto lens (PN 1979, AF Nikkor 70-210 mm f/4-5.6, Nikon Corporation, Minato, Tokyo, Japan) was used in a setup similar to that described in section 2.2.1.1. Images measured 512 pixels x 256 pixels and covered a region measuring approximately 26 mm x 13 mm at the focal plane. The camera was set up to capture 7 frames for each focus at 50-microsecond intervals with a 44.5-microsecond exposure. The period of frame capture began with the expansion of the bubble cloud and ended at the approximate time of collapse. Prior to firing each two-pulse burst, a single frame was captured in which no cavitation activity was present. Images from this experiment were assessed qualitatively to evaluate the impact of the presence of diffusely distributed residual nuclei at *focus 1* on *de novo* cloud formation at *focus 2*. The morphology and position of the *de novo* cloud and the resulting lesion formed at *focus 2* were examined.

For experiments in clear gel phantoms, a high-speed camera (Phantom v2012, Vision Research, Wayne, NJ) equipped with a telephoto lens (PN 1922, Nikkor AF 28 mm f/2.8D, Nikon Corporation, Minato, Tokyo, Japan) and teleconverter (MC 2X N-AF DGII, Bower, Long Island City, NY) backlit with an LED light source (CLU550-3626C1-40AL7G4-B24, Citizen Electronics,

Fujiyoshida, Japan) was operated in continuous mode to collect images. Images had a resolution of 128 pixels x 96 pixels and covered a field of view measuring 18 mm x 13.5 mm at the focal plane. Frames were captured at 500,000 frames per second with an exposure of 285 ns. Frame-capture was initiated at approximately 8 microseconds prior to the arrival of each acoustic pulse at the focus and continued for a duration of 400 microseconds for each pulse. 200 pulses were fired at each focus and a 5-s pause was applied between each two-pulse burst to provide sufficient time for residual nuclei to dissolve. 10 samples per parameter-combination were treated, each at an untreated location in the gel phantom.

In this experiment, images were post-processed in MATLAB using a script that measured the area of the *de novo* clouds for each focus throughout the image sequence. These data were then used to determine the collapse-time and maximum projected area of these clouds which served as proxies for the capacity to induce cavitation damage [82], [216]–[218]. The script masked peripheral bubbles and re-excited residual nuclei and then used the *imbinarize* function to segment the *de novo* clouds. An example of this functionality applied to a single two-pulse burst is presented in figure 3.4.

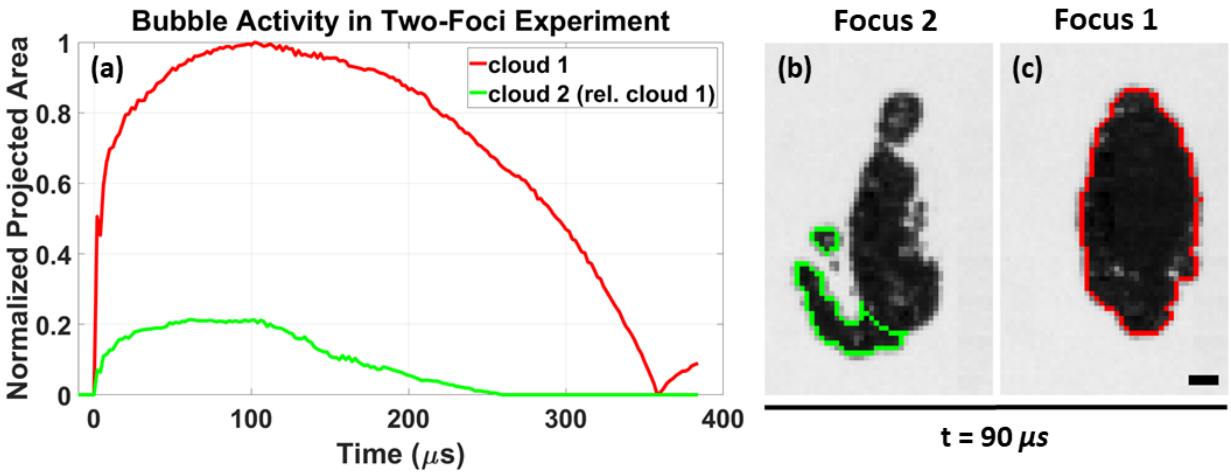

Figure 3. 4. Characteristic examples of bubble cloud behavior in two-foci experiment. Foci were separated by 1 mm (center to center) in this example. PRP = 5 ms. Data displayed were from the 15th two-pulse burst. (a) Projected area of bubble cloud as a function of time. Data have been normalized with respect to the maximum area of the cloud at focus 1. (b) Image of cavitation activity resulting from a pulse directed at focus 2. In this frame, a diffusely distributed population of residual nuclei persisting at focus 1 has been re-excited to cavitate inertially. The cloud formed by de novo cavitation appears highlighted in green as segmented by the analysis script. (c) Image of cavitation cloud formed de novo at focus 1. Perimeter of cloud is highlighted in red as segmented by analysis script. t = 0 corresponds to the initial expansion of each bubble cloud. Frames displayed in (b) and (c) were captured 90 microseconds following their respective initial expansions. Scale bar = 1 mm.

For an ablation grid consisting of numerous foci, the majority of residual nuclei at a given time would be expected to exist in a coalesced state due to the EFS-BC effect described previously in this chapter. In a second set of two-foci experiments, the formation of a *de novo* bubble cloud in close proximity to a densely clustered population of coalesced bubbles was investigated. The experiment was structured identically to the first set of two-foci experiments with the exception that 48 EFS-BC pulses were fired (temporally) between the pulses directed at *focus 1* and *focus 2*. These experiments were performed in clear, degassed gel phantoms measuring 127 mm x 70 mm x 13 mm. The EFS sequence for this experiment is shown in figure 3.5b. Here the local PRP was 5 ms and the global PRP was 100 microseconds. Spacing was varied from 1 to 5 mm. Experiments were performed in clear gel phantoms using the same high-speed imaging setup described immediately above (Phantom v2012, etc.). No frames were collected for EFS-BC pulses which fell outside the growth and collapse cycle of the cloud formed

at *focus 1*. Images from this experiment were assessed qualitatively by examining the morphology and position of the cloud formed *de novo* at *focus 2*.

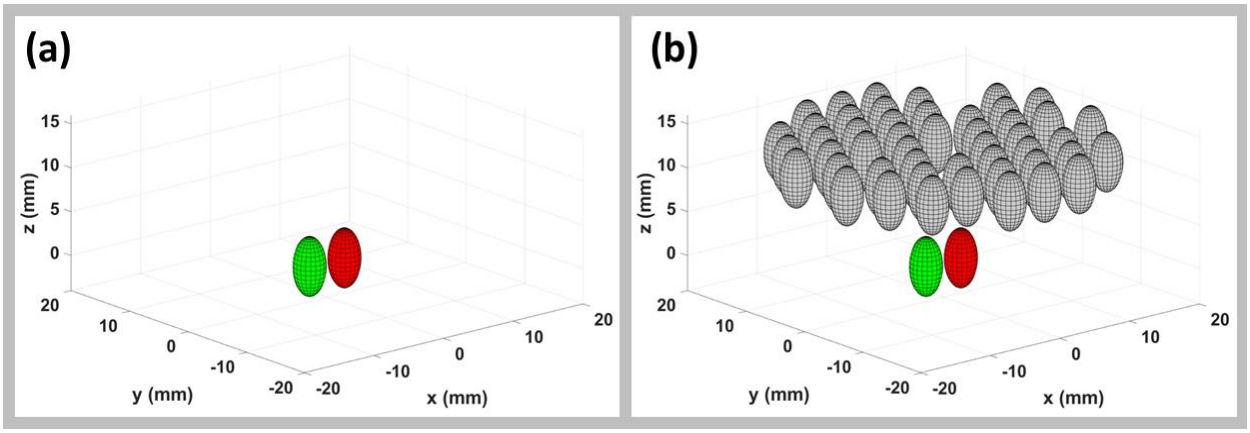

Figure 3. 5. Diagrams showing focal positions in two-foci experiments. Focus 1 appears in red at position (2.5, 0, 0). Focus 2 appears in green at position (-2.5, 0, 0). EFS-BC foci appear in grey. (a) Two-foci experiment where no EFS-BC pulses were applied. (b) Two-foci experiment in which 48 EFS-BC pulses were fired between foci 1 and 2.

3.2.3 Basic EFS Sequence Design

Results from two-foci experiments indicated that sequential EFS foci should be separated spatially by $d_{xy} \geq 4$ mm in the lateral direction (please see section 3.3.2 for more detail). The lateral diameter of the portion of the focus which exceeds the intrinsic threshold is approximately 3 mm. If the same relationship were to hold in the axial direction, an appropriate minimum spacing would be $d_z \geq$ ~8 mm. To test this hypothesis, a specialized EFS grid was constructed which was composed of 144 foci arranged to form a rectangular shape, measuring approximately 30 mm x 8 mm x 30 mm in the x, y, and z-directions respectively. Foci were spaced 3.5 mm apart in the lateral plane and 5 mm apart in the axial plane. Three EFS

sequences were constructed in order to evaluate the impact of the 4 and 8-mm minimum foci-spacing conditions derived from the two-foci experiments. The first sequence was arranged in a raster patter in which the therapy beam began at the grid position at (-13.1, -3, -12.5) and progressed in the x, z, and y-directions respectively along directly adjacent foci. This sequence was intended to serve as a near-worst case control in which the foci-spacing condition was violated with all but the first pulse of the burst. In the second sequence, the firing order was arranged in a random pattern which was stored and repeated for each burst. In this configuration, the foci-spacing condition was maintained for at least 6 pulses for 70.8 % of grid positions. A third sequence was constructed in which the steering grid was decimated into eight interleaved sub-grids as shown in figure 3.6. The firing-order for each sub-grid was arranged in a raster pattern similar to the first EFS sequence, however, because the grid was decimated, the foci-spacing condition was maintained for at least 6 pulses for 100% of grid positions. Results discussed in section 3.3.1 indicated that 5.2 ± 0.5 EFS-BC pulses were sufficient to achieve bubble coalescence at 20% gas concentration.

The efficiency and homogeneity of fractionation were evaluated for each sequence in an RBC phantom measuring 127 mm x 70 mm x 22 mm and containing a central, opaque layer approximately 0.5 mm thick using an experimental setup similar to that shown in figure 2.2. The progression of fractionation was monitored optically by positioning a high-speed digital camera (Phantom v210, Vision Research Inc., Wayne, NJ) with a telephoto lens (PN 1979, AF Nikkor 70-210 mm f/4-5.6, Nikon Corporation, Minato, Tokyo, Japan) facing the broad side of the phantom and centered on the transducer's geometric focus. Continuous-wave (CW) illumination was provided by a film projector (Carousel 4400, Kodak Company, Rochester, NY)

positioned on the opposite side of the water tank from the camera. Images measured 800 pixels x 800 pixels and covered an area of approximately 34 mm x 34 mm at the focal plane. The camera was setup to capture one frame per pulse, timed to precede the firing of the pulse by several milliseconds such that the gel was free of visible bubbles and relatively stationary at the time of frame-capture.

Images were post-processed in MATLAB using a script which segmented regions of treated RBC phantom by applying the *im2bw* function and then cropping the image such that only a rectangular region inset from the scalloped border was considered. The fraction of treated material was calculated as the ratio of the bright pixels to the total number of pixels enclosed by the rectangular region.

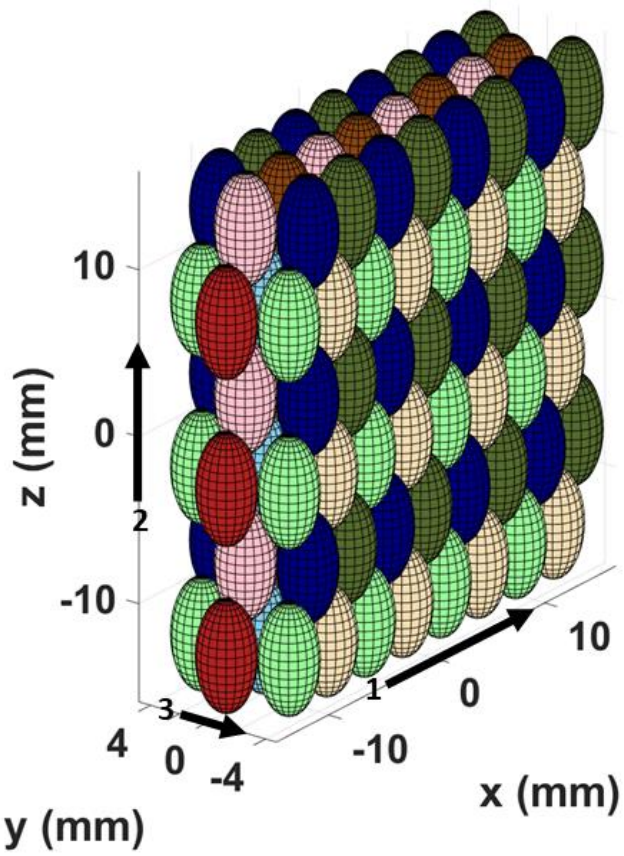

Figure 3. 6. Diagram of positions for basic structured EFS sequence arranged in an interleaved configuration. Grid contained interleaved 8 sub-grids which together comprised 144 points. The firing order of the sub-grids was red, dark blue, light blue, dark green, pink, tan, dark brown, and finally light green. The sequence began lower left corner and proceeded according to the black arrows labeled 1-3. Ultrasound propagated in the positive z-direction.

3.2.4 Gel Phantom Preparation

Experiments in which BC behavior was investigated for large-volume ablation were performed in agarose gel phantoms measuring 50 mm x 40 mm x 50 mm which provided a margin of approximately 1 cm between the lesion and the edge of the gel. One group of phantoms for large-volume ablation contained only gel to allow robust optical imaging of cavitation. To monitor the progression of ablation, a second group of phantoms with identical

dimensions was prepared with a layer 1 mm thick containing red blood cells (RBCs) at 5% concentration and positioned in the middle of the phantom. Similar to the approach described previously [162], the RBC layer was initially opaque and became transparent tracking with the progression of cavitation damage, thereby allowing real-time optical monitoring. Porcine blood obtained from a local abattoir (Dunbar Meat Packing, Milan, MI) where it was mixed 10:1 with citrate-phosphate-dextrose solution (C7165, Sigma-Aldrich, St. Louis, MO, USA). RBC phantoms were then stored in a bath of phosphate buffered saline held at either approximately 20% or 100% gas concentration for ≥ 48 hours prior to use.

3.2.5 Experimental Setup for Large-Volume Ablation

3.2.5.1 Transparent Gel Phantoms

This experiment served to monitor the activity of residual nuclei in the context of a large-volume ablation treatment using an interleaved EFS sequence which was selected to present the progression of BC to the camera in a manner that could be easily recognized. Agarose gel phantoms measuring 50 mm x 40 mm x 50 mm were treated with 200 pulses per EFS focus at PRFs of 1 kHz and 5 kHz and monitored by high speed camera (Phantom V2012, Vision Research, Wayne, NJ) equipped with a telephoto lens (107-306, Sigma Corporation, Ronkonkoma, NY) and backlit as described above. Frames measured 640 pixels x 752 pixels and covered a region measuring 35.6 mm x 41.9 mm at the focal plane. The camera was set up to capture twenty frames per pulse at intervals of 25 μs beginning at 50 μs following the firing of

the pulse. Frames captured prior to the arrival of the pulse at the EFS focus were subsequently used for background subtraction during image processing. The exposure was set to 24 μs. Each pulse was intended to serve three purposes in this experiment: 1) generation of a cavitation bubble cloud within the high-gain focal region, 2) coalescence of residual nuclei generated at recently treated foci by means of low-gain regions of the therapy beam, and 3) acoustical probing for visualization of bubbles which have a static size below the resolution limit of the camera. The time-interval of frame capture was approximately 125-149 μs following firing the pulse. This interval was selected to account for the time of flight and corresponding range of phasing delays associated with the distance of these EFS sites from the geometric focus.

3.2.5.2 RBC Phantoms

This experiment sought to demonstrate the ablation efficacy of the EFS-BC technique by monitoring cavitation damage produced in tissue-mimicking phantoms. The setup was identical to that used in the previous sub-section with the exception that only one frame per repetition of the EFS sequence was captured following the completion of each EFS grid repetition. The authors define a single repetition as the delivery of 1 pulse per location throughout each focus of the 1000-foci grid. Images were analyzed in MATLAB by segmenting regions of intact material within a rectangular region inset from the lesion boundary and measuring approximately 22 mm x 29 mm. Segmentation was performed by a locally adaptive binarization method [174]. The extent of fractionation was defined as the ratio of the number of unfractionated pixels within a rectangular region to the total area of this region. Complete

fractionation was defined as the ratio of unfractionated pixels to total region pixels being equal to 1.

3.2.6 EFS Grid and Interleaved EFS Sequence

To demonstrate proof of principle for large-volume ablation using EFS-BC, a 1000-foci EFS grid was constructed in which foci were arranged in a 10x10x10 modified hexagonal close-packed structure with center-center spacing of d_{xy} = 2.5 mm in the lateral direction and d_z = 3.3 mm spacing the axial direction, resulting in a total volume of approximately 27 mL centered about the point (0, 0, 0). The overall 1000-foci EFS grid was then decimated into 8 separate, interleaved 125-foci sub-grids. By arranging the firing order of the EFS sequence to execute each sub-grid sequentially, it maintained the condition that foci temporally adjacent in the firing order were separated by at least $2d_{xy}$ in the lateral direction and $2d_z$ in the axial direction. The goal of this approach was to reduce the cavitation memory effect by coalescing residual nuclei prior to exposing recently-cavitated focal positions to high-gain regions of subsequent EFS beams. The spacing and sub-grid firing order, shown in figure 3.7 by arrows 1-3, was selected to display the activity of residual nuclei for observation by the high-speed camera.

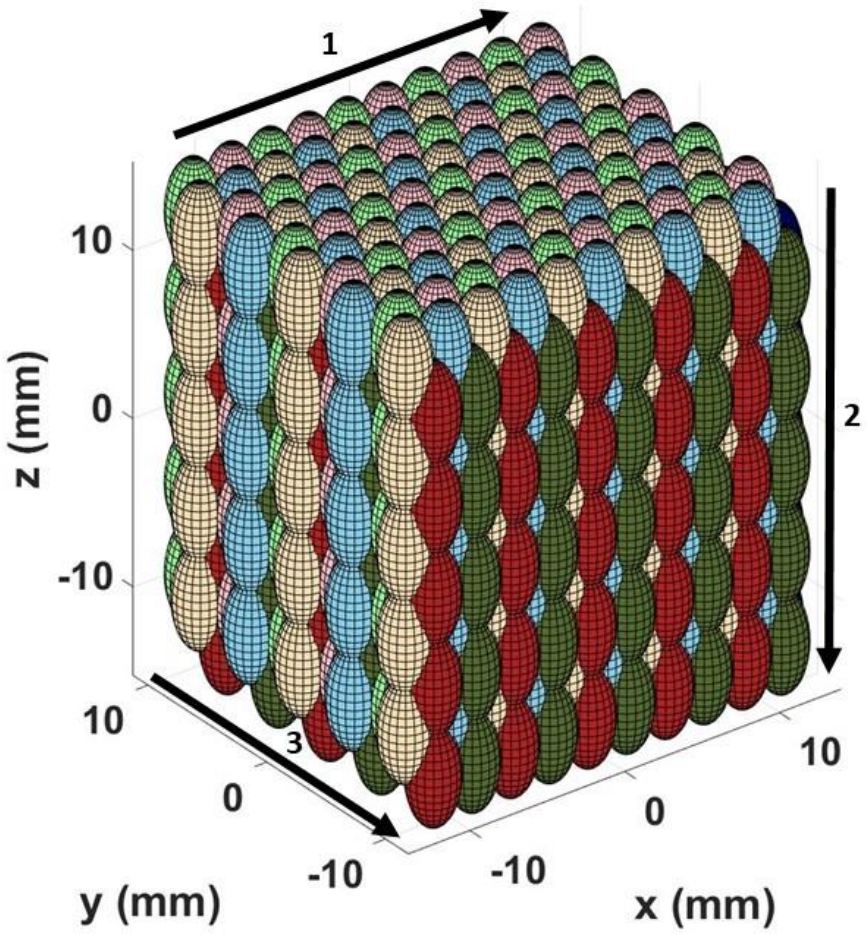

Figure 3. 7. Diagram of EFS positions for proof of principle in a 1000-foci 3D steering grid. The firing order of the eight 125-foci sub-grids was red, dark blue, light green, light blue, dark green, dark brown (not visible in displayed orientation), pink, and light brown. The firing order within each sub-grid progressed as indicated by the numbered arrows starting in the upper left corner. The optical camera was oriented along the y-axis. Units are millimeters. Ultrasound propagation was in the positive z-direction.

3.2.7 Algorithmic EFS Sequence Design

The interleaved sequence described in the previous section provides a starting point for strategic EFS sequence design. This section describes the design of an algorithm which has the potential to achieve greater flexibility, for example, in a situation where the grid spacing is very

fine or heterogeneous. From a theoretical perspective, the problem of iterating over a set of positions such that consecutive positions are separated by a prescribed distance is similar to a branch of discrete mathematics known as *coding theory* [219]. In this context, a *code* represents a subset of points within a finite set where each point is separated from the others by a minimum distance and each point corresponds to a *codeword*. Communications theory describes error detection and correction methods which allow the robust transmission of digital data through noisy communications networks [220], [221]. A common and simple error detection scheme is the use of *parity bits* separated by a given Hamming-distance [221], [222]. A parity bit is appended onto a binary string to make the number of 1-bits either even or odd. If one of the bits is flipped in transmission, the parity of the string will be altered, signaling the presence of an error. The construction of an EFS sequence which addresses persistent residual nuclei can be construed as a generalization of the same concept. Here, the finite set is a list containing all of the EFS grid positions where interactions between therapy pulses and residual nuclei dictate minimum Euclidean (rather than Hamming) distances between positions.

Ordered decimation schemes like the one used to generate the interleaved sequence discussed above become much more challenging to construct when the decimation factor is greater than 8. However, a similar deterministic solution may exist and could perhaps be found by adapting methods from existing work on linear codes over finite fields [223], [224]. The need for advanced ordering schemes is likely to arise in the foreseeable case where each global pulse has a unique spatial location and the density of steering positions is on the order of 10^4 per milliliter. This approach is desirable because it takes advantage of the radial gradient in fractionation efficiency observed for a single lesion. This has not been attempted in our lab due

to the memory constraints of FPGA digital driving circuits in use up to this point. It has been observed that the material at the center of a histotripsy lesion is fractionated within the first few pulses, with the radius of fractionation approaching the final lesion perimeter asymptotically [83], [86]. In this case it may also be desirable to employ heterogeneous grid spacing such that regions near the perimeter have a denser concentration of foci.

Rather than seeking a deterministic solution, this section presents an algorithmic approach to EFS sequence design which begins with a randomized firing order and then performs a series of selection and swapping operations when a violation of the spatio-ordering constraint is detected. After a number of iterations, a permutation of the firing order is generated which meets the constraint for every pulse in the sequence. To begin, a rectangular grid of 1000 points with lateral spacing of 1 grid unit and axial spacing of 2 grid units was defined in MATLAB as a randomized list in a manner similar to that described in section 2.2.2. These arbitrary grid units were defined to simplify algorithm construction and were later scaled appropriately to the physical dimensions of the experiment. Each point was assigned an “exclusion zone” – an ellipsoidal region surrounding the point measuring 2.5 grid units along the minor axis and 5 grid units along the major axis as displayed in figure 3.8.

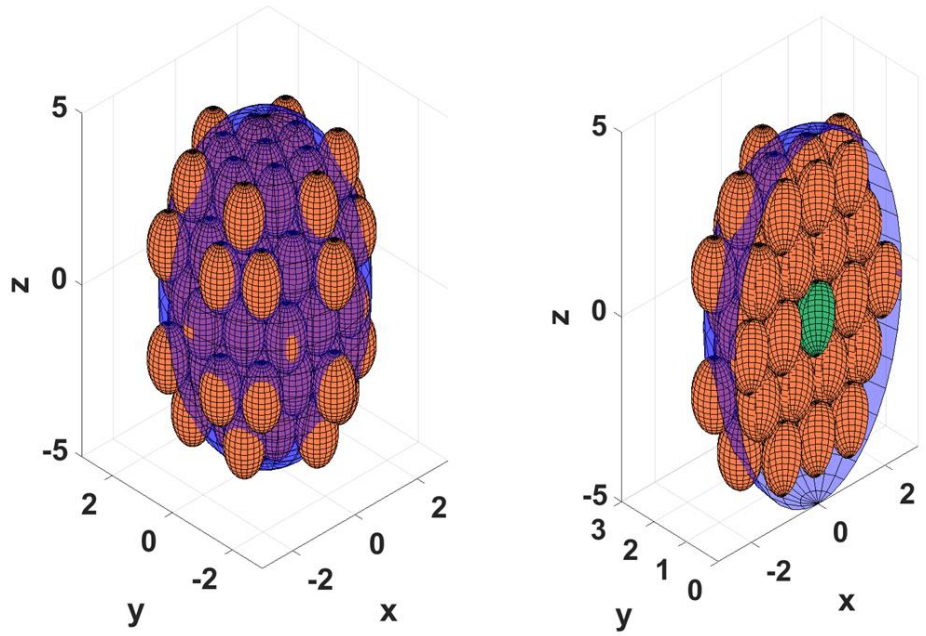

Figure 3. 8. Left: rendering of an exclusion zone (EZ) centered about the central point (0, 0, 0). Right: cross-section view of the exclusion zone. Boundary of the EZ appears in translucent blue. Points falling within the EZ appear as red-orange ellipsoids. Central point appears as a green ellipsoid in the section view on the right. In this case, the EZ contains 87 points including the central point.

The algorithm functioned by selecting the first point from the initial list of points in randomized order and adding it to a list called *walk*. It then found all points residing within the exclusion zone (EZ) for this point and placed those points on a dynamic "timeout" list where they would remain for 20 additional point selections. With each new selection of an allowable point, the surrounding points in its EZ would be added to the timeout list. Once the timeout list was fully populated (after 20 selections), the selection of a new point would also correspond to the oldest set of points on the timeout list coming off the timeout list and going back onto the list of allowable points. As the length of *walk* approached the total number of points in the grid (typically within the last 10 of the 1000 total points), the algorithm would exhaust the list of allowable points and produce violations of the spatio-ordering constraint. When this situation

was encountered, the algorithm would implement a point-swapping method so that allowable points would appear on the list of available points. The swapping operation sometimes required numerous iterations, but the end result was a sequence which produced no violations running continuously in a chain. That is, the list could be run in a circular fashion without any of the first 20 points of the walk violating the EZ constraint of the last 20 points of the walk. A simplified two-dimensional diagram illustrating this technique is displayed in figure 3.9. The scripts comprising this algorithm can be found in appendix under the heading *walk scripts*. The author is grateful to Professors Thomas Wenisch and Grant Shoenebeck for their assistance in conceptually framing this problem and to Akshay Rao for assistance in writing the code.

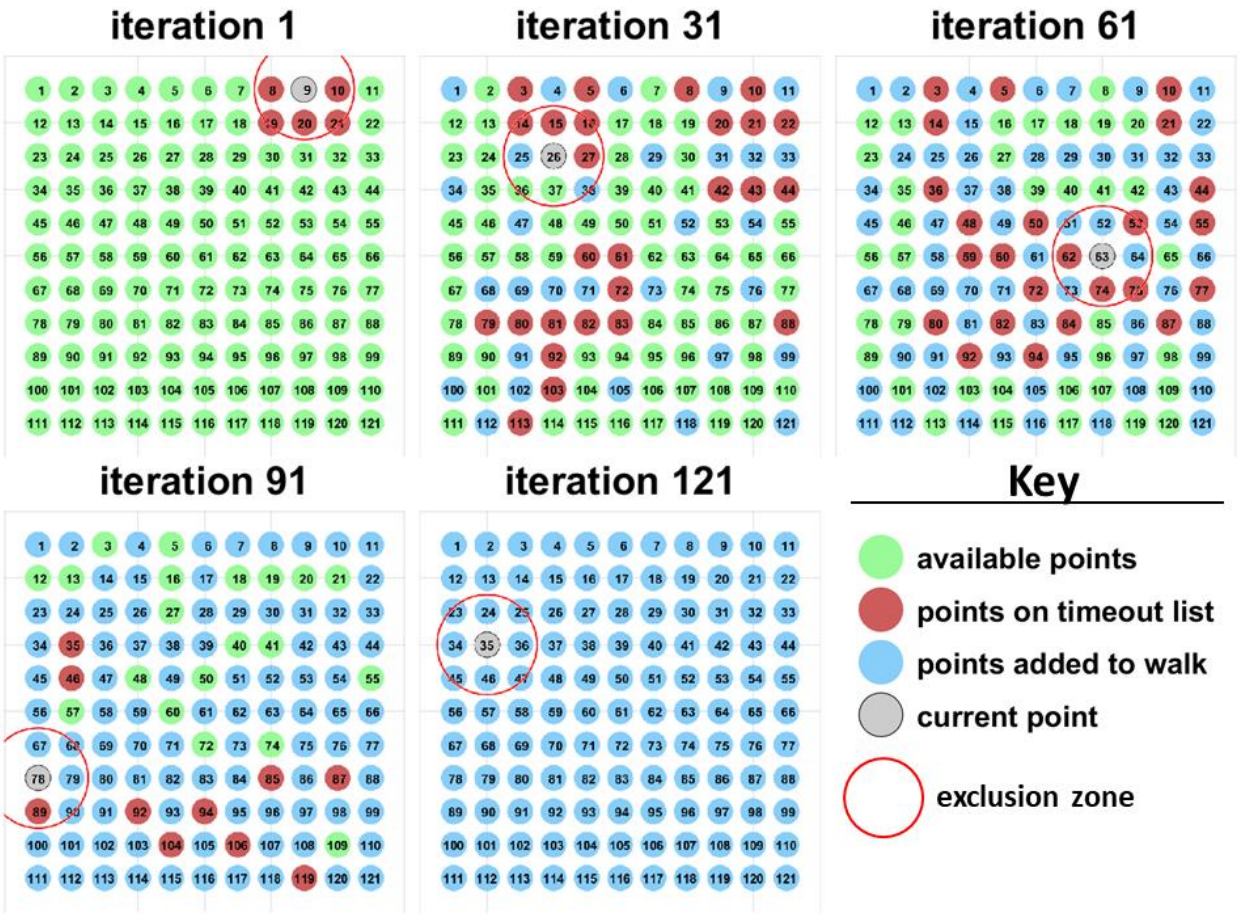

Figure 3. 9. Two-dimensional illustration of the functionality of the walk construction algorithm. Square grid measures 11 points on a side each spaced 1 grid unit apart. Available points appear in green; points on the timeout list appear in red; points which have been added to the walk appear in blue; the point currently under consideration for a given iteration appears in grey; the exclusion zone measures 1.5 grid units in radius and appears as a red circle. The length of the timeout list was 10 iterations. No point-swapping operation was performed for this demonstration. A video in which each frame is available from the author upon request.

The performance of the algorithmic EFS sequence was evaluated by examining each point in the sequence and determining the number of subsequent steps through the sequence until a violation of that point's EZ was encountered. The same analysis was then performed for a randomized firing sequence and the two results were compared in figure 3.17.

3.2.8 Comparison of EFS Sequences

The 1000-foci EFS grid described in section 3.2.6 was used for comparing four EFS sequences: a raster sequence, a repeated random sequence, an interleaved sequence each as described in section 3.2.3, and finally, the algorithmic sequence described in section 3.2.7. The global PRF was 400 Hz, continuous.

Experiments in which BC behavior was investigated for large-volume ablation were performed in RBC phantoms measuring 50 mm x 40 mm x 50 mm and prepared as described in section 3.2.5.2 with gas concentration of approximately 20%. The imaging setup and imaging processing techniques were identical to those described in section 3.2.5.2.

3.3 Results

3.3.1 Isolated Focus

Representative high-speed imaging sequences of the coalescence behavior of residual nuclei at an isolated focus under the influence of low-gain regions of the therapy beam appear in figure 3.10b and 3.10d. Frames corresponding to EFS positions 2:50 were captured when residual nuclei were at their approximate maximum re-excitement radii. In addition to driving BC, EFS pulses 2:50 provided a mechanism for interrogating the spatial distribution of residual nuclei which would otherwise be too small to resolve with the imaging equipment used. Control data appear in figures 3.10a and 3.10c.

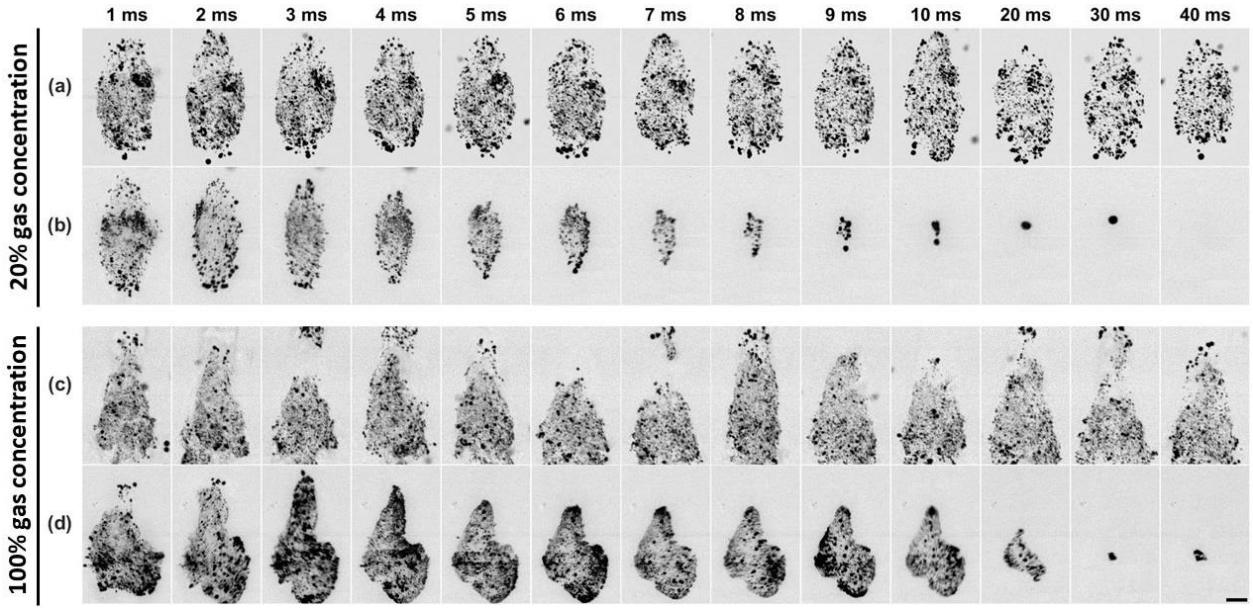

Figure 3. 10. Representative high-speed imaging sequences of coalescence behavior of residual nuclei under the influence of low-gain regions of the therapy beam in agarose gel with 20% (b) and 100% (d) gas concentration. Control image sequences in which only one EFS pulse is applied as a probe to the population of residual nuclei in gel with 20% (a) and 100% (c) gas concentration. The time of image capture relative to initial cavitation expansion appears above each column. PRF = 1 kHz for sequences (b) and (d). Scale bar = 1 mm.

BC behavior was tracked by measuring the maximum projected extent of the residual microbubble population. PRFs tested ranged from 50 Hz to 5 kHz. These data are displayed in figure 3.11. For gels with 20% gas concentration, the number of pulses required to achieve BC ranged from 4.2 ± 0.6 pulses at 50 Hz PRF to 22.6 ± 7.0 pulses at 5 kHz PRF. For gels with 100% gas concentration, the number of pulses required to achieve BC ranged from 27.0 ± 9.6 pulses at 50 Hz PRF to 41.6 ± 3.3 pulses at 5 kHz PRF. No coalescence effect was observed for control data in which a single probe pulse was used. These results provide strong support for our

hypothesis that low-gain regions of the transmitted sound field generated by a histotripsy transducer during EFS can be used to drive BC.

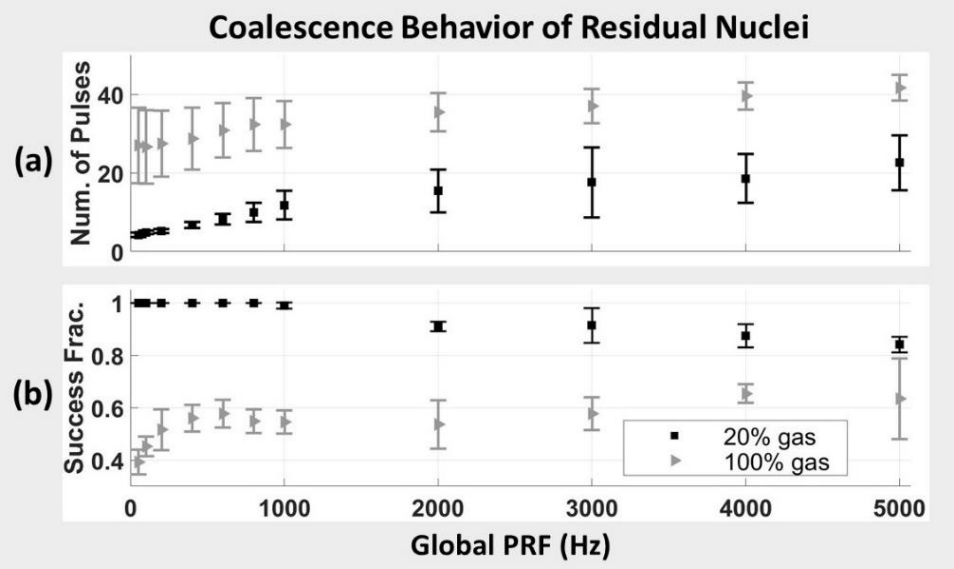

Figure 3. 11. Coalescence behavior of residual nuclei at EFS position 1 under the influence of low gain regions of the therapy beam while electronically steering the therapy focus throughout EFS positions 2:50. (a) Mean number of pulses from EFS positions 2:50 required to achieve coalescence to a single bubble or dense bubble cloud no more than 1 mm in greatest dimension. Error bars represent ± standard deviation of successful samples. (b) Success fraction in achieving coalescence to a single bubble or dense bubble cloud no more than 1 mm in greatest dimension within 49 EFS pulses. Samples collected using gel with 20% gas concentration appear as black squares. Samples collected using gel with 100% gas concentration appear as grey triangles.

The complete disappearance of residual microbubbles within approximately 0-5 EFS pulses following complete coalescence was commonly observed in gel at 20% gas concentration treated with PRF ≤ 1 kHz. In moderate-PRF cases (≤ 100 Hz), bubble disappearance commonly preceded complete coalescence. These data are displayed in figure 3.12 and a representative image appears in the final frame of figure 3.10b. The annihilation of a cavitation bubble driven at high amplitude in degassed media has been described previously in the literature and has been postulated to result from high-amplitude surface instabilities which promote fission of the

bubble into a very large number of very small daughter bubbles which then dissolve rapidly [225]–[229]. The size and number of daughter bubbles produced by fission may be dictated by the order of the surface oscillation mode present prior to collapse [132], [172]. Daughter bubbles may also be near resonance size with respect to the transmitted pulse [204]. A possible explanation for the difference in annihilation behavior observed between degassed and gas-saturated samples is differing concentrations of water vapor and gas within the bubbles [230]. As Bailey et al. noted, the presence of gas tends to cushion the collapse of the bubble while water vapor, which tends to condense, does not [231].

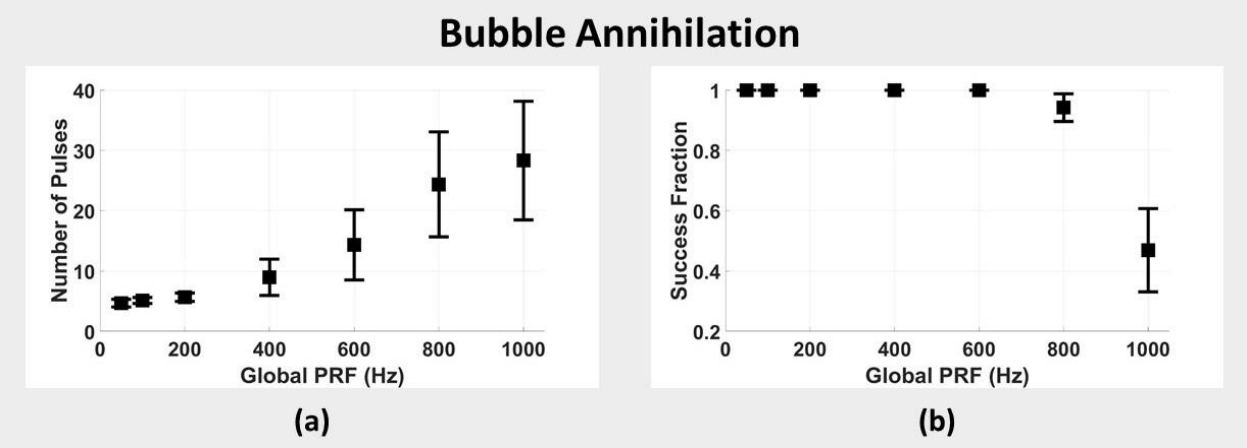

Figure 3. 12. Annihilation of residual nuclei at EFS position 1 under the influence of low gain regions of the therapy beam while electronically steering the therapy focus throughout EFS positions 2:50 in agarose gel at 20% gas concentration. (a) Number of pulses required to achieve annihilation. Each datum represents the mean of successful samples ± standard deviation. (b) Success fraction for achieving annihilation. Each datum represents the mean of ten samples ± standard deviation.

By comparing the time required to achieve coalescence and annihilation of residual microbubbles, it can be seen that this active BC strategy is considerably faster than the passive approach. At 50 Hz PRF, the slowest PRF tested, the time required to remove all residual nuclei

from gel at 20% gas concentration by BC and annihilation was 93 ± 13 ms compared to 1.0 ± 0.4 s relying on passive dissolution alone. While bubble annihilation was not observed at any PRF in gel with 100% gas concentration or for PRF > 1 kHz in gel with 20% gas concentration, the consolidation of residual nuclei into a region 1 mm or less in diameter is expected to reduce the impact of the cavitation memory effect compared to the initial distribution of residual nuclei which encompassed the entire focal region. The time required to coalesce residual microbubbles to a region < 1 mm in diameter was 84 ± 11 ms and 540 ± 190 ms using EFS-BC at 50 Hz PRF compared to 1.0 ± 0.4 s and 170 ± 110 s to achieve passive dissolution in gel with 20% and 100% gas-saturation, respectively.

In gel phantoms with 20% gas concentration, the success rate of achieving BC within 49 pulses decreased slightly with increasing PRF. BC was achieved in 100 ± 0% of cases for PRF ≤ 800 Hz. BC was achieved in 98.9 ± 1.2% cases at 1 kHz PRF and in 84.1 ± 3.0% of cases at 5 kHz PRF. In gel phantoms with 100% gas concentration, the success rate for achieving BC increased somewhat with increasing PRF. Here, BC was achieved in 39.2 ± 4.7% of samples at 50 Hz PRF and 63.4 ± 15.3% of samples at 5 kHz. For all EFS BC tests, 10 samples were collected for each PRF at new, untreated locations in the gel. Each sample location was treated with 100 bursts of the EFS sequence. Thus, values reported here represent the mean ± the standard deviation of 1000 EFS bursts.

3.3.2 Two-Foci Experiments

3.3.2.1 *De Novo* Cloud Formation in Proximity to Dispersed Residual Nuclei

A total of 24 two-foci lesion-pairs were generated in RBC phantoms with PRP values of 5 ms and 5 s and spacing ranging from 1 mm to 10 mm. Images of the cavitation activity induced by the pulse directed at *focus 2* and the resulting lesion were evaluated qualitatively to assess the morphology and position of this *de novo* cloud. Characteristic images displayed in figure 3.13 show that in all cases, the pulse directed at *focus 2* re-excited some residual nuclei at *focus 1*. When the PRP was 5 ms and the two foci were separated by < 4 mm, the size of the *de novo* bubble cloud formed by the second pulse was diminished and the position of this cloud was commonly shifted slightly toward the transducer and the cloud's long axis was tilted. The attenuation of cloud size can be attributed to shielding. The shift in position and orientation can be attributed to scattering. It is interesting to note that in all of the control frames displayed in figure 3.13, some degree of bubble activity is observed at *focus 1*, suggesting that even after 5 s, residual nuclei generated by the first pulse have not completely dissolved. This prolonged dissolution behavior may be due to stabilization by organic molecules found in and amongst the RBCs used to make the phantom as suggested in section 2.4.

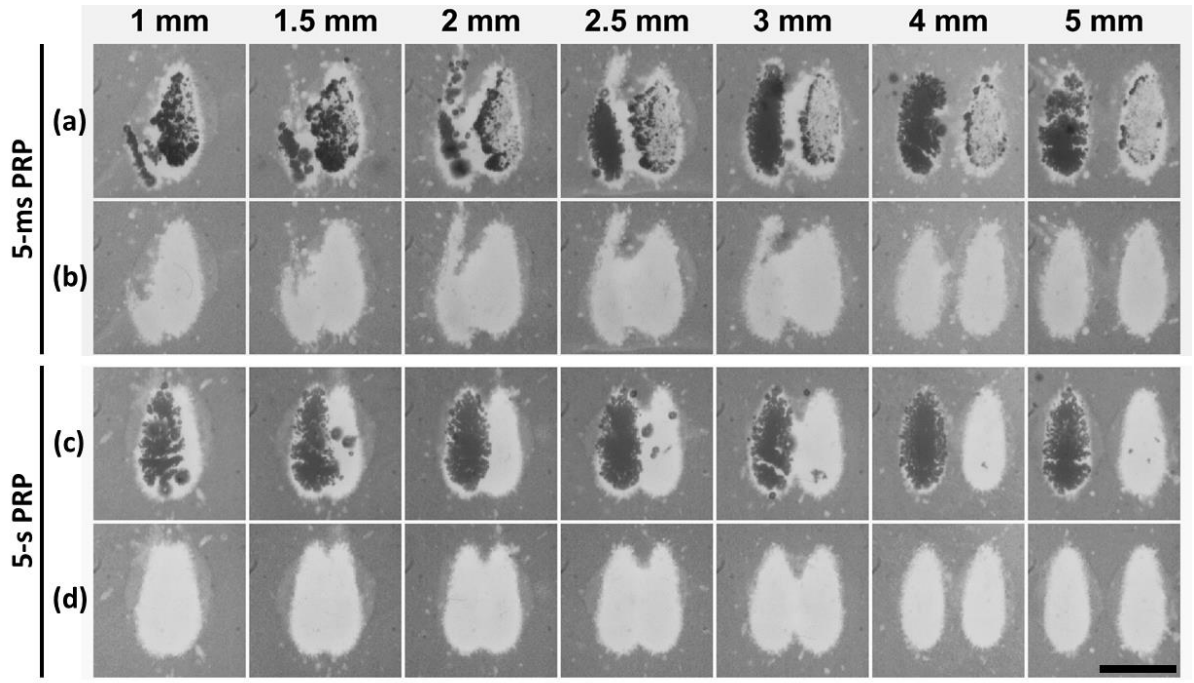

Figure 3. 13. Images of RBC phantom featuring bubble clouds and resulting cavitation damage. Focus 1 is on the right and focus 2 on the left for each image. One pulse per burst was applied to each of two foci at the interval specified to the right of each pair of rows. The pause between bursts was 5 s for both cases. The spacing between foci appears above each column. (a) and (b): 5-ms PRP. (a) Bubble images show dramatic re-excitation of residual nuclei. Degree of re-excitation and degree of distortion of the second focus vary inversely with spacing distance. (b) Images captured following the cessation of bubble activity. (c) and (d): 5-s PRP. (c) Bubble images. (d) Images captured following the cessation of bubble activity. Direction of ultrasound propagation as from bottom to top of images. Scale bar = 5 mm.

A total of 600 two-foci lesions were formed in clear gel phantoms. PRP ranged from 500 microseconds to 5 s and spacing from 1 to 10 mm (N=10 for each spacing and PRP combination). Analysis of these high-speed imaging data was performed by measuring the maximum projected area and collapse-time of the *de novo* cloud initiated by the pulse directed at *focus 2*. As displayed in figure 3.14 and consistent with qualitative observations in RBC phantoms, it was found that the maximum projected area of the *de novo* cloud formed by the second pulse was dramatically attenuated when sequential foci-spacing was < 4 mm and PRP < 5 s, the degree of attenuation increasing with decreasing spacing. For PRP = 5 s, the maximum

projected area of the de novo cloud formed at *focus 2* did not vary with spacing and re-excitation of residual nuclei at *focus 1* was not observed. Aside from the control dataset where PRP was 5 s, little variation was observed between PRP values ranging from 500 microseconds to 500 ms. Similarly, the collapse-time of the *de novo* cloud formed by the second pulse decreased with decreasing focal spacing for all PRP except the 5-s control dataset. However, unlike maximum projected area, collapse-time slightly decreased with shorter PRP even when the focal spacing was > 4 mm. The discrepancy in PRP-dependence for area and collapse-time is a curious result since the two would be expected scale similarly. As a whole, these data are consistent with the qualitative assessment of the RBC phantom results in suggesting that directly sequential foci should be separated by ≥ 4 mm.

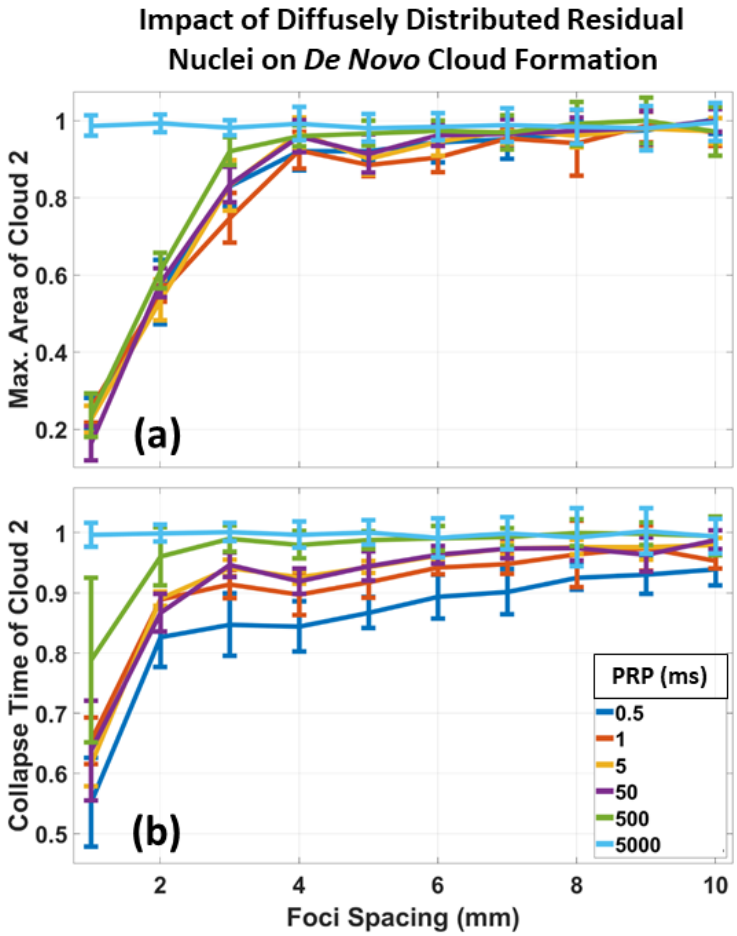

Figure 3. 14. Metrics of bubble activity of at focus 2 normalized to mean values for focus 1. (a) Maximum projected area of the cloud at focus 2. (b) Collapse time of the cloud at focus 2. The size (using projected area as a proxy) and collapse time of a cavitation bubble cloud have been shown to scale with its destructive capacity.

3.3.2.2 De Novo Cloud Formation in Close Proximity to Coalesced Residual Nuclei

The formation of a *de novo* cavitation bubble could at *focus 2* was assessed in a second set of two-foci experiments in which 48 EFS-BC pulses were applied between the pulses directed at *focus 1* and *focus 2*. In these experiments, residual nuclei at *focus 1* were commonly driven to merge into a single bubble or to annihilation by the EFS-BC pulses. Figure 3.15 displays images

of bubble activity resulting from the pulse directed at *focus 2,* 5 ms following the first pulse. The top row features images of bubble activity in which no EFS-BC pulses were applied (as was the case in the previous section). The bottom row, however, features images in which 48 EFS-BC pulses were applied during the 5 ms period between firing at *focus 1* and *focus 2*. In the top row of images, residual nuclei are diffusely distributed throughout the region of *focus 1* and contribute to scattering for focal spacing < 4 mm. In the bottom row of images, residual nuclei have been coalesced to a single bubble or dense cluster near the center of *focus 1* and contribute to a lesser degree of scattering and only appreciably in the case when focal spacing was 1 mm.

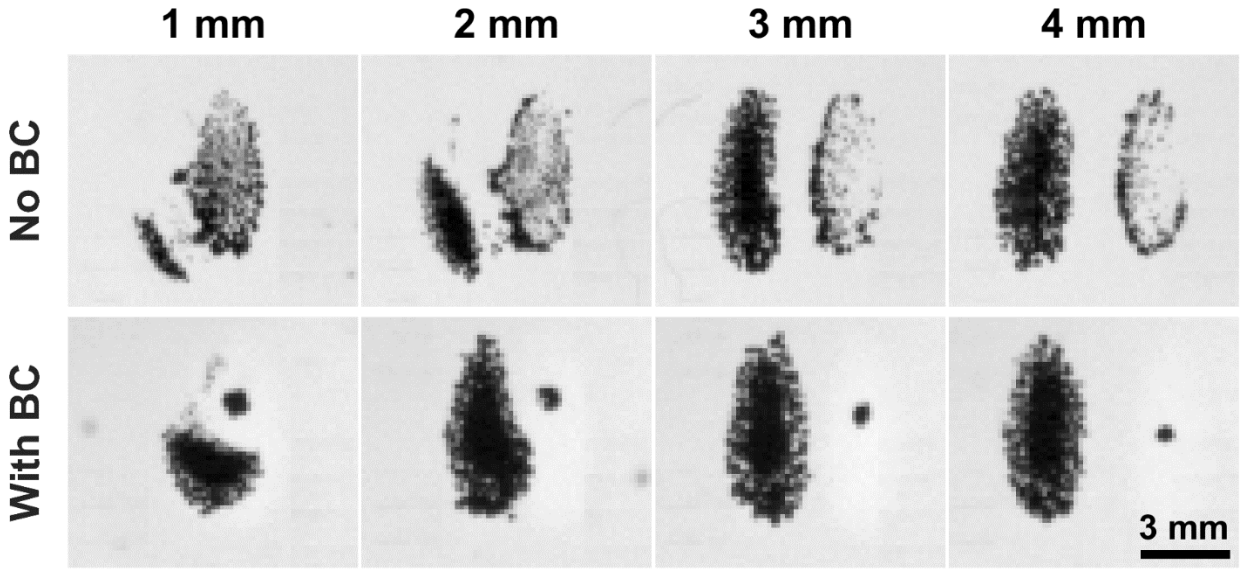

Figure 3. 15. Images of bubble activity resulting from pulse directed at focus 2 for the cases of no bubble coalescence (top row) and 48 EFS-BC pulses between the pulses fired at focus 1 and focus 2 (bottom row). Focus 1 is on the right and focus 2 on the left for each image. Spacing of focus 1 and focus 2 is displayed above each column. Local PRP was 5 ms for both rows. For the bottom row, the global PRP (including EFS-BC pulses) was 100 microseconds. The time of frame capture was within 10 microseconds of the transmitted pulse arriving at the focus. In the top row of images, re-excited residual nuclei are visible in each frame as a diffusely distributed cloud on the right. The *de novo* cloud appears progressively attenuated and shifted as focal spacing decreases. In the bottom row, the coalesced bubble cloud persisting from the residual nuclei generated at focus 1 appears above the *de novo* cloud in the first frame. Here, the bubble appears to block sound from reaching the distal portion of the focus. In subsequent frames, the coalesced bubble from focus 1 appears to the right of the *de novo* cloud and only minimally impacts its formation. The direction of ultrasound propagation is from the bottom to the top of images.

These results present a stark contrast between *de novo* cloud formation in close proximity to a population of diffusely distributed residual nuclei (top row of figure 3.15) and in close proximity to a coalesced single bubble (bottom row of 3.15). The contribution of the EFS-BC effect suggests that foci-spacing could be as close as ~2 mm in a strategic EFS sequence once coalescence of residual nuclei has been achieved (following approximately 10-30 EFS-BC pulses).

The image in figure 3.15 featuring 1-mm spacing for the two-foci experiment with BC reveals the extent to which a small, highly localized bubble population can shield regions of the focus distal to these nuclei. A similar phenomenon is displayed in figure 3.24. It would seem that this phenomenon would negatively impact the ablation process in a histotripsy volume treatment. However, the apparent lesion-scale mobility and mixing which takes place in a large-volume treatment may help to mitigate this potential problem.

3.3.3 Strategic EFS Sequences for Large-Volume Ablation

3.3.3.1 Performance of Basic EFS Sequence

The spatiotemporal constraints illuminated by the two-foci experiments were applied to the design of a basic strategic EFS sequence in which the steering grid was decimated into 8 interleaved sub-grids. These sub-grids were then scanned one at a time and in this manner, the minimum focal separation conditions established by the two-foci experiments were

maintained. Interleaved and random steering sequences were compared. Figure 3.16a displays images of fractionation progression in an RBC phantom captured after applying various numbers of EFS bursts. It can be seen that the interleaved sequence outperforms the random sequence which outperforms the raster sequence in terms of homogenization efficiency and completeness. A total of 3 RBC phantoms were tested for each EFS sequence. Fig. 3.18b displays the percent of fractionation achieved for each EFS sequence as a function of pulse number. In order to achieve 90% fractionation, the raster sequence required 167.7 ± 22.0 pulses, the random sequence, 121.3 ± 44.5 pulses, and the interleaved sequence 80.3 ±24.6 pulses. The number of pulses required to achieve 90% fractionation was found to be significantly different between the raster and interleaved sequences (p=0.01) but not between the raster and random sequence (p=0.18) or between the random and interleaved sequences (p=0.23).

It was observed that after 200 pulses, regions of incomplete fractionation in phantoms treated with the random sequence were found in the same location within the grid across all samples. An examination of the random steering sequence revealed that these locations corresponded to regions in the EFS grid where violations of the spatiotemporal guidelines were spatially densest. That is, these tended to be the areas in which, by chance, temporally adjacent positions in the firing sequence corresponded to spatially proximal locations in the grid.

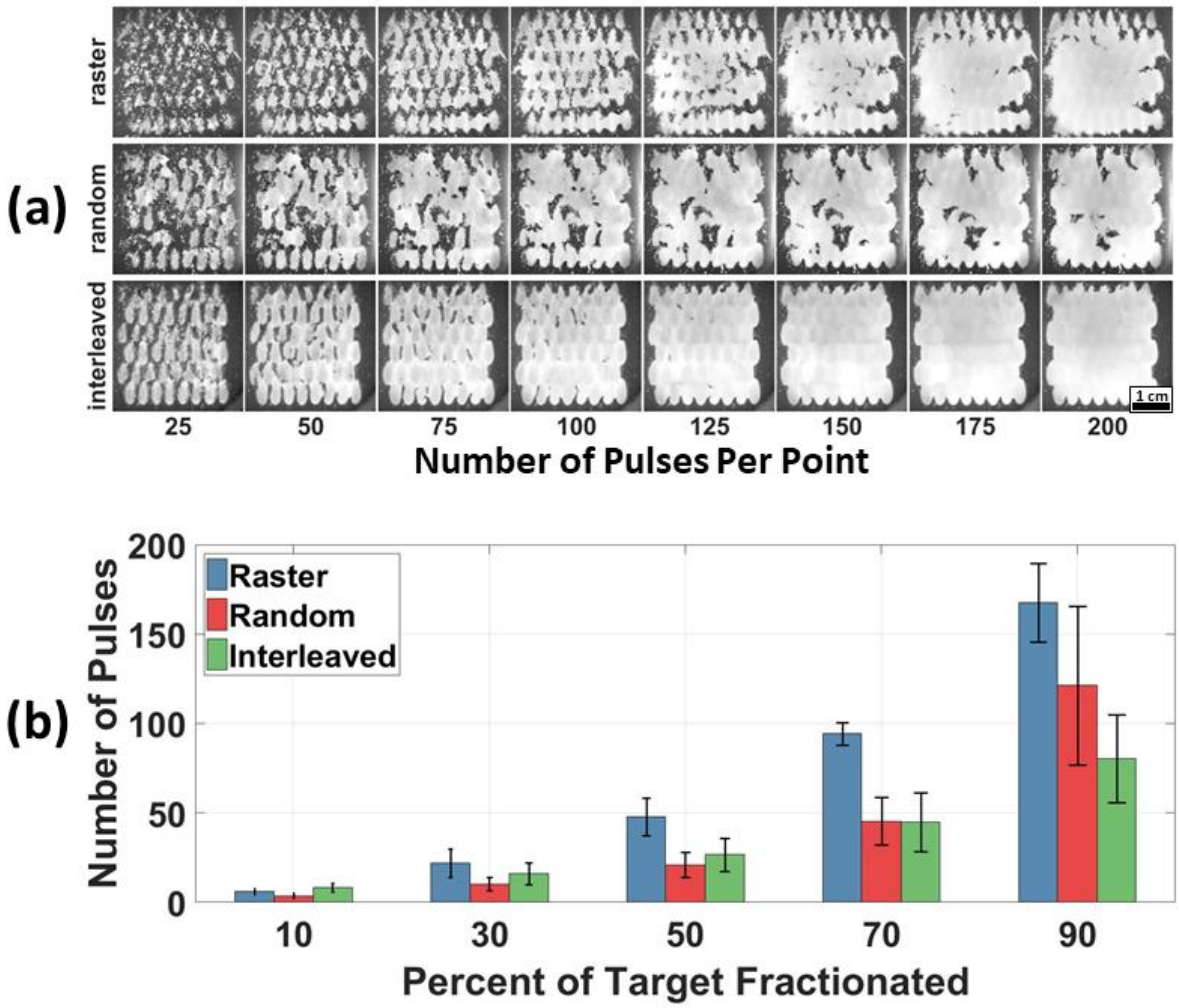

Figure 3. 16. (a) Characteristic images of RBC phantoms treated with EFS sequences arranged in raster, random, and interleaved patters, respectively. Direction of ultrasound propagation was from bottom to top of images. (b) Progression of fractionation in RBC phantoms for EFS sequences employing raster, random, and interleaved scanning patters. N=3 for each EFS sequence.

3.3.3.2 Performance of Algorithm

The performance of the algorithmic EFS sequence was evaluated by examining each point in the sequence and determining the number of subsequent steps through the sequence until a violation of that point's exclusion zone (EZ) was encountered. The same analysis was then performed for a randomized firing sequence and the two results were compared graphically.

The results of this analysis appear in figure 3.17 where it can be seen that the algorithmic sequence maintains the prescribed EZ separation for at least 20 steps for each point. Interestingly, the mean number points until an EZ violation is encountered is 34.8 ± 27.1 (mean ± standard deviation) for the random sequence and 26.4 ± 25.2 for the algorithmic sequence.

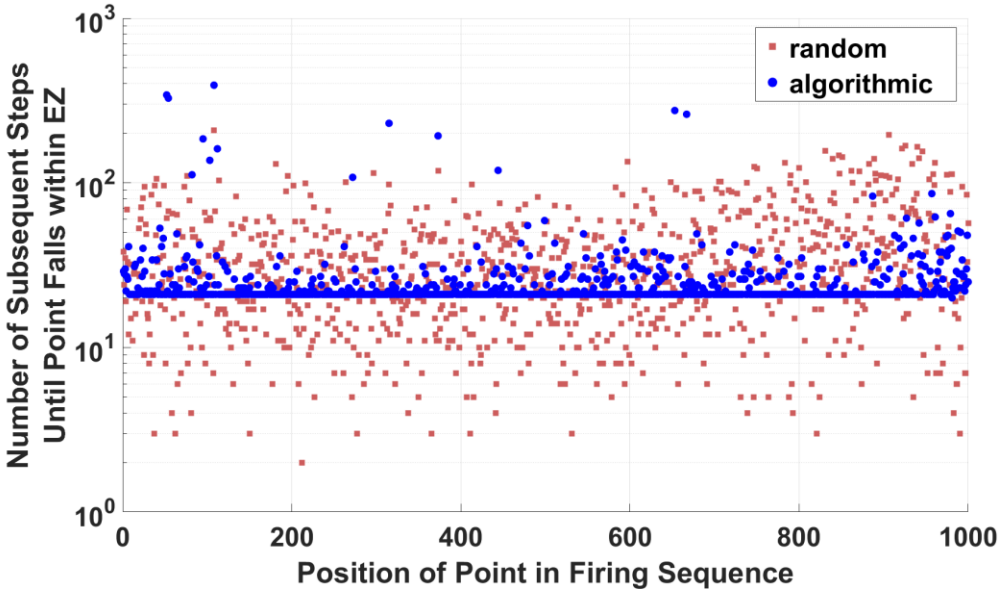

Figure 3. 17. Graphical representation of random (red squares) and algorithmic (blue circles) EFS sequences. For each point 1-1000 in the sequence plotted along the horizontal axis, the distance (in subsequent steps through the sequence) until a violation of that point's exclusion zone (EZ) is plotted along the horizontal axis.

3.3.3.3 Performance of EFS 1000-Foci EFS Sequences

Bubble Coalescence Behavior in Transparent Gel Phantoms

Representative images displaying the coalescence behavior of residual nuclei while executing a 1000-foci EFS sequence at 1 kHz PRF in transparent gel phantoms appear in figure 3.18. Similar results were found at 5 kHz PRF. These images show the expansion of the *de novo*

cavitation bubble cloud at the current EFS focus generated within the high-gain focal region of the therapy beam as well as re-excitement of residual nuclei persisting from previous pulses by lower-gain regions of the beam. BC behavior was assessed qualitatively by observing the spatial extent of residual bubble populations as a function of the number EFS-BC pulses they had experienced since their creation. For both gas concentrations tested, the current EFS focus was trailed by discrete populations of residual nuclei at locations corresponding to the EFS foci which recently preceded it. Consistent with results described in section 3.3.1, these populations of residual microbubbles diminished in spatial extent as a function of the number of EFS-BC pulses applied. For phantoms at 20% gas concentration, it was common for a cloud of residual nuclei generated by a given focus to disappear entirely after approximately 10 subsequent EFS-BC pulses. For phantoms at 100% gas concentration, coalesced populations of residual bubbles were observed to persist for >50 pulses following their generation.

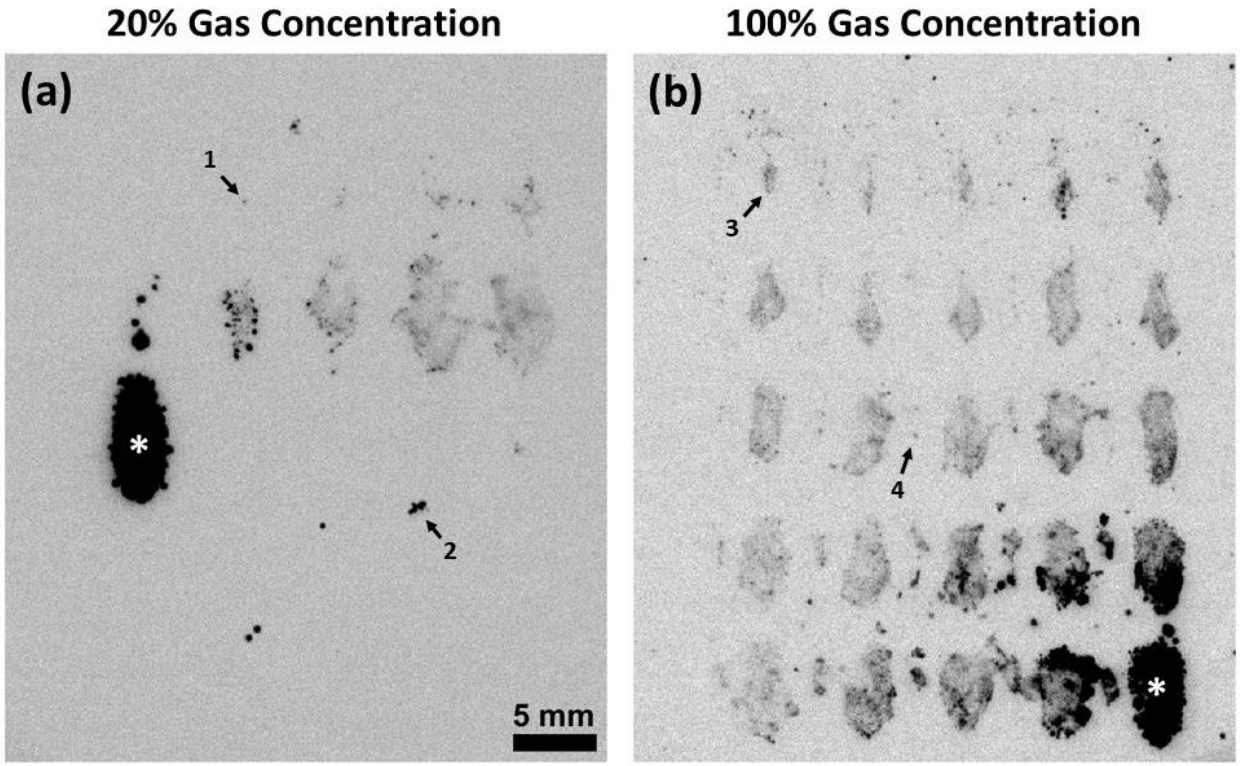

Figure 3. 18. Images of bubble activity while executing a 1000-foci EFS grid in agarose gel phantoms at (a) 20% gas concentration and (b) 100% gas concentration. An asterisk indicates current EFS focus in each image. The time-interval of frame-capture was approximately 125-149 μs following firing the pulse. Progression of firing order was from left to right starting in the upper left corner of each image. Trailing the current foci are progressively more-coalesced clouds of residual nuclei generated by preceding pulses. Arrow 1 indicates the smallest visible coalesced bubble trailing the current EFS focus in image (a). Arrow 2 indicates an example of a small cluster of bubbles persisting for approximately 22 pulses at the time of frame-capture. Arrow 3 indicates a population of bubbles generated 24 pulses prior to the current pulse and having undergone nearly complete coalescence. Arrow 4 indicates a faintly visible coalesced population of bubbles generated 38 pulses prior to the current pulse. These images suggest that the number of pulses necessary to achieve BC in a 1000-foci grid is consistent with data displayed in figures 3.10 and 3.11 in which a single focus in isolation was monitored. PRF = 1 kHz. Direction of ultrasound propagation was from bottom to top of images. Scale bar applies to both images.

Large-Volume Ablation in RBC Phantoms

To demonstrate the therapeutic capacity of the EFS-BC technique, RBC phantoms were treated with the same acoustic parameters applied to transparent gels as described in the previous section. Representative images of lesions generated using 1 kHz PRF in RBC phantoms at 20% and 100% gas concentration appear in figures 3.19a and 3.19b, respectively. For RBC phantoms at 20% gas concentration, 59.5 ± 12.1 repetitions of the EFS sequence were found to

be sufficient to achieve 99.9% fractionation, corresponding to a treatment rate of 27± 6 mL/min. For RBC phantoms at 100% gas concentration and treated with 1 kHz PRF, 123.4 ± 14.5 repetitions were found to be sufficient to achieve 99.9% fractionation, corresponding to a treatment rate of 13 ± 2 mL/min. figure 3.19c displays the progression of fractionation as a function of the number of repetitions of the EFS grid. For RBC phantoms at 20% gas concentration and treated with 5 kHz PRF, 150.0 ± 26.0 repetitions were sufficient to achieve 99.9% fractionation, corresponding to an ablation rate of 55.2 ± 9.6 mL/min. These data support the applicability of the EFS-BC technique for large-volume ablation using a large 3D steering grid. N = 5 samples for the 1 kHz data. N = 4 for the 5 kHz data.

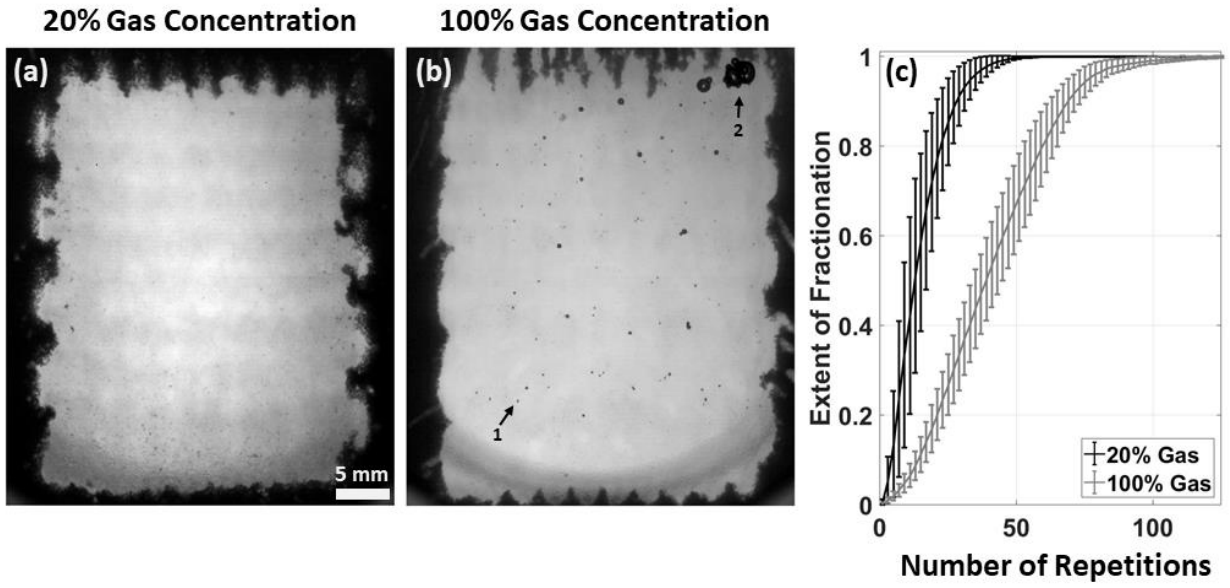

Figure 3. 19. Treatment of RBC phantoms with a 1000-foci EFS grid at 1 kHz PRF. (a) Representative image of RBC phantom with 20% gas concentration following the application of 60 repetitions of 1000-foci EFS grid. (b) Representative image of RBC phantom with 100% gas concentration following the application of 123 repetitions of 1000-foci EFS grid. Arrow 1 indicates an example of a bubble likely coalesced from a single EFS focus and consistent with the results of isolated-focus experiments described in section 3.3.1. Arrow 2 indicates a cluster of large bubbles resulting from a secondary coalescence process in which the coalesced bubbles from multiple foci would agglomerate, translate toward the distal portion of the lesion, and merge. This phenomenon was observed following approximately 90 repetitions of the 1000-foci EFS grid. Direction of ultrasound propagation was from bottom to top of images. (c) Progression of fractionation as a function of the number of repetitions of the EFS grid applied to the phantom. A value of 0 represents no fractionation and a value of 1 represents complete fractionation. Each datum and error bar represent the mean and standard deviation, respectively, of five samples.

The treatment of a large volume at 1 kHz and 5 kHz PRF helps illuminate the role of persistent residual nuclei on the per-pulse efficiency of homogenization. Results displayed in figure 3.10 show that bubble coalescence requires more pulses at higher PRF. Figure 3.20a shows that per-pulse fractionation efficiency is lower at 5 kHz than at 1 kHz. Figure 3.20b displays the relative efficiency of the two treatments for a given value of fractionation extent ranging from none (0) to complete (1). A possible explanation for the diminished per-pulse fractionation efficiency observed at 5 kHz PRF relative to 1 kHz PRF is greater number and spatial extent of residual bubble populations at a given time during the treatment.

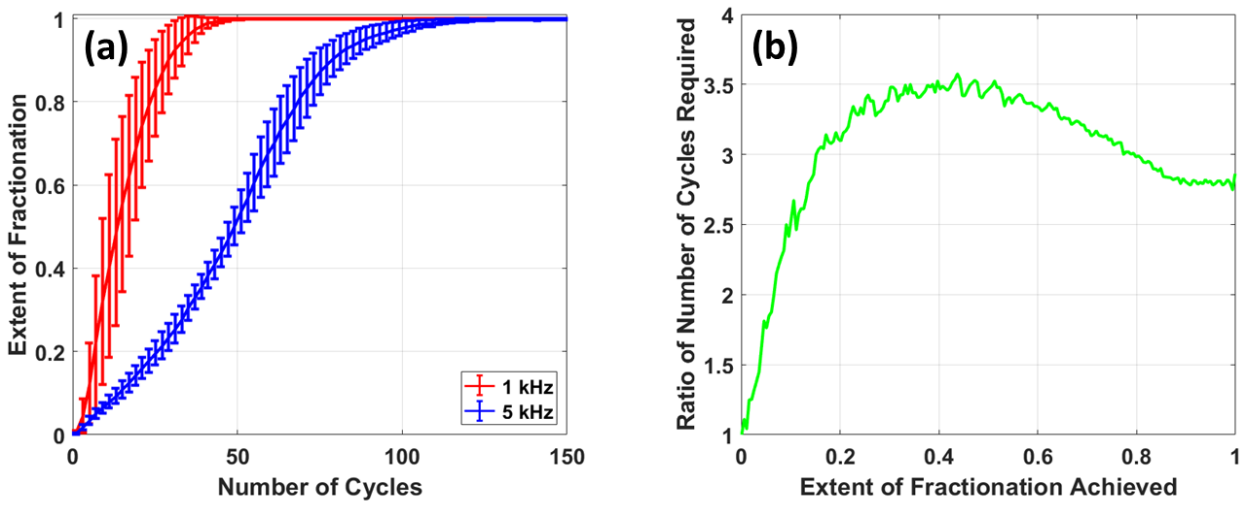

Figure 3. 20. Comparison of treatment of RBC phantoms with 20% gas concentration with a 1000-foci EFS grid at 1 kHz and 5 kHz PRF. (a) Extent of fractionation as a function of the number of cycles applied at 1 kHz PRF (red line) and 5 kHz PRF (blue line). Zero is defined as the starting (untreated) state of the phantom and 1 is defined as complete fractionation. (b) Ratio of the number of cycles required a given extent of fractionation. For example, the number of cycles required to achieve 99.9% fractionation was 52.4 ± 11.6 cycles at 1 kHz PRF and 150.0 ± 26.0 cycles at 5 kHz. Thus, for this value of fractionation extent, the ratio of the number of cycles required at 5 kHz to that at 1 kHz is 2.77. Each datum and error bar represent the mean and standard deviation, respectively, of four samples.

As an aside, an image sequence was collected at 40,000 frames/s with 20 frames per pulse for each of the 1000 foci in the EFS grid with the same experimental setup in order to investigate secondary coalescence of bubbles on the order of 100 microns into bubbles on the order of several millimeters (see figure 3.19b). Interestingly, these large bubbles were observed to oscillate radially, approximately at their respective resonance frequencies. Bubbles also displayed high-amplitude surface oscillations. A continuous fission-fusion process similar to that noted in the single-focus EFS-BC experiments was observed at this much larger scale as well. A likely explanation for this response by bubbles on the order of millimeters despite being several orders of magnitude larger than resonance (a bubble resonant at the center frequency of the therapy array would have a radius of approximately 11 microns) is the high-amplitude,

broadband emissions associated with cavitation expansion and collapse. In addition to emitting shock waves with frequency content on the order of 10 MHz, each cavitation cloud formed by a therapy pulse appeared to produce a “sloshing” effect with frequency content on the order of the reciprocal of the collapse time (~3 kHz).

Comparison of EFS Sequences

The per-pulse therapeutic efficiency of the four EFS sequences described above was compared. Figure 3.21 displays the number of pulses required to achieve various levels of fractionation ranging from 10-90% completion. The random sequence was found to be significantly more efficient than the raster sequence which served as a control ($p<0.05$, Student’s t-test) for each extent of fractionation examined. The interleaved and algorithmic sequences were found to be significantly more efficient within the approximately 0-50% range of fractionation but not thereafter. When the interleaved and algorithmic sequences were compared to the random sequence, it was found that the random sequence was slightly more efficient but only significantly so at the earlies stages of fractionation. These results are unexpected and inconsistent with previous experiments in the smaller EFS grid displayed in figure 3.16.

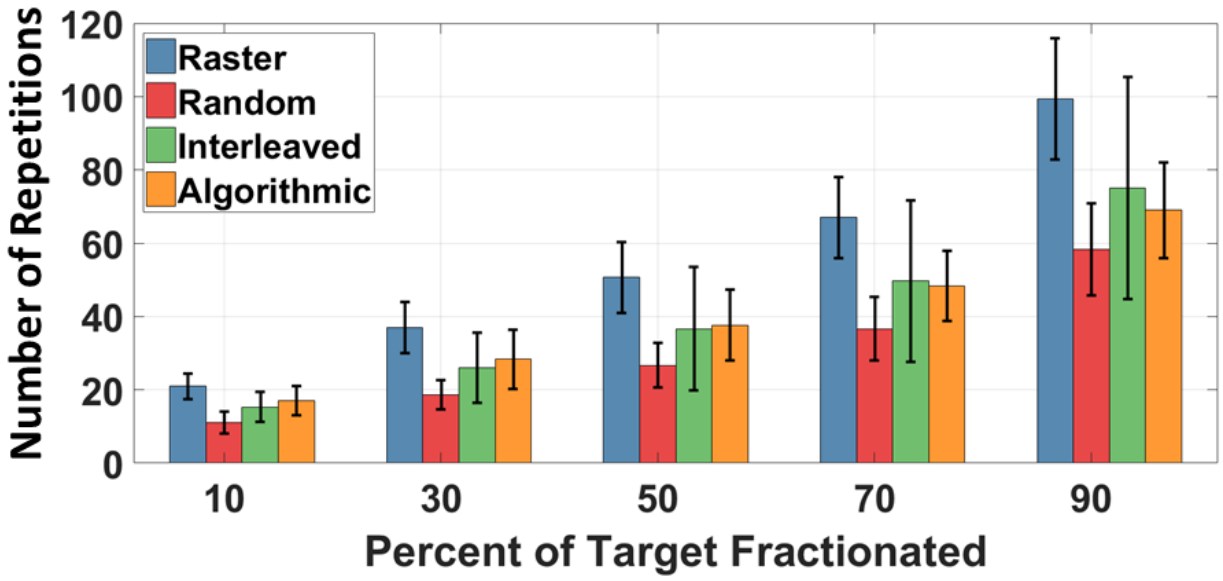

Figure 3. 21. Comparison of the number of repetitions of the firing sequence for the full EFS grid required to achieve a given level of fractionation within an RBC phantom for raster, random, interleaved, and algorithmic EFS sequences. Error bars represent ± standard deviation of the mean.

Table 3. 1. p-values relative to (a) raster EFS sequence and (b) random EFS sequence. p-values calculated using Student's t-test.

(a) p-values Relative to Raster Sequence			
% frac.	Random	Interleaved	Algorithmic
10	0.0098	0.014	0.020
30	0.012	0.023	0.038
50	0.014	0.047	0.055
70	0.021	0.09	0.077
90	0.036	0.35	0.22

(b) p-values Relative to Random Sequence		
% frac.	Interleaved	Algorithmic
10	0.016	0.043
30	0.0199	0.11
50	0.074	0.22
70	0.41	0.48
90	0.32	0.49

3.4 Discussion

3.4.1 Efficacy of the EFS-BC Technique

This study demonstrates a novel acoustic technique for driving the coalescence of residual nuclei by using low-gain regions of the therapy beam during EFS. Similar to previous BC studies from our lab, the approach was to direct short bursts of low-amplitude ultrasound to promote the aggregation and coalescence of residual nuclei mediated by the secondary Bjerknes force [93]–[97] . However, rather than using an acoustic sequence separate from therapy pulses as in previous studies, the technique described herein utilizes low-gain regions of the therapy beam to drive BC. By employing specially-designed EFS sequences, each pulse served the dual-purpose of generating cavitation at the present EFS therapy-focus as well as driving BC at recently treated foci which harbor populations of residual microbubbles. This EFS-BC method supplies a foundational component for a volume-ablation approach which could achieve higher treatment rates without the deposition of additional acoustic energy associated with a traditional, separate BC sequence. The ultimate treatment rate of histotripsy *in vivo* is limited by the cavitation memory effect and the heating of tissue surrounding the therapy target. The findings in this study are significant in part because they demonstrate proof of principal regarding management of residual nuclei without the deposition of any additional acoustic energy during histotripsy therapy.

The mechanism responsible for bubble coalescence is postulated to be the secondary Bjerknes force [93]–[97]. This mutually attractive force between two microbubbles varies with

the inverse of the square of their separation distance [89]–[92]. The dynamics of a cloud of insonified residual microbubbles can be described as an *N-body* problem somewhat analogous to gravitational interactions in a galaxy or the electromagnetic interactions in a plasma where the system possesses a volumetric centroid [227], [232]–[234]. In this study, clouds of residual microbubbles under the influence of EFS-BC pulses, coalesced to the approximate centroid of the initial distribution of residual nuclei within the focal zone. While the cloud and coalesced bubble(s) were observed to translate slightly in aggregate away from the transducer due to the primary Bjerknes force, the mutual attraction mediated by the secondary Bjerknes force dominated the motion of individual microbubbles within the cloud. Nonlinear behavior encountered at high driving pressures is likely responsible for the disparity in the magnitude of the two Bjerknes forces. Mettin *et al.* found that at high driving pressures, the magnitude of the secondary Bjerknes force may increase by a factor of 10^3-10^6 relative to the linear response associated with lower pressures [207]. The nonlinear regime for the secondary Bjerknes force begins at approximately 50 kPa [207], [235]–[237]. Pressures experienced at EFS position 1 while firing at EFS positions 2:50 (P+, P- = 3.5 ± 0.7, 2.7 ± 0.6 MPa) were two orders of magnitude higher than the threshold for nonlinearity. Additionally, the radius of a single bubble linearly resonant in water [177], [238] at driving frequency of 250 kHz is 11 µm which is within the range of residual nuclei generated in the present study. The additional stiffness of tissue or tissue-mimicking gel would be expect to elevate the resonant radius [231].

The number of pulses required to achieve BC was consistently higher for gel phantoms with 100% gas concentration compared to those with 20% as displayed in figure 3.11. While a precise formulation of the relevant bubble dynamics is beyond the scope of this study, the

authors hypothesize that the greater number, number density, and spatial distribution of residual bubbles generated at 100% gas concentration and the potential of these microbubbles to grow by rectified diffusion to well beyond resonance size are likely responsible for the disparity. Additionally, it was observed that for both gas concentrations tested, the number of pulses required to achieve BC increased with PRF, the trend being more pronounced at 20% gas concentration. The authors attribute this trend to passive dissolution of very small bubbles between pulses. Control data for gel phantoms at 20% gas concentration indicate that expanded bubbles near or below the high speed camera's resolution limit (~8 μm diameter), which appear as a haze between larger, individually resolvable bubbles, are no longer detectable after approximately 10 ms as displayed in figure 3.10a. The theoretical model of Epstien and Plesset applied here predicts that dissolution times < 10 ms would correspond to bubbles with static radii of <1 μm [87], [153], [164].

In cases where complete coalescence was not achieved after the application of 49 BC pulses, the failure can be attributed to two mechanisms. 1) It was observed that the first pulse applied to an untreated region of gel generated a cloud of residual nuclei distributed throughout the therapy focus and in higher number than subsequent pulses (see figure 2.10). These microbubbles were observed to begin aggregating but at a slower rate, suggesting that they were tunneling [86], [162], [198], [199] through regions of mostly-intact gel. Based on this slowed but not completely impeded motion, it is likely that these residual bubbles would have completely coalesced had more BC pulses been applied. 2) While many residual microbubble clouds coalesced to a single bubble or dense bubble cluster, some residual microbubble clouds split as the coalesced, forming two or more of these structures, often separated by ~3-7 mm.

These structures exhibited only weak attraction, likely due to the separation distance (the secondary Bjerknes force varies with r^{-2}) and diminished response to BC pulses as many microbubbles merged and grew beyond resonance size. When separate coalesced bubble clusters were observed, they were aligned along the direction of sound propagation. It is expected that this configuration would achieve much of the benefit of a single coalesced bubble by possessing a similarly small scattering cross-section for incident therapy pulses.

For the cases where bubble annihilation was possible, the therapy focus could be immediately returned to this location to generate *de novo* cavitation without the influence of any pre-existing micron-scale bubbles. In the cases where bubble annihilation was not observed (high PRF and high gas concentration), scattering of the incident pulse was observed. This phenomenon is displayed in figures 3.15 and 3.24.

The decision to transmit only 49 BC pulses was made primarily with the design of advanced EFS sequences in mind. The design-intent of these sequences was to produce an algorithm which would steer the focus to a given position and then fire subsequent pulses to positions selected from a list of allowable foci which excluded those within a prescribed distance of the given focus, maintaining this condition for a given number of pulses. Ideally, by the time the given focus came off the timeout list, its residual nuclei would be coalesced or annihilated. Preliminary analysis of the problem suggested that the upper limit for the length of the timeout list would be approximately 20 EFS positions for a grid comprised of 1000 foci and an exclusion radius of two grid spacing intervals. More detail is provided on advanced EFS sequence design in section 3.2.7. Additionally, increasing the number of BC pulses would have required a longer

burst repetition period for the case of 50 Hz PRF and this would have extended the already long duration for which the transducer was required to be submerged during experimentation.

3.4.2 Observations of Coalesced Bubbles and Potential Applications to Aberration Correction

Following the application of each EFS-BC burst, the monitored focus of gels at 100% gas concentration were commonly observed to contain several tightly clustered bubbles, typically with one bubble on the order of 100 microns and several others on the order of 10 microns. At least one bubble with a static radius ≥ 10 μm was found to persist for the 5 s between EFS bursts in all but 63 of 11,000 EFS bursts applied. An example of one such cluster of bubbles appears in the final frame of figure 3.10d. No visible bubble was observed to persist for the 5-s period between bursts in any gel with 20% gas concentration.

Several studies have demonstrated the potential of microbubbles for aberration correction [239]–[242]. The BC technique described in the present study has the potential to provide a quasi-stable scattering target which could be used for applications like aberration correction or tracking of tissue-motion completely noninvasively and without the need for any exogenous contrast agent. Section 4.2 of this dissertation investigates the formation of single and multi-bubble scattering targets by using a specialized bubble coalescence technique based on the findings of the present chapter.

The resolution, frame-rate, and exposure-time of the high-speed imaging setup used for the EFS-BC experiment were not ideally suited for imaging the dynamic activity of these small

bubble systems. However, at both gas concentrations, the images of the activity of coalesced bubbles and bubble clusters (displayed in figure 3.22) suggests that these structures were undergoing repeated fusion and fission events in which bubbles would appear to merge and subsequently eject daughter bubbles. A similar phenomenon has been documented previously in the literature [207], [226]–[228], [231], [243], [244]. Dense, stably-bound bubble cluster systems, sometimes referred to as *bubble grapes*, have been observed experimentally in cases where the assumptions made in the linear formulation of the secondary Bjerknes force (fluid incompressibility, adiabatic behavior of gas in bubbles, separation between bubbles much greater than bubbles' radii, bubble sphericity, absence of nonlinear oscillations) [232], [236], [245], [246] no longer hold due to high acoustic pressure amplitudes.

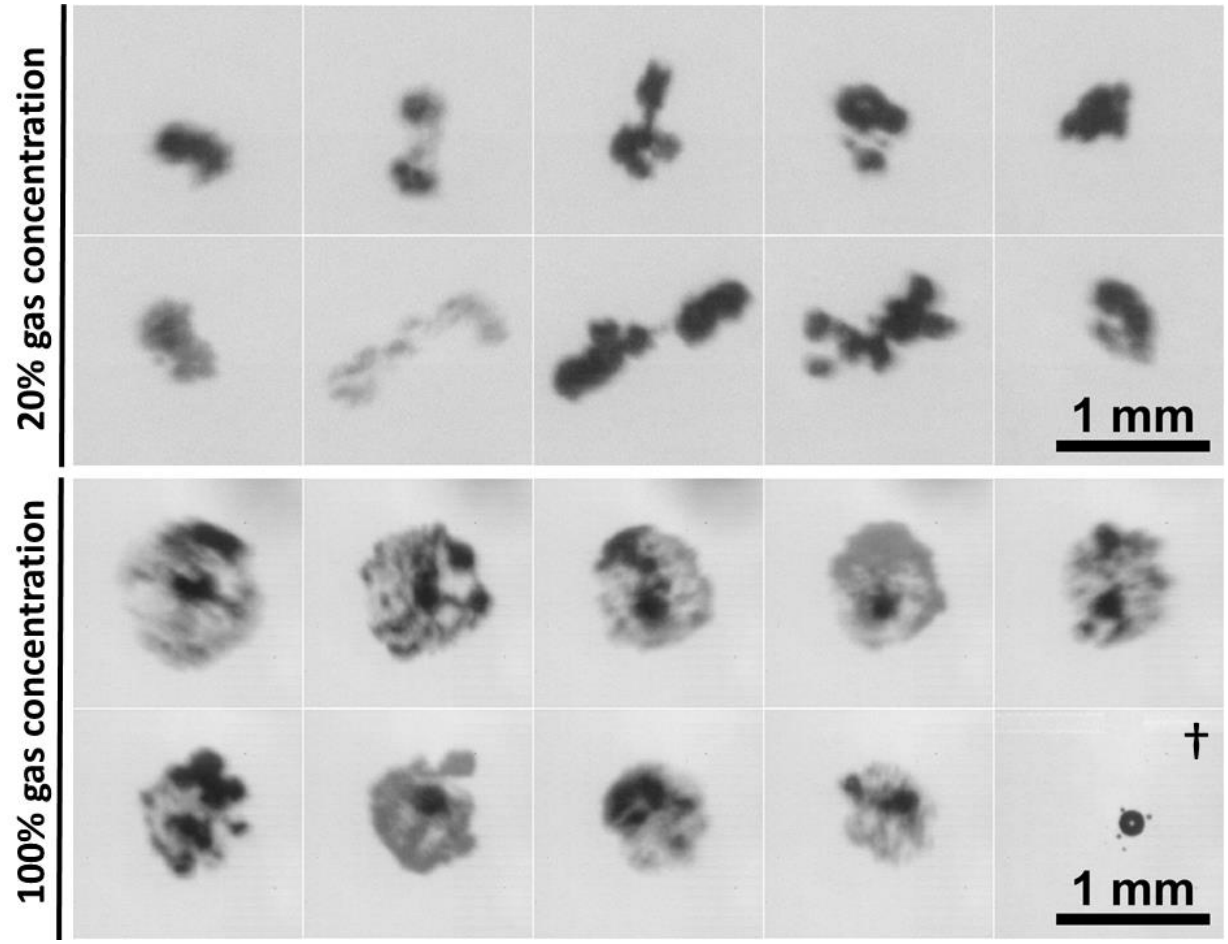

Figure 3. 22. Characteristic high-speed images of coalesced cluster of residual nuclei excited by separate EFS-BC pulses fired at 5 kHz in degassed gel (top rows) and gas-saturated gel (bottom rows), respectively. All frames within the respective top and bottom row groupings were captured sequentially, separated by 200 microseconds except the indicated with † which was captured approximately 5 s following the other images and displays the bubble cluster in a quasi-static state (no acoustic excitation). For both groups, bubbles appear to exhibit continuous fusion and fission events about a central locus.

The size of the largest bubble persisting between cycles was found to increase with PRF and burst-number as shown in figure 3.23. This bubble was found to be as large as 96 µm in static radius and would be expected to persist for ~6 hours before dissolving in gas-saturated water [87]. The general trend of bubble growth as a function of the number of pulses applied can be attributed to rectified diffusion [247]–[253]. The more rapid growth in bubble size observed at higher PRF may be attributed to the sound field produced by cavitation activity at EFS positions

2:49. With BC pulses transmitted at 5 kHz, each cavitation event at foci 2:50 produces high-amplitude signals upon expansion and collapse, thereby effectively driving the bubble at a frequency which is closer to resonance for these large bubbles [238]. The saturation behavior of bubble growth in this setting can be explained by sequestering of available gas from the focal zone into the bubble.

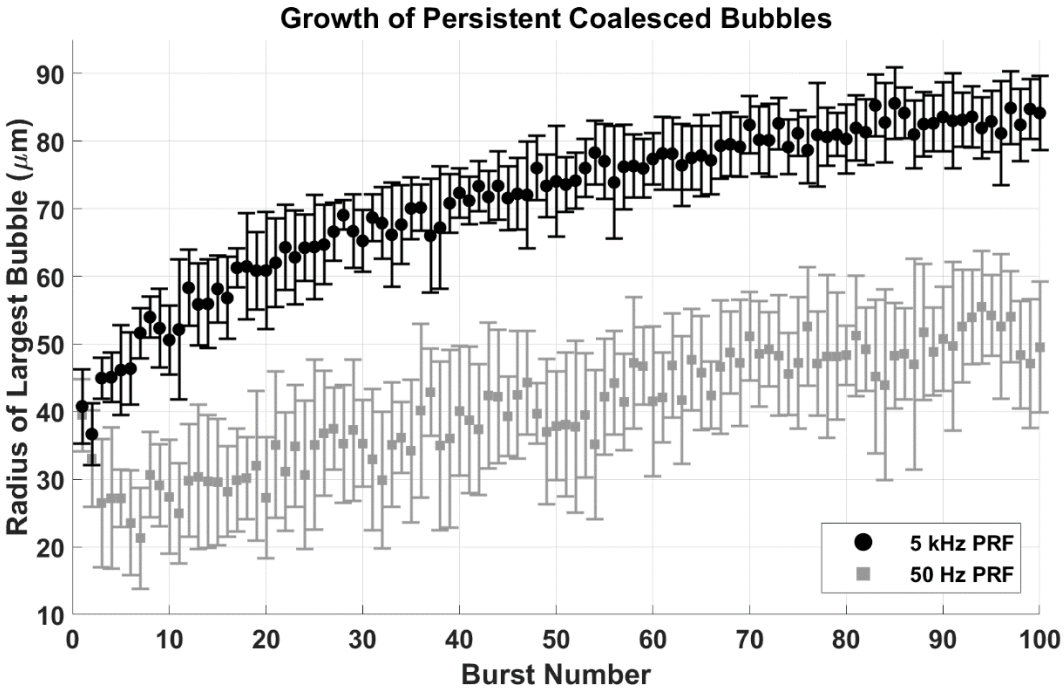

Figure 3. 23. Mean size of largest coalesced bubble persisting for 5 s between EFS bursts in gel phantoms at 100% gas concentration. These bubbles were observed to increase in size as a function of the number of EFS bursts applied with more dramatic initial growth observed at higher PRF.

As displayed in fig. 3.24, the presence of even a single microbubble can have a profound impact on cavitation nucleation behavior. It was observed that a single bubble near the center of the focus was capable of shielding the region of the focus distal to it. This observation likely has important implications for large-volume ablation, particularly *in vivo*, where coalesced

residual microbubbles would be expected to persist for long periods of time. Additionally, the inertial re-excitation behavior of a microbubble displayed in fig. 3.24(e-g) is significant as a potential tool for investigating the mechanism(s) by which cavitation activity produce tissue-damage. Evidence from a series of ad hoc, anecdotal experiments in an RBC phantom suggest that re-excited microbubbles, in the absence of any *de novo* cavitation and despite generating apparently large strains, have little to no destructive capacity (data not shown). This would suggest that the destructive effect of cavitation activity relies heavily on the initial explosive growth of individual bubbles.

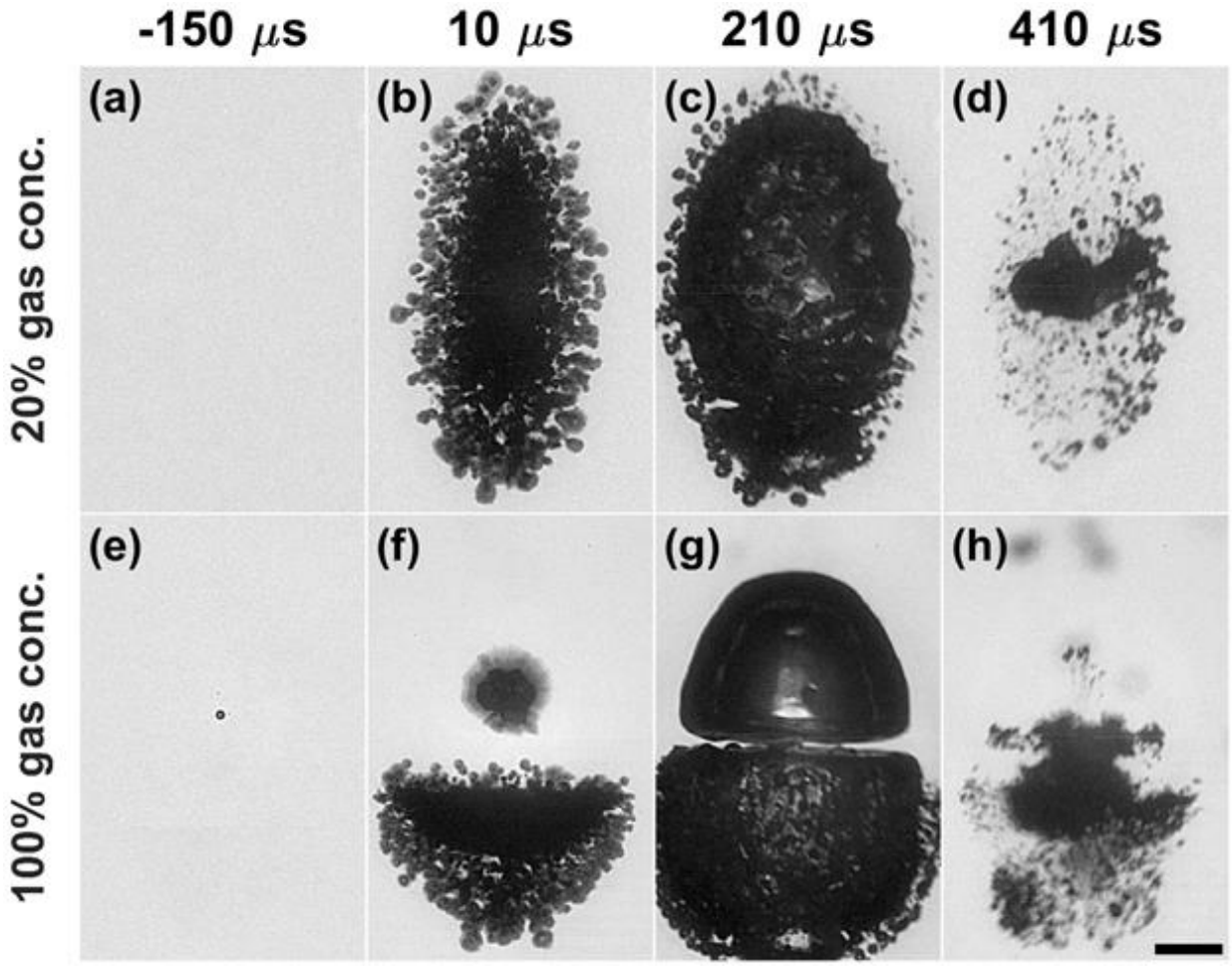

Figure 3. 24. High-speed images of cavitation activity at EFS focus 1 during treatment at 5 kHz for samples with approximately 20% (top row) and 100% (bottom row) gas concentrations, respectively. Time with respect to the arrival of EFS pulse 1 appears above each column. t=0 corresponds to the arrival of EFS pulse 1 at the monitored focus. Frames (a) and (e) show the initial conditions of the respective foci immediately prior to the arrival of the pulse. In the degassed gel, the 5 s between EFS bursts was sufficient for coalesced residual bubbles to dissolve completely. However, in the gas-saturated gel, a dense cluster of coalesced residual bubbles (similar to that displayed in figure 3.22) are present near the center of the focus. The frames captured at t=10 microseconds show highly distinct cavitation nucleation behavior for these two different initial conditions. (f): The presence of the coalesced bubble in the gas-saturated case generates what appears to be strong scattering behavior in the proximal region and shielding in the distal region. Frames (c) and (g): correspond to the arrival of EFS pulse 2 and reveal the position of peripheral bubbles surrounding the primary cloud. The persistent bubble, re-excited by EFS pulse 1, has several interesting features: its size is comparable to that of the proximal cloud scattered off it, its surface is smooth rather than ragged, and it is not surrounded by any peripheral bubbles. Frames (d) and (h) correspond to the arrival of EFS pulse 3 and reveal the position of residual nuclei during or shortly following the first cavitation collapse. Note that the distribution of residual nuclei in frame (h) is predominantly biased toward the region occupied by the scattered, *de novo* cloud. Direction of ultrasound propagation was from bottom to top of images. Scale bar = 1 mm.

3.4.3 Strategic EFS Sequences

This study demonstrates a novel technique for the design of a strategic EFS sequence. Design parameters were first established by investigating the interactions between residual nuclei and therapy pulses in a simple model comprised of two EFS positions. These parameters were then applied to the design of a basic strategic EFS sequence in which the grid was decimated into 8 interleaved sub-grids such that sequential foci were separated by a predetermined value. Finally, an algorithm was constructed which allowed the generalization of the spatio-ordering constraints established by the two-foci experiment to be applied to an EFS grid of arbitrary configuration.

Comparisons of EFS grids used a control case in which the focus was scanned in a raster pattern where one pulse was delivered to each point in the grid sequentially for *N* repetitions. A better control might have been to apply *N* pulses to each grid point before moving on the next in a raster fashion that would more closely capture the approach of using a histotripsy transducer not employing electronic focal steering. The result would have likely been further diminished ablation efficiency and greater peripheral damage.

The per-pulse fractionation rate observed for the 1000-foci EFS grid applied to RBC phantoms at 20% gas concentration is approximately twice as fast that observed in a previous study using similar acoustic parameters in which fractionation progression at a single lesion was monitored [86]. The authors attribute this increase in per-pulse efficiency to the BC effect and to greater mobility of material within the 1000-foci lesion. It was observed that during the first approximately 15 EFS sequence repetitions, fractionation occurred primarily at discrete

locations centered about the EFS points with material between EFS points remaining largely unfractionated and stationary. After approximately 15 repetitions, unfractionated material could be seen translating in directions generally inward from the lesion perimeter and opposite the direction of ultrasound propagation. This result suggests that the destructive capacity of a cavitation cloud is most pronounced near its center and that perhaps a more finely-spaced EFS grid would facilitate a greater per-pulse fractionation efficiency. While the FPGA digital circuit driving system used in the present study was limited to distributing 1024 EFS positions throughout 27 mL, an EFS sequence could be conceived in which each of the total number of pulses (= N_{foci}*$N_{repetitions}$) delivered throughout the treatment would correspond to a unique spatial position within the treatment volume. Such an approach would more homogeneously distribute what appears to be the most efficient portion of each focus (its center), thereby better utilizing its ablation capacity. By comparison, ablation rates common for thermal ablation using high-intensity focused ultrasound (HIFU) and radio frequency (RF) ablation are approximately 2 mL/min [17], [18], [254], [255].

The EFS-BC technique is intended to accelerate the large-volume ablation such as tumors in the liver, kidney, and pancreas. The two limiting factors for treatment speed for histotripsy are the persistence of diffusely distributed residual nuclei and the risk of heating. Previous studies have suggested that it may be advantageous to arrange an EFS sequence strategically for volume ablation such that spatial positions of temporally adjacent EFS foci are separated sufficiently in space so that residual nuclei do not compromise therapeutic cavitation activity [86], [94]. Using a passive strategy like this for the management of residual nuclei, treatment speed is ultimately constrained by the dissolution time of residual nuclei and the steerable

range of the transducer. The BC effect observed herein is likely inherent to any EFS sequence to some extent and is believed to account partly for the enhanced efficiency of EFS over mechanical steering alone [55]. However, a strategic EFS-BC sequence is fundamentally different from an EFS sequence based on passive dissolution in that the management of residual nuclei is based on the number of pulses required to achieve BC rather than a fixed dissolution time. Additionally, previous studies using separate BC sequences achieved BC but deposited 30% additional acoustic energy. When using a high PRF to achieve a high ablation rate for a large-volume target, the additional acoustic energy may pose the risk of heating overlying and surrounding tissue. The EFS-BC technique demonstrated herein has the potential to remove the need for the additional energy deposition associated with a separate BC sequence. In the present study, we demonstrate the use of a strategic EFS-BC sequence to treat a large volume. The presented EFS-BC method may allow us to circumvent the limiting factors of cavitation memory effect and the risk of heating, thus enabling a more rapid ablation of a large volume.

While the present study was restricted to the intrinsic threshold regime of histotripsy (also referred to as microtripsy) [142], it is expected that the EFS-BC technique described herein would be applicable for pulsing regimes with a greater number of acoustic pulse-cycles including shock scattering [68] and boiling histotripsy [256]. In these cases, the additional cycles may drive BC more rapidly. For shock scattering, the persistence of a large coalesced bubble, located centrally within each EFS location could be particularly beneficial as it could function as a scattering target for subsequent pulses and perhaps alleviate some of the need for sustaining pulses [83], [257]. Similarly, for boiling histotripsy, the more rapid formation of such a centrally

located bubble could be beneficial if the proposed mechanism of action is indeed ultrasonic atomization [258].

Heat deposition and the cavitation memory effect impose ultimate treatment rate limitations on histotripsy. This study demonstrates proof of principle regarding a novel method for mitigating the cavitation memory effect by utilizing low-gain regions of the therapy sound field to drive the aggregation and coalescence of residual nuclei by means of the secondary Bjerknes force during electronic focal steering. Because the technique utilizes each pulse for the dual-purpose of generating cavitation at the current therapy focus as well as driving bubble coalescence, it is more energy-efficient than using a separate acoustic sequence. By addressing the cavitation memory effect without the deposition of any additional heat beyond that of the therapy sequence, the technique described in this study has the potential to elevate the achievable treatment rate of histotripsy volume ablation using electronic focal steering.

This study evaluated the relative performance of EFS sequences arranged in raster, random, interleaved, and algorithmic firing orders. Based on results of the two-foci experiments described in section 3.3.2, it was hypothesized that per-pulse fractionation efficiency could be improved by implementing an EFS strategy which reduced the interaction between the high-gain region of the therapy beam and populations of nascent, diffusely distributed residual microbubbles. This hypothesis was supported for the cases in which the number of foci in the EFS grid was small (see figures 3.13 and 3.16) but not in the cases tested in this section in which the number of foci was large (see figure 3.21). Results indicated that the random sequence was most efficient, particularly early on, but that differences in efficiency diminished as the

treatment approached completion, except for the raster sequence which remained poorly efficient.

The discrepancy may be explained by the enhanced lesion-scale mixing associated with a full 3D grid and continuous pulsing. In this setting, islands of unfractionated material were observed to persist only until they began to translate throughout the lesion volume whereupon they were quickly destroyed. Mixing localized to an individual focus may be attributable in part to the stochastic nature of cavitation cloud formation which is drastically more complex in the presence of numerous mobile bubbles. As mentioned briefly in section 3.3.3, partially fractionated material in RBC phantoms was observed to translate in bulk several centimeters inward from the lesion boundary and opposite the direction of sound propagation before being completely destroyed. This phenomenon may be attributable to the same mechanism which generated oscillatory motion of the medium described by Miller et al. in references [196], [197], [259] and which the authors of those studies speculated might be caused by asymmetry in the formation and collapse of bubble clouds. When rafts of partially destroyed RBC material are unmoored from surrounding material, the oscillatory motion could result in a net translation.

The design of the algorithmic sequence was based on maximizing the number of firings in the EFS sequence before the therapy beam was directed at a region within a predefined exclusion zone (EZ) for a given focus. Further investigation, if warranted, might glean some theoretical insight from the observation that, as highlighted in section 3.3.3.2, while the minimum number of steps before and EZ violation was encountered was always ≥ 20, the mean value for this parameter was actually higher for the random sequence (34.8 ± 27.1) than for the

algorithmic sequence (26.4 ± 25.2), suggesting that perhaps it was this parameter that should have been the focus of the optimization algorithm.

It is unclear to what extent acoustic parameters including f-number, center frequency, PRF, burst repetition frequency, the number of total grid points, the spacing of grid points, and others influenced the per-pulse efficiency of each EFS sequence. However, future histotripsy systems under development in our lab will have lower f-number, higher frequency, and the ability to store a greater number of focal positions in memory. As described in section 3.3.3, an ideal sequence would likely be one where each point has a unique spatial location to distribute more evenly the apparent maximally destructive center of each focus. In such a case with a much greater number of foci and much finer grid spacing, the importance of avoiding "clusters" of nearest neighbor encounters as found in figure 3.16a and the theoretical basis of which is described in section 3.3.3.3. With the histotripsy systems currently under development in our lab, one solution might be to randomize the order of the EFS sequence for each burst rather than repeating the same initially randomized sequence as described in this study.

Beyond implications for the total number of pulses required to complete the treatment and the rate at which pulses can be fired without compromising fractionation efficiency, the size and spatial distributions of the total population of residual microbubbles are likely to play a critical role in tissue heating. The rate of heat absorption by the host medium has been shown to increase dramatically and abruptly with the onset of cavitation [260]. Farney et al. proposed that viscous damping of stably oscillating bubbles and inertial collapse (which shifts acoustic power into higher, more readily absorbed frequencies) are the mechanisms responsible for cavitation-enhanced heating [261], [262]. From a thermal perspective, the EFS-BC approach

presents two potential advantages by consolidating microscopic bubbles: fewer total bubbles, a smaller scattering cross section, and a shift in the mean resonance frequency of the bubble population away from the frequency of therapy pulses.

Chapter 4

Compensation Methods for Respiratory Motion During Histotripsy Treatment

Like radiation therapy and several imaging modalities, histotripsy is sensitive to the periodic respiratory motion of abdominal organs, which typically oscillate at approximately 0.2-0.3 Hz [98], [99], with 0.5-4 cm peak-to-trough amplitude [100]–[107], and at up to 1.5-3 cm/s [107]–[112] during normal respiration. Without compensation for respiratory motion there is an elevated risk of under-treating target-tissue, damaging adjacent healthy tissues [108], [113], and prolonging treatment times. This chapter reviews existing methods for respiratory motion compensation, explores the feasibility of integrating these methods with histotripsy therapy, and presents a novel cavitation-based motion tracking method in which residual cavitation nuclei were used as a fiducial marker and tracked throughout a predefined trajectory by a histotripsy therapy system capable of receiving acoustic backscatter signals.

4.1 Review of Contemporary Methods for the Mitigation of Respiratory Motion

4.1.1 Gating of Voluntary Respiration

The position of abdominal organs is nearly static for a period of time following expiration. This period, commonly referred to in the context of respiratory motion compensation as the gating window, lasts for 1-3 s under normal respiration [98], [102], [263]. Restricting the application of therapeutic energy to the gating window is a standard practice in radiation therapy [105], [107], [114]–[117] and has been demonstrated successfully in numerous focused ultrasound (FUS) therapy studies both pre-clinically and clinically [98], [113], [264]–[270].

Gating performed under voluntary respiration is minimally invasive and does not require the use of analgesia or anesthesia. Using this modality, patients' natural respiratory motion can be monitored by several techniques including spirometry [105], [122], [271], external optical sensors [102], [112], [267], [272], fluoroscopy [102], [273], high-speed MRI [104], [106], or a combination thereof which can then supply trigger signals to fire or halt firing of the therapy system based on some predetermined respiratory excursion threshold [267]. Characterization of the patient's respiratory pattern can also be performed prior to treatment and serve as a guide for establishing the gating threshold. Previous studies have shown strong correlation between direct measurements by MRI and fluoroscopy and externally derived signals (skin fiducial markers, etc.) which can then be used to generate a predictive model of organ motion. However, these studies also revealed irregularity, transient phase-shifts in respiratory patterns [271], transient organ deformation [123], [263], [274]–[277], contributions from cardiac motion

[110], [263], [278], and discrepancies between sensors placed at different positions on the abdomen [271] all of which degrade the ability of such external sensors to predict the motion of internal target tissues reliably [271]. Additionally, while respiratory patterns trend toward a steady state after several minutes [271], involuntary and spontaneous bodily functions including swallowing, coughing, and muscle spasms disrupt regular respiratory patters [98].

Training patients to breathe at regular intervals by providing audio or visual guides has been found to be effective for modulating the diaphragm's excursion-amplitude but was not found to enhance the overall predictive capacity of external sensors significantly [272]. Previous studies have also demonstrated the feasibility of applying therapy while the patient underwent voluntary apnea (prolonged breath-hold), however, interpatient variability and intraoperative pain limited the success of this approach [267], [279]. The augmentation of voluntary apnea by the administration of pure oxygen has been explored [280] but has not been widely adopted.

The ablative effect of thermal therapies including HIFU requires maintaining continuous temperature elevation within target tissues for a prescribed period of time [281]–[283]. Pausing thermal HIFU for periods of respiratory motion during gating results in cooling of target-tissue by thermal diffusion and perfusion-mediated convection [4], [19]. This effect can be mitigated by increasing the time-averaged intensity of the therapeutic pulses [265] but with the elevated risk of collateral damage to surrounding and intervening healthy tissues. Conversely, the therapeutic mechanism of histotripsy is purely mechanical (acoustic cavitation) and as a result, the therapeutic effect is cumulative. Beyond considerations for maintaining a clinically practical duration of treatment, histotripsy is insensitive to prolonged interruptions of therapy. Results from EFS-BC experiments described in section 3.3 of this dissertation showed that ablation

efficiency during continuously pulsed large-volume ablation had only modest PRF-dependence. Furthermore, it is likely that pausing for several seconds between high PRF bursts would afford small residual cavitation nuclei sufficient time to dissolve passively, ameliorating the impact of elevated PRF on treatment efficiency. Together these observations suggest that high-PRF bursts of histotripsy could be applied within the gating window provided by normal, voluntary respiration. This strategy would afford the same time-averaged duty cycle as the continuous treatment of a static or motion-tracked target and maintain the same treatment-time.

4.1.2 Forced Respiration Techniques Under Anesthesia and Analgesia

Under general anesthesia and/or analgesia (used as a neuromuscular block), spontaneous respiration can be entirely depressed and instead supported and controlled by ventilation. The respiratory cycle can then be dictated with robust consistency and also interrupted for periods of apnea as long as 30-150 s, followed by corresponding periods of recovery [269], [284]. Similar to the approach taken under voluntary, spontaneous respiration, therapeutic energy is delivered during periods (gating windows) when the target's respiratory motion is temporarily halted. While the greatest level of control is achieved under the use of anesthesia together with analgesia, the trend in the standard of care is shifting toward the use of procedural sedation and analgesia (PSA) alone due to higher complications associated with general anesthesia (GA) [98], [268], [270].

As an alternative to standard ventilation where gas is exchanged similarly to physiological function, there is growing interest in constant flow ventilation (CVF) [285] and high frequency jet ventilation (HFJV) [286] for ablation procedures including lithotripsy and RFA [286]–[289]. These techniques deliver a stream of air to the lungs through an inserted tube under general anesthesia with the result of nearly eliminating respiratory motion all together. HFVJ is the preferred method as it employs pulsatile (~2-7 Hz) flow which promotes greater turbulent mixing within the alveoli [289]. Denys et al. demonstrated the restriction of motion in the liver, kidneys, and lung to less than 0.3 mm in the posterior-anterior and medial-ventral directions and less than 3.75 mm (CT slice thickness used for measurement) in the craniocaudal direction [289]. Limitations of CVF and HFJV include the inability to treat patients with COPD and certain targets which are accessible only during deep inspiration [286], [289].

4.1.3 Abdominal Compression

The application of distributed pressure to the abdomen has been shown to reduce respiratory motion of abdominal organs by as much as 62% and is widely used in stereotactic body radiation (SBRT) [290]–[294]. The author of this dissertation was not able to find any literature describing the use of abdominal compression in FUS therapy for the explicitly stated purpose of mitigating respiratory motion. However, several in vivo studies performed in large animals have employed an acoustic coupling method which positioned a structure containing approximately 10-20 L of water above the ablation region with the subject supine and also

pressed the therapy transducer into the subject at the site of treatment [53], [58], [59], [205], [295]–[298]. This coupling method likely produced a similar restrictive effect on respiratory motion.

4.1.4 Motion Compensation by Electronic Focal Steering

As noted in Chapter 2 of this dissertation, a phased array FUS transducer is capable of rapidly adjusting the position of the high-gain focal zone through electronic focal steering. Together with a suitable imaging modality for guidance, an integrated therapy system can monitor the dynamic position of target-tissue and update the position of the therapy focus in real-time such that the therapy focus follows the target-tissue predictively and synchronously throughout the target-tissue's trajectory. The feasibility of this tissue-motion tracking approach has been demonstrated previously with imaging performed by MRI [299]–[301], b-mode ultrasound [62], [113], [122], [302], [303], or the therapy array itself [118]–[121].

Interestingly, "navigator echoes" based on temperature rise at the therapy focus can be used with MR-guidance to confirm registration between the target-tissue and the therapy system [304]. Similarly, the histotripsy cavitation bubble cloud can be detected in real-time by MRI by designing a specialized acquisition sequence sensitive to the chaotic mixing that follows cavitation collapse [305], [306]. Previous studies have also shown that histotripsy damage resulting from a single histotripsy pulse delivered to liver, clot, and RBC phantom is detectable by MRI [307], [308]. The use of cavitational histotripsy navigation pulses may not be deemed clinically practical due to the inherent associated tissue damage. However, a histotripsy system

could, perhaps, deliver sub-intrinsic-threshold pulses at a sufficient rate to produce MR-detectable but reversible hyperthermia at the focus for the purpose of navigation.

Limitations of MRI for motion tracking include a modest frame rate, the need for MR-compatible hardware, and higher procedural costs. Ultrasound b-mode imaging for motion tracking is limited by poor resolution for deep targets, 2D images of 3D motion for linear arrays, and low frame rates and high costs of matrix arrays. Between speckle tracking and feature tracking performed with the therapy array, feature tracking is the more robust of the two methods [122] but requires the proximity of a prominent feature (vessel, etc.) to the target. If this condition is not met, the deformable nature of organs like the liver [122]–[124] may introduce targeting errors when no proximal feature is available for tracking. Thus, there exists an unmet need for a motion-tracking method capable of achieving a moderately high sampling rate (approximately 20 Hz [263]) for deep tissue targets, ideally with an *in situ* fiducial marker.

4.2 Cavitation-Based Motion Tracking

4.2.1 Introduction

Of the techniques for respiratory motion compensation described in the previous section, using a therapy array with integrated receive capability to perform imaging is among the simplest and most elegant. Additionally, our lab is currently developing therapy systems with integrated receive capability for the purpose of cavitation-based aberration correction [240]

which would also be suitable for motion-tracking imaging [120]. To provide a robust feature for motion tracking in cases where none is near the target-tissue, we present preliminary findings toward the use of a novel cavitation-based tacking beacon we term a “fiducial bubble cloud” (FBC) which is somewhat analogous to the “laser guide star” technique commonly used in adaptive optics astronomy [240], [309].

To this end, we generated a small cavitation bubble cloud with a single pulse which exceeded the intrinsic threshold by a small margin, followed by a train of low-amplitude maintenance pulses delivered at 400 Hz PRF. Residual bubbles persisting after the collapse of the cloud generated by the first pulse were rapidly coalesced and re-excited as a highly localized, quasi-stable system of densely clustered bubbles similar to the EFS-BC effect described in Chapter 3 of this dissertation. This dense bubble system served as the FBC, generating signals which could be received by selected channels of the therapy system. These signals were then used to perform a multilateration localization operation to determine the position of the bubble cloud acoustically. These data were then compared to optical position data which were collected simultaneously. To evaluate the ability of this approach to receive acoustic data which could faithfully capture complex motion with abrupt changes in velocity, an FBC was generated and sustained in a tissue-mimicking gel phantom which was then translated by a motorized positioning system through a three-dimensional trajectory.

4.2.2 Methods

4.2.2.1 Experimental Setup

The transducer used for this study, as previously described [310], was a hemispherical phased array with 256 individually addressable elements. It had a center frequency of 500 kHz, a 30 cm aperture, and a 15 cm focal distance. It was controlled by a field programmable gate array (FPGA) digital circuit and generated acoustic pulses approximately 1.5-cycles in duration. Histotripsy pulses in this study generated cavitation by the intrinsic threshold mechanism (also termed *microtripsy*) [151]. Acoustic pressure measurements were performed using a hydrophone with robust directivity-response (HGL-0085, Onda, Sunnyvale, CA). The acoustic pressure used for experimentation commonly exceeded the operating rage of hydrophone and in some cases generated cavitation instantaneously, precluding the use of a fiberoptic probe hydrophone for direct measurement. For the calibration procedure, each of the array's modules was driven individually at the voltage used for experimentation. Individual waveforms were then summed in a linear fashion to estimate the therapy waveform.

In addition to the ability to transmit acoustic pulses, 160 of the array's 256 channels were equipped with specialized circuitry which permitted the simultaneous reception of acoustic signals. The receive-circuit consisted of a nonlinear voltage compressor in parallel with the high-voltage driving circuit and an analog-to-digital converter (ADC). The nonlinear voltage compressor attenuated transmitted driving signals which were on the order of several kV as well as received electrical signals which could be >100 V. Attenuation of large electrical signals was necessary to protect the ADC as its operating voltage range was 0-3.3 V. Originally designed

for a transcranial experiment where it was necessary to detect shockwaves generated by cavitation bubble cloud nucleation and strong reflections from the skull, the voltage compressor had a dynamic range of approximately 10 mV to 300 V. Input signals above 300 V were clipped. ADCs had an 8-bit digitizer and sampled signals at 20 MHz which were then transmitted to a PC running Linux for storage and processing. Scripts used for instrument-control were written in Python.

Experiments were performed in cylindrical tissue-mimicking agarose hydrogel phantoms measuring approximately 15 mm in diameter and 65 mm in length molded and supported by a modified 10 mL syringe (part number 26265, Excelint International Medical Products) as shown in figure 4.1. The end of the barrel of the syringe near the Luer fitting was cut off exposing the bore. The piston was trimmed flush at the point where the plunger attached and was drilled and tapped to accept an 8-32 fastener, allowing it to mate to a standard half-inch optical rod. Later experiments used a custom 3D printed piston with anchoring features which rigidly held the gel fast. Agarose gel was prepared by adding low melting point agarose powder (DSA20070, Dot Scientific, Burton, MI) at 1 g per 100 ml to deionized water and bringing the mixture to a boil. A previous study in our lab found the elastic modulus of gels prepared with this agarose concentration to be 21.7 ± 1.0 kPa which is on the order of physiological values of abdominal soft tissue (Vlaisavljevich et al 2015a). The molten gel was then vacuum filtered to 0.2 μm (12-566-218, Thermo Scientific, Waltham, MA) to remove dust and debris, poured into the inverted syringe-mold with the piston in the fully retracted position and allowed to cool to room temperature. Prior to use, phantoms were stored in a room temperature water bath held at approximately 100% dissolved gas concentration with respect to saturation as measured by a

dissolved oxygen probe (Orion Start A323, Thermo Scientific, Waltham, MA, USA). During use, the piston was depressed, exposing the desired portion of gel. This design provided an unobstructed acoustic signal path from the transducer to the focus.

Figure 4. 1. Photograph of agarose gel phantom in modified syringe used for molding and fixturing the gel during experimentation.

Experiments and calibration procedures were performed in a glass tank (ADB13530, Fish Tanks Direct, North Venice, FL) measuring approximately 60 cm x 60 cm x 30 cm containing roughly 100 L of deionized water degassed to approximately 20% gas concentration to reduce the potential for incidental cavitation in the water surrounding the gel or on the surface of the hydrophone. To reduce the impact of gas diffusing out of the gas-saturated gel phantom and into the degassed water, phantoms were used for experimentation immediately upon transfer from their storage tank to the experimentation tank. The transducer was oriented facing the surface of the water. Two high-speed cameras (Phantom v2012 and Phantom v210, Vision Research, Wayne, NJ were oriented orthogonally in the lateral plane and with their fields of view aligned to viewing ports located on the rim of the transducer's scaffold. A diagram of the experimental setup is displayed in figure 4.2. The cameras were equipped with 100 mm f/2.8 telephoto lenses (ATXAFM100PRON, Tokina, Tokyo, Japan) and were backlit by custom LED

light sources (BXRC-50C10K1-D-74, Bridgelux, Fremont, CA) operated in continuous mode. Each camera was set to capture one frame per acoustic pulse with an exposure of 10 µs. Frames were square, measuring 640 pixels per side and covering a region approximately 30 mm per side (47 microns/pixel). The timing of frame-capture was set to 113 µs following firing the earliest phased array element such that the midpoint of the exposure was approximately synchronized with the maximum expansion radii of small bubbles.

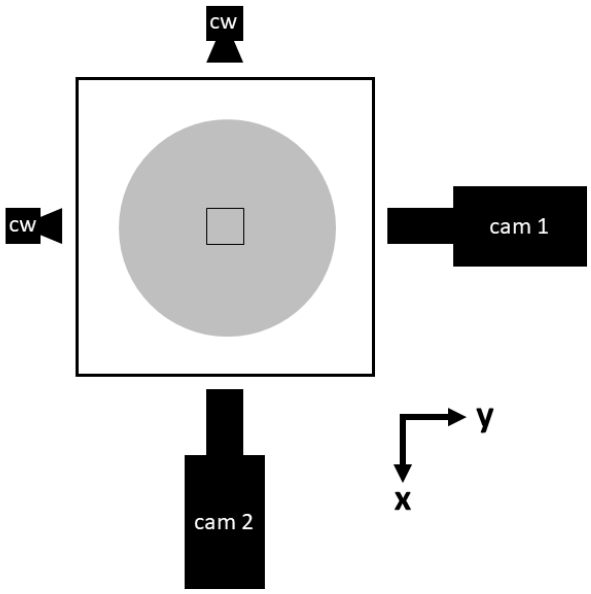

Figure 4. 2. Diagram of experimental setup. Vision Research Phantom v2010 is labeled cam 1. Vision Research Phantom v210 is labeled cam 2. Continuous wave light sources are labeled cw. Water tank appears as the larger square. Transducer facing in the positive z-direction (out of the page) appears as a grey circle. Projected view of EFS trajectory and motor path appear as smaller square. References to the coordinate system place the origin at the geometric focus. Not to scale.

4.2.2.2 Trajectory of Gel Phantom and EFS Sequence

The gel phantom was affixed rigidly to a 3-axis linear positioning system with the long axis of the phantom oriented in the vertical (z) direction. During experimentation the positioning

system was programmed to translate the gel at 12.5 mm/s through a periodic trajectory which traced the edges of a 20 mm cube as shown in figure 4.3 over a period of approximately 16 s. At the beginning of the experimental sequence, an FBC was initiated and sustained by maintenance pulses while the gel was stationary. After approximately 2 s, the gel was set in motion along the trajectory with the array directing pulses to the gel's current location by utilizing a synchronized EFS sequence.

The EFS sequence was established to mimic the path of the positioner by recording a sequence of images at 400 Hz which captured the position of a rigidly mounted brass sphere 3.18 mm in diameter (9617K32, McMaster-Carr, Elmhurst, IL). The brass sphere served as an indicator and took the place of gel phantom as it traversed the trajectory. These images were then post-processed in MATLAB (2017b, The Mathworks, Natick, MA) to identify and record the position of the indicator at each time-point. Data specifying the pixel coordinates of the center of the indicator were then fitted to the known positions of the corners of the trajectory, readily identifiable in the high-speed images. This procedure also allowed for the correction of parallax which would otherwise contribute errors of up to 0.6 mm as the trajectory included positions ± 10 mm outside the optical focal planes of the cameras. The resulting vector contained 6729 positions. Because the FPGA could store a maximum of 1024 positions, this vector was decimated by a factor of 7 such that it contained 962 points. During experimentation, 7 pulses were delivered to each point before moving to the next in the sequence. For periods when the positioner was at maximum velocity, EFS positions were spaced approximately 0.22 mm apart.

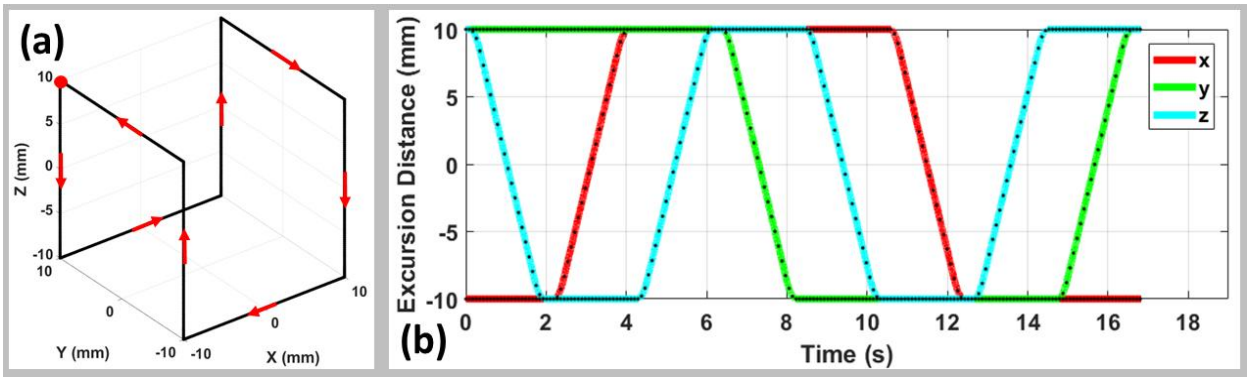

Figure 4. 3. (a) 3D diagram of the synchronized EFS and positioner trajectory. Red dot indicates starting point (-10, 10, 10). Red arrows indicate direction of progression. (b) 2D diagram of trajectory. Positioner trajectory appears as continuous, solid lines. EFS positions appear as black dots. Every 5th EFS position is displayed to make individual positions distinguishable. Acoustic propagation was in the z-direction.

4.2.2.3 Generation and Maintenance of the Fiducial Bubble Cloud

The *de novo* cavitation threshold was measured by positioning a gas-saturated gel phantom at the geometric focus and firing pulses at 1 Hz PRF. The power supply was initially set to 0 V and slowly increased until cavitation was observed with approximately 90% of pulses. Using this method, the threshold was found to found to be 22 MPa. This value is consistent with the results of Vlaisavljevich et al. who observed that in water with 90% oxygen concentration, the probability of generating cavitation with a single, 1.5-cycle, 21 MPa P-, 500 kHz pulse was 70% (please see fig. 5 of ref. [152]). To ensure that the initiation pulses generated a robust cavitation cloud and to provide a sufficiently large population of residual cavitation nuclei with which to form the FBC, initiation pulses were tuned to have approximately 24 MPa P-.

Next, the parameter-space of PRF and P- were coarsely swept to determine suitable values for maintaining the FBC indefinitely. The amplitude of maintenance pulses was modulated by

adjusting the charge time of the capacitors within the FPGA digital circuit driving system. The maximum allowable charge time of 5 µs was used for initiation pulses. The effective minimum charge time was found to be approximately 75 ns. Below this value, transistors would not reliably switch. Between 500 ns and 5 µs, pressure response was found to be linear with charge time. It was observed that an FBC could be maintained at (paired) P- and PRF values as low as approximately 800 kPa and 200 Hz, respectively and that the minimum PRF necessary to maintain the FBC was observed to decrease with increasing P-. For example, at approximately 9 MPa P-, 25 Hz PRF was sufficient to sustain the FBC indefinitely.

For experimentation, FBC maintenance pulses were tuned to have 3.7 to 5.0 MPa P- across the EFS range employed by the motion trajectory. These values were selected to provide an FBC which was reliably detectable by the therapy array's receive system. The minimum detection threshold of the receive system was approximately 40 mV. Signals on the order of 5 mV could be detected using an oscilloscope connected directly to a passively listening array element but this approach was not amenable to multilateration due to the limitations on the number of receivers that could be used. A characteristic image sequence displaying the initiation of a de novo cloud, followed by the aggregation of its residual nuclei and maintenance of this dense bubble system as an FBC is displayed in figure 4.4.

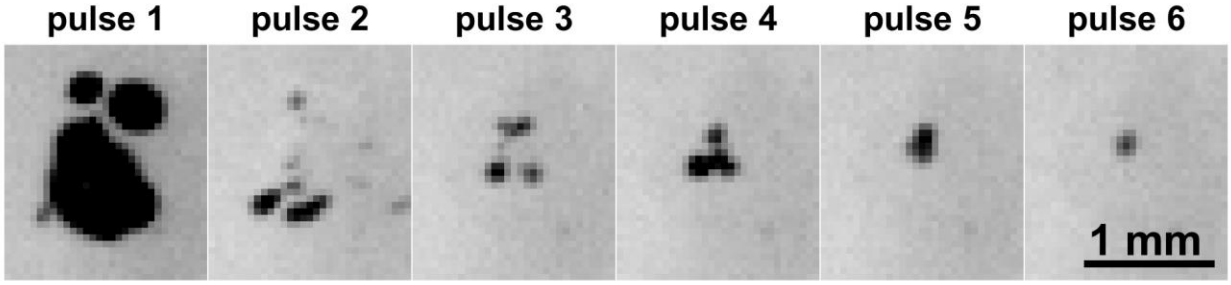

Figure 4. 4. Characteristic image sequence displaying the initiation of a de novo cloud (pulse 1), followed by the aggregation of its residual nuclei (pulses 2-5) and repeated excitation of this dense bubble system as an FBC (pulse 6 and beyond). Time of frame capture is approximately 113 microseconds following firing the pulse. Direction of ultrasound propagation is from bottom to top of images.

Prior to experimental data collection, the region where the FBC was generated was homogenized by the application of 50 pulses with 24 MPa P- delivered at 1 Hz PRF. In a clinical setting, it is likely that this initial homogenization step could be greatly accelerated by interleaving a burst of bubble coalescence pulses between homogenization pulses. In this manner, the practicality of establishing the FBC within a single respiratory gating window is preserved.

4.2.2.4 Optical Data Analysis

Optical data were analyzed by a script written in MATLAB which read images from native *.cine* files and converted them to double format. The background was subtracted using a reference image in which the gel phantom was absent. Images were converted to binary using the adaptive thresholding function, *bradley* [174], blurred by a Gaussian filtering operation, and then converted to binary again by the *imbinarize* function. The initial position of the bubble cloud was identified manually and a search window measuring 30 pixels by 30 pixels was centered about the cloud, masking the remainder of the image. The position of the bubble cloud was added to a dynamic list which stored the most recent 20 positions as the script processed the images sequentially. After the 20^{th} image, the position data on the dynamic list

were averaged and this position was then used to update the position of the search window. In this manner, the search window tracked the bubble cloud throughout its trajectory, roughly centered about the cloud. For each frame, the position of the bubble cloud were recorded and then stored together in a *.mat* file.

4.2.2.5 Acoustic Data Analysis

Acoustic data were analyzed by a script written in MATLAB which functioned by importing data from native *.npy* files and converting image matrices to *uint8* format. Individual acoustic traces were then analyzed separately by first converting to double format and removing any DC offset which may have been present. Background subtraction was then performed using a dataset which had been collected with the initiation pulse amplitude set to zero such that an FBC was not generated. Data were then Gaussian low-pass filtered with the cutoff frequency set to approximately 1.25 MHz. The envelope of the waveform was then calculated using the envelope function with *n* set to 20 and the envelope type set to 'peak'. The waveform was then windowed such that values falling outside the range 200-250 microseconds were set equal to zero.

The arrival-time of the FBC signal was calculated by two methods which were then averaged. The first method performed edge-detection by recording the time-points for the first (t_0) and last (t_1) timepoint for which the envelope which exceeded half the peak amplitude. The arrival-time was then defined to be $t_{edge} = t_0 - 0.7(t_1 - t_0)$. This metric was derived empirically but is

similar to that of Zhang et al. [311]. The second method performed peak-detection using the *findpeaks* function with the 'MinPeakProminence' parameter set to the peak amplitude of the windowed envelope vector. For this method, the arrival-time was defined as the timepoint corresponding to the peak minus its full-width-at-half-maximum (FWHM). Time-of-flight was calculated by subtracting the EFS delay applied to the channel under consideration.

The position of the FBC was calculated by a multilateration operation for each pulse. With knowledge of the position of each transducer element and the time of flight from each element to the FBC, the position of the FBC was determined by solving a system of equations of the form

$$(x - x_n)^2 + (y - y_n)^2 + (z - z_n)^2 = s_n^2 \qquad (4.1)$$

where (x, y, z) were the coordinates of the FBC and (x_n, y_n, z_n) were the coordinates of the n^{th} receiver element, s_n was the distance from the n^{th} receiver to the FBC, and the total number of receiver elements was 160 [121], [312], [313]. The system of equations was solved for (x, y, z) by using the nonlinear least-squares solver *lsqnonlin* with the 'Algorithm' option set to 'levenberg-marquardt'.

4.2.2.6 Unfocused Pulses for Maintenance and Interrogation of a Stably Cavitating Single Fiducial Bubble

The primary method for cavitation-based motion tracking investigated in this study was sustaining an inertially cavitating FBC with focused pulses. However, as an aside, the feasibility

of sustaining and interrogating a stably cavitating single fiducial bubble (SFB) with unfocused, lower-amplitude pulses was also briefly investigated. If viable, this approach might benefit from reduced acoustic energy deposition and the absence of the need to update the EFS position of sustaining pulses. The pressure distribution of a single array element is displayed in figure 4.5 and shows a much broader focal zone than that that of the transducer array as a whole.

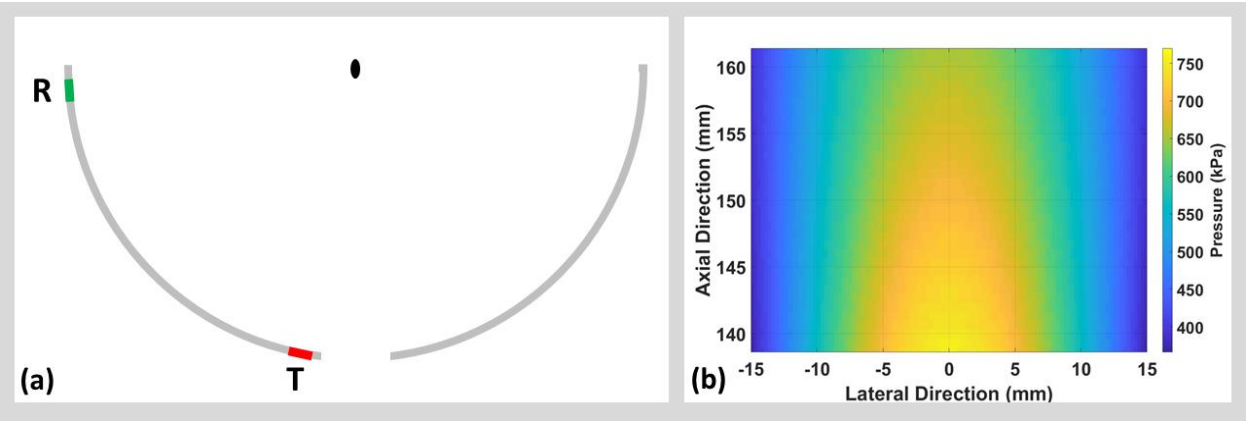

Figure 4. 5. (a) Diagram displaying the array (outlined in grey), the module which transmitted acoustic pulses (red, marked T), the module which received backscattered signals from the bubble (green, marked R), and the focus (appearing as a black ellipse). (b) FOCUS simulation displaying the maximum pressure distribution generated by a single 500 kHz array element oriented along the acoustic axis. The direction of sound propagation was from bottom to top and the coordinates are set such that the center transducer's face is at the origin. The focal distance of the therapy array was 150 mm.

The pulse sequence for this experiment was the same as above with the exception that after generating cavitation with the first pulse (24 MPa P-), rather than firing EFS pulses, only one element, located near the center of the aperture, transmitted pulses with approximately 700 kPa P- at the array's geometric focus. During setup experiments, the SFB signal was found to be too small for the therapy system to receive reliably. Instead, a second element, located on the perimeter of the aperture, was disconnected from the driving system and connected directly to an oscilloscope (LC574AL, LeCroy Corporation, Chestnut Ridge, NY) set to average 25 pulses. As

in the previous experiment, a background dataset was collected in which the amplitude of the first pulse was set to zero.

The position of the SFB was monitored optically by high speed camera. However, because the SFB was extremely faint (barely discernable by eye while viewing footage from the experiment), attempts at post-processing these images were not successful.

Acoustic signals from the SFB held at stationary at (10, 10, 10) were analyzed in MATLAB by first importing data from the oscilloscope to the PC. The background trace was then subtracted from the received signal with the SFB present.

4.2.3 Results

4.2.3.1 Fiducial Bubble Cloud

The feasibility of receiving acoustic signals from a small, densely distributed system of continuously re-excited population of residual cavitation nuclei along a 16-cm trajectory was investigated. The position of this fiducial bubble cloud was monitored optically and acoustically. Representative position data for a single cycle through the motion trajectory are displayed in figure 4.6. The mean error in measured acoustic position was calculated by comparing each acoustic position datum to the corresponding optical datum collected at the same time. Error calculated in this manner was averaged across the entire trajectory and for all samples and is summarized in table 4.1.

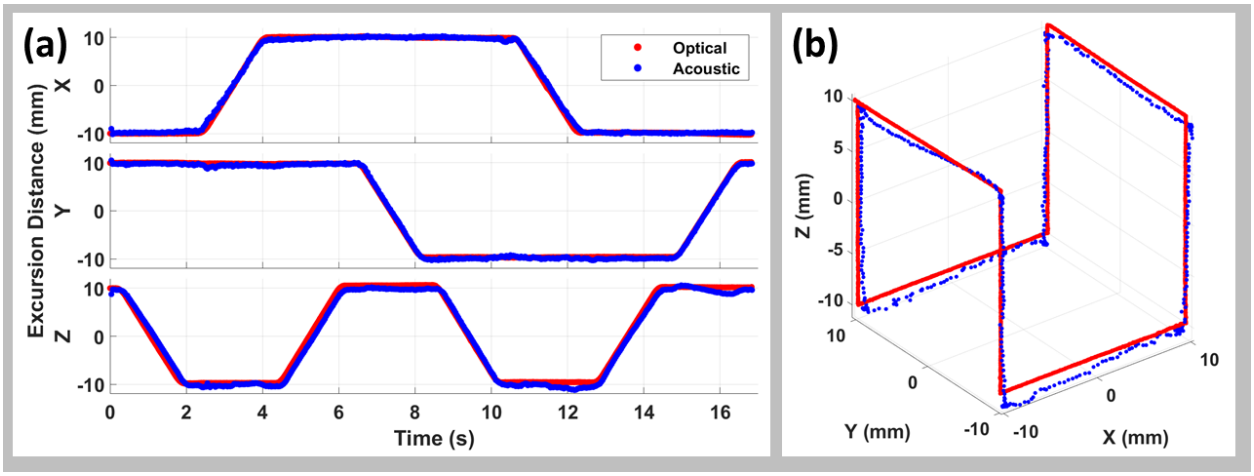

Figure 4. 6. Characteristic optical (red dots) and acoustic (blue dots) data collected as the FBC and gel traversed the trajectory. (a) 2D plots displaying position data in the x, y, and z-directions as a function of time. (b) 3D plot of displaying position data. Initial position was (-10, 10, 10). Motion first progressed in the negative z-direction.

Table 4. 1. Error in measured acoustic position relative to measured optical position. N = 10 samples, each of which contained 481 data points.

Direction	Error (mm)		
	Mean ± SD	**Minimum**	**Maximum**
x	-0.14 ± 0.37	-2.17	1.08
y	0.11 ± 0.34	-0.98	1.08
z	0.55 ± 0.47	-0.75	2.55
r	0.70 ± 0.33	0.01	2.53

4.2.3.2 Stably Cavitating Single Fiducial Bubble

The feasibility of driving a single bubble roughly 30 microns in diameter to cavitate stably with unfocused pulses from a single therapy array element and using a second array element to receive backscatter signals was investigated. It was found that 400 kHz PRF pulses from a single,

unfocused array element generating approximately 700 kPa at 15 cm were sufficient to coalesce residual cavitation nuclei into a stationary single bubble and drive this bubble to cavitate stably for approximately 45 s before it was no longer detectable optically or acoustically. The author acknowledges that optical and acoustic monitoring used in this sub-study were not well suited for the detection of very small signals. Optical monitoring was set up to capture a wide field of view and large focal depth. A better approach would have been to use a camera with smaller pixels, a shorter depth of field, and a smaller field of view. Acoustic monitoring for this experiment, and also for the FBC experiment, would have benefitted from greater sensitivity and at the ADCs and receiver-elements with greater bandwidth.

A representative example of the acoustic waveforms is displayed in figure 4.7 where it can been seen that the SNR is approximately 0.2. Because the background is composed primarily of direct and reflected signals from the driving element with minimal random contributions, averaging and background subtraction yield a clearly discernable signal from the SFB. For a control run which lacked the initiation pulse which generated the population of residual nuclei, the SFB signal was not observed. Additionally, the SFB signal was strongest immediately after the formation of the SFB and faded in amplitude over the course of approximately 45 s until it was no longer detectable which coincided with its disapperance from optical detection. These results are consistent with the coarse P- and PRF parameter-space sweep which found that focused pulses at 800 kPa P- and 200 Hz were sufficient to sustain an FBC.

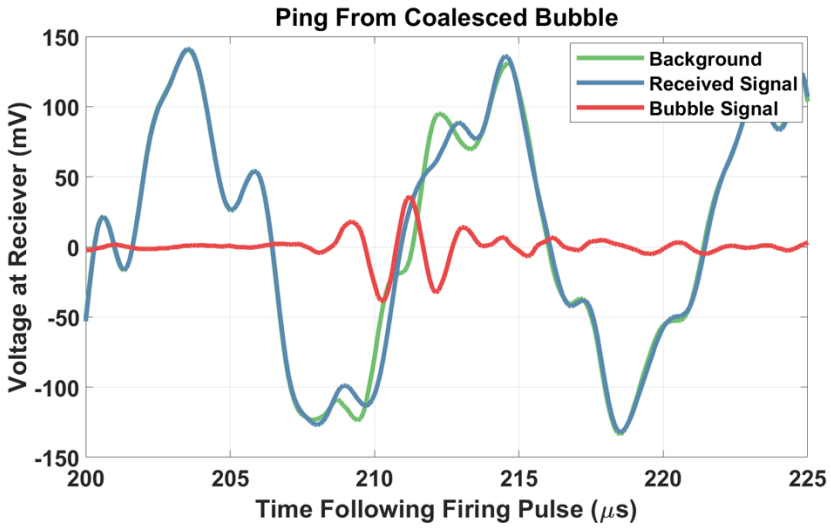

Figure 4. 7. Characteristic acoustic waveforms collected during single fiducial bubble experiment. Background signal (green) was collected during a control run where cavitation was not generated (as it normally would be with the first pulse) but sustaining pulses were applied as usual. The signal received when a SFB was present (blue) is distinct from the control waveform within the anticipated window of arrival. Subtracting the background signal from the received SFB signal allows the component of the signal produced by the SFB to be viewed in isolation (red).

Several attempts were made to translate the gel phantom throughout the trajectory used for the FBC experiment following the initiation of the SFB. It was found that the SFB would persist for approximately 6 cm of the trajectory (~6 s) before becoming undetectable optically. It is believed that this discrepancy in the persistence-time is attributable to the variation in pressure due to the module's directivity experienced by the SFB. When the motor system was used to move the gel manually between (10, 10, 10) and (10, 10, -10), the SFB persisted for approximately 45 s as in the stationary case.

4.2.4 Discussion

This study demonstrates the basic feasibility a novel acoustic technique for the noninvasive generation of an endogenous acoustic fiducial marker and the reception of robust acoustic signals from this marker which can be used for location tracking. A *de novo* cavitation bubble cloud was generated measuring approximately 0.9 mm in lateral diameter and 1.3 mm in axial diameter using a single 24 MPa P- histotripsy pulse. The residual cavitation nuclei persisting following the collapse of this cloud were coalesced and driven to cavitate by the application of subsequent, lower-amplitude pulses. The cloud functioned as a fiducial marker by emitting strong acoustic signals from a region on the order of 100 microns, effectively acting as a point-source.

This study investigated two approaches to sustaining and interrogating the acoustic fiducial marker. The first approach applied low-amplitude focused pulses generated by the full array which tracked with the position of the fiducial bubble cloud within a gel phantom as it traversed a predefined trajectory. The author termed this tightly localized, self-attracting, stable bubble system a *fiducial bubble cloud* (FBC). Characterization of the dynamics of the FBC was not attempted in this study but is likely that bubble aggregation, both of the initial residual nuclei population which immediately follow collapse or later following fission and ejection of daughter bubbles from the FBC, was driven by the secondary Bjerknes force [89]–[93], [95], [177], [207]. Fission of coalesced bubbles is attributable to surface instabilities encountered at high driving pressure [207], [226]–[228], [243], [244]. For a more detailed discussion of these phenomena, please see section 3.4.2 of this dissertation.

Interestingly, while cavitation clouds generated *de novo* by 24 MPa P- pulses produced the expected homogenization effect which is the hallmark of histotripsy therapy, the violent re-excitation of coalesced residual cavitation nuclei by approximately 5 MPa P- pulses did not appear to produce an appreciable degree of homogenization. This is evidenced by the ability of the lesion-boundary to restrict the motion of the FBC. The FBC was observed to form in the approximate geometric center of the lesion, having drawn together residual nuclei diffusely distributed throughout the volume of the lesion. Once coalescence was complete, the FBC was observed to translate up to 560 microns in the z-direction over the course of the next 100 pulses, likely under the influence of the primary Bjerknes force [91], [177], [208]–[211], and halt abruptly at this position which corresponded to the approximate position of the lesion-boundary. When the gel had traversed the full trajectory and returned to its initial position, the FBC was found to have translated only an additional 80 microns in the z-direction over the course of some roughly 7300 pulses. The apparent absence of bubble tunneling [86], [162], [198], [199] can be attributed to the modest driving amplitude which likely did not generate *de novo* cavitation. As discussed in Section 3.4.2, the inertial re-excitation of microbubbles, in the absence of any *de novo* cavitation may have only minimal ablative capacity. In preliminary setup experiments, it was noted that an FBC generated in water (rather than gel) was less stable, providing further support for the hypothesis that the lesion boundary serves to confine the motion of the FBC.

Several factors limit the clinical practicality of using this approach in conjunction with histotripsy therapy. First, the total amount of acoustic energy deposited to intervening and surrounding tissues would be elevated, perhaps to a significant extent, by the use of pulses with

800 kPa to 5 MPa P- delivered at PRF on the order of 200 Hz. Second, concurrent cavitation-based motion tracking and histotripsy therapy could be problematic. Contributions from the direct and reflected waves of histotripsy therapy pulses could degrade the SNR of FBC signals. While the sensitivity of the receive-hardware within the therapy system could be improved, the irregularity of background signals generated during histotripsy therapy, could make identifying the FBC signal impractical. Third, aberration induced by refraction and speed of sound variation associated with soft tissue could make the delicate focusing required to sustain the FBC challenging and confound acoustic signal transmission from the FBC to the receivers. Fourth, it is unclear how the prospect of creating a lesion within healthy parenchyma for the purpose of motion tracking will be received by clinicians. Though it is worth noting that the volume of this lesion could be as small as ~1 microliter.

To address some of these concerns, a second approach to sustaining and interrogating the acoustic fiducial marker was investigated. Rather using focused pulses generated by the entire array, a single array element was fired at full power, generating a sound field with a much broader pressure distribution near the array's geometric focus. The resulting acoustic fiducial marker, termed a single bubble fiducial (SFB), was driven to cavitate stably for approximately 45 s and emitted signals which were detectable by an element of the therapy array. This approach deposited less acoustic energy and would be impervious to the effects of soft tissue aberration for driving the bubble. However, signals emitted by the SBF would be susceptible to soft tissue aberration along their path to the receivers. Additionally, the use of an unfocused module for interrogation of the SFB would provide less favorable conditions for the SNR of the bubble with respect to tissue scattering. With more sensitive equipment, the reception of SFB signals could

be made to benefit from a degree of focusing, however if excitation is provided by a beam with broad beam, tissue scatter throughout the illuminated zone would contribute unfavorably to noise.

A possible strategy for improving the SFB approach would be to implement harmonic and subharmonic imaging techniques [314], [315]. Harmonic [316] and subharmonic [317], [318] emissions are hallmarks of bubbles undergoing high-amplitude forced oscillations [177]. Scattering of acoustic pulses takes place almost entirely at the fundamental frequency, with small contributions at higher harmonics and even less at subharmonic frequencies [316][319]–[321]. Beyond providing the most favorable SNR, subharmonics might also be an attractive option when considering the size of the bubble, the bandwidth requirements of the receiving elements, and the driving pressure needed to induce a strong subharmonic response [315], [321]. Additional, and possibly complimentary, strategies might include pulse inversion [321] and amplitude or power modulation [322].

A more detailed understanding of the relevant bubble dynamics governing each acoustic bubble fiducial marker has the potential to enhance this technique and bolster its clinical potential. Subsequent studies might investigate the tuning of parameters like the beam profile, acoustic pressure, driving frequency, and duty cycle in an effort to promote rectified diffusion. Such an approach could provide longer-lived bubbles with more energy-efficient pulsing schemes.

Chapter 5

Design and Fabrication Techniques for a Phased Array with Arbitrarily Shaped, Densely Packed, and Replaceable Elements

Large phased array ultrasound therapy transducers are generally constructed as either sparsely packed arrays (~60% aperture utilization) [323] in which each element shares a common geometry and is often easily replaceable, or as densely packed arrays (~85% aperture utilization) with elements which typically do not share a common geometry and are not practically replaceable. Here we present a novel design, amenable to readily accessible fabrication techniques, for a therapeutic ultrasound array with high packing-density (92% aperture utilization) and easily replaceable modular elements.

*Note: a portion of this chapter was submitted for publication as listed below.

1. **J.E. Lundt**, T.L. Hall, A.P. Duryea, T.I. Gerhardson, Z. Xu. Therapeutic Ultrasound Phased Array with Arbitrarily Shaped, Densely Packing, Removable Modular Elements. International Symposium on Therapeutic Ultrasound, Barcelona, Spain, June 13-15, 2019. Accepted.

5.1 Introduction and Motivation

5.1.1 Maximization of Aperture Utilization

The need to maximize aperture utilization is motivated by three principle considerations: acoustic aberration and attenuation encountered during *in vivo* treatment, the need for a broad electronic focal steering range to treat large volumes, and constraints on aperture-size imposed by acoustic access [324]. The author defines aperture utilization as the ratio of active surface area of piezoelectric material to the total surface area of the aperture. Regions occupied by the perimeter of modular elements consisting of housing material or empty space between modules are categorized as inactive area.

Acoustic aberration results from reflection, refraction, and variations in the speed of sound encountered as the acoustic signal propagates from the transducer through the coupling medium and various tissue-structures on its way to the target. Each of these effects has the potential to perturb the coherence and position of the intended focus. Aberration and corrective measures thereof have been studied extensively for transcranial ultrasound therapy applications [148], [242], [310], [325], [326] and for applications in soft tissue to a lesser extent [187], [240], [327]–[332]. Acoustic attenuation alone due to absorption and scattering in soft tissue can be as high as roughly 6 dB for the frequencies and target-depths applicable for abdominal histotripsy [73], [315], [333], [334]. The presence of residual cavitation nuclei [83], [95], [131], [136]–[138] which may arise near the target [83], [95] or pre-focally (on the skin for

example) [296] can also contribute strongly to attenuation and scattering of the incident therapy pulse [68], [79]–[82], [135], [335], [336]. Anecdotal experience in our lab suggests that for a given driving voltage, there is an approximately 50% pressure loss associated with going from the free field to an *in vivo* tissue target at moderate depth (around 5 cm at 1 MHz for example) due the cumulative effects of aberration, attenuation, and nonlinear propagation. While some of the aforementioned sources of pressure loss can be mitigated by adjusting phase delays and other strategies, others, like soft-tissue attenuation, can only be overcome by increasing the transducer's power output (for a given therapy system).

For set values of the array's dimensions, element-count, element-size, frequency, etc., the EFS range is dictated by pressure output. As mentioned in Chapter 1 of this dissertation, a therapy array with the ability to generate cavitation up to roughly 2 cm from the geometric focus in every direction by EFS will likely be a cornerstone for the clinical translation of histotripsy for large targets.

The form-factor of a focused ultrasound (FUS) phased array is typically derived from considerations of patient anatomy and clinical practicality. The transducer must conform to the available acoustic window such that bone and gaseous structures including the lung and bowel do not obstruct the acoustic propagation path [51], [324], [337] and the transducer must not be so large that positioning, acoustic coupling, and imaging become burdensome.

5.1.2 Easily Replaceable Elements

When a FUS phased array is new, the performance characteristics of individual elements fall within a narrow range. In the case of an array with replaceable elements, each element can be tested prior to inclusion in the array and substituted if found to be deficient. Ideally, each element would produce an acoustic waveform similar in shape and amplitude. Over time, however, the population of elements undergoes differential degradation process in which many elements display little or no decrease in performance while others display diminished amplitude, distortion, or no output at all. A similar trend has been reported for ultrasound imaging systems with failures attributed primarily to delamination, failed electrical connections, and mechanical damage [338]–[341]. For FUS systems, the problem of degradation may be more severe due to the extreme driving conditions applied to piezoelectric materials [342], [343] and the high cost and long lead-time of highly specialized FUS transducers relative to mass produced ultrasound imaging probes. Like imaging probes, current FUS phased array designs with high aperture utilization do not permit the replacement of failed elements. Thus, there is an unmet need for a densely packed FUS phased array design which can accommodate the easy replacement of failed elements.

5.2 Design

As discussed in in Chapter 1 of this dissertation, large HCC was selected as the first-indication test-case for this work. As such, the transducer described in this section was designed to be physically suitable for the treatment of liver tumors >3 cm in diameter in human subjects. Testing of this initial iteration of the device will be performed in an *in vivo* porcine model predicated on the assumption that porcine abdominal and liver anatomy is a suitable proxy for human anatomy [73], [298], [344]–[346].

5.2.1 Selection of the Center Frequency

Considerations for selecting the center frequency of the array included frequency-dependent parameters such as focal-zone dimensions, electronic focal steering range, soft-tissue attenuation, the incidental and intrinsic cavitation thresholds, focal gain, pressure output, and nonlinear acoustic propagation. Using a low center frequency has several advantages. The FWHM of the achievable EFS pressure-profile scales roughly linearly with the reciprocal of frequency [260], [347]–[349]. Acoustic signals at lower frequencies experience less attenuation [315], [333], [334] which can be seen in the power law of the attenuation coefficient,

$$\alpha = \alpha_0 f^n \tag{5.1}$$

where α is expressed in units of dB/cm, n ranges from 1 to 2 for soft tissues, and f is the center frequency expressed in units of MHz [315]. Additionally, the intrinsic cavitation threshold decreases slightly with frequency [152] and waveforms experience less nonlinear distortion for a given propagation distance [350], [351].

Using a low center frequency also has several potential disadvantages. Notably, regions outside the focus are more susceptible to incidental cavitation [67], [78], [152], [173], [352], [353]. Previous experience in our lab demonstrated that at 250 kHz, for example, the incidental threshold was too low to be clinically practical for many indications. *In vitro* experiments at this frequency, using high speed imaging, revealed that even in filtered deionized water which was degassed to approximately 10% oxygen concentration, widespread incidental cavitation resulting from weak nuclei [163], [354] was pervasive even several centimeters from the focus. Lundt *et al.* observed incidental cavitation and bubble tunneling in *ex vivo* bovine hepatic tissue at 250 kHz (see fig. 9 of ref. [86]). Similarly, an *in vivo* porcine experiment at 250 kHz, targeting the liver resulted in trauma to the lungs which was attributed to post-focal incidental cavitation. These results are consistent with literature on extracorporeal shockwave lithotripsy (ESWL) which also employ waveforms with high-amplitude, low-frequency rarefactional excursions [355]–[359]. Our lab has not performed a thorough examination of incidental cavitation as a function of frequency; however, numerous previous *in vitro* and *in vivo* studies suggest that this problem does not manifest when the center frequency is ≥ 500 kHz.

In the absence of attenuation, pressure output scales linearly with frequency [348], [349] and focal gain is also greater at higher frequencies due to a more confined focal zone [360], making higher frequencies desirable for small transducers and indications in superficial tissues.

For deep histotripsy targets like the liver, however, the selection of an optimal center frequency [348], [361], [362] can be distilled largely to the opposing considerations of focal pressure and attenuation. Previous studies have found the optimal frequency to be around 500-800 kHz for transcranial applications [361], [362]. To guide the selection of a center frequency for this array, a series of tests were performed in our lab using test-elements at 0.5, 0.7, 0.9, 1, and 2 MHz together with known aberrators. Consistent with the transcranial literature and with similar frequency optimization experiments performed at HistoSonics for soft tissue applications, 750 kHz was found to be optimal and was selected as the center frequency.

5.2.2 Material Selection

Piezoeramic and 1-3 piezocomposite materials are commonly used in FUS applications. The primary distinction between the two is that piezoceramic is a monolithic material whereas 1-3 piezocomposites are composed of very small rods of piezoceramic material oriented along the axis of sound propagation and embedded in a passive polymer matrix [363], [364]. 1-3 piezocomposites are commonly fabricated by the “dice-and-fill” method in which a sheet of piezoceramic material is cut partially through at regular intervals in orthogonal directions, leaving behind a matrix of square columns. The void between columns is then filled with epoxy and material is removed from each face in a subsequent grinding operation. This and other methods for fabricating piezocomposites are discussed in refs. [365] and [366].

1-3 piezocomposites present several advantages for FUS applications. Their acoustic impedance is approximately 8-12 MRayl which is closer to that of soft tissue (~1.5 MRayl) than piezoceramics (20-30 MRayl), resulting greater transmittance from the piezoelectric material into aqueous media [314], [364], [367], [368]. Substanial anisotropy reduces the development of oscillatory modes other than the thickness mode (direction of sound propagation) [364], [369]. The presence of polymeric material between ceramic pillars can also afford piezocomposites a degree of mechanical flexibility not possible with ceramic material, thereby more readily accommodating a broader spectrum of geometric designs [369], [370]. Finally, peizocomposites exhibit a wider bandwidth [369], [370] which may be of particular interest for receive-capable phased arrays since signals from cavitation events typically have frequency content much higher than the center frequency of outgoing therapy pulses. The disadvantages of piezocomosites include substantially higher cost, lower power efficiency [370], and thin, sputtered or plated electrodes which necessitate the use of specialized soldering techniques.

Recently, a variation of piezoceramic with high porosity has become commercially available. High porosity affords a roughly two-fold decrease acoustic impedance [371]–[373] and some capacity to suppress undesirable oscillatory modes while retaining the desirable characteristics of nonporous piezoceramics.

To compare the performance of piezocomosite and porous piezoceramic materials, our lab performed a series of basic experiments in which individual modules were constructed and compared using 1-3 piezocomposite (DL-53, Del Piezo, West Palm Beach, FL) and porous piezoceramic with 14 MRay acoustic impedance (Pz36, Ferroperm Piezoceramics A/S, Kvistgaard, Denmark). Both piezoelectric materials had a center frequency of 750 kHz and

measured approximately 17 mm x 17 mm x 2 mm. The piezoelectric materials were assembled in 3D printed housings with two bonded matching layers (λ/4 thickness each) and had an open air-backing. The first matching layer was made of a composite stereolithography material (PerFORM, Protolabs, Maple Plain, MN) and had an acoustic impedance of 5.1 MRayl. The second matching layer was made of selective laser sintered nylon (PA 12, Protolabs, Maple Plain, MN) and had an acoustic impedance of 2.2 MRayl. These test modules were driven at PRF ranging from 100 Hz to 5 kHz. At 1 kHz, it was found that the maximum achievable P- surface pressure before failure were 2.17 MPa and 6.79 MPa for the composite and Pz36, respectively. Pressure waveforms from each element were then measured at 15 cm from the surface of the transducer. At the maximum driving voltage, the module constructed with piezocomposite generated 2.9 kPa/mm^2 at 15 cm, whereas the Pz36 module generated 5.4 kPa/mm^2 at 15 cm.

A final test was performed in a similar manner using a design similar to the final one described in Section 5.2.5 using Pz36. The module used for this test generated 6.4 kPa/mm^2 at 14 cm. The later datum was subsequently used to calibrate linear acoustic simulations. In light of these results and considering its lower cost ($1.57/cm^2 for Pz36 and $5.17/cm^2 for DL-47 at the time of this writing, both in moderate quantities), PZ36 was selected as the material for the transducer described in this study. The author would like to thank Tyler Gerhardson for fabricating test fixtures and performing much of the testing of these materials.

5.2.3 Basic Array Geometry

The hemispherical phased arrays used in this dissertation were selected as a convenient starting point for the investigation of EFS for large volume ablation with the knowledge that hemispherical geometry would not be practical for many indications. The entangled nature of experimentation and array design was a limitation. To establish the f-number, focal distance, and aperture-profile for a liver-specific array, our lab, in collaboration with HistoSonics, Inc. (Ann Arbor, MI) procured and analyzed a set of de-identified human CT scans (N = 21) using a script written in MATLAB. Mimics software (Materialise NV, Leuven, Belgium) was used to segment tissue structures and generate masks for each 2D CT image corresponding to liver, skin, bone, lung, bowel, and stomach. Mimics was then used to construct a 3D model of the liver and divide it into 8 functional units (or segments) based on anatomical features established by Couinaud classification [374], [375]. Within each functional unit, one target point was established at the approximate center of mass and one at a point distal to the main, anterior acoustic window. Data were then analyzed in MATLAB by projecting rays from the target point to approximately evenly distributed discrete points on a sphere with a center at the target point and a radius equal to the transducer's proposed focal length. Each ray was assigned a binary value (blocked or unblocked). Blocked status was assigned to those that fell outside the scan region (by intersecting structures within the superior-most or inferior-most 2D CT images), intersected occlusive tissue structures (lung, stomach, bowel, and bone), or fell on an intracorporeal portion of the sphere.

With the available acoustic windows for each patient identified, a “common aperture” was established by 1) aligning all target points and rotating the acoustic windows with respect to each other to achieve maximum overlap, 2) summing the acoustic windows to generate a “heat map” showing the variation in overlap on the summed aperture surface, and 3) setting a threshold to exclude regions where less than 80% of the aperture was common across all cases analyzed. The model predicted that with the exception of liver segment 7 (as defined by the Couinaud classification [374], [375]) would be readily accessible to this aperture with the achievable P- diminishing with increasing BMI. The author would like to thank Alexander Duryea for performing the analysis of the human CT data.

Based on the results of this analysis and comparison of the proposed aperture-geometry to a set of porcine CT scans (N = 4), a spherical section defined by a truncated circular aperture-profile measuring 234 mm in diameter along the widest dimension and 165 mm along the orthogonal dimension was selected. A focal length of 140 mm was selected, providing a working distance of 77 mm as measured from the outermost flank of the transducer to the focus along the primary axis. A hole measuring 55 mm was also established in the center of the aperture to accommodate a standard commercial curvilinear ultrasound imaging probe. A CAD rendering of the aperture-surface generated in SolidWorks (Dassault Systèmes, Vélizy-Villacoublay, France) appears in figure 5.1.

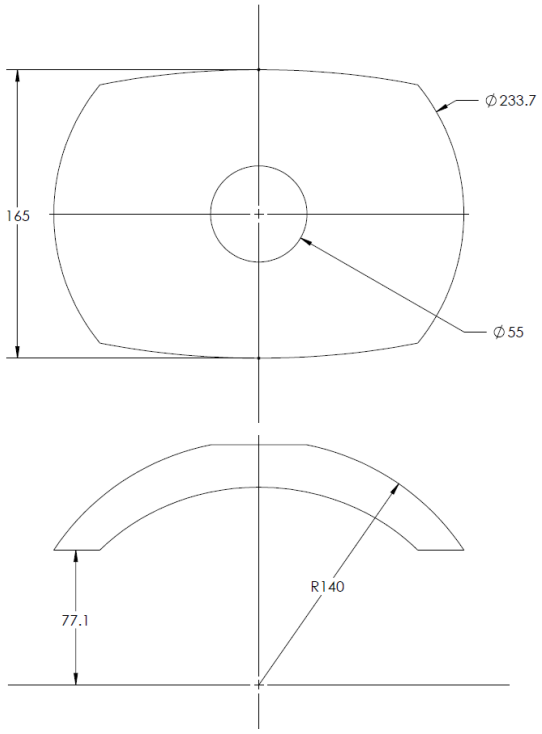

Figure 5. 1. CAD rendering of the active area of the transducer. Dimensions are in mm.

The upper size limit of array-elements was constrained by the topographical variation of the speed of sound within tissue in the direction orthogonal to sound propagation. To get a sense for the scale of this variation, our lab performed local time-of-flight measurements on a slab of porcine abdominal tissue [201]. A single 500 kHz transducer element with a diameter of 20 mm was aligned axially with a needle hydrophone (HNR-0500, Onda, Sunnyvale, CA, USA) at a distance of approximately 10 cm. Mounted rigidly with respect to each other, the element-hydrophone pair was affixed to a motorized positioner. Readings were taken in the free field with only water between the element and hydrophone. Next, the pork-slab was mounted between the pair and the motorized positioner was used to scan a grid of points measuring 4 cm x 4 cm. Variation in times of arrival were found to be 250 ns, 400 ns, and 800 ns over 1 cm^2 ,

4 cm^2, and 16 cm^2 regions, respectively. At 750 kHz, these time-shifts correspond to 19%, 30%, and 60% of a period, respectively. Thus, the target size for transducer elements was set to approximately 1 cm^2.

5.2.4 Segmentation of the Aperture into Discrete Elements and Linear Acoustic Simulation

Using the array geometry defined in the previous section, a series of MATLAB scripts were written to simulate the electronic focal steering range as a function of element-count. The first script (see *liverTxLayout.m* in the appendix) functioned by segmenting the aperture into nesting arc segment-shaped elements with approximately equal aspect ratio and surface area. Arc segments were generated by dividing the aperture into concentric rings and then further dividing each ring in the azimuthal direction. Having roughly square (vs. elongated rectangular, for example) elements was thought to improve the ability to perform localization through the reception of acoustic signals. Having roughly equal surface area for each element simplified the construction of the array's electronic driving circuitry. Triangular regions along the array's flanks were left unpopulated for these reasons and due to the high additional per-element cost associated with making eight additional shapes for which there would be only 16 elements. If a similar design were to be produced commercially, these regions could be made active more practically by amortizing the cost over a large number of units.

The script functioned by looping through a series of targeted element-counts ranging from 25 to 750 in increments of 25 elements. In order to maintain the input geometric constraints,

the actual element-count was allowed to deviate from the targeted count by approximately 5%. If a precise number of elements were desired, the basic aperture dimensions could be modified slightly to accommodate this requirement. After each iteration, the script saved a data file containing the 3D information fully defining each element (center position, profile, area etc.). A rendering of the segmented aperture generated in MATLAB appears in figure 5.2.

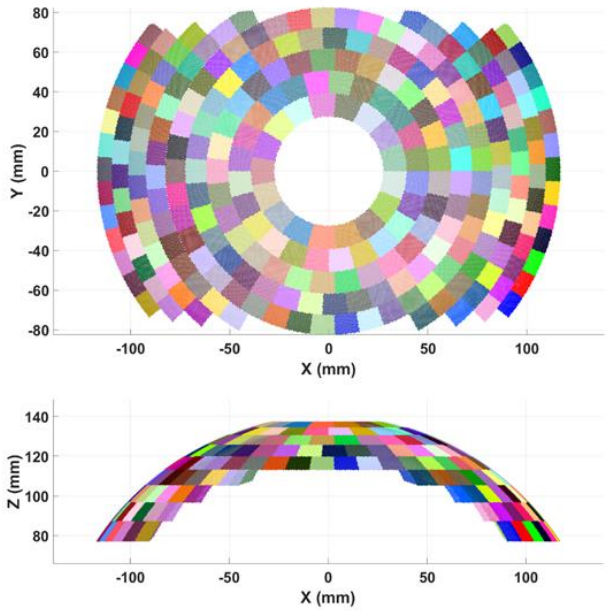

Figure 5. 2. Rendering of the aperture segment in MATLAB. Aperture displayed contains 258 elements.

The second script (see *liverArray_FOCUS.m* in the appendix) simulated the electronic focal steering (EFS) range of the apertures defined by the first script by integrating functionality from FOCUS software [212]–[214]. It functioned by loading the element-position data for a given aperture configuration and supplying these data to the *get_circ* function in FOCUS which generated a circular FOCUS transducer for each array element with a radius derived from the area of the input element. The decision to approximate the array's arc segment-shaped

elements as circles was made in the interest of accelerating computation time and in light of the results of a collaboration with HistoSonics in the summer of 2017 which showed little difference in the beam profile when elements were small (on the order of a few cm or less) and evaluated in the far field (~15 cm). The *cw_pressure* function was used to generate a vector of the pressure distribution for each module individually. The *coordinate_grid* parameter for *cw_pressure* was defined as a one-dimensional array ranging from -80 mm to 80 mm along the axis of interest and centered about the geometric focus. Each axis (x, y, and z) was considered separately in this manner. The medium was set to *lossless*, the number of divisions of integral points to use was set to 10, and the frequency of the array was set to 750 kHz. Vectors output by *cw_pressure* were then summed to generate the maximum achievable EFS pressure along the axis under consideration. For each aperture-configuration, the contribution of a perimeter around each element measuring 250 microns necessary for electrical insulation and mechanical clearance was subtracted from the total area. Selected results of this analysis are displayed in figure 5.3.

This analysis revealed that an array with 384 elements, each with an area of 99.4 ± 7.2 mm^2, would be near optimal and have an estimated FWHM EFS range of 32 mm in the least-steerable direction. As discussed later, the number of elements had to be reduced to 260 in order to satisfy practical design considerations. At this EFS position, 16 mm off axis in the y-direction, the proposed array-configuration was estimated to generate 111 MPa in the free field. The full width of the EFS range in the y-direction at 26 MPa (approximate intrinsic threshold in the free field [152]) and 52 MPa (approximate de-rated threshold *in vivo*) were estimated to be 50 mm

and 44 mm, respectively. An aperture with 384 approximately 1-cm^2 elements was used as the starting point for the mechanical design.

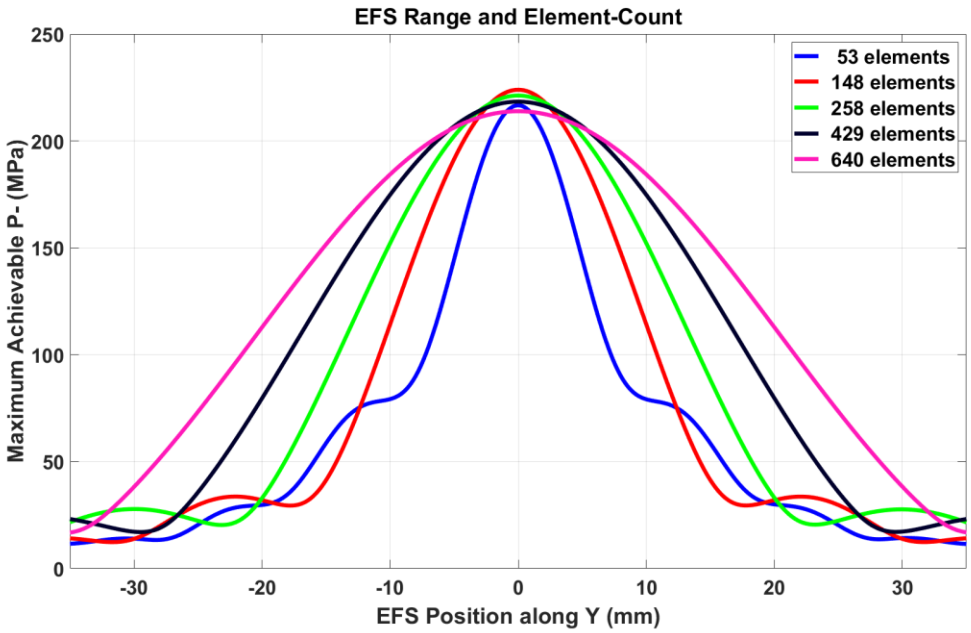

Figure 5. 3. Electronic focal steering range as a function of element count. Simulated maximum achievable P- is estimated based on linear summation. The model assumed a gap between elements' active piezoelectric material of 0.5 mm. Utilizing the full aperture (in the absence of any gaps or unpopulated regions at the aperture's flanks), the maximum P- at the focus was estimated to be 246 MPa. Packing-density is modest for low element-counts (due to the unpopulated triangular regions on the array's flanks), optimal near 150 elements, and begins to diminish thereafter at higher element-counts (due to the increased area occupied by inter-element gaps). Selected data are displayed to reduce clutter.

5.2.5 Modular, Replaceable Elements

5.2.5.1 Constraints on the Size of Elements

Arrays with replaceable elements commonly utilize a design in which the element's cable is passed through a hole in the array's scaffold larger in diameter than the connector. The

element may be affixed to the scaffold by mating threads on the interior of the hole [376] or secured on the backside of the scaffold by a nut modified with by the addition of a slot to form a C-shape which allows the cable to pass through it [377]. A threaded mounting hole requires the element to be rotated which inherently constrains the packing density of the aperture. The C-nut design allows more design flexibility but nevertheless requires significant spacing between elements to allow clearance for the nuts and a tightening tool to rotate.

The mechanical design of modular elements for this array was based on the through-hole configuration but rather than a C-nut, the module was held fast by a removable low-profile stainless steel retaining ring (93576A110, McMaster-Carr, Elmhurst, IL) which mated with a radial groove on the shaft of the module. An o-ring was fitted between the module and the scaffold on the concave side to provide a small spring force (approximately 7 N). This allowed the module to be rigidly fixed during use and absorbed slight dimensional deviations from parts' nominal values, easing installation. Please see figure 5.4 for more detail.

The diameter of the through-hole in the scaffold is dictated by the connector which passes through it and the size of the element which it retains. In turn, the diameter of the hole determines the minimum spacing and size of elements. It is therefore desirable to use the smallest connector which meets other practical considerations. Previous experience in our lab has found that the voltage ratings claimed by manufacturers can be inaccurate for our application using short pulses at high voltage. To select a connector, we soldered 2-m sections of micro-coaxial cable (9432 WH033, Alpha Wire, Elizabeth, NJ) to a variety of candidate connectors and applied pulses increasing in voltage up to 4 kV while monitoring for arcing with a 1000x attenuation high voltage probe (P6015A, Tektronix, Beaverton, OR). The connectors we

evaluated included SMA, SMB, and MCX. Ultimately, the smallest connector to pass this testing reliably was the SMA-style connector which can be purchased in a configuration with a 9-mm greatest diametral extent (132296, Amphenol RF, Danbury, CT). While a custom connector could be manufactured (or modified starting from an existing connector) with smaller dimensions and adequate voltage-handling capacity, this avenue was beyond the scope, timeline, and budget of this research.

The size of the selected connector and corresponding scaffold through-hole then necessitated revision of element-size to a minimum value of 11.4 mm which provides a tight fit for the connector, o-ring, and adjacent elements. To relax clearances and provide easier manufacturability and fit, the element size was set to 12 mm. Supplying this value to the aperture design and linear acoustic simulation scripts described in the previous section, resulted in a configuration with 258 elements, a mean area of 146.7 mm^2 ± 6.2 mm^2. P- at the geometric focus was estimated to be 221 MPa and the EFS range was estimated to be 26.2 mm and 36 mm at FWHM and 52 MPa, respectively. The scaffold and modules were designed in Solidworks. During CAD design, minor adjustments were made to azimuthal element positions and numbers, resulting in a design with 260 elements. Images and renderings of the modules appear in figure 5.4. Relative to the area of the full aperture displayed in figure 5.1, this design achieved 88.4% active area. Relative to the area of the full aperture minus the area of triangular regions at the aperture's flanks, this design achieved 92.1% active area. As previously mentioned, the triangular regions (which constitute approximately 4% of the total area of the aperture) could be easily populated with active material if so desired.

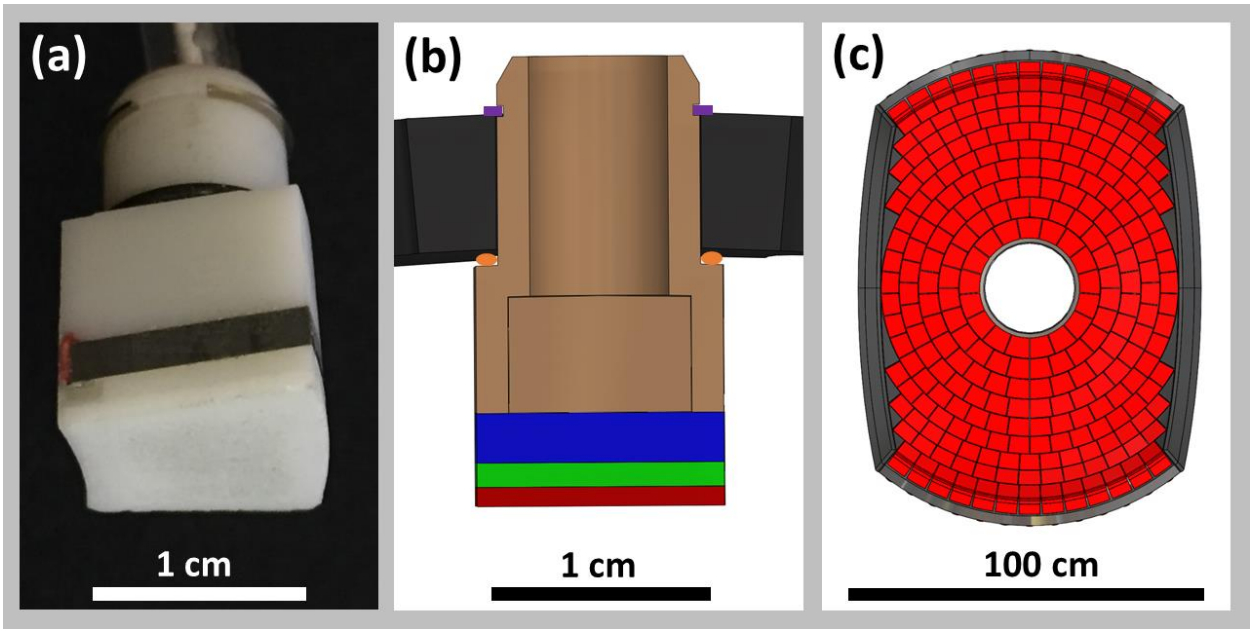

Figure 5. 4. (a) Image of assembled module prior to epoxy coating. (b) CAD cross-section of module in scaffold. Red: nylon quarter wavelength matching layer (0.91 mm thick); green: polyacrylamide quarter-wavelength matching layer (1.14 mm thick); blue: piezoceramic; brown: backing-mount; orange: o-ring; purple: retaining clip; black: scaffold. (c) CAD rendering of transducer. View along acoustic axis. Modules appear in red.

5.2.5.2 Thin Coat of Epoxy as an Electrically Insulating Enclosure

Previous studies in our lab demonstrated the use of 3D printing to produce housings which totally enclosed the piezoelectric material and potted it in epoxy [376]. This design is simple and self-aligning but leaves an acoustically passive perimeter which can be no thinner than approximately 0.5-1.25 mm around the element's surface. Together with a small allowance for mechanical clearance between elements, this sets the minimum gap between piezoelectric elements at slightly greater than 1 mm.

To overcome this limitation, the present study demonstrates a novel technique for enclosing and electrically insulating the element by applying a 125-microns thick layer of epoxy (JARO-343, Jaro Corporation, Ipswich, MA) with exceptionally high dielectric strength (1-2 kV per 25

microns at 75-microns thickness – manufacturer's claim) to replace the 3D printed perimeter of the housing and serve as a very thin electrical insulator as shown in figure 5.5.

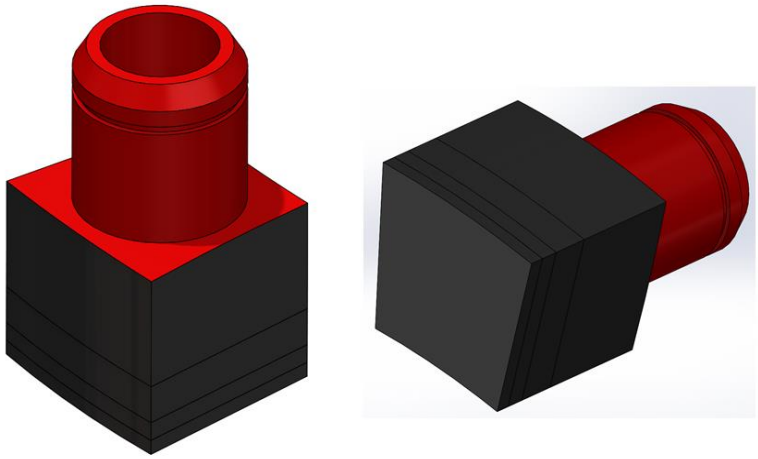

Figure 5. 5. CAD rendering of module assembly (without cable or strain relief). Uncoated surfaces appear in red. Surfaces coated with thin layer of epoxy appear in black.

In this manner, the gap between active piezoelectric components can be greatly diminished, resulting in substantially higher active area for the acoustically emissive surface of the element. For example, if a square piece of piezoelectric material with length *L* on a side and an enclosure thickness of *T* are assumed, the ratio of active area on the surface of the assembled element (that of the piezo material) to total surface area of the acoustically emissive face of the enclosure is described by,

$$R = \frac{(L - 2T)^2}{L^2} \tag{5.2}$$

where the term within the brackets represents the length of the piezoelectric material. In the case of 3D printed housing, the term *T* must also include a small mechanical clearance between the housing and the crystal. As displayed in figure 5.6, the relative loss of active area is marginal for large elements but substantial for small ones. Assuming a 12-mm square element and a nominal 0.13-mm clearance between the 3D printed housing and the peizoceramic, the active area is 17-61% greater using epoxy-coating for insulation rather than a 3D printed housing.

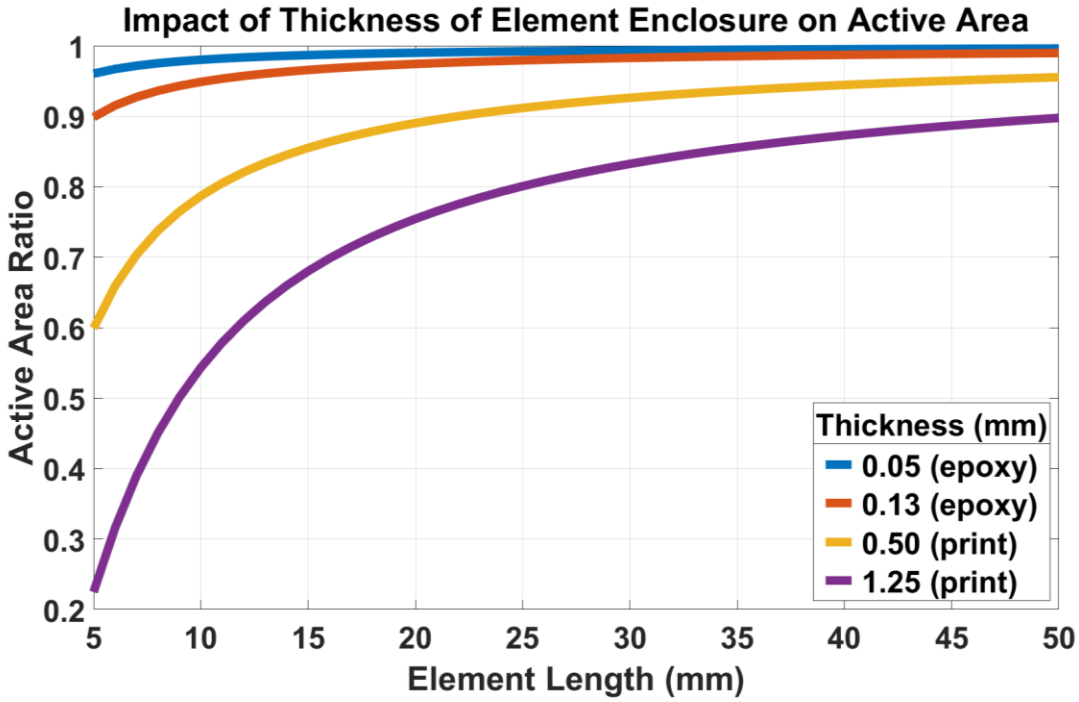

Figure 5. 6. Comparison of techniques for providing an electrically insulating enclosure for elements square elements of various sizes. For small elements, a 3D printed enclosure occupies a substantial portion of the acoustically emitting surface of the element. By instead stacking and bonding element-components such that their profiles are flush, then coating this assembly in a thin layer of epoxy for electrical insulation, the ratio of active area to total area of the acoustically emissive surface can be greatly improved.

5.2.6 Transducer Scaffold

The transducer's scaffold, which served as a rigid mount for elements, was machined from 6061-T-6 aluminum and type 3 hard anodized per MIL-A8625 with a minimum thickness of 0.05 mm to provide corrosion resistance. The scaffold incorporated a cylindrical projection on the backside which had a bore 50 mm in diameter and a bolt pattern at the end of the bore. This feature was used to mount the transducer to a positioning system and house the mechanism which controlled the ultrasound imaging probe. The ultrasound imaging probe (C7-3/50, Ultrasonix Medical Corporation, Richmond B.C., Canada) was secured within a 3D printed clamshell-style housing which was then fastened to a hallow actuation shaft machined from acetal copolymer. The actuation shaft fit within the bore of the scaffold and could be precisely rotated by a modified optical rotation stage (RSP-2T, Newport Corporation, Irvine, CA). The actuation shaft could also be extended up to 71 mm from its retracted position near the therapy elements as shown in figure 5.7. Please see appendix for selected technical drawings of machined parts.

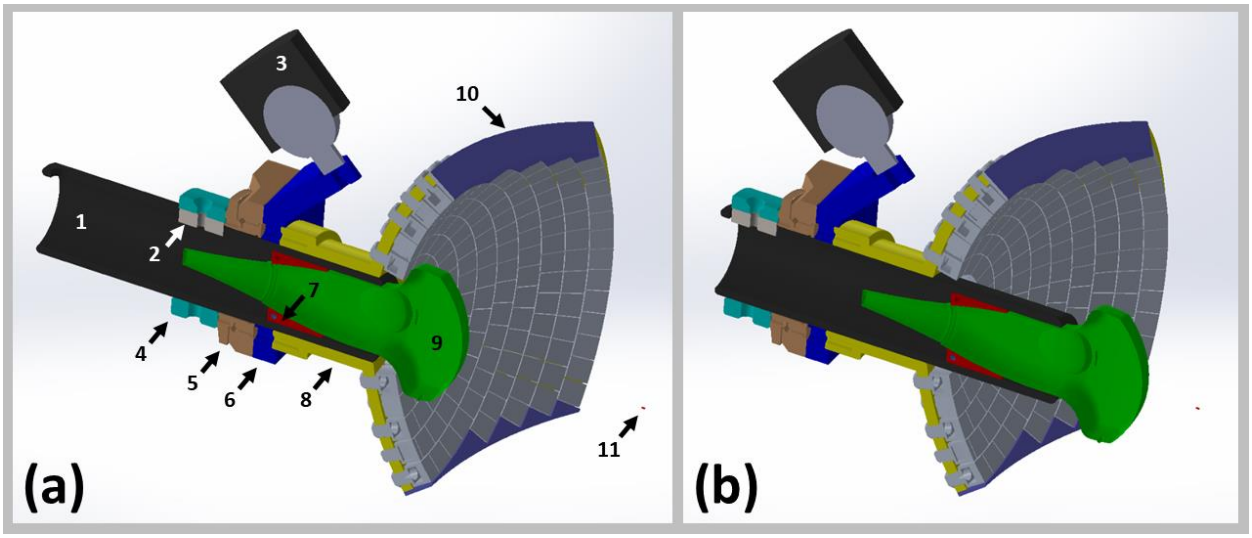

Figure 5. 7. CAD renderings of array assembly with imaging probe (a) retracted and (b) extended. 1) actuation shaft 2) parallel key with taped hole (KESSM12_25, MISUMI USA, Schaumburg, IL) 3) ball head mount (part number 12652, Really Right Stuff, LLC, Lehi, UT) 4) actuation shaft mount 5) optical rotation stage 6) mounting bracket 7) 3D printed clamshell mount for imaging probe 8) scaffold 9) imaging probe 10) 3D printed trim piece 11) geometric focus of the transducer.

5.3 Fabrication and Assembly

5.3.1 Producing Arbitrarily Shaped Elements

Piezoceramic bulk materials are typically manufactured by hydraulically pressing a granular mix of piezoelectric and an organic binder material into a mold. Basic geometric shapes like disks and plates as well as slightly more complex shapes like cylinders and hemispheres are commonly formed this way. The “green” material is then sintered at high temperature to form a crystalline structure of PZT and to evacuate the binder material. Once cool, elements can be trimmed and finished by machining with diamond coated tooling. As a final step, electrodes are applied and the material is poled above the Curie temperature. For large-volume production of the arc segments described in this study, it would likely be feasible to press elements into

slightly oversized shapes and perform a machining or grinding operation to achieve good tolerances. However, for the low quantities used in this project, this approach would be prohibitively expensive and time-consuming.

Starting from a larger sheet of material, a dicing saw is commonly used to form piezoceramics into rectilinear shapes. More complex two-dimensional shapes can be formed by CNC milling operations but require specialized tooling and elevate the risk of locally de-poling the material by frictional heating. Waterjet cutting presents two key advantages for shaping piezoelectric materials. First, arbitrary and even highly intricate shapes can be cut from delicate materials like ceramic or glass due to the very small and localized machining force [378]–[380]. Second, because waterjet cutting does not elevate the temperature of the work-piece, there is no risk of thermal damage [378]. Our experience from interacting with several waterjet cutting vendors and evaluating several samples has been that most can comfortably hold standard machining tolerances (± 0.13 mm) and a few can hold as good as ± 0.06 mm. Thus, Pz36 parts for this project were cut from a larger sheet using precision waterjet cutting.

5.3.2 Assembly Fixtures and Methods

As discussed in section 5.2.6 and displayed in figure 5.4, the two matching layers, piezoceramic, and element-mount share a common profile and stack flush with each other, therefore requiring a fixture for alignment during assembly. Assembly fixtures consisted of a vise-like clamp with reliefs that conformed to the element's profile and applied pressure to the

four lateral sides of the stack. A 1 kg weight was positioned on top of the stack to apply force along the axis of the module. A rendering of this system is displayed in figure 5.8. Assembly clamps were 3D printed in a single operation using a combination of rigid acrylic polymer (VeroWhitePlus, Stratasys, Rehovot, Israel) and elastomeric material (Agilus30, Stratasys, Rehovot, Israel). The relief features in the clamp's jaws featured a profile which closely matched that of the element and produced a slight interference fit (approximately 0.06 mm per side) when the jaws were closed. The main body of each side of the clamp was made from rigid material while the inset profile of the relief feature was lined with a 1-mm layer of elastomeric material (approximately shore 40A durometer) designed to conform to the profile of the element-stack. The corners of the inset profile featured small cutouts which served as vents for excess epoxy. Because the array contained 9 unique arc-segment shapes, each required a unique assembly clamp. Clamping force was supplied by a doubled rubber band which surrounded the exterior of the clamp.

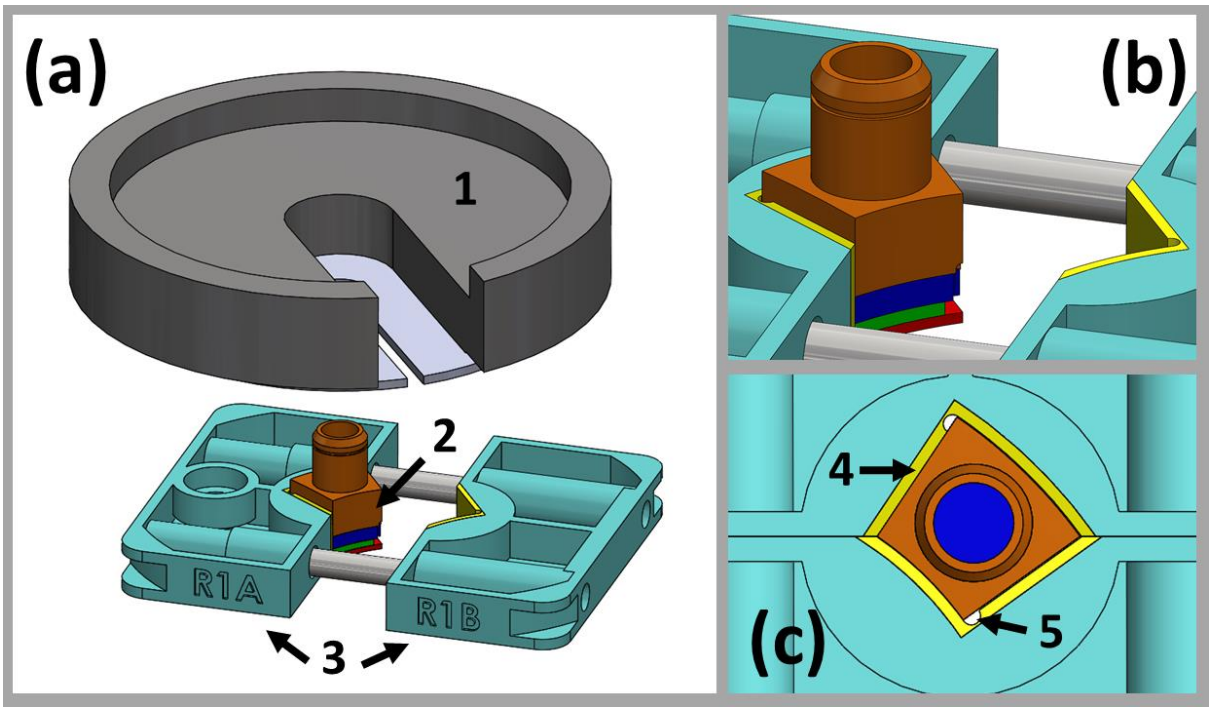

Figure 5. 8. CAD rendering of module in assembly vise. (a) Angled view with vise (3) open and weight (1) above stack of element components (2). Close-up view of element in open vise. (3) Top view of element in closed vise. (4) Indicates elastomeric portion of jaw. (5) Indicates vent for excess epoxy.

The two matching layers, Pz36 material, and the backing-mount were joined using 2-part epoxy (E-120HP, Loctite, Düsseldorf, Germany). Surfaces of the assembly fixture which came into contact with epoxy were covered in adhesive-backed PTFE tape (PN 6305A16, McMaster-Carr, Elmhurst, IL) and coated with canola oil cooking spray (Item 1058015, Costco Wholesale Corporation, Issaquah, WA) prior to use. Dimensions of the clamp and the desired level of mechanical interference were specified to account for the thickness of the PTFE tape (approximately 0.11 mm). Following application of epoxy to components to be joined and insertion into the clamp, the backing-mount was filled with epoxy and a custom strain relief mounted on the cable was inserted into the bore of the backing-mount. Two weights (PH0264B1, Eisco Labs, Ambala - 133104, India), which together constituted 1 kg, were placed

on top of the stack of parts. The bottom weight had a washer (PN 98264A275, McMaster-Carr, Elmhurst, IL) with a slot cut into it affixed to it to serve as an adapter.

The epoxy was allowed to cure for at least 24 hours before removing the element from the clamp. The element was trimmed and lightly sanded using 600-grit sandpaper to remove any excess epoxy which may have accumulated on the exterior surfaces. Elements were then cleaned and coated with a 125-microns thick layer of epoxy with high dielectric strength epoxy (JARO-343, Jaro Corporation, Ipswich, MA).

5.4 Characterization

At the time of this writing, modules for the inner-most rings (83 total including extras) were completed and the remainder were in processing at the epoxy coating vendor. A sample of N=10 from each ring-group were characterized for their pressure output and ability to handle high voltage. Modules were driven with a roughly 1.5-cycle pulse having 3 kV peak-to-peak amplitude. A calibrated hydrophone (HGL-0085, Onda, Sunnyvale, CA) was positioned along the module's primary acoustic axis at a distance of 140 mm. The pressure output was measured to be 5.26 ± 0.22 kPa/mm^2, 5.56 ± 0.14 kPa/mm^2, 5.46 ± 0.06 kPa/mm^2 for rings, 1, 2, and 3, respectively. Extrapolating these results to the remainder of the array suggests that the array will produce 190 ± 7 MPa by linear summation. This value is 14% lower than the 221 MPa predicted based on the value derived from a preliminary test module. The discrepancy may be attributable to wetting of the front matching layer of test module which was not coated and was exposed directly to water during testing. In the coated modules, this porous matching layer

likely retains a small amount of air. Higher pressure output and the desired EFS range may still be achievable however, as 3 kV was selected a conservative driving limit and may prove to be well under the ultimate driving voltage limit. Future designs would likely benefit from a non-porous front matching layer or masking it during the coating process.

5.5 Conclusions

This study demonstrates a novel design and fabrication techniques for a focused phased array ultrasound transducer with 92% aperture utilization and arbitrarily shaped, replaceable elements. High aperture utilization is important for applications like large, highly steerable arrays or small arrays (rodent, laparoscopic arrays, etc.) where elements are approximately 1 cm^2 or smaller. The design and fabrication methods described herein are expected to be neatly transferrable to a broad range of applications for phased array FUS transducers. The design could serve as a practical means of fabricating the fully populated random phased arrays described by the theoretical method of Rosnitskiy *et al.* [323].

The materials for the transducer constructed for this study cost approximately $17,000 at the time of this writing. Much of this cost could be reduced by purchasing materials in larger volumes, exploring alternate vendors, and using alternate materials. Micro-coaxial cable, for example, was the largest single expenditure (accounting for 23% of the total cost) and could likely be sourced for less. By comparison the cost of the raw Pz36 material and waterjet cutting accounted for 6% and 16% respectively. Additionally, 3D printed parts, which accounted for

22% of the cost would be readily amenable to conventional high-volume manufacturing techniques like injection molding, machining and perhaps stamping.

Table 5. 1. Bill of Materials. Subtotals were calculated as the product of the unit price at the volume purchased and the quantity used for a single array.

line	Item Description	Vendor or Manufacturer	Quantity Used	Quantity Ordered	Unit Price (USD)	Subtotal (USD)	% of total cost
1	Micro-coaxial cable	Alpha Wire	Eight 10-m spools	Ten 100-m spools	503.172	4025.40	23.2
2	Aluminum array scaffold	Classic Turing	1	2	3440.00	3440.00	19.8
3	Stereolithography components	Protolabs	260	367	11.08	2880.80	16.6
4	Waterjet cutting	Meyer	260	367	10.96	2849.60	16.4
5	SMA connectors	Amphenol RF	260	500	3.819	992.94	5.7
6	Pz36, 750 kHz, 60 mm x 60 mm plates	Meggitt	17	50	56.50	960.50	5.5
7	Epoxy coating of elements	Jaro	260	260	3.50	910.00	5.2
8	White selective laser sintering parts	Protolabs	260	367	3.20	832	4.7
9	Retention ring	McMaster-Carr	260	260	0.953	247.78	1.4
10	Black selective laser sintering parts	Protolabs	2	2	87.25	175.00	1
11	o-ring	McMaster-Carr	260	300	0.1964	58.92	0.3
	total					17,372.94	100

While a precise estimation of the ablation rate would require accounting for complex nonlinear acoustics, thermal absorption, and physiologically dynamic perfusion, among other factors, an order-of-magnitude estimation of an achievable ablation rate can be calculated by a scaling factor derived from the relative volumes of the therapy foci of this array and that of the

250 kHz hemisphere used in Chapters 2 and 3 of this dissertation. Assuming that the linear extent of the focus scales proportionately with frequency, the focus for this 750 kHz array will be roughly 3 times smaller in diameter and 27 times smaller in volume. Therefore, an ablation rate on the order of 2 mL/min can be reasonable expected if thermal considerations are ignored.

Chapter 6

Summary and Future Work

6.1 Summary

This dissertation demonstrates the feasibility of methods and systems which enable the rapid, noninvasive ablation of large tissue structures using histotripsy. It is the author's hope that the research and development efforts described herein will further histotripsy toward clinical translation and eventual widespread clinical use. This chapter summarizes the work presented in this dissertation and discusses several potential avenues for further research based on its findings.

6.1.1 Rapid Ablation of a Large Tissue-Volume Enabled by Histotripsy with EFS

First, the feasibility of using histotripsy with electronic focal steering (EFS) for large-volume ablation was established. A highly steerable phased array transducer was selected for this study, rather than a single-focus transducer, based on previous experience in our lab which revealed that the persistence of residual cavitation nuclei in a phenomenon known as the cavitation memory effect necessitated a focal scanning strategy capable of very rapid scanning rates. The EFS strategy pursued in the first study [86] used a series of single-focus experiments to establish acoustic parameters including PRF and focal spacing. These results were then carried over to large-lesion ablation experiments in *ex vivo* bovine liver tissue in which a randomized 1000-foci EFS grid was used. Results from this effort indicated that this EFS approach was capable of generating 36-mL lesions at 3.3 mL/min, substantially faster than the ablation rates of contemporary technologies which are commonly around 2 mL/min [14], [15].

Second, while the development an algorithm for strategically arranging the firing order of EFS positions was underway, the observation that low-gain regions of the therapy beam were inducing bubble coalescence was the basis for a follow-on study [215]. This study investigated the formation of residual nuclei and their dissolution behavior, established proof of principle for the EFS-BC technique using a single, isolated focus, established several strategic EFS sequences based on these findings, and finally evaluated these sequences in tissue-mimicking phantoms. A novel method in which low-gain regions of the therapy beam were utilized to drive the coalescence of residual nuclei via the secondary Bjerknes force was developed and validated. Results demonstrated 99.9% complete ablation of a 27-mL volume (equivalent to a

sphere 3.7 cm in diameter) within 30 s. This ablation rate is more than 25 times greater than that of contemporary techniques and may facilitate the adoption of cavitation-based FUS where thermally-based FUS was found to be too slow (among other issues).

6.1.2 Compensation for Respiratory Motion

First, existing methods for respiratory motion compensation were reviewed and the feasibility of integrating these methods with histotripsy therapy were explored. Second, a novel cavitation-based motion tracking technique was demonstrated. Using this technique, residual cavitation nuclei were coalesced into a small bubble-system and used as an *in situ* fiducial marker which was tracked throughout a predefined trajectory by a histotripsy therapy system capable of receiving acoustic backscatter signals. Results demonstrated the feasibility of receiving acoustic signals from this fiducial cavitation bubble cloud throughout a 16-cm trajectory with a mean error of 0.7 ± 0.3 mm.

6.1.3 Design and Fabrication of a Novel Phased Array Transducer

A novel design and fabrication techniques were developed for a real-time-imaging guided, highly steerable phased array histotripsy transducer for liver ablation featuring arbitrarily shaped, densely, packed, and easily replaceable elements. The transducer design methods presented herein implemented a series of algorithms which analyzed human CT data to define the geometry of the array's aperture, divided the aperture into discrete, nesting elements, and

simulated the electronic focal steering range of this aperture as a function of the number of elements into which it was divided. Novel fabrication methods facilitated a very small gap (0.5 mm) between active piezoelectric material which resulted in a packing density >90%. Simulation showed that this array will be capable of electronically steering over a range sufficient to treat tissue-targets up to 3.6 cm in diameter in porcine or human subjects.

6.2 Future Work

6.2.1 EFS Grid Spacing

The new histotripsy systems under development in our lab will have the ability to store on the order of 10^4 EFS locations in memory and the ability to perform basic computations on the FPGAs. This functionality will open several avenues for EFS which were previously inaccessible.

First, as mentioned in Chapter 3, the ability to assign a unique EFS position to each pulse throughout a treatment in treatment grid is expected to maximize the destructive capacity of cavitation events. In this setting, grid spacing would be on the order of $\lambda/100$. Optical data from previous studies using RBC phantoms show that the homogenization effect is first observed at the center of the focal zone and progresses radially outward, with the extent of homogenization following a sigmoid curve as a function of the number of pulses applied. For an isolated lesion nearing complete homogenization, the cloud appears to “pluck” material from the peripheral boundary of the lesion and translate it to the center of the focus where it is

subsequently destroyed. These dynamics suggest that the cloud's destructive capacity decreases in some fashion with radial distance from the center. Thus, the dependence of large-lesion ablation progression on EFS focal spacing [347] merits further investigation.

Second, previous studies have employed EFS grids with homogenous spacing intervals [73], [86], [196]. For treatment applied across a broad EFS range where focal pressure and focal dimensions diminish significantly with distance from the geometric focus, grid spacing either over or under-samples regions of the grid. This issue could be addressed by either tuning the acoustic pressure throughout the grid to be uniform or, alternatively, by applying heterogeneous grid spacing based on the relative focal dimensions at a given grid position.

Focal dimensions as a function of EFS position could be simulated using software such as FOCUS [212]–[214]. From here, foci could be optimally nested with a prescribed degree of overlap. A two-dimensional representation of such a scheme appears in figure 6.1.

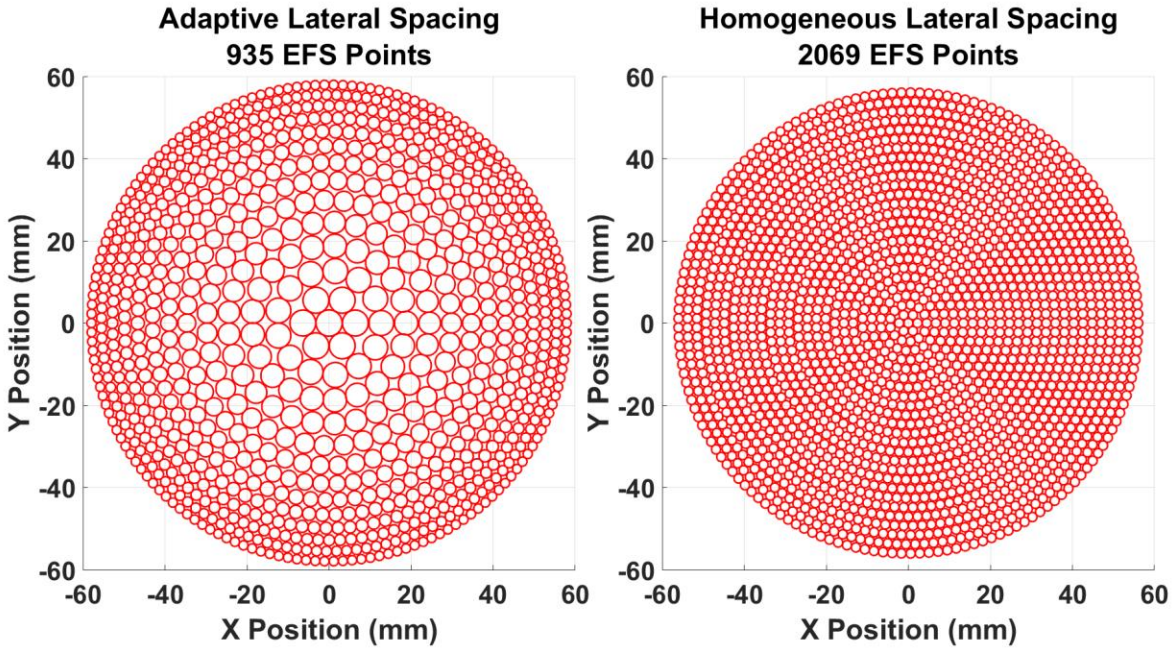

Figure 6. 1. Plots depicting examples of two-dimensional EFS grids with adaptive, heterogeneous spacing (left) and homogeneous spacing (right) in the lateral plane across the approximate full free-field EFS range of the 250 kHz, 256-element hemispherical phased array described in Chapters 2 and 3 of this dissertation. Foci are displayed with no overlap to reduce clutter.

A similar two-dimensional EFS layout is currently being implemented as part of an ongoing *in vivo* porcine study in collaboration with Dr. Kevin Ward in which histotripsy is being used for eschar debridement in burns to the skin. Preliminary testing has been performed on pork chops burned *post mortem* as well as *ex vivo* tissue burned *in vivo* and then excised. Figure 6.2 displays images collected before (6.2a) and following (6.2b) histotripsy debridement treatment applied with the 250 kHz hemispherical transducer described in Chapter 2. Post mortem samples were muscle tissue (pork chops) purchased from a local grocery store and prepared by degassing under vacuum while submerged in saline for 2 hours. Thermal damage was induced by pressing a stainless steel cylinder measuring 50 mm in diameter and heated to 250 °C into the sample for 60 s. The EFS grid consisted of 510 homogeneously distributed points arranged

in the shape of a disk 46 mm in diameter and with the charge time for each position programmed such that pressure was approximately uniform and set to 35 MPa P- in an attempt to achieve uniform debridement across the treatment zone. Further testing is currently underway using a 64-element hemispherical phased array histotripsy transducer with a 73-mm focal distance and burn samples collected from an *in vivo* porcine model.

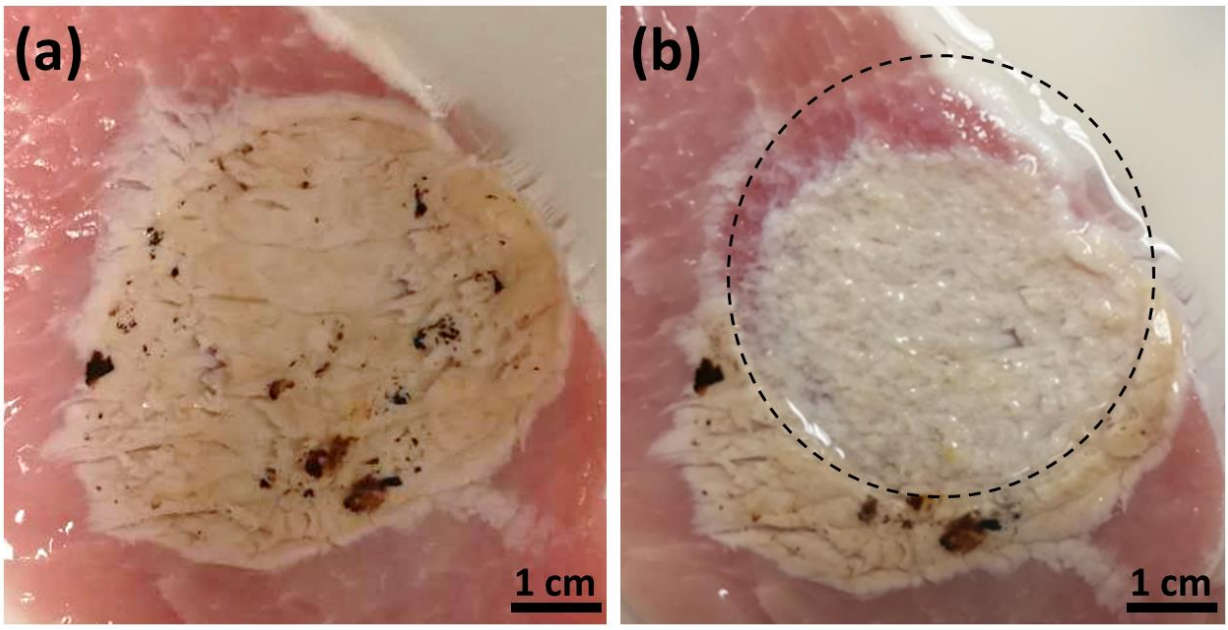

Figure 6. 2. Images of porcine muscle tissue burned for 60 s with a stainless steel cylinder heated to roughly 250 °C prior to (a) and following (b) histotripsy debridement treatment.

6.2.2 Optimization of EFS Sequences

Further development of the EFS strategies described in Chapter 3 would likely benefit from investigating the underlying physical mechanisms driving per-pulse efficiency in volumetric histotripsy ablation. Based on results of the two-foci experiments described in section 3.2.2, it

was hypothesized that per-pulse fractionation efficiency could be improved by implementing an EFS strategy which eliminated encounters between the high-gain region of the therapy beam and populations of nascent, diffusely distributed residual microbubbles for 20 steps through the firing sequence. 20 pulses had been shown to be sufficient to produce a substantial amount of bubble coalescence via the EFS-BC effect. This hypothesis was supported for the cases in which the number of foci in the EFS grid was small (see figures 3.13 and 3.16) but not in cases where the number of foci was large (see figure 3.21). As discussed in section 3.3.3.3, other parameters such as the mean rather than the minimum number pulses before a violation of the exclusion zone (EZ) is encountered might prove to be more fruitful targets for the optimization of EFS sequences.

As discussed in section 3.3.3, partially fractionated material in RBC phantoms was observed to translate in bulk several centimeters inward from the lesion boundary and opposite the direction of ultrasound propagation before being destroyed completely. If this phenomenon is indeed driven by the mechanism of asymmetric growth and collapse of the bubble cloud proposed by Miller et al. [196], [197], [259], perhaps an EFS sequence could be designed to exploit this mixing effect to accelerate therapy.

6.2.3 Phasing Techniques

Beyond the aforementioned EFS strategies which use canonical intrinsic threshold histotripsy (microtripsy) waveforms and seek to maximize the coherent alignment of the primary

rarefactional excursion of each pulse at the focus, there are may be several methods for converting more of the therapy beam's acoustic energy into cavitation based on alternative phasing schemes. The sector-vortex method, first described in the 1980s by Cain and Umemura for hyperthermia applications [381], generates a laterally enlarged, annular focus and may be further enhanced by incorporating simultaneous concentric-ring phasing [382]. Several recent studies have employed similar phasing approaches for cavitation-based therapies as well [82], [383]–[386]. With sufficient headroom, it is likely that similar strategies could be implemented for histotripsy ablation of large volumes with EFS.

In addition to phasing schemes in which each pulse contains a fixed center frequency, it may be possible to steer the therapy beam efficiently by transmitting multi-cycle, frequency-swept pulses (also known as *chirps*). The process of arranging phases, frequencies, and delays would likely be arduous or intractable *a priori* but might be approachable algorithmically through some iterative optimization process. The author of this dissertation would like to acknowledge Tim Hall as the primary contributor to conceiving this approach.

6.2.4 Variable Pulse and Burst Repetition Frequencies

The pulsing schemes tested in this dissertation used a single PRF for a given treatment, applied continuously for large-volume ablation. In section 4.1.1 of this dissertation, the author proposed applying high-PRF bursts of histotripsy pulses only during the respiratory gating window and halting therapy when the target-tissue was undergoing excursion, suggesting that

this approach might also provide sufficient time for small residual nuclei to dissolve between bursts. Anecdotal observations of high-speed imaging data collected during large-volume ablations in degassed tissue-mimicking gel with PRF on the order of several hundred Hz suggest that the number of residual nuclei in the sound field grows as a function of the number of EFS-grid repetitions applied, saturating after approximately 10 repetitions. Pausing and resuming treatment after several seconds seemed to "reset" the medium as expected. Topics for further investigation might include this approach and temporal variation of PRF throughout a large-volume histotripsy treatment as the number of peripheral bubbles was shown to decrease as a function of pulse-number for a single focus pulsed at low PRF (see figure 2.10).

6.2.5 Bubble Coalescence in Soft Tissue and *In Vivo*

Several previous studies have demonstrated histotripsy bubble coalescence (BC) in tissue-mimicking agarose gel phantoms [95], [97], [215] but none has demonstrated the effect in tissue. While tissue is more resistant to histotripsy ablation than agarose gel for a given elastic modulus due to the presence of collagen and other connective structures [387], [388], it may be more favorable for BC due to porosity [389] and microvasculature which could afford cavitating residual microbubbles an additional degree of mobility. The bubble tunneling effect displayed in section 2.3 and described in references [162], [198], [199], if applicable in this context, would also likely benefit BC.

The viscosity of the tissue as it progresses from a deformable solid to a multiphase fluid, may play an important role in the dynamics of bubble coalescence. Previous studies which considered viscous effects on two-bubble systems showed that, as one would expect, viscous drag slows coalescence and interestingly that the secondary Bjerknes force can be repulsive rather than attractive under certain conditions [232], [390], [391]. Because assigning an appropriate value of viscosity to tissue would likely be challenging, the best approach may be to proceed with empirical testing.

Monitoring in such an experiment could be performed optically if tissue clearing methods for large samples [392], [393] would preserve representative mechanical properties found *in vivo*. Ultrasound imaging would also be an attractive option as previous experience in our lab has shown that the physical extent of the residual nuclei population is readily discernable by this method [61], [205], [296].

6.2.6 Aberration Correction

Previous studies in our lab have demonstrated the use of cavitation expansion signals generated by a high-amplitude, many-bubble cloud for localization and aberration correction but were limited in precision due to the multiple shockwaves emitted by the several-millimeters-wide population of explosively expanding individual bubbles [187], [377]. Efforts to generate a single *de novo* cavitation bubble consistently in these studies were not successful. Chapter 4 of this dissertation demonstrated that a highly localized, quasi-stable bubble system

initiated by coalesced residual microbubbles could be used as a localization beacon in gel; however, in a scattering medium like tissue, the SNR might prove to be too low.

A method for the generation of a single coalesced bubble and its inertial re-excitation for the purpose of aberration correction is the subject of an ongoing study in our lab. Thus far, we have demonstrated that a single coalesced bubble can be generated with an 89% success rate using the 500 kHz, *f* 1.8 transducer previously described [95] but using EFS pulses for BC rather than the bubble removal module. A coalesced bubble with static radius on the order of a few microns can then be re-excited by a pulse with a sub-threshold amplitude (~20 MPa P-) to a maximum radius of approximately 0.3 mm and in the process, emit a single spherical shockwave as displayed in figure 6.3. This shockwave is readily detectable by the receive-system of the therapy array, though the amplitude of the shock is unknown at this time because the system has not been calibrated for this purpose.

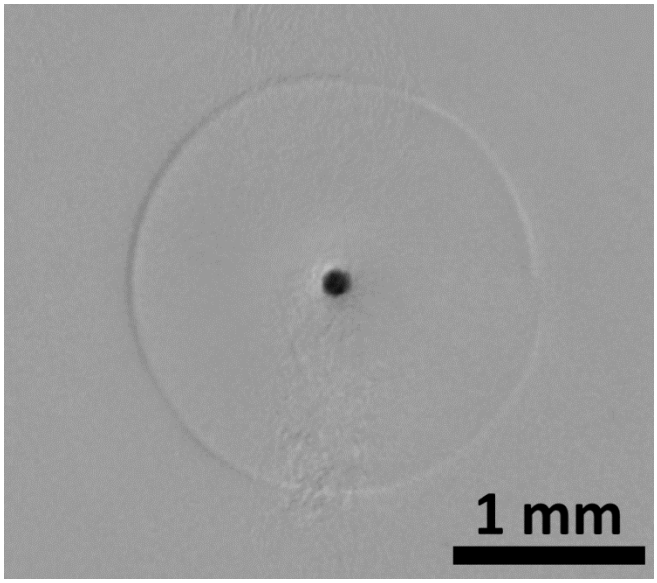

Figure 6. 3. Shockwave emitted from a single bubble generated by the coalescence of residual nuclei and then re-excited by a histotripsy pulse with approximately 20 MPa P-.

6.2.7 Stable Driving of Coalesced Bubbles for Therapy

In addition to localization, it might be possible to employ coalesced residual microbubbles for therapeutic purposes by driving them to cavitate stably with a separate acoustic beam at a very low frequency (tens of kHz) and moderate pressure amplitude (a few MPa P-). Using a low frequency would have the advantages of lower attenuation, less absorption and tissue heating, and would more closely match the resonant frequency of these large bubbles. Anecdotal experience with driving coalesced bubbles at 250 kHz and 500 kHz suggested that this stable cavitation activity had much less destructive capacity than *de novo* cavitation in an RBC phantom. Investigating this phenomenon in more detail might further illuminate the mechanism and effective range of histotripsy's therapeutic effect. For instance, an experiment could modulate the amplitude of oscillation and thereby study the impact of various strain levels on surrounding media [217].

6.2.8 Intrinsic Threshold Histotripsy for Large-Volume Ablation *In Vivo*

Previous studies have demonstrated the ability of histotripsy to ablate a large volume of tissue *in vivo* using shock-scattering [73] and boiling mechanisms [50], [52] for bubble cloud formation. Both of these techniques rely on waveforms with multiple cycles (3-5 or more) and

the reflection and inversion of their high-amplitude, shocked compressional excursions from small cavitation bubbles generated by the expansion of incidental nuclei [68], [256]. By contrast, the use of intrinsic threshold histotripsy (microtripsy) *in vivo* has been limited to thrombolysis where a small focal zone and high precision are paramount [56]. Intrinsic threshold histotripsy uses short pulses with roughly 1.5 cycles with rarefactional excursions sufficiently high to nucleate cavitation with the incident waveform alone [142]. Intrinsic threshold histotripsy deposits less acoustic energy per pulse, but it is unclear which mechanism is ultimately most efficient when couched in terms of maximizing the ablated volume per unit of energy deposited as heat in the surrounding tissue. Because heat deposition is expected to impose the ultimate treatment rate limitation on histotripsy *in vivo*, further investigation into this topic and whether shock-scattering histotripsy is amenable to electronic focal steering is warranted.

Aside from which modality of histotripsy will ultimately prove best-suited for clinical application, *in vivo* validation studies using the highly steerable array described in Chapter 5 and currently under construction in our laboratory should be performed. Topics for these studies should include basic proof of principle regarding the use of intrinsic threshold histotripsy for large-volume ablation and aberration correction in an *in vivo* setting.

Appendix

A.1 Selected MATLAB Scripts

A.1.1 ReadCineFileImageNoHandle.m

This script permits the rapid processing of a large number of *.cine* files. The original version ReadCineFileImage.m was supplied by Vision Research (Wayne, NJ). Modifications were conceived by Jonathan Lundt and implemented by Akshay Rao. The modified script creates a single handle for a larger processing loop. This modification prevents the script from crashing and executes the load operation ~5X faster.

```
function [matlabIm, unshiftedIm] = ReadCineFileImage(fileName, imageNo, showImage, cineHandle)
%Read an image specified by imageNo from a cine located at the path specified by fileName parameter.
% RETRUNS:
% matlabIm - 1D Gray/3D RGB matrix. For 16bpp images the pixel values are alligned to 16bits
% unshiftedIm - 1D Gray/3D RGB matrix with image pixel values unshifted

% Usage:
% LoadPhantomLibraries();
% RegisterPhantom(true); %Register the Phantom dll's ignoring connected cameras.
%                        %Use this function once at the begining of your work
% [matlabIm, origIm] = ReadCineFileImage('D:\Cine\test.cine', -3000, true);
% other work with cine files
% ......................
% UnregisterPhantom(); %Use this function when you finished your work
% UnloadPhantomLibraries();
```

```
%% Nested cineHandle functions

function [ HRES, pixels, IH ] = PhGetCineImageLocal( CH, imRng, BufferSize )

   pixels = zeros(BufferSize, 1, 'uint8');
   pPixel = libpointer('uint8Ptr', pixels);
   pImRng = libpointer('tagIMRANGE', libstruct('tagIMRANGE', imRng));
   pIH = libpointer('tagIH', get(libstruct('tagIH')));
   [HRES, dummyAll] = calllib('phfile', 'PhGetCineImage', CH, pImRng, pPixel, uint32(BufferSize), pIH);
   OutputError(HRES);
   pixels = pPixel.Value;
   IH = pIH.Value;

end
function [ HRES ] = PhGetCineInfoLocal( CH, InfName, pInfVal)
% pInfVal is a libpointer to the desired information

[HRES, dummyAll] = calllib('phfile','PhGetCineInfo', CH, uint32(InfName), pInfVal);
OutputError(HRES);

end

%% Get information about cine
%read the saved range
pFirstIm = libpointer('int32Ptr',0);
PhGetCineInfo(cineHandle, PhFileConst.GCI_FIRSTIMAGENO, pFirstIm);
firstIm = pFirstIm.Value;
pImCount = libpointer('uint32Ptr',0);
PhGetCineInfoLocal(cineHandle, PhFileConst.GCI_IMAGECOUNT, pImCount);
lastIm = int32(double(firstIm) + double(pImCount.Value) - 1);
if (imageNo<firstIm || imageNo>lastIm)
   error(['Image number must be in saved cine range [' num2str(firstIm) ';' num2str(lastIm) ']']);
end
%get cine image buffer size
pInfVal = libpointer('uint32Ptr',0);
PhGetCineInfoLocal(cineHandle, PhFileConst.GCI_MAXIMGSIZE, pInfVal);
imgSizeInBytes = pInfVal.Value;
%The image flip for GetCineImage function is inhibated.
pInfVal = libpointer('int32Ptr',false);
PhSetCineInfo(cineHandle, PhFileConst.GCI_VFLIPVIEWACTIVE, pInfVal);
%Create the image reange to be readed
imgRange = get(libstruct('tagIMRANGE'));
%take one image at imageNo
imgRange.First = imageNo;
imgRange.Cnt = 1;

%% Read the cine image into the buffer
%The image will have image processings applied
% [HRES, unshiftedIm, imgHeader] = PhGetCineImage(cineHandle, imgRange, imgSizeInBytes);
```

```
% Nested function to prevent cineHandle copying; see top of file

[HRES, unshiftedIm, imgHeader] = PhGetCineImageLocal(cineHandle, imgRange, imgSizeInBytes);

%% Read image information from header
isColorImage = IsColorHeader(imgHeader);
is16bppImage = Is16BitHeader(imgHeader);

%% Transform 1D image pixels to 1D/3D image pixels to be used with MATLAB
if (HRES >= 0)
   [unshiftedIm] = ExtractImageMatrixFromImageBuffer(unshiftedIm, imgHeader);
   if (isColorImage)
      samplespp = 3;
   else
      samplespp = 1;
   end
   bps = GetEffectiveBitsFromIH(imgHeader);
   [matlabIm, unshiftedIm] = ConstructMatlabImage(unshiftedIm, imgHeader.biWidth,
imgHeader.biHeight, samplespp, bps);
end

%% Show image
if (showImage)
   if (isColorImage)
      figure, image(matlabIm,'CDataMapping','scaled'),colormap('default');
   else
      figure, image(matlabIm,'CDataMapping','scaled'),colormap(gray(2^8));
   end
end
end
```

A.1.2 Walk Scripts

The overall functionality of this set of scripts is described in section 3.2.7. The concept and architecture of the scripts were conceived by Jonathan Lundt, Thomas Wenisch, Grant Shoenebeck, and Akshay Rao. Early iterations of the scripts were written by Jonathan Lundt. The final versions appearing below were written by Akshay Rao.

A.1.2.1 steering.m

```
clear all
close all
clc

%% Walker

tot_violations = 0;
runs = 100;
lowest_violations = 1000;

for ii=1:runs
   % Run walk algorithm
   % Inputs:
   % x, y, z of grid
   % dxy, dz for point spacing
   % x, y, z of exclusion zone ellipse
   % timeout length
   walk = Walkerv4(10, 10, 10, 1, 2, 2.5, 2.5, 5, 20);
   completed = walk.walk_grid();
   % Check if algorithm quit early
   % (Check the Walker file to change violation threshold for quitting)
   if (~completed)
      continue;
   end
   walk.run_diagnostics();

   % Simulate the walk to ensure no errors
   simulate = Simulatorv4(10, 10, 10, 1, 2, 2.5, 2.5, 5, 20);
   [violations] = simulate.simulate(walk.get_walk());
   if (violations < lowest_violations)
      lowest_violations = violations;
      best_walk = walk.get_walk_with_coords();
```

```
    end
    clear walk
    clear simulate
end

close all
```

A.1.2.2 Walkerv4.m

```
classdef Walkerv4 < handle
    properties
        % Matrix of "point" objects
        grid

        % Stores INDEXES to the corresponding point in grid
        walk

        % Current point within a walk
        walk_i

        % Exclusion zones
        ez

        % Number of forced violations during a walk
        violations

        % EZ timeout
        timeout

        num_excluded_each_i
        violations_vec
        curr_excluded

        % Number of times a certain stage of "swap_point" fails
        stage_1_fails
        stage_2_fails
        stage_3_fails
        stage_4_fails
        stage_5_fails

        % Matrix of swapped point pairs
        swap_locs
    end

    methods
```

```
%% Constructor %%
% Generates grid of points
function obj = Walkerv4(x_dim, y_dim, z_dim, dxy, dz, ez_x, ez_y, ez_z, timeout_in)
  if nargin > 0
    % INPUT:
    % grid dimensions
    % dxy = x-y center-center spacing
    % dz = z-z plane-plane spacing
    % ez dimensions
    % timeout length
    g = 1;
    f = 1;

    % Preallocate arrays
    x_c = zeros(x_dim, y_dim, z_dim, 'single');
    y_c = zeros(x_dim, y_dim, z_dim, 'single');
    z_c = zeros(x_dim, y_dim, z_dim, 'single');

    % Find x, y, z points that follow spacing pattern
    for kk = 1:z_dim
      g = ~g;
      f = 1;
      for jj = 1:y_dim
        f = ~f;
        for ii = 1:x_dim
          x_c(ii, jj, kk) = dxy*(ii-1+f/2+g/2);
          y_c(ii, jj, kk) = dxy*(cos(pi/6)*(jj-1)+g*tan(pi/6)/2);
          z_c(ii, jj, kk) = dz*sqrt(2/3)*(kk-1);
        end
      end
    end

    % Reshape
    x_c_r = reshape(x_c, [], 1);
    y_c_r = reshape(y_c, [], 1);
    z_c_r = reshape(z_c, [], 1);
    clear x_c;
    clear y_c;
    clear z_c;

    % Center around origin by subtracting mean
    x_center = x_c_r - mean(x_c_r);
    y_center = y_c_r - mean(y_c_r);
    z_center = z_c_r - mean(z_c_r);
    clear x_c_r;
    clear y_c_r;
    clear z_c_r;

    mat_grid = [x_center, y_center, z_center];

    % Add indexes and randomize
```

```
        indexes = (1:size(mat_grid, 1))';
        mat_grid = [indexes mat_grid];
        master = mat_grid(randperm(size(mat_grid, 1)), :);
        clear indexes;
        clear mat_grid;

        % Define exclusion zones and distance matrix
        for ii=1 : size(master, 1)
            % Iterate through each point, and test if every other point
            % is inside or on the ellipse
            % Satisfies (x-xo)^2 / (a^2) + (y-y0)^2 / (b^2) + (z - z0) / (c^2) <= 1
            vecs = sum( (((master(:, 2:4) - master(ii, 2:4)).^2) ./ ([ez_x ez_y ez_z]).^2), 2 );

            % If vec <=1, add to exclusion zone (unless it's the point in question)
            indexes = find(vecs <= 1);
            indexes( indexes(:) == ii, :) = [];
            obj.ez{ii} = indexes;
        end

        % Convert to Point objects
        for point = 1 : size(master(:, 1))
            new_point = Point;
            new_point.coord = [master(point, 2:4)];
            new_point.index = master(point, 1);
            new_point.timer = timeout_in;
            new_point.status = 'u';
            new_point.dist = sqrt(sum(((master(:, 2:4) - master(point, 2:4)).^2), 2));
            new_point.dist_sum = sum( new_point.dist );
            obj.grid = [obj.grid; new_point];
        end

        obj.timeout = timeout_in;
        obj.violations = 0;
        obj.num_excluded_each_i = [];
        obj.violations_vec = [];

        obj.walk_i = 1;

        obj.stage_1_fails = 0;
        obj.stage_2_fails = 0;
        obj.stage_3_fails = 0;
        obj.stage_4_fails = 0;
        obj.stage_5_fails = 0;

        obj.swap_locs = [];
        obj.curr_excluded = [];
    end
end

%% walk_grid %%
% Runs main walk algorithm
```

```
    function [finished] = walk_grid(this)
%         figure
%         hold on;
%         for ii=1 : size(this.grid)
%           scatter3(this.grid(ii,1).coord(1,1), this.grid(ii,1).coord(1,2),
this.grid(ii,1).coord(1,3),'MarkerFaceColor','b');
%         end

        for ii=1 : size(this.grid, 1)
          % Retrieve next point
          [curr_point_index, violation] = get_next_point_min_dist(this);

%           % Plot point
%           point = this.grid(curr_point_index);
%           scatter3(point.coord(1,1), point.coord(1,2), point.coord(1,3),'MarkerFaceColor','r');
%           set(gca,'XLim',[-7 7],'YLim',[-7 7],'ZLim',[-7 7]);

          % Check for forced violation
          if (violation)
            this.violations = this.violations + 1;

            % Abort walk if above some violations threshold
            if (this.violations >= 0)
              disp(['Walk aborted at ' num2str(ii)]);
              finished = false;
              return;
            end

          end
          this.violations_vec = [this.violations_vec this.violations];

          % Add to walk
          this.grid(curr_point_index).status = 'v';
          this.walk = [this.walk; curr_point_index];

          % Subtract distance from other points
          for p = 1 : size(this.grid(:, 1))
            this.grid(p).dist_sum = this.grid(p).dist_sum - this.grid(p).dist(curr_point_index);
          end

          % Retrieve EZ
          curr_ez = this.ez{curr_point_index};

          % Change points in curr_point's EZ to excluded
          for p = 1 : size(curr_ez(:, 1))
            % If point has already been excluded, increase time accordingly
            % Ignore if already visited
            % scatter3(this.grid( curr_ez(p) ).coord(1,1), this.grid( curr_ez(p) ).coord(1,2),
this.grid( curr_ez(p) ).coord(1,3),'MarkerFaceColor','r');
            if (this.grid( curr_ez(p) ).status == 'e')
              this.grid( curr_ez(p) ).timer = this.timeout;
```

```
            this.grid( curr_ez(p) ).excluded_by = curr_point_index;
        elseif (this.grid( curr_ez(p) ).status == 'u')
            this.grid( curr_ez(p) ).status = 'e';
            this.grid( curr_ez(p) ).excluded_by = curr_point_index;
        end
    end

    % If walk_i is >= 980, check if any remaining points are
    % within their exclusion zones, and mark them excluded
    if (this.walk_i >= (1000 - (this.timeout - 1)))
        beginning_p_i = this.walk(this.walk_i - (1000 - this.timeout));
        beginning_p_ez = this.ez{beginning_p_i};

        for jj=1:size(beginning_p_ez)
            if (this.grid( beginning_p_ez(jj) ).status ~= 'v')
                this.grid( beginning_p_ez(jj) ).timer = this.timeout;
                this.grid( beginning_p_ez(jj) ).status = 'e';
                this.grid( beginning_p_ez(jj) ).excluded_by = beginning_p_i;
            end
        end
    end

    % Decrement timers and update curr_excluded
    this.curr_excluded = [];
    [curr_num_excluded] = decrement_timers(this, 1);
    this.num_excluded_each_i = [this.num_excluded_each_i curr_num_excluded];

    this.walk_i = this.walk_i + 1;

  end
  finished = true;
end

%% get_next_point %%
% Finds the next valid point to add to the walk
% Point is valid if its status is unvisited ('u')
% If no valid point is found, will call "swap_point()"
% If no possible swap is found, will call "free_point()"
% If "free_point" is called, return violation as true
function [point_index, violation] = get_next_point(this)

  for p=1 : size(this.grid(:, 1))
    if (this.grid(p).status == 'u')

      point_index = p;
      violation = false;
      return;
    end
  end

  % No non-excluded points are found
```

```
      % First attempt to swap points
      for p=1 : size(this.curr_excluded)
        % Don't swap with any of the first 20 points
        % (Makes following EZ rules easier between cycles)
        for q=21 : size(this.walk)
          [point_swapped, point] = swap_point(this, p, q);
          if (point_swapped)
            point_index = point;
            violation = false;
            return;
%             for p=1 : size(this.grid(:, 1))
%               if (this.grid(p).status == 'u')
%                 point_index = p;
%                 violation = false;
%                 return;
%               end
%             end
%
%             disp('ERROR');
          end
        end
      end

      % Can't swap: must free point from EZ
      [point_index, violation] = free_point(this);
      return;

    end

    %% get_next_point_min_dist %%

    function [point_index, violation] = get_next_point_min_dist(this)

      % Find unvisited point with smallest distance to other points
      min_point_index = -1;
      min_dist = Inf(1);
      for p=1 : size(this.grid(:, 1))
        if (this.grid(p).status == 'u')
          if (this.grid(p).dist_sum < min_dist)
            min_dist = this.grid(p).dist_sum;
            min_point_index = p;
          end
        end
      end

      % Find element that maximizes distances between other points
      if (min_point_index ~= -1)
        point_index = min_point_index;
        violation = false;
        return;
```

```
  else
    % No non-excluded points are found

    % First attempt to swap points
    for p=1 : size(this.curr_excluded)
      % Don't swap with any of the first 20 points
      % (Makes following EZ rules easier between cycles)
      for q=21 : size(this.walk)
        [point_swapped, point] = swap_point(this, p, q);
        if (point_swapped)
          point_index = point;
          violation = false;
          return;
        end
      end
    end

    % Can't swap: must free point from EZ
    [point_index, violation] = free_point(this);
    return;
  end
end

%% swap_point %%
% Swaps a currently excluded point P with a previously walked
% point Q
% Swap must be Legal
% Legal:
%   - (1) P cannot be excluded where Q is; that is, cannot be
%       in an EZ between [Q - timeout, Q]
%   - (2) Q cannot be excluded where P is; that is, cannot be in an
%       EZ between [walk_i - timeout, walk_i]
%   - (3) P should not exclude other points ahead of Q, between [Q, Q + timeout]
%   - (4) IF Q is being swapped into the interval [end -
%       timeout, end], Q cannot exclude points at the
%       beginning of the walk (since the walk rolls over)
% Also, to increase chances of valid future points:
%   - (5) Q cannot exclude remaining unselected points
function [point_swapped, point] = swap_point(this, p, q)
  point = -1;
  % Check if this Q was swapped in previously
  % Skip if so
  if (size(this.swap_locs) ~= 0)
    x = find(this.swap_locs(:,2) == q);
    if (size(x) ~= 0)
      point_swapped = false;
      return;
    end
  end

  p_i = this.curr_excluded(p);
  q_i = this.walk(q);
```

```
% Check (1)
for q0 = q - this.timeout : q - 1
   q0_i = this.walk(q0);
   q0_ez = this.ez{q0_i};
   x = find(q0_ez == p_i);
   if (size(x) ~= 0)
      this.stage_1_fails = this.stage_1_fails + 1;
      point_swapped = false;
      return;
   end
end

% Check (5)
q_i_ez = this.ez{q_i};
for ii=1 : size(this.curr_excluded)
   % Skip current point being swapped out
   if (ii == p)
      continue;
   end
   in_ez = find(q_i_ez == this.curr_excluded(ii));
   if (size(in_ez) ~= 0)
      % Illegal: one of the remaining points will be excluded
      % by q (swap not useful)
      point_swapped = false;
      this.stage_5_fails = this.stage_5_fails + 1;
      return;
   end
end

% Check (3)
for q0 = q + 1 : min(q + this.timeout, size(this.walk))
   q0_i = this.walk(q0);
   y = find(this.ez{p_i} == q0_i);
   if (size(y) ~= 0)
      % Illegal: a point after q is excluded by p
      this.stage_3_fails = this.stage_3_fails + 1;
      point_swapped = false;
      return;
   end
end

% Check (2)
w0 = this.walk_i - (this.timeout + 1);
for ii=w0:w0+this.timeout
   w0_i = this.walk(ii);
   w0_ez = this.ez{w0_i};
   z = find(w0_ez == q_i);
   if (size(z) ~= 0)
      point_swapped = false;
      this.stage_2_fails = this.stage_2_fails + 1;
      return;
```

```
    end
  end


  % Check (4)
  if (this.walk_i >= (1000 - (this.timeout - 1)))
    q_ez = this.ez{q_i};

    for ii=1:(this.walk_i-(1000 - this.timeout))
      beginning_p = this.walk(ii);
      z = find(q_ez == beginning_p);
      if (size(z) ~= 0)
        point_swapped = false;
        this.stage_4_fails = this.stage_4_fails + 1;
        return;
      end
    end

  end

  % All conditions passed - proceed with swap
  this.walk(q) = p_i;
  this.grid(q_i).status = 'u';
  this.grid(p_i).status = 'v';

  point_swapped = true;
  point = q_i;
  this.swap_locs = [this.swap_locs; this.walk_i q];
  return;

end

%% free_point %%
% Frees a point that is currently excluded to allow the walk to continue
% Finds the point with the smallest remaining timer before non-exclusion
function [point_index, violation_after] = free_point(this)
  % Find excluded point with lowest timer, and free it
  % Also save a list of currently excluded points
  lowest_t = realmax;
  lowest_p = [];
  curr_excluded = [];
  for p=1 : size(this.grid(:, 1))
    if (this.grid(p).status == 'e')
      curr_excluded = [curr_excluded ; p];
      if (this.grid(p).timer < lowest_t)
        lowest_p = p;
        lowest_t = this.grid(p).timer;
      end
    end
  end
```

```
    point_index = lowest_p;

    % Must violate an EZ
    violation_after = true;
    return;
end

%% decrement_timers %%
% Iterates through all points and decrements timers if excluded
% Returns number of currently excluded points
function [curr_num_excluded] = decrement_timers(this, amount)
    num_excluded = 0;
    for p = 1 : size(this.grid(:, 1))
        % If point is excluded, decrement timer
        if (this.grid(p).status == 'e')

            this.grid(p).timer = this.grid(p).timer - amount;

            % If it reaches 0, change to unvisited status
            if ( this.grid(p).timer == 0)
                this.grid(p).status = 'u';
                % Reset timer
                this.grid(p).timer = this.timeout;
            else
                % Record excluded point
                num_excluded = num_excluded + 1;
                this.curr_excluded = [this.curr_excluded; p];
            end
        end
    end

    curr_num_excluded = num_excluded;
end

%% get_walk %%
% Create an array of indexes to the original, non-randomized list
% Can only be called after walk_grid
function [walk_out] = get_walk(this)
    walk_out = [];
    for ii=1:size(this.walk)
        index = this.grid(this.walk(ii)).index;
        walk_out = [walk_out; index];
    end
end

function [walk_out] = get_walk_with_coords(this)
    walk_out = [];
    for ii=1:size(this.walk)
        index = this.grid(this.walk(ii)).index;
        walk_out = [walk_out; index this.grid(this.walk(ii)).coord];
    end
```

```
    end

    function run_diagnostics(this)
      % Ensure valid walk
      uniq = unique(this.walk);
      if (size(uniq) ~= size(this.walk))
        disp('Error: duplicate points in walk');
      end

      % disp(['Walk violations: ' num2str(this.violations)]);
      figure
      subplot(2,1,1)
      plot ([1:1:1000], this.num_excluded_each_i);
      title('Number of excluded points at each iteration');
      subplot(2,1,2)
      plot ([1:1:1000], this.violations_vec);
      title('Number of accumulated violations at each iteration');
    end

    function plot_status(this)
      hold on;
      for p = 1 : size(this.grid(:, 1))
        % If point is excluded, decrement timer
        coord = this.grid(p).coord;
        if (this.grid(p).status == 'e')
          scatter3(coord(1, 1), coord(1, 2), coord(1, 3), 'MarkerEdgeColor','r');
        elseif (this.grid(p).status == 'v')
          scatter3(coord(1, 1), coord(1, 2), coord(1, 3), 'MarkerEdgeColor','g');
        elseif (this.grid(p).status == 'u')
          scatter3(coord(1, 1), coord(1, 2), coord(1, 3), 'MarkerEdgeColor','b');
        end
      end
    end
  end
end
```

A.1.2.3 Simulatorv4.m

```
classdef Simulatorv4 < handle

  %% Simulator %%
  % Takes grid parameters and walk as input, and checks for violations
  % Accounts for violations when rolling over to beginning of walk

  properties
    grid
    ez
```

```
  walk
  timeout
  tot_violations
  violation_loc
end

methods
  function obj = Simulator(x_dim, y_dim, z_dim, dxy, dz, ez_x, ez_y, ez_z, timeout_in)
    if nargin > 0
      % INPUT:
      % grid dimensions
      % dxy = x-y center-center spacing
      % dz = z-z plane-plane spacing
      % ez dimensions
      % timeout length
      g = 1;
      f = 1;

      % Preallocate arrays
      x_c = zeros(x_dim, y_dim, z_dim, 'single');
      y_c = zeros(x_dim, y_dim, z_dim, 'single');
      z_c = zeros(x_dim, y_dim, z_dim, 'single');

      % Find x, y, z points that follow spacing patter
      for kk = 1:z_dim
        g = ~g;
        f = 1;
        for jj = 1:y_dim
          f = ~f;
          for ii = 1:x_dim
            x_c(ii, jj, kk) = dxy*(ii-1+f/2+g/2);
            y_c(ii, jj, kk) = dxy*(cos(pi/6)*(jj-1)+g*tan(pi/6)/2);
            z_c(ii, jj, kk) = dz*sqrt(2/3)*(kk-1);
          end
        end
      end

      % Reshape
      x_c_r = reshape(x_c, [], 1);
      y_c_r = reshape(y_c, [], 1);
      z_c_r = reshape(z_c, [], 1);
      clear x_c;
      clear y_c;
      clear z_c;

      % Center around origin by subtracting mean
      x_center = x_c_r - mean(x_c_r);
      y_center = y_c_r - mean(y_c_r);
      z_center = z_c_r - mean(z_c_r);
      clear x_c_r;
      clear y_c_r;
      clear z_c_r;
```

```
        mat_grid = [x_center, y_center, z_center];

        % Add indexes
        indexes = (1:size(mat_grid, 1))';
        master = [indexes mat_grid];
        clear indexes;

        % Define exclusion zones
        for ii=1 : size(master, 1)
            % Iterate through each point, and test if every other point
            % is inside or on the ellipse
            % Satisfies (x-xo)^2 / (a^2) + (y-y0)^2 / (b^2) + (z - z0) / (c^2) <= 1
            vecs = sum( (((master(:, 2:4) - master(ii, 2:4)).^2) ./ ([ez_x ez_y ez_z]).^2), 2 );

            % If vec <=1, add to exclusion zone (unless it's the point in question)
            indexes = find(vecs <= 1);
            indexes( indexes(:) == ii, :) = [];
            obj.ez{ii} = indexes;
        end

        % Convert to Point objects
        for point = 1 : size(master(:, 1))
            new_point = Point;
            new_point.coord = [master(point, 2:4)];
            new_point.index = master(point, 1);
            new_point.timer = timeout_in;
            new_point.status = 'u';
            obj.grid = [obj.grid; new_point];
        end

        obj.timeout = timeout_in;
        obj.tot_violations = 0;
        obj.violation_loc = [];
    end
end

function [tot_violations] = simulate(this, walk)
    tot_ez = [];
    amount = 1;
    for ii=1:size(walk)
        curr_point_index = walk(ii);

        % Check to see if this point is in a current ez
        % If there's a violation, mark with "-1"
        in_ez = find(tot_ez == curr_point_index);
        if (size(in_ez) ~= 0)
            this.tot_violations = this.tot_violations + 1;
            this.violation_loc = [this.violation_loc; ii -1 tot_ez(in_ez(1))];
        end
```

```
this.grid(curr_point_index).status = 'v';

% Retrieve EZ
curr_ez = this.ez{curr_point_index};

% Change points in curr_point's EZ to excluded
for p = 1 : size(curr_ez(:, 1))
   % If point has already been excluded, increase time accordingly
   % Ignore if already visited
   if (this.grid( curr_ez(p) ).status == 'e')
      this.grid( curr_ez(p) ).timer = this.timeout;
   elseif (this.grid( curr_ez(p) ).status == 'u')
      this.grid( curr_ez(p) ).status = 'e';
      this.grid( curr_ez(p) ).timer = this.timeout;
   end
end

% Decrement timers
tot_ez = [];
for p = 1 : size(this.grid(:, 1))
   % If point is excluded, decrement timer
   if (this.grid(p).status == 'e')
      this.grid(p).timer = this.grid(p).timer - amount;

      % If it reaches 0, change to unvisited status
      if ( this.grid(p).timer == 0)
         this.grid(p).status = 'u';
         % Reset timer
         this.grid(p).timer = this.timeout;
      else
         % Add to curr_ez, with the point that excluded
         % it
         tot_ez = [tot_ez; p];
      end
   end
end

% Also, if ii >= 981, make sure point doesn't exclude a
% beginning point
% Mark this sort of violation with "-2"
if (ii >= (1000 - (this.timeout - 1)))
   for jj=1:(ii - (1000 - this.timeout))
      beginning_p = walk(jj);
      z = find(curr_ez == beginning_p);
      if (size(z) ~= 0)
         this.tot_violations = this.tot_violations + 1;
         this.violation_loc = [this.violation_loc; ii -2 jj];
      end
   end
end
```

```
            end
            disp(['Actual violations: ' num2str(this.tot_violations)]);
            tot_violations = this.tot_violations;
        end
    end
end
```

A.1.2.4 Point.m

```
classdef Point
    properties
        index
        coord
        status
        timer
        excluded_by
        dist
        dist_sum
    end
end
```

A.1.3 liverTxLayout.m

This script functions by segmenting the aperture into nesting arc segment-shaped elements with approximately equal aspect ratio and surface area. Arc segments are generated by dividing the aperture into concentric rings and then further dividing each ring in the azimuthal direction. Coordinates specifying elements' sizes and positions are then exported.

```
%%%%%%%%%%%%%%%%%%% DIMENSIONS FROM CAD %%%%%%%%%%%%%%%%%%%%%%%%%
R0 = 140;                       % focal length (mm)
A0 = 39921.05;                  % area in mm^2 (with hole and no radius on corner)
RmajAp = 233.68/2;              % major aperture radius of aperture
RminAp1 = 82.5;                 % minor radius of ellipse defining aperture minor radius
RminAp2 = 202.92;               % major radius of ellipse defining aperture minor radius
elMajAp = acos(RmajAp/R0);      % elevation of edge of major aperture
elMinAp = pi/2 - asin(RminAp1/R0);  % elevation of edge of minor aperture
rc = 26;                        % radius of center element or hole

[V ~] = SpiralSampleSphereCap(1e5,elMajAp);
V=V*R0;                                 % scale sphere
V(find(V(:,1).^2/RminAp2^2 + V(:,2).^2/RminAp1^2>1),:)=[];  % trim to make define minor aperture
[AZ,EL,R] = cart2sph(V(:,1),V(:,2),V(:,3)); AZ=AZ+pi;   % convert to spherical coords and set az range 0-2pi

% %confirm aperture
% figure
% scatter3(V(:,1),V(:,2),V(:,3),'r.'); hold on
% txSurf = stlread('C:\Users\labuser\Documents\SolidWorks Local\Liver
Transducer\liverArray_FL12_rev00.stl');
% x=txSurf.vertices(:,1); y=txSurf.vertices(:,3); z=txSurf.vertices(:,2);
% V = [x y z];
% [AZ,EL,R] = cart2sph(V(:,1),V(:,2),V(:,3));
% % scatter3(V(:,1),V(:,2),V(:,3),'b.');
% axis equal
% xlabel('X'); ylabel('Y'); zlabel('Z')
% hold on
% [X,Y,Z] = sphere(200);
% % surf(R0*X,R0*Y,R0*Z)
% set(gcf, 'position', [1        41       1920       1083])
```

```
%%
% set element parameters
ael = 100;          % target area for individual element (mm^2)
N = round(A0/ael);          % total number of elements
lel = sqrt(ael);       % target element side length (mm)

% create center element
% rc = sqrt(ael/pi);         % radius of center element or hole

el0 = pi/2-asin(rc/R0);     % elevation of perimeter of center element

% force one of the elevation rings to line up with the minor aperture edge
A_in = pi*RminAp1^2;          % area of inner aperture
A_out = A0-A_in;              % area of outer aperture
N_in = round(A_in/A0*(N-1));       % number of elements in inner aperture
N_out = round(A_out/A0*(N-1));     % number of elements in outer aperture

% establish elevations for inner aperture
P0_in = el0-elMinAp;                    % angle spanning minor aperture to center element edge
nel_in = round(P0_in*R0/lel);               % number of elevations in inner aperture
del_in = P0_in/nel_in;                  % angle step size
elCent_in = elMinAp+del_in/2:del_in:el0;       % vector of elevation centers
elVec_in = elMinAp:del_in:el0;              % edges of element elevations

% establish elevations for outer aperture
P0_out = elMinAp-elMajAp;                   % angle spanning major to minor aperture edges
nel_out = round(P0_out*R0/lel);             % number of elevations in outer aperture
del_out = P0_out/nel_out;                   % angle step size
elCent_out = elMajAp+del_out/2:del_out:elMinAp; % element centers
elVec_out = elMajAp:del_out:elMinAp;

elCent = [elCent_out elCent_in];
elVec = [elVec_out elVec_in(2:end)];

% find the number of azimuth divisions for each elevation
rElCent = R0*cos(elCent);         % radius at each elevation
rElEdge = R0*cos(elVec);
nazDiv = round(2*pi*rElCent/lel);   % vector of azimuthal divisions

% set the phase of azimuthal divisions to start at the minor aperture edge
t=-pi/2:0.001:0;
x=RminAp2*cos(t);
y=RminAp1*sin(t);
rElp = sqrt(x.^2+y.^2);
for ii=1:nel_out
   [val idx] = min(abs(rElp-rElEdge(ii)));
   az0(ii) = atan(y(idx)/x(idx));
end
az00 = [az0+2*pi zeros(1,nel_in)];

% % check az0 positions
```

```
% plot3(x,y,zeros(size(x))); hold on
% for ii=1:nel_out
%     x=rElEdge(ii)*cos(t);
%     y=rElEdge(ii)*sin(t);
%     plot3(x,y,zeros(size(x)))
% end
% [xa,ya,za] = sph2cart(az0,elVec(1:nel_out),R0*ones(1,nel_out));
% scatter3(xa,ya,za,'k'); hold on

cnt=1;
for elNum=1:length(elCent)
   colors = distinguishable_colors(nazDiv(elNum));
   colors = colors(randperm(size(colors,1)),:);
   for azNum=1:nazDiv(elNum)
      %specify sector to isolate
      azmin = (azNum-1)*2*pi/nazDiv(elNum)+az00(elNum);
      azmax = azNum*2*pi/nazDiv(elNum)+az00(elNum);
      if az00(elNum)~=0
         if azmin>2*pi
            azmin=azmin-2*pi;
         end
         if azmax>2*pi
            azmax=azmax-2*pi;
         end
      end
      elmin = elVec(elNum);
      elmax = elVec(elNum+1);

      %isolate sector
      az=AZ; el=EL; r=R;              % establish temporary coords
      if azmin>azmax
         az(az<azmin & az>azmax)=NaN;    %for sectors straddling az=0,2pi
      else
         az(az<azmin | az>azmax)=NaN;
      end
      el(el<elmin | el>elmax)=NaN;

      %convert back to cartesion coords and plot
      [X,Y,Z] = sph2cart(az,el,r);
%       scatter3(X,Y,Z,'.','filled','MarkerEdgeColor',colors(ii,:)); hold on

      %reduce the size of the meshes by deleting NaNs
      sphMesh = [az,el,r];
      sphMesh(any(isnan(sphMesh),2),:)=[];
      cartMesh = [X,Y,Z];
      cartMesh(any(isnan(cartMesh),2),:)=[];

      % store sectors in a structure
      SS1(cnt).coords =  [azmin azmax elmin elmax];   % SS for sector structure
      SS1(cnt).sphMesh =  sphMesh;
      SS1(cnt).cartMesh =  cartMesh;
      SS1(cnt).azNum = azNum;
```

```
        SS1(cnt).elNum = elNum;
        cnt=cnt+1;
        SS2(elNum,azNum).coords =  [azmin azmax elmin elmax];
        SS2(elNum,azNum).sphMesh =  sphMesh;
        SS2(elNum,azNum).cartMesh =  cartMesh;

        % store data from first sector from each elevation
        if azNum==1
            azMat(elNum,:) = [azmin azmax];
            perims(elNum,:) = (rElEdge(elNum)+rElEdge(elNum+1))*(azmax-azmin)+2*R0*(elmax-elmin);
        end
    end
end
% size(sectStruct)
%%
%%%%%%%%%%%%%%%%%%  DELETE -X OUTER APERTURE
%%%%%%%%%%%%%%%%%%%%%%%%%%%%%%%%
ii=1;
while ii<=length(SS1)
    if SS1(ii).coords(3)<elVec_out(end) && (SS1(ii).coords(1)>pi/2 && SS1(ii).coords(1)<3*pi/2)
        SS1(ii) = [];
        ii=ii-1;
    end
    ii=ii+1;
end
% size(sectStruct)
%%

%%%%%%  REBUILD THE -X OUTER APERTURE AS A MIRROR OF +X  %%%%%%%%%%%%%%%%%%
cntr=length(SS1)+1;
for ii=1:length(SS1)
    if SS1(ii).coords(3)<elVec_out(end) &&...
        (SS1(ii).coords(1)<pi/2 || SS1(ii).coords(1)>3*pi/2 ||...
        SS1(ii).coords(2)<pi/2 || SS1(ii).coords(2)>3*pi/2)
        %mirror the cartesian mesh about y and write a new struct element
        X1 = -SS1(ii).cartMesh(:,1);
        Y1 = SS1(ii).cartMesh(:,2);
        Z1 = SS1(ii).cartMesh(:,3);
        SS1(cntr).cartMesh = [X1,Y1,Z1];
        %convert sphere coords to cart, mirror, and convert back
        azmin0 = SS1(ii).coords(1);
        azmax0 = SS1(ii).coords(2);
        elmin0 = SS1(ii).coords(3);
        elmax0 = SS1(ii).coords(4);
        [xmin,ymin,zmin] = sph2cart(azmin0,elmin0,R0);
        [xmax,ymax,zmax] = sph2cart(azmax0,elmax0,R0);
        [azmin1,elmin1,r] = cart2sph(-xmin,ymin,zmin);
        [azmax1,elmax1,r] = cart2sph(-xmax,ymax,zmax);
        SS1(cntr).coords = [azmin1 azmax1 elmin1 elmax1];
        SS1(cntr).elNum = SS1(ii).elNum;
        [AZ1, EL1, R1] = cart2sph(X1,Y1,Z1);
        SS1(cntr).sphMesh = [AZ1, EL1, R1];
```

```
      cntr=cntr+1;
   end
end
% size(sectStruct)

%%
%%%%%%%%%% CREATE STRUCT THAT INCLUDES ONLY >83% COMPLETE ELEMENTS
%%%%%%%%%%%%%
for ii=1:length(SS1)
   numPt(ii) = size(SS1(ii).sphMesh,1);    % number of mesh points in each sector
end
%    figure
%    scatter(1:length(numPt), numPt/max(numPt))
%    grid on
%    ylim([.8 1])

cnt=1;
for ii=1:length(SS1)
   if SS1(ii).elNum <= nel_out && size(SS1(ii).sphMesh,1)<.83*max(numPt)
      idxPart(cnt)=ii;
      cnt=cnt+1;
   end
end
SS3 = SS1;
SS3(idxPart)=[];
disp([num2str(size(SS3,2)+1) ' elements in final aperture'])
disp([num2str(length(elCent)) ' elevation rings'])

%%
%%%%%%%%%%%%%  MEASURE DIMENSIONS OF ELEMENTS BY ELEVATION
%%%%%%%%%%%%%%%%%%%%%%
% http://mathworld.wolfram.com/Zone.html
clear elArea
for ii=1:length(elCent)
   elAreaByEl(ii) = 2*pi*R0^2*(sin(SS2(ii,1).coords(4))-sin(SS2(ii,1).coords(3)))*...
      (SS2(ii,1).coords(2)-SS2(ii,1).coords(1))/(2*pi);
   W(ii) = (SS2(ii,1).coords(2)-SS2(ii,1).coords(1))*R0*sin(pi/2-elCent(ii));
   H(ii) = (SS2(ii,1).coords(4)-SS2(ii,1).coords(3))*R0;
   WH(ii) = W(ii)*H(ii);
end
% figure
% plot(elArea); hold on; plot(ael*ones(length(elArea))); hold off

%%
%%%%%%%%%%%%%%%%%%%%%  Count elements at each elevation %%%%%%%%%%%%%%%%%%%
for jj=1:size(SS3,2)
   elAzMat(jj,:) = [SS3(jj).elNum SS3(jj).azNum]; % [ring number, element number or index]
end

for ii=1:length(elCent)
   N_elEl(ii,:) = numel(find(elAzMat(:,1)==ii));    % number of elements at a given elevation
end
```

```
%%
%%%%%%%%%%%%%%%%%% ELEMENT AREA AND POSITIONS %%%%%%%%%%%%%%%%%%%%%%
% vector of all element areas
elArea0 = [];
for ii=1:length(N_elEl)
   elArea0 = [elArea0; elAreaByEl(ii)*ones(N_elEl(ii),1)]; % area of the first element from each elevation
end
elArea0(end+1) = ael;

% azimuthal positions for first elements at each elevation
azCent = (azMat(:,2)-azMat(:,1))/2+azMat(:,1);
azSpan = azMat(:,2)-azMat(:,1);

% all element centers
cnt=1;
for ring=1:length(N_elEl)
   % stop making element centers when you get to the edge of the outer
   % aperture
   if ring<=nel_out
      nr = N_elEl(ring)/2; % outer aperture
   else
      nr = N_elEl(ring);  % inner aperture
   end
   % create center positions
   for jj=1:nr
      elCentSph(cnt,:) = [azCent(ring)+azSpan(ring)*(jj-1) elCent(ring) R0];
      cnt=cnt+1;
   end
   % once the outer aperture is constructed, mirror it
   if ring==nel_out
      cnt=cnt+length(elCentSph);
      [xt, yt, zt] = sph2cart(elCentSph(:,1), elCentSph(:,2), elCentSph(:,3));
      [azt, elt, rt] = cart2sph(-xt, yt, zt); % mirror outer aperture
      elCentSph = [elCentSph; [azt, elt, rt]];
   end
end
% elCentSph(cnt,:) = [0 pi/2 R0];      % add center element position
[elCentCart(:,1), elCentCart(:,2), elCentCart(:,3)] = sph2cart(elCentSph(:,1),elCentSph(:,2),elCentSph(:,3));

% generate a table of dimensions and positions of the first element from each elevation
delta_az = azMat(:,2)-azMat(:,1);
colNames = {'Ring','ElCount','ElArea','ElPerim','elMin','elCent','elMax','azMin','azCent','azMax','delta_az'};
elementDataRad = [flipud((1:length(elCent))'),N_elEl,elAreaByEl',perims,elVec(1:end-1)',elCent',...
   elVec(2:end)', azMat(:,1),azCent, azMat(:,2), delta_az];
Trad = array2table(elementDataRad,'VariableNames',colNames);
elementDataDeg = [elementDataRad(:,1:4) rad2deg(elementDataRad(:,5:end))];
Tdeg = array2table(flipud(elementDataDeg),'VariableNames',colNames)

%%
%%%%%%%%%%%%%%%%%% PLOT
%%%%%%%%%%%%%%%%%%%%%%%%%%%%%%%%%%%%%%%%%%%%%%%%%%%%%%%%%%%%%%%%%%%%
```

```
clf
% % center element
% az=AZ; el=EL; r=R;
% el(el<el0)=NaN;
% el(el>pi/2)=NaN;
% [X,Y,Z] = sph2cart(az,el,r);
% scatter3(X,Y,Z,'.','filled','MarkerEdgeColor','k');
hold on

% the rest
sectors = SS3;
colors = distinguishable_colors(length(sectors));
for ii=1:length(sectors)
   if isempty(sectors(ii).sphMesh)==0
      az=sectors(ii).sphMesh(:,1); el=sectors(ii).sphMesh(:,2); r=sectors(ii).sphMesh(:,3);
      [X,Y,Z] = sph2cart(az,el,r);
      scatter3(X,Y,Z,'.','filled','MarkerEdgeColor',colors(ii,:)); hold on
   end
end

% element center positions
scatter3(elCentCart(:,1), elCentCart(:,2), elCentCart(:,3),'filled')

axis equal
xlabel('X'); ylabel('Y'); zlabel('Z')
view([0   90])
set(gcf, 'position', [1        41       1920       1083])
grid on

%%
% save sector structure data
% save('FL120elementData_20171219.mat','elCentCart','elementDataRad','elementDataDeg',...
%    'Trad','Tdeg','R0','elCentSph','elCentCart','elArea0')

% export element center positions
fileID = fopen('elCenters_20180709.txt','w');
fprintf(fileID,'%6s %12s\n','x','exp(x)');
fprintf(fileID,'%6.2f %12.8f\n',elCentCart);
fclose(fileID);
```

A.1.4 liverArray_FOCUS.m

This script simulates the electronic focal steering (EFS) range of the apertures defined by *liverTxLayout.m* by integrating functionality from FOCUS software. It loads the element-position data for a given aperture configuration and supplies these data to the *get_circ* function in FOCUS which generated a circular FOCUS transducer for each array element with a radius derived from the area of the input element.

```
cd(main)
matDir = dir('*.mat');

fvec = 1:30;
cnt =1;
for md=fvec
   clearvars -except matDir main md elCountTotal dec md1 cnt fvec
   cd(main)

   addpath(genpath('C:\Users\labuser\Box Sync\BoxMATLAB\downloaded_scripts'))
   addpath(genpath('C:\Users\labuser\Box Sync\BoxMATLAB\FOCUS'))
   fname = matDir(md).name;
   load(fname)

   fs=25;
   colors = distinguishable_colors(length(fvec));

   % Establish transducer
   ii=1;
   elCentCartm = elCentCart/1000; %convert to meters
   nelements = length(elCentCart);
%    eeGap =
   for ii=1:nelements
      elRad = sqrt(elArea0(ii)/1000^2/pi);
      euler = [3*pi/2-elCentSph(ii,2), 0, elCentSph(ii,1)];
      transducer(ii) = get_circ(elRad, elCentCartm(ii,:), euler);
   end

   % % check element layout and euler angles
   % draw_array(transducer)
   % axis equal
   % set(gcf, 'position', [1        41       1920       1083])
   % xlabel('X'); ylabel('Y'); zlabel('Z')
```

```
% Pressure scaling factor
eeGap = .5e-3;   % edge-edge gap between ceramic elements (includes housing); units in meters
elCountVec = elementDataRad(:,2);
elArea = elementDataRad(:,3)/10^6;  % units of m^2
elPerim = elementDataRad(:,4)/10^3; % units of m
Area_fullAperture = sum(elArea.*elCountVec);
Area_withGaps = Area_fullAperture-eeGap/2*sum(elPerim.*elCountVec);
PscaleGap = Area_withGaps/Area_fullAperture;
elCountTotal(cnt) = sum(elCountVec)+1;     % total number of elements in the array

f0 = 750e3;
sos = 1490;
lambda = sos/f0;
win = 80e-3;
d = lambda/10;
ds = round(d/5,ceil(log10(1/lambda))+2)*5; %round to the nearest decimal with a 5
delta = [ds ds ds];
medium = set_medium('lossless');
ndiv = 10;
dflag = 1;

figure(1)
%%%%%%%%%%% MAXIMUM STEERING PRESSURE ALONG X %%%%%%%%%%%%%%%%%%
x = -win:ds:win;
coord_grid = set_coordinate_grid(delta, x(1), x(end), 0, 0, 0, 0);
for elNum = 1:nelements
   px(:,:,elNum) = abs(cw_pressure(transducer(elNum), coord_grid, medium, ndiv, f0));
end
pxsum = squeeze(sum(px,3));
pxmax = max(pxsum(:));
pxnorm = pxsum/pxmax; %normalized pressure
pxnorm2 = PscaleGap*pxnorm;
figure(1); set(gcf, 'position', [1        41       1920       1083])
plot(x*1000,pxnorm2,'color',colors(cnt,:),'linewidth',5)
xlabel('Steering Position along X (mm)'); ylabel('Normalized P-');
title('Maximum Achievable P- for EFS Along Y=Z=0')
grid on; hold on; set(gca,'fontsize',fs); set(gca,'fontweight','bold')
ylim([0 1]); xlim([-60 60])

figure(2)
%%%%%%%%%%% MAXIMUM STEERING PRESSURE ALONG Y %%%%%%%%%%%%%%%%%%
y = -win:ds:win;
coord_grid = set_coordinate_grid(delta,0,0,y(1),y(end),0,0);
for elNum = 1:nelements
   py(:,:,elNum) = abs(cw_pressure(transducer(elNum), coord_grid, medium, ndiv, f0));
end
pysum = squeeze(sum(py,3));
pymax = max(pysum(:));
pynorm = pysum/pymax; %normalized pressure
pynorm2 = PscaleGap*pynorm;
figure(2); set(gcf, 'position', [1        41       1920       1083])
```

```
    plot(y*1000,pynorm2,'color',colors(cnt,:),'linewidth',5)
    xlabel('EFS Position along Y (mm)'); ylabel('Maximum Achievable P- (Normalized)');
    title('EFS Range and Element-Count')
    grid on; hold on; set(gca,'fontsize',fs); set(gca,'fontweight','bold')
    ylim([0 1]); xlim([-35 35])

    figure(3)
    %%%%%%%%%%%% MAXIMUM STEERING PRESSURE ALONG Z %%%%%%%%%%%%%%%%%%
    z = -win:ds:win;
    coord_grid = set_coordinate_grid(delta,0,0,0,0,z(1),z(end));
    for elNum = 1:nelements
       pz(:,:,elNum) = abs(cw_pressure(transducer(elNum), coord_grid, medium, ndiv, f0));
    end
    pzsum = squeeze(sum(pz,3));
    pzmax = max(pzsum(:));
    pznorm = pzsum/pzmax; %normalized pressure
    figure(3); set(gcf, 'position', [1        41       1920       1083])
    plot(z*1000,pznorm)
    xlabel('Steering Pos. along z (mm)'); ylabel('Normalized P-');
    title('Maximum Achievable P- for EFS Along X=Y=0')
    grid on; hold on; set(gca,'fontsize',fs)

    cnt = cnt+1;
end
```

A.2 Selected Technical Drawings

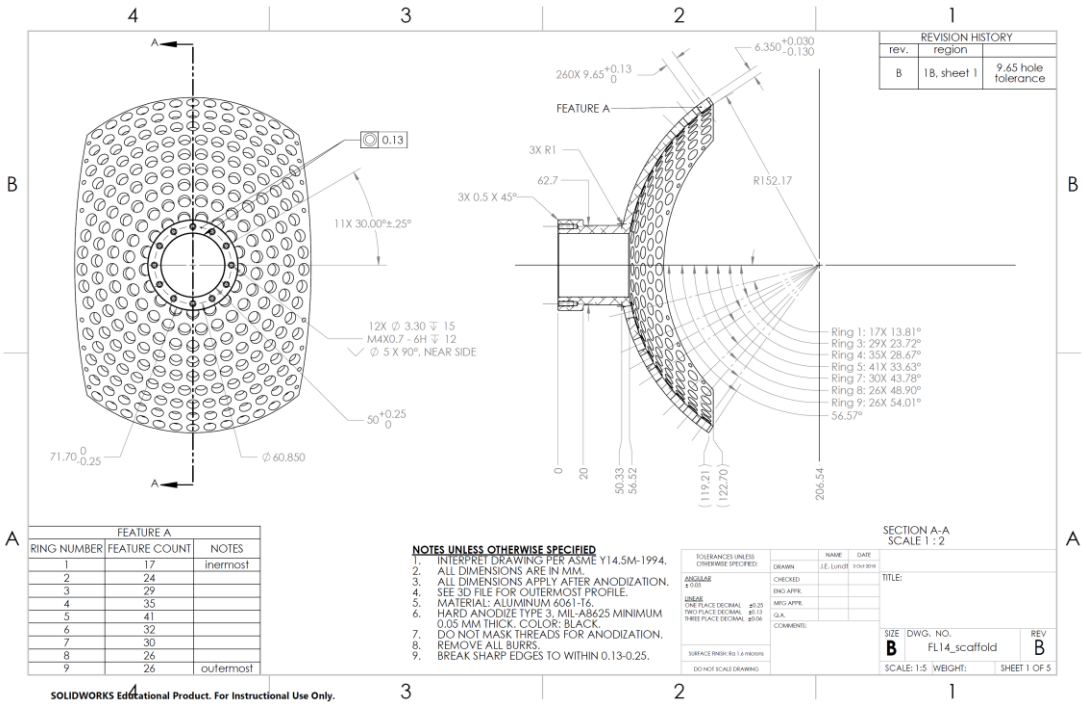

Figure A.2.1. 1. Technical drawing of liver array scaffold. Sheet 1 of 5.

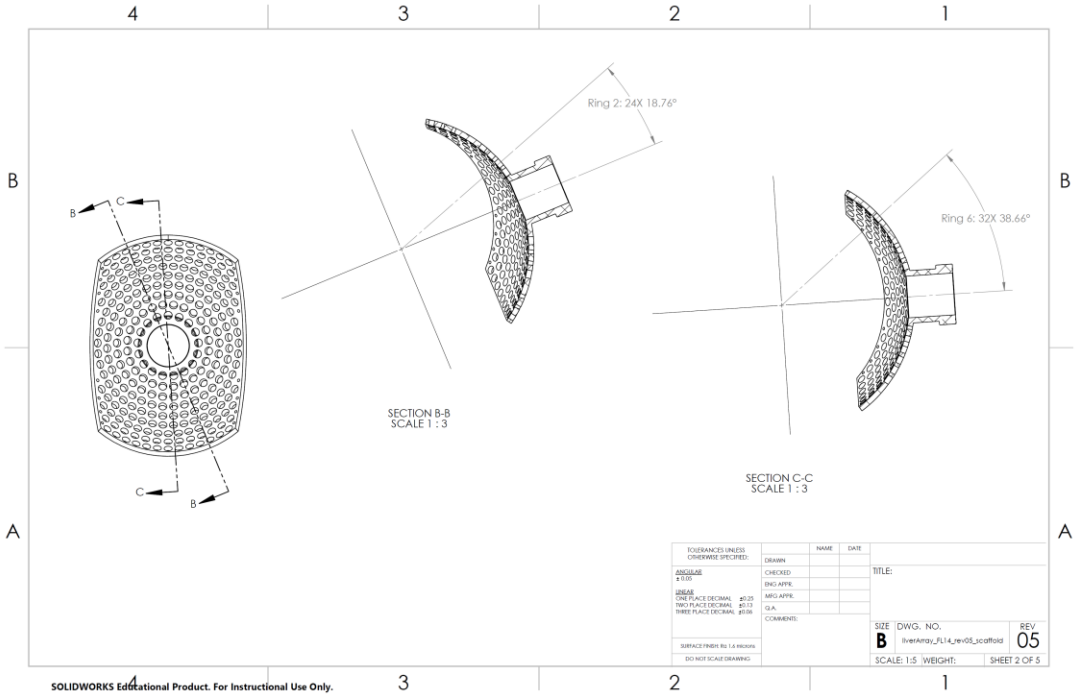

Figure A.2.1. 2. Technical drawing of liver array scaffold. Sheet 2 of 5.

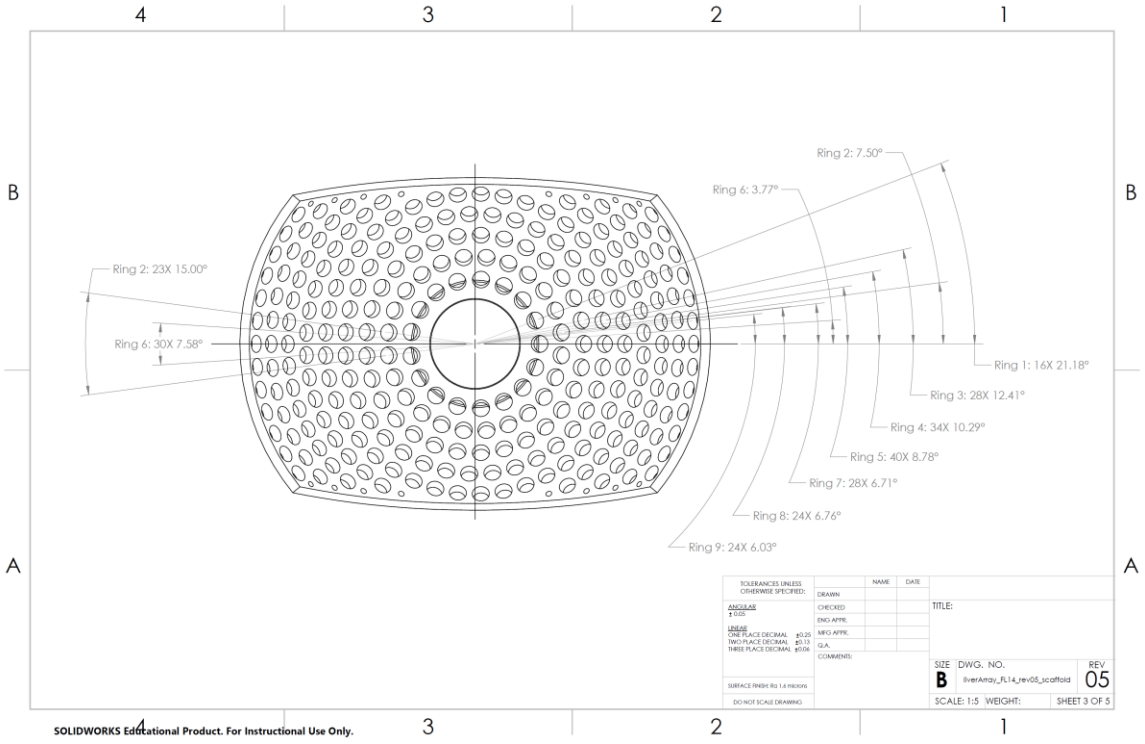

Figure A.2.1. 3. Technical drawing of liver array scaffold. Sheet 3 of 5.

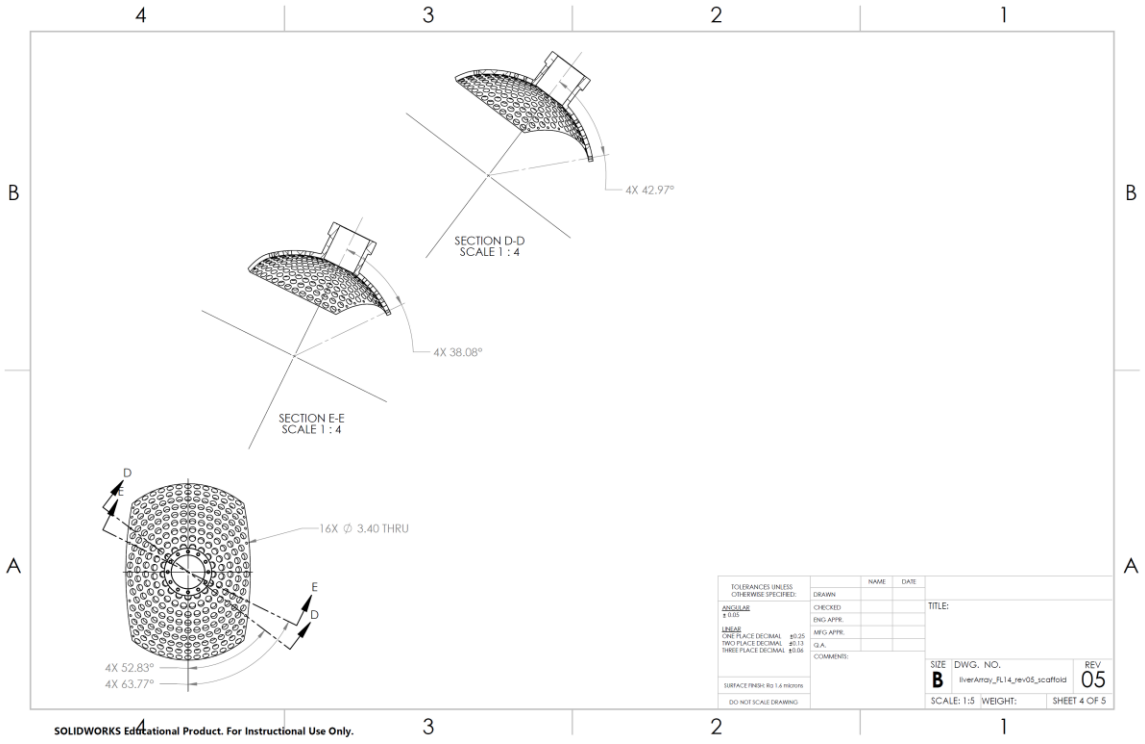

Figure A.2.1. 4. Technical drawing of liver array scaffold. Sheet 4 of 5.

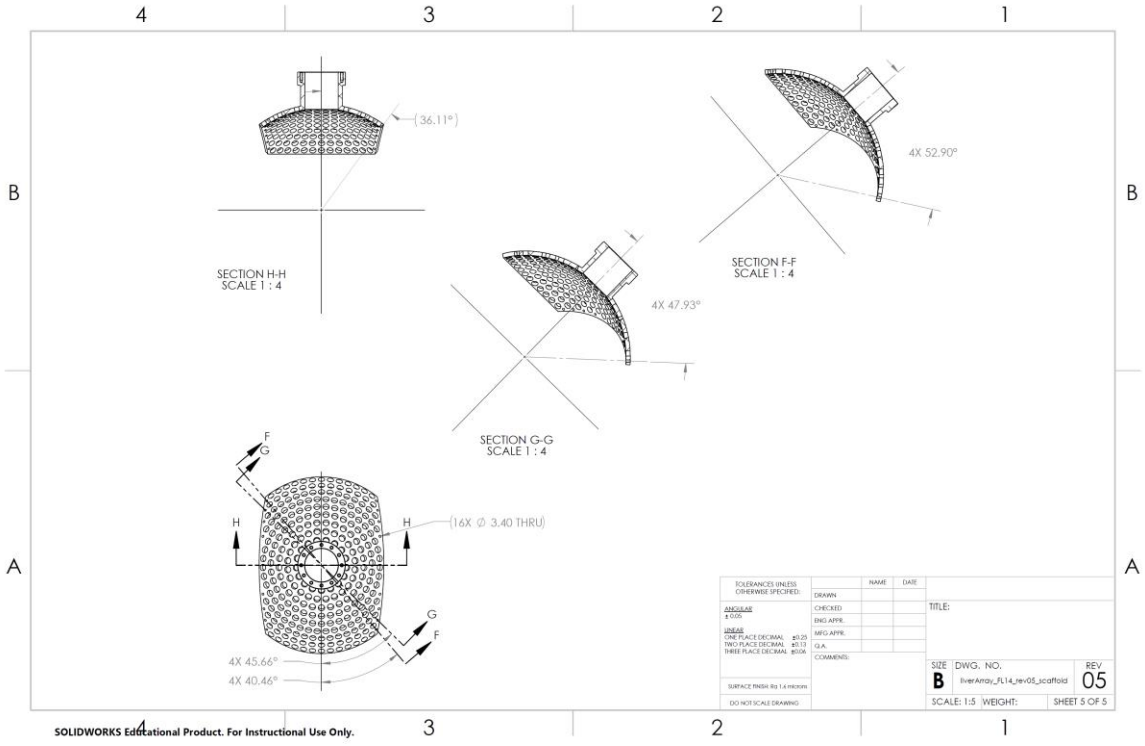

Figure A.2.1. 5. Technical drawing of liver array scaffold. Sheet 4 of 5.

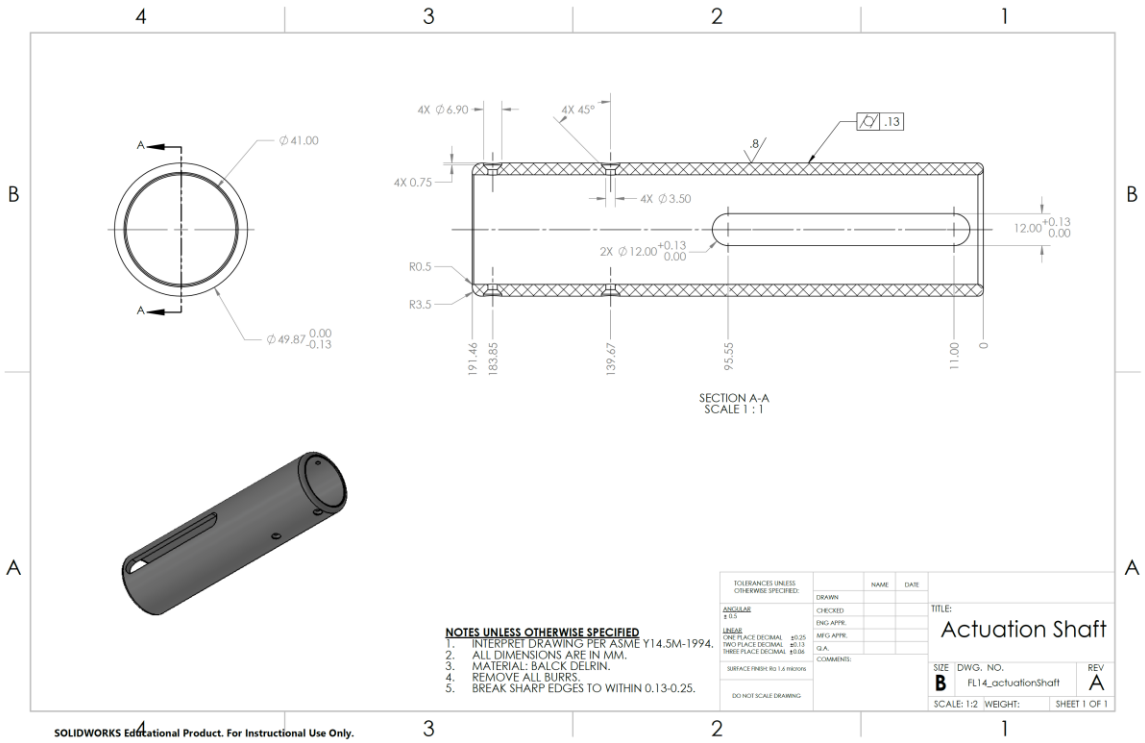

Figure A.2.1. 6. Technical drawing of imaging probe actuation shaft for liver array. Mates with the imaging probe via a 3D printed adapter which is then affixed to this part with flat-head fasteners. 3D geometry of the imaging probe was supplied by the manufacturer.

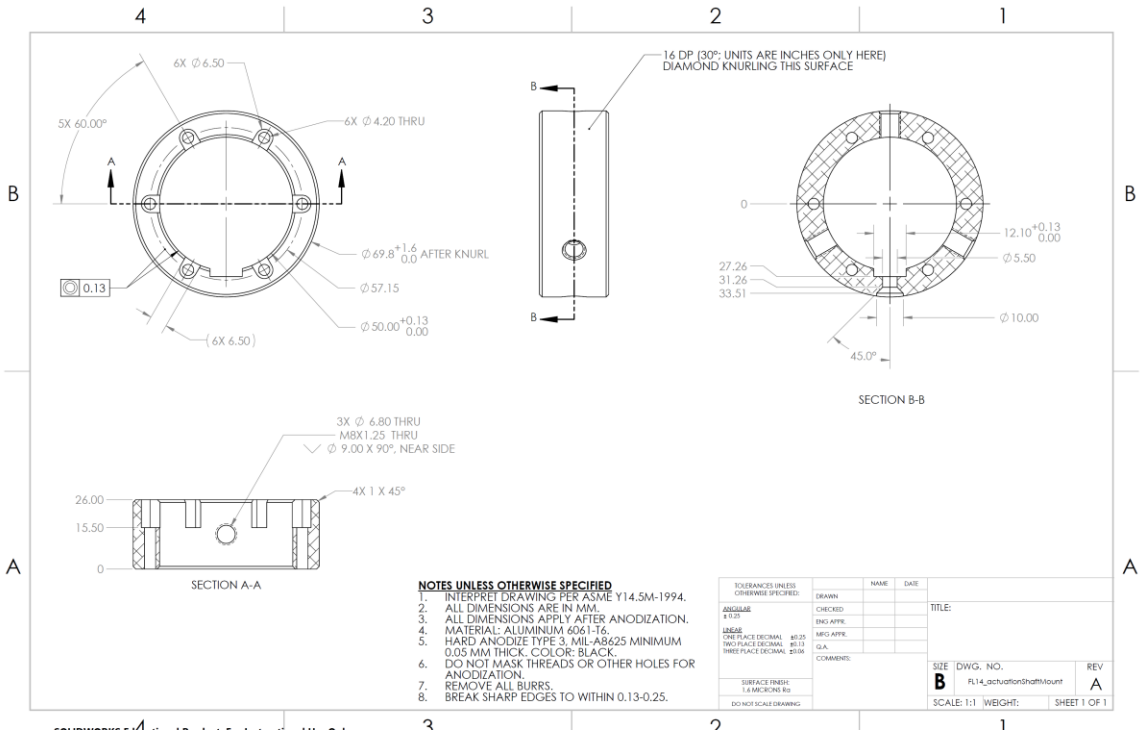

Figure A.2.1. 7. Technical drawing of the actuation shaft mount. Mated actuation shaft to rotation stage. Knurled surface provided user with grip for rotation feature.

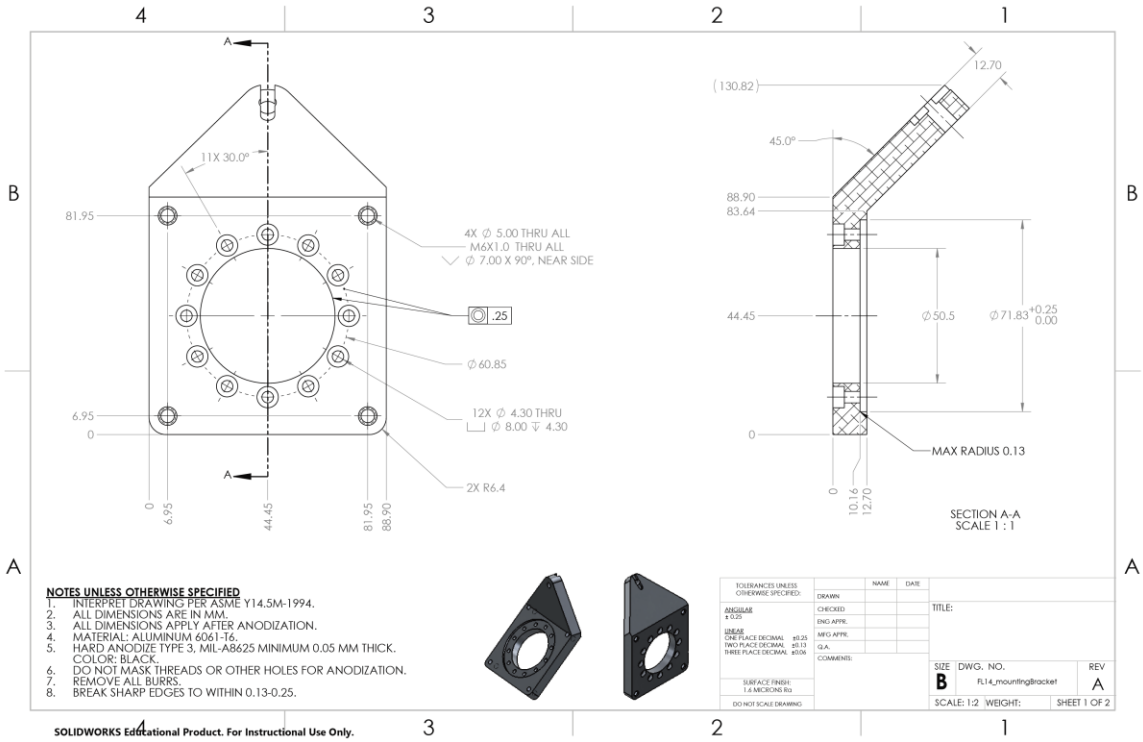

Figure A.2.1. 8. Technical drawing of mounting bracket. attaches to rear of scaffold and serves as mounting point for rotation stage and external positioning system for overall control of the transducer.

References

[1] P.-C. Liang, H.-S. Lai, T. T.-F. Shih, C.-H. Wu, and K.-W. Huang, "The pilot experience upon surgical ablation of large liver tumor by microwave system with tissue permittivity feedback control mechanism," *BMC Surg.*, vol. 14, no. 1, p. 82, 2014.

[2] J. Scheele, R. Stang, A. Altendorf-Hofmann, and M. Paul, "Resection of colorectal liver metastases," *World J. Surg.*, vol. 19, no. 1, pp. 59–71, 1995.

[3] J. P. McWilliams, S. Yamamoto, S. S. Raman, C. T. Loh, E. W. Lee, D. M. Liu, and S. T. Kee, "Percutaneous Ablation of Hepatocellular Carcinoma: Current Status," *J. Vasc. Interv. Radiol.*, vol. 21, no. 8, pp. S204–S213, Aug. 2010.

[4] J. McWilliams, E. Lee, S. Yamamoto, C. Loh, and S. Kee, "Image-Guided Tumor Ablation: Emerging Technologies and Future Directions," *Semin. Intervent. Radiol.*, vol. 27, no. 03, pp. 302–313, Sep. 2010.

[5] M. C. Jansen, R. van Hillegersberg, R. A. F. M. Chamuleau, O. M. van Delden, D. J. Gouma, and T. M. van Gulik, "Outcome of regional and local ablative therapies for hepatocellular carcinoma: a collective review," *Eur. J. Surg. Oncol.*, vol. 31, no. 4, pp. 331–347, May 2005.

[6] T. Livraghi, F. Meloni, M. Di Stasi, E. Rolle, L. Solbiati, C. Tinelli, and S. Rossi, "Sustained complete response and complications rates after radiofrequency ablation of very early hepatocellular carcinoma in cirrhosis: Is resection still the treatment of choice?," *Hepatology*, vol. 47, no. 1, pp. 82–89, Nov. 2007.

[7] P. Tombesi, "Resection vs thermal ablation of small hepatocellular carcinoma: What's the first choice?," *World J. Radiol.*, vol. 5, no. 1, p. 1, 2013.

[8] S. A. Curley, "Radiofrequency Ablation of Malignant Liver Tumors," *Oncologist*, vol. 6, no. 1, pp. 14–23, Feb. 2001.

[9] R. Tateishi, S. Shiina, T. Teratani, S. Obi, S. Sato, Y. Koike, T. Fujishima, H. Yoshida, T. Kawabe, and M. Omata, "Percutaneous radiofrequency ablation for hepatocellular carcinoma," *Cancer*, vol. 103, no. 6, pp. 1201–1209, Mar. 2005.

[10] S. Thamtorawat, R. M. Hicks, J. Yu, S. Siripongsakun, W.-C. Lin, S. S. Raman, J. P. McWilliams, M. Douek, S. Bahrami, and D. S. K. Lu, "Preliminary Outcome of Microwave Ablation of Hepatocellular Carcinoma: Breaking the 3-cm Barrier?," *J. Vasc. Interv. Radiol.*, vol. 27, no. 5, pp. 623–630, May 2016.

[11] J. P. Kirkpatrick, "Principles and Practice of Stereotactic Radiosurgery," *Int. J. Radiat. Oncol.*, vol. 72, no. 4, p. 1267, Nov. 2008.

[12] R. D. Timmerman, B. D. Kavanagh, L. C. Cho, L. Papiez, and L. Xing, "Stereotactic Body Radiation Therapy in Multiple Organ Sites," *J. Clin. Oncol.*, vol. 25, no. 8, pp. 947–952, Mar. 2007.

[13] F. Wu, Z.-B. Wang, W.-Z. Chen, H. Zhu, J. Bai, J.-Z. Zou, K.-Q. Li, C.-B. Jin, F.-L. Xie, and H.-B. Su, "Extracorporeal High Intensity Focused Ultrasound Ablation in the Treatment of Patients with Large Hepatocellular Carcinoma," *Ann. Surg. Oncol.*, vol. 11, no. 12, pp. 1061–1069, Dec. 2004.

[14] F. Wu, "Extracorporeal high intensity focused ultrasound ablation in the treatment of 1038 patients with solid carcinomas in China: an overview," *Ultrason. Sonochem.*, vol. 11, no. 3–4, pp. 149–154, May 2004.

[15] F. WU, Z.-B. WANG, W.-Z. CHEN, J. BAI, H. ZHU, and T.-Y. QIAO, "Preliminary Experience Using High Intensity Focused Ultrasound for the Treatment of Patients With Advanced Stage Renal Malignancy," *J. Urol.*, vol. 170, no. 6, pp. 2237–2240, Dec. 2003.

[16] F. Wu, Z. B. Wang, W. Z. Chen, J. Z. Zou, J. Bai, H. Zhu, K. Q. Li, F. L. Xie, C. B. Jin, H. B. Su, and G. W. Gao, "Extracorporeal focused ultrasound surgery for treatment of human solid carcinomas: Early Chinese clinical experience," *Ultrasound Med. Biol.*, vol. 30, no. 2, pp. 245–260, 2004.

[17] Y. Kim, B. Keserci, A. Partanen, H. Rhim, H. K. Lim, M. J. Park, and M. O. Köhler, "Volumetric MR-HIFU ablation of uterine fibroids: Role of treatment cell size in the improvement of energy efficiency," *Eur. J. Radiol.*, vol. 81, no. 11, pp. 3652–3659, Nov. 2012.

[18] M. O. Köhler, C. Mougenot, B. Quesson, J. Enholm, B. Le Bail, C. Laurent, C. T. W. Moonen, G. J. Ehnholm, and E. S. Ebbini, "Volumetric HIFU Ablation guided by Multiplane MRI Thermometry," in *AIP Conference Proceedings*, 2009, vol. 1113, no. 2009, pp. 228–230.

[19] T. a Leslie and J. E. Kennedy, "High-intensity Focused Ultrasound Principles, Current Uses, and Potential for the Future," *Ultrasound Q.*, vol. 22, no. 4, pp. 263–272, Dec. 2006.

[20] P. Liang, Y. Wang, X. Yu, and B. Dong, "Malignant Liver Tumors: Treatment with Percutaneous Microwave Ablation—Complications among Cohort of 1136 Patients," *Radiology*, vol. 251, no. 3, pp. 933–940, Jun. 2009.

[21] T. Livraghi, L. Solbiati, M. F. Meloni, G. S. Gazelle, E. F. Halpern, and S. N. Goldberg, "Treatment of Focal Liver Tumors with Percutaneous Radio-frequency Ablation: Complications Encountered in a Multicenter Study," *Radiology*, vol. 226, no. 2, pp. 441–451, Feb. 2003.

[22] P. Prakash, "Theoretical Modeling for Hepatic Microwave Ablation," *Open Biomed. Eng. J.*, vol. 4, no. 1, pp. 27–38, Feb. 2010.

[23] D. Yang, M. C. Converse, D. M. Mahvi, and J. G. Webster, "Measurement and Analysis of Tissue Temperature During Microwave Liver Ablation," *IEEE Trans. Biomed. Eng.*, vol. 54, no. 1, pp. 150–155, Jan. 2007.

[24] G. L. Tyson, Z. Duan, J. R. Kramer, J. a. Davila, P. a. Richardson, and H. B. El–Serag, "Level of α-Fetoprotein Predicts Mortality Among Patients With Hepatitis C–Related Hepatocellular Carcinoma," *Clin. Gastroenterol. Hepatol.*, vol. 9, no. 11, pp. 989–994, Nov. 2011.

[25] H. B. El-Serag, D. L. White, and Z. Nurgalieva, "Epidemiology of Hepatocellular Carcinoma," in *Gastrointestinal Oncology*, vol. 9, Oxford, UK: Blackwell Publishing Ltd., 2005, pp. 409–420.

[26] H. B. El-Serag and F. Kanwal, "Epidemiology of hepatocellular carcinoma in the United

States: Where are we? Where do we go?," *Hepatology*, vol. 60, no. 5, pp. 1767–1775, Nov. 2014.
[27] S. Parikh and D. Hyman, "Hepatocellular Cancer: A Guide for the Internist," *Am. J. Med.*, vol. 120, no. 3, pp. 194–202, 2007.
[28] F. X. Bosch, J. Ribes, M. Díaz, and R. Cléries, "Primary liver cancer: Worldwide incidence and trends," *Gastroenterology*, vol. 127, no. 5, pp. S5–S16, Nov. 2004.
[29] T. M. Pawlik, K. a. Delman, J. N. Vauthey, D. M. Nagorney, I. O. L. Ng, I. Ikai, Y. Yamaoka, J. Belghitti, G. Y. Lauwers, R. T. Poon, and E. K. Abdalla, "Tumor size predicts vascular invasion and histologic grade: Implications for selection of surgical treatment for hepatocellular carcinoma," *Liver Transplant.*, vol. 11, no. 9, pp. 1086–1092, 2005.
[30] S. a. Shah, J. K. Smith, Y. Li, S. C. Ng, J. E. Carroll, and J. F. Tseng, "Underutilization of therapy for hepatocellular carcinoma in the medicare population," *Cancer*, vol. 117, no. 5, pp. 1019–1026, Mar. 2011.
[31] X.-P. Chen, F.-Z. Qiu, Z.-D. Wu, Z.-W. Zhang, Z.-Y. Huang, and Y.-F. Chen, "Long-term outcome of resection of large hepatocellular carcinoma," *Br. J. Surg.*, vol. 93, no. 5, pp. 600–606, May 2006.
[32] G. Tsoulfas, A. Mekras, P. Agorastou, and D. Kiskinis, "Surgical treatment for large hepatocellular carcinoma: does size matter?," *ANZ J. Surg.*, vol. 82, no. 7–8, pp. 510–517, Jul. 2012.
[33] C.-N. Yeh, W.-C. Lee, and M.-F. Chen, "Hepatic Resection and Prognosis for Patients With Hepatocellular Carcinoma Larger Than 10 cm: Two Decades of Experience at Chang Gung Memorial Hospital," *Ann. Surg. Oncol.*, vol. 10, no. 9, pp. 1070–1076, Jan. 2003.
[34] K. M. Ng, T. D. Yan, D. Black, F. C. K. Chu, and D. L. Morris, "Prognostic determinants for survival after resection/ablation of a large hepatocellular carcinoma," *HPB*, vol. 11, no. 4, pp. 311–320, Jun. 2009.
[35] D. Pandey, K.-H. Lee, C.-T. Wai, G. Wagholikar, and K.-C. Tan, "Long Term Outcome and Prognostic Factors for Large Hepatocellular Carcinoma (10 cm or more) after Surgical Resection," *Ann. Surg. Oncol.*, vol. 14, no. 10, pp. 2817–2823, Sep. 2007.
[36] S. a. Shah, A. C. Wei, S. P. Cleary, I. Yang, I. D. McGilvray, S. Gallinger, D. R. Grant, and P. D. Greig, "Prognosis and Results After Resection of Very Large (≥10 cm) Hepatocellular Carcinoma," *J. Gastrointest. Surg.*, vol. 11, no. 5, pp. 589–595, Apr. 2007.
[37] K. K. Ng, J.-N. Vauthey, T. M. Pawlik, G. Y. Lauwers, J.-M. Regimbeau, J. Belghiti, I. Ikai, Y. Yamaoka, S. a Curley, D. M. Nagorney, I. O. Ng, S. T. Fan, and R. T. Poon, "Is Hepatic Resection for Large or Multinodular Hepatocellular Carcinoma Justified? Results From a Multi-Institutional Database," *Ann. Surg. Oncol.*, vol. 12, no. 5, pp. 364–373, May 2005.
[38] A. L. Young, H. Z. Malik, M. Abu-Hilal, J. A. Guthrie, J. Wyatt, K. R. Prasad, G. J. Toogood, and J. P. a Lodge, "Large Hepatocellular Carcinoma: Time to Stop Preoperative Biopsy," *J. Am. Coll. Surg.*, vol. 205, no. 3, pp. 453–462, Sep. 2007.
[39] C. A. Cain, "Controlled ultrasonic tissue erosion," in *Journal of the Acoustical Society of America*, 2003, vol. 113, no. 4, p. 2280.
[40] Z. Xu, A. Ludomirsky, L. Y. Eun, T. L. Hall, B. C. Tran, J. B. Fowlkes, and C. a Cain, "Controlled ultrasound tissue erosion.," *IEEE Trans. Ultrason. Ferroelectr. Freq. Control*, vol. 51, no. 6, pp. 726–736, 2004.
[41] Z. Xu, J. B. Fowlkes, E. D. Rothman, A. M. Levin, and C. a Cain, "Controlled ultrasound

tissue erosion: the role of dynamic interaction between insonation and microbubble activity.," *J. Acoust. Soc. Am.*, vol. 117, no. 1, pp. 424–435, 2005.
[42] J. E. Parsons, C. a. Cain, G. D. Abrams, and J. B. Fowlkes, "Pulsed cavitational ultrasound therapy for controlled tissue homogenization," *Ultrasound Med. Biol.*, vol. 32, no. 1, pp. 115–129, 2006.
[43] J. C. Simon, O. A. Sapozhnikov, Y. N. Wang, V. A. Khokhlova, L. A. Crum, and M. R. Bailey, "Investigation into the mechanisms of tissue atomization by high-intensity focused ultrasound," *Ultrasound Med. Biol.*, vol. 41, no. 5, pp. 1372–1385, 2015.
[44] Y. N. Wang, T. Khokhlova, M. Bailey, J. H. Hwang, and V. Khokhlova, "Histological and Biochemical Analysis of Mechanical and Thermal Bioeffects in Boiling Histotripsy Lesions Induced by High Intensity Focused Ultrasound," *Ultrasound Med. Biol.*, vol. 39, no. 3, pp. 424–438, 2013.
[45] J. Xu and T. A. Bigelow, "Experimental Investigation of the Effect of Stiffness, Exposure Time and Scan Direction on the Dimension of Ultrasound Histotripsy Lesions," *Ultrasound Med. Biol.*, vol. 37, no. 11, pp. 1865–1873, 2011.
[46] J. Xu, T. A. Bigelow, and G. M. Riesberg, "Impact of Preconditioning Pulse on Lesion Formation During High-Intensity Focused Ultrasound Histotripsy," *Ultrasound Med. Biol.*, vol. 38, no. 11, pp. 1918–1929, 2012.
[47] T. A. Bigelow, C. L. Thomas, H. Wu, and K. M. F. Itani, "Histotripsy Treatment of S. Aureus Biofilms on Surgical Mesh Samples Under Varying Pulse Durations," *IEEE ITransactions Ultrason. Ferroelectr. Freq. Control*, vol. 64, no. 10, pp. 1420–1428, 2017.
[48] G. R. Schade, J. Keller, K. Ives, X. Cheng, T. J. Rosol, E. Keller, and W. W. Roberts, "Histotripsy focal ablation of implanted prostate tumor in an ACE-1 canine cancer model," *J. Urol.*, vol. 188, no. 5, pp. 1957–1964, 2012.
[49] N. R. Styn, J. C. Wheat, T. L. Hall, and W. W. Roberts, "Histotripsy of VX-2 Tumor Implanted in a Renal Rabbit Model," vol. 24, no. 7, pp. 1145–1150, 2010.
[50] T. D. Khokhlova, Y.-N. Wang, J. C. Simon, B. W. Cunitz, F. Starr, M. Paun, L. A. Crum, M. R. Bailey, and V. A. Khokhlova, "Ultrasound-guided tissue fractionation by high intensity focused ultrasound in an in vivo porcine liver model," *Proc. Natl. Acad. Sci.*, vol. 111, no. 22, pp. 8161–8166, 2014.
[51] T. Li, T. Khokhlova, E. Maloney, Y. N. Wang, S. D'Andrea, F. Starr, N. Farr, K. Morrison, G. Keilman, and J. H. Hwang, "Endoscopic high-intensity focused US: Technical aspects and studies in an in vivo porcine model (with video)," *Gastrointest. Endosc.*, vol. 81, no. 5, pp. 1243–1250, 2015.
[52] M. Hoogenboom, D. Eikelenboom, M. H. den Brok, A. Veltien, M. Wassink, P. Wesseling, E. Dumont, J. J. Fütterer, G. J. Adema, and A. Heerschap, "In vivo MR guided boiling histotripsy in a mouse tumor model evaluated by MRI and histopathology," *NMR Biomed.*, vol. 29, no. 6, pp. 721–731, 2016.
[53] A. D. Maxwell, G. Owens, H. S. Gurm, K. Ives, D. D. Myers, and Z. Xu, "Noninvasive treatment of deep venous thrombosis using pulsed ultrasound cavitation therapy (histotripsy) in a porcine model," *J. Vasc. Interv. Radiol.*, vol. 22, no. 3, pp. 369–377, 2011.
[54] A. D. Maxwell, C. a. Cain, A. P. Duryea, L. Yuan, H. S. Gurm, and Z. Xu, "Noninvasive Thrombolysis Using Pulsed Ultrasound Cavitation Therapy - Histotripsy," *Ultrasound*

Med. Biol., vol. 35, no. 12, pp. 1982–1994, 2009.
[55] X. Zhang, G. E. Owens, C. A. Cain, H. S. Gurm, J. Macoskey, and Z. Xu, "Histotripsy Thrombolysis on Retracted Clots," *Ultrasound Med. Biol.*, vol. 42, no. 8, pp. 1903–1918, 2016.
[56] X. Zhang, J. J. Macoskey, K. Ives, G. E. Owens, H. S. Gurm, J. Shi, M. Pizzuto, C. A. Cain, and Z. Xu, "Non-Invasive Thrombolysis Using Microtripsy in a Porcine Deep Vein Thrombosis Model," *Ultrasound Med. Biol.*, vol. 43, no. 7, pp. 1378–1390, 2017.
[57] T. L. Hall, C. R. Hempel, K. Wojno, Z. Xu, C. a. Cain, and W. W. Roberts, "Histotripsy of the Prostate: Dose Effects in a Chronic Canine Model," *Urology*, vol. 74, no. 4, pp. 932–937, 2009.
[58] C. R. Hempel, T. L. Hall, C. a. Cain, J. B. Fowlkes, Z. Xu, and W. W. Roberts, "Histotripsy fractionation of prostate tissue: Local effects and systemic response in a canine model," *J. Urol.*, vol. 185, no. 4, pp. 1484–1489, 2011.
[59] S. E. Darnell, T. L. Hall, S. a. Tomlins, X. Cheng, K. a. Ives, and W. W. Roberts, "Histotripsy of the Prostate in a Canine Model: Characterization of Post-Therapy Inflammation and Fibrosis," *J. Endourol.*, vol. 29, no. Xx, p. 150218132025001, 2015.
[60] Z. Xu, G. Owens, D. Gordon, C. Cain, and A. Ludomirsky, "Noninvasive creation of an atrial septal defect by histotripsy in a canine model," *Circulation*, vol. 121, no. 6, pp. 742–749, 2010.
[61] G. E. Owens, R. M. Miller, G. Ensing, K. Ives, D. Gordon, A. Ludomirsky, and Z. Xu, "Therapeutic ultrasound to noninvasively create intracardiac communications in an intact animal model," *Catheter. Cardiovasc. Interv.*, vol. 77, no. 4, pp. 580–588, 2011.
[62] R. M. Miller, Y. Kim, K. W. Lin, G. Owens, C. A. Cain, and Z. Xu, "Real-time motion tracking for non-invasive ultrasound cardiac therapy using histotripsy," *IEEE Int. Ultrason. Symp. IUS*, pp. 935–938, 2011.
[63] A. P. Duryea, A. D. Maxwell, W. W. Roberts, Z. Xu, T. L. Hall, and C. a. Cain, "In vitro comminution of model renal calculi using histotripsy," *IEEE Trans. Ultrason. Ferroelectr. Freq. Control*, vol. 58, no. 5, pp. 971–980, 2011.
[64] A. P. Duryea, T. L. Hall, A. D. Maxwell, Z. Xu, C. A. Cain, and W. W. Roberts, "Histotripsy erosion of model urinary calculi.," *J. Endourol.*, vol. 25, no. 2, pp. 341–344, 2011.
[65] A. P. Duryea, W. W. Roberts, C. A. Cain, and T. L. Hall, "Controlled Cavitation to Augment SWL Stone Subdivision: Mechanistic Insights In Vitro," *IEEE ITransactions Ultrason. Ferroelectr. Freq. Control*, vol. 60, no. 2, pp. 301–309, 2013.
[66] J. Gateau, J. F. Aubry, D. Chauvet, A. L. Boch, M. Fink, and M. Tanter, "In vivo bubble nucleation probability in sheep brain tissue," *Phys. Med. Biol.*, vol. 56, no. 22, pp. 7001–7015, 2011.
[67] J. R. Sukovich, Z. Xu, Y. Kim, H. Cao, T. S. Nguyen, A. S. Pandey, T. L. Hall, and C. A. Cain, "Targeted Lesion Generation Through the Skull Without Aberration Correction Using Histotripsy," *IEEE Trans. Ultrason. Ferroelectr. Freq. Control*, vol. 63, no. 5, pp. 671–682, 2016.
[68] A. D. Maxwell, T.-Y. Wang, C. a. Cain, J. B. Fowlkes, O. a. Sapozhnikov, M. R. Bailey, and Z. Xu, "Cavitation clouds created by shock scattering from bubbles during histotripsy," *J. Acoust. Soc. Am.*, vol. 130, no. 4, p. 1888, 2011.
[69] E. Vlaisavljevich, A. Maxwell, M. Warnez, E. Johnsen, C. a Cain, and Z. Xu, "Histotripsy-

Induced Cavitation Cloud Initiation Thresholds in Tissues of Different Mechanical Properties," *IEEE Trans. Ultrason. Ferroelectr. Freq. Control*, vol. 61, no. 2, pp. 341–352, 2014.

[70] Y. Kim, E. Vlaisavljevich, G. E. Owens, S. P. Allen, C. a Cain, and Z. Xu, "In vivo transcostal histotripsy therapy without aberration correction," *Phys. Med. Biol.*, vol. 59, no. 11, pp. 2553–2568, 2014.

[71] F. Winterroth, Z. Xu, T. Y. Wang, J. E. Wilkinson, J. B. Fowlkes, W. W. Roberts, and C. a. Cain, "Examining and analyzing subcellular morphology of renal tissue treated by histotripsy," *Ultrasound Med. Biol.*, vol. 37, no. 1, pp. 78–86, 2011.

[72] E. Vlaisavljevich, Y. Kim, G. Owens, W. Roberts, C. Cain, and Z. Xu, "Effects of tissue mechanical properties on susceptibility to histotripsy-induced tissue damage.," *Phys. Med. Biol.*, vol. 59, no. 2, pp. 253–70, 2014.

[73] E. Vlaisavljevich, Y. Kim, S. Allen, G. Owens, S. Pelletier, C. Cain, K. Ives, and Z. Xu, "Image-Guided Non-Invasive Ultrasound Liver Ablation Using Histotripsy: Feasibility Study in an In Vivo Porcine Model," *Ultrasound Med. Biol.*, vol. 39, no. 8, pp. 1398–1409, 2013.

[74] Y. Kim, T. Wang, Z. Xu, and C. a Cain, "Lesion Generation Through Ribs Using Histotripsy Therapy Without Aberration Correction," *IEEE Trans. Ultrason. Ferroelectr. Freq. Control*, vol. 58, no. 11, pp. 2334–2343, 2011.

[75] T. L. Hall, J. B. Fowlkes, and C. a. Cain, "A real-time measure of cavitation induced tissue disruption by ultrasound imaging backscatter reduction," *IEEE Trans. Ultrason. Ferroelectr. Freq. Control*, vol. 54, no. 3, pp. 569–575, 2007.

[76] T. Y. Wang, T. L. Hall, Z. Xu, J. B. Fowlkes, and C. a. Cain, "Imaging feedback of histotripsy treatments using ultrasound shear wave elastography," *IEEE Trans. Ultrason. Ferroelectr. Freq. Control*, vol. 59, no. 6, pp. 1167–1181, 2012.

[77] T. Wang, Z. Xu, F. Winterroth, T. L. Hall, J. B. Fowlkes, E. D. Rothman, W. W. Roberts, and C. a Cain, "Quantitative ultrasound backscatter for pulsed cavitational ultrasound therapy- histotripsy," *IEEE Trans. Ultrason. Ferroelectr. Freq. Control*, vol. 56, no. 5, pp. 995–1005, 2009.

[78] Y. Kim, T. Hall, Z. Xu, and C. Cain, "Transcranial histotripsy therapy: A feasibility study," *IEEE Trans. Ultrason. Ferroelectr. Freq. Control*, vol. 61, no. 4, pp. 582–593, 2014.

[79] Y. A. Pishchalnikov, J. A. McAteer, M. R. Bailey, I. V. Pishchalnikova, J. C. Williams, and A. P. Evan, "Acoustic shielding by cavitation bubbles in Shock Wave Lithotripsy (SWL)," *AIP Conf. Proc.*, vol. 838, pp. 319–322, 2006.

[80] M. Arora, L. Junge, and C. D. Ohl, "Cavitation cluster dynamics in shock-wave lithotripsy: Part 1. Free field," *Ultrasound Med. Biol.*, vol. 31, no. 6, pp. 827–839, 2005.

[81] L. V Wijngaarden, "One-Dimensional Flow of Liquids Containing Small Gas Bubbles," *Annu. Rev. Fluid Mech.*, vol. 4, no. 1, pp. 369–396, 1972.

[82] T. Y. Wang, Z. Xu, T. L. Hall, J. B. Fowlkes, W. W. Roberts, and C. a. Cain, "Active focal zone sharpening for high-precision treatment using histotripsy," *IEEE Trans. Ultrason. Ferroelectr. Freq. Control*, vol. 58, no. 2, pp. 305–315, 2011.

[83] T.-Y. Wang, Z. Xu, T. L. Hall, J. B. Fowlkes, and C. a. Cain, "An Efficient Treatment Strategy for Histotripsy by Removing Cavitation Memory," *Ultrasound Med. Biol.*, vol. 38, no. 5, pp. 753–766, 2012.

[84] H. Wiksell and A. -C Kinn, "Implications of cavitation phenomena for shot intervals in

extracorporeal shock wave lithotripsy," *Br. J. Urol.*, vol. 75, no. 6, pp. 720–723, 1995.
[85] W. W. Roberts, T. L. Hall, K. Ives, J. S. Wolf, J. B. Fowlkes, and C. a. Cain, "Pulsed cavitational ultrasound: A noninvasive technology for controlled tissue ablation (histotripsy) in the rabbit kidney," *J. Urol.*, vol. 175, no. 2, pp. 734–738, 2006.
[86] J. E. Lundt, S. P. Allen, J. Shi, T. L. Hall, C. A. Cain, and Z. Xu, "Non-invasive, Rapid Ablation of Tissue Volume Using Histotripsy," *Ultrasound Med. Biol.*, vol. 43, no. 12, pp. 2834–2847, 2017.
[87] P. S. Epstein and M. S. Plesset, "On the Stability of Gas Bubbles in Liquid-Gas Solutions," *J. Chem. Phys.*, vol. 18, no. 11, pp. 1505–1509, 1950.
[88] P. B. Duncan and D. Needham, "Test of the Epstein-Plesset model for gas microparticle dissolution in aqueous media: Effect of surface tension and gas undersaturation in solution," *Langmuir*, vol. 20, no. 7, pp. 2567–2578, 2004.
[89] V. Bjerknes, *Fields of Force: Supplementary Lectures, Applications to Meteorology*, 1st ed. New York: Columbia University Press, 1906.
[90] M. Kornfeld and L. Suvorov, "On the destructive action of cavitation," *J. Appl. Phys.*, vol. 15, no. 6, pp. 495–506, 1944.
[91] F. G. Blake, "Bjerknes Forces in Stationary Sound Fields," *J. Acoust. Soc. Am.*, vol. 21, no. 5, p. 551, 1949.
[92] M. D. Rosenberg, "Gaseous-Type Cavitation in Liquids," *Tech. Memo. No. 26, Acoust. Res. Lab. Harvard Univ.*, 1953.
[93] A. P. Duryea, H. A. Tamaddoni, C. A. Cain, W. W. Roberts, and T. L. Hall, "Removal of Residual Nuclei Following a Cavitation Event Using Low-Amplitude Ultrasound," *IEEE Trans. Ultrason. Ferroelectr. Freq. Control*, vol. 61, no. 10, pp. 1619–1626, 2014.
[94] A. P. Duryea, C. A. Cain, W. W. Roberts, H. A. Tamaddoni, and T. L. Hall, "Removal of Residual Bubble Nuclei Following a Cavitation Event: A Parametric Study," *IEEE Trans. Ultrason. Ferroelectr. Freq. Control*, vol. 62, no. 9, pp. 1605–1614, 2015.
[95] A. P. Duryea, W. W. Roberts, C. A. Cain, and T. L. Hall, "Removal of Residual Cavitation Nuclei to Enhance Histotripsy Fractionation of Soft Tissue," *IEEE Trans. Ultrason. Ferroelectr. Freq. Control*, vol. 62, no. 12, pp. 2068–2078, 2015.
[96] A. P. Duryea, W. W. Roberts, C. A. Cain, and T. L. Hall, "Removal of Residual Cavitation Nuclei to Enhance Histotripsy Erosion of Model Urinary Stones," *IEEE Trans. Ultrason. Ferroelectr. Freq. Control*, vol. 62, no. 5, pp. 896–904, 2015.
[97] A. Shi, Z. Xu, J. Lundt, H. A. Tamaddoni, T. Worlikar, and T. L. Hall, "Integrated Histotripsy and Bubble Coalescence Transducer for Rapid Tissue Ablation," *IEEE Trans. Ultrason. Ferroelectr. Freq. Control*, vol. PP, no. c, p. 1, 2018.
[98] B. D. de Senneville, C. Moonen, and M. Ries, "MRI-Guided HIFU Methods for the Ablation of Liver and Renal Cancers," in *Myrmecological News*, vol. 14, 2016, pp. 43–63.
[99] E. S. Worm, M. Høyer, W. Fledelius, and P. R. Poulsen, "Three-dimensional, time-resolved, intrafraction motion monitoring throughout stereotactic liver radiation therapy on a conventional linear accelerator," *Int. J. Radiat. Oncol. Biol. Phys.*, vol. 86, no. 1, pp. 190–197, 2013.
[100] J. D. Zhao, Z. Y. Xu, J. Zhu, J. J. Qiu, W. G. Hu, L. F. Cheng, X. J. Zhang, and G. L. Jiang, "Application of active breathing control in 3-dimensional conformal radiation therapy for hepatocellular carcinoma: The feasibility and benefit," *Radiother. Oncol.*, vol. 87, no. 3,

pp. 439–444, 2008.
[101] J. W. Wong, M. B. Sharpe, D. a. Jaffray, V. R. Kini, J. M. Robertson, J. S. Stromberg, and A. a. Martinez, “The use of active breathing control (ABC) to reduce margin for breathing motion,” *Int. J. Radiat. Oncol. Biol. Phys.*, vol. 44, no. 4, pp. 911–919, 1999.
[102] R. Wagman, E. Yorke, E. Ford, P. Giraud, G. Mageras, B. Minsky, and K. Rosenzweig, “Respiratory gating for liver tumors: Use in dose escalation,” *Int. J. Radiat. Oncol. Biol. Phys.*, vol. 55, no. 3, pp. 659–668, 2003.
[103] S. C. Davies, “Ultrasound quantitation of respiratory organ motion in the upper abdomen,” *Br. J. Radiol.*, no. 1, 1994.
[104] S. Shimizu, H. Shirato, B. Xo, K. Kagei, T. Nishioka, S. Hashimoto, K. Tsuchiya, H. Aoyama, and K. Miyasaka, “Three-dimensional movement of a liver tumor detected by high-speed magnetic resonance imaging,” *Radiother. Oncol.*, vol. 50, no. 3, pp. 367–370, 1999.
[105] H. D. Kubo, B. C. Hill, P. Med, T. Neicu, H. Shirato, L. M. Burk, Y. Z. Lee, and J. Matthew, “Physics in Medicine & Biology Related content Respiration gated radiotherapy treatment : a technical study Respiration gated radiotherapy treatment : a technical study,” 1996.
[106] S. Shimizu, H. Shirato, H. Aoyama, S. Hashimoto, T. Nishioka, A. Yamazaki, K. Kagei, and K. Miyasaka, “High-speed magnetic resonance imaging for four-dimensional treatment planning of conformal radiotherapy of moving body tumors,” *Int. J. Radiat. Oncol. Biol. Phys.*, vol. 48, no. 2, pp. 471–474, 2000.
[107] H. Shirato, S. Shimizu, T. Kunieda, K. Kitamura, M. Van Herk, K. Kagei, T. Nishioka, S. Hashimoto, K. Fujita, H. Aoyama, K. Tsuchiya, K. Kudo, and K. Miyasaka, “Physical aspects of a real-time tumor-tracking system for gated radiotherapy,” *Int. J. Radiat. Oncol. Biol. Phys.*, vol. 48, no. 4, pp. 1187–1195, 2000.
[108] F. Marquet, J. F. Aubry, M. Pernot, M. Fink, and M. Tanter, “Optimal transcostal high-intensity focused ultrasound with combined real-time 3D movement tracking and correction,” *Phys. Med. Biol.*, vol. 56, no. 22, pp. 7061–7080, 2011.
[109] P. J. Bryan, S. Custar, J. R. Haaga, and V. Balsara, “Respiratory movement of the pancreas: An ultrasonic study,” *J. Ultrasound Med.*, vol. 3, no. 7, pp. 317–320, 1984.
[110] C. S. Ross, D. H. Hussey, E. C. Pennington, W. Stanford, and J. F. Doornbos, “Analysis of movement of intrathoracic neoplasms using ultrafast computerized tomography,” *Int. J. Radiat. Oncol. Biol. Phys.*, vol. 18, no. 3, pp. 671–677, 1990.
[111] D. P. Gierga, J. Brewer, G. C. Sharp, M. Betke, C. G. Willett, and G. T. Y. Chen, “The correlation between internal and external markers for abdominal tumors: Implications for respiratory gating,” *Int. J. Radiat. Oncol. Biol. Phys.*, vol. 61, no. 5, pp. 1551–1558, 2005.
[112] R. H. Abhilash, S. Chauhan, M. V. Che, C. C. Ooi, R. A. Bakar, and R. H. G. Lo, “Quantitative study on the effect of abnormalities on respiration-induced kidney movement,” *Ultrasound Med. Biol.*, vol. 42, no. 7, pp. 1681–1688, 2016.
[113] R. M. Miller, Y. Kim, K. W. Lin, C. a. Cain, G. E. Owens, and Z. Xu, “Histotripsy Cardiac Therapy System Integrated with Real-Time Motion Correction,” *Ultrasound Med. Biol.*, vol. 39, no. 12, pp. 2362–2373, 2013.
[114] S. S. Vedam, P. J. Keall, V. R. Kini, and R. Mohan, “Determining parameters for respiration-gated radiotherapy,” *Med. Phys.*, vol. 28, no. 10, pp. 2139–2146, 2001.

[115] H. D. Kubo and B. C. Hill, “Physics in Medicine & Biology Respiration gated radiotherapy treatment: a technical study study,” *Phys. Med. Biol.*, vol. 41, no. 1, pp. 83–91, 1996.
[116] L. Dietrich, T. Tücking, S. Nill, and U. Oelfke, “Compensation for respiratory motion by gated radiotherapy: An experimental study,” *Phys. Med. Biol.*, vol. 50, no. 10, pp. 2405–2414, 2005.
[117] Q. Ren, S. Nishioka, H. Shirato, and R. I. Berbeco, “Adaptive prediction of respiratory motion for motion compensation radiotherapy,” *Phys. Med. Biol.*, vol. 52, no. 22, pp. 6651–6661, 2007.
[118] B. M. Schwartz and N. J. McDannold, “Ultrasound echoes as biometric navigators,” *Magn. Reson. Med.*, vol. 69, no. 4, pp. 1023–1033, 2013.
[119] F. Marquet, M. Tanter, M. Pernot, J.-F. Aubry, G. Montaldo, and M. Fink, “Compensating for bone interfaces and respiratory motion in high-intensity focused ultrasound,” *Int. J. Hyperth.*, vol. 23, no. 2, pp. 141–151, 2007.
[120] F. Marquet, M. Pernot, J.-F. Aubry, M. Tanter, G. Montaldo, and M. Fink, “In-vivo non-invasive motion tracking and correction in High Intensity Focused Ultrasound therapy,” in *2006 International Conference of the IEEE Engineering in Medicine and Biology Society*, 2006, no. August, pp. 688–691.
[121] M. Pernot, M. Tanter, and M. Fink, “3-D real-time motion correction in high-intensity focused ultrasound therapy,” *Ultrasound Med. Biol.*, vol. 30, no. 9, pp. 1239–1249, 2004.
[122] E. J. Harris, N. R. Miller, J. C. Bamber, J. R. N. Symonds-Tayler, and P. M. Evans, “Speckle tracking in a phantom and feature-based tracking in liver in the presence of respiratory motion using 4D ultrasound,” *Phys. Med. Biol.*, vol. 55, no. 12, pp. 3363–3380, 2010.
[123] M. von Siebenthal, G. Székely, A. J. Lomax, and P. C. Cattin, “Systematic errors in respiratory gating due to intrafraction deformations of the liver.,” *Med. Phys.*, vol. 34, no. 9, pp. 3620–3629, 2007.
[124] M. von Siebenthal, G. Székely, a Lomax, and P. Cattin, “Inter-subject modelling of liver deformation during radiation therapy.,” *Med. Image Comput. Comput. Assist. Interv.*, vol. 10, no. Pt 1, pp. 659–666, 2007.
[125] K. B. Bader and V. Bollen, “The influence of gas diffusion on bubble persistence in shock-scattering histotripsy,” *J. Acoust. Soc. Am.*, vol. 143, no. 6, pp. EL481-EL486, 2018.
[126] T. J. Matula, P. R. Hilmo, B. D. Storey, and A. J. Szeri, “Radial response of individual bubbles subjected to shock wave lithoripsy pulses in vitro,” *Phys. Fluids*, vol. 14, no. 3, pp. 913–921, 2002.
[127] A. J. Coleman, M. J. Choi, J. E. Saunders, and T. G. Leighton, “Acoustic emission and sonoluminescence due to cavitation at the beam focus of an electrohydraulic shock wave lithotripter,” *Ultrasound Med. Biol.*, vol. 18, no. 3, pp. 267–281, 1992.
[128] Y. Tomita and A. Shima, “High-Speed Photographic Observations of Laser-Induced Cavitation Bubbles in Water,” *Acustica*, vol. 71, pp. 161–171, 1990.
[129] a. M. Lake, Z. Xu, J. E. Wilkinson, C. a. Cain, and W. W. Roberts, “Renal Ablation by Histotripsy-Does it Spare the Collecting System?,” *J. Urol.*, vol. 179, no. 3, pp. 1150–1154, 2008.
[130] Z. Xu, T. L. Hall, J. B. Fowlkes, and C. a. Cain, “Optical and acoustic monitoring of bubble dynamics at a tissue-fluid interface in ultrasound tissue erosion,” *AIP Conf. Proc.*, vol. 829, no. April, pp. 343–347, 2007.

[131] H. G. Flynn and C. C. Church, “A mechanism for the generation of cavitation maxima by pulsed ultrasound,” *J. Acoust. Soc. Am.*, vol. 505, pp. 505–512, 1984.
[132] C. E. Brennen, “Fission of collapsing cavitation bubbles,” *J. Fluid Mech.*, vol. 472, pp. 153–166, 2002.
[133] I. Akhatov, O. Lindau, A. Topolnikov, R. Mettin, N. Vakhitova, and W. Lauterborn, “Collapse and rebound of a laser-induced cavitation bubble,” *Phys. Fluids*, vol. 13, no. 10, pp. 2805–2819, 2001.
[134] C. C. Church, “A theoretical study of cavitation generated by an extracorporeal shock wave lithotripter,” *J. Acoust. Soc. Am.*, vol. 86, no. 1, pp. 215–227, 1989.
[135] Y. A. Pishchalnikov, O. A. Sapozhnikov, M. R. Bailey, J. A. McAteer, J. C. Williams, A. P. Evan, R. O. Cleveland, and L. A. Crum, “Interactions of cavitation bubbles observed by high-speed imaging in shock wave lithotripsy,” *AIP Conf. Proc.*, vol. 838, pp. 299–302, 2006.
[136] A. Henglein, “Sonochemistry: Historical developments and modern aspects,” *Ultrasonics*, vol. 25, pp. 6–16, 1987.
[137] J. B. Fowlkes and L. A. Crum, “Cavitation threshold measurements for microsecond length pulses of ultrasound,” *J. Acoust. Soc. Am.*, 1988.
[138] O. Yavas and P. Leiderer, “Enhanced acoustic cavitation following laser-induced bubble formation: long-term memory effect,” vol. 72, no. 1994, pp. 2021–2024, 1994.
[139] A. Henglein and M. Gutiérrez, “Chemical reactions by pulsed ultrasound: Memory effects in the formation of NO-3 and NO-2 in aerated water,” *Int. J. Radiat. Biol.*, vol. 50, no. 3, pp. 527–533, 1986.
[140] T. D. Khokhlova, W. L. Monsky, Y. A. Haider, A. D. Maxwell, Y. N. Wang, and T. J. Matula, “Histotripsy Liquefaction of Large Hematomas,” *Ultrasound Med. Biol.*, vol. 42, no. 7, pp. 1491–1498, 2016.
[141] V. A. Khokhlova, J. B. Fowlkes, W. W. Roberts, G. R. Schade, Z. Xu, T. D. Khokhlova, T. L. Hall, A. D. Maxwell, Y.-N. Wang, and C. A. Cain, “Histotripsy methods in mechanical disintegration of tissue: Towards clinical applications,” *Int J Hyperth.*, vol. 31, no. 2, pp. 1464–5157, 2015.
[142] K. W. Lin, Y. Kim, A. Maxwell, T. Y. Wang, T. Hall, Z. Xu, J. Fowlkes, and C. Cain, “Histotripsy beyond the intrinsic cavitation threshold using very short ultrasound pulses: Microtripsy,” *IEEE Trans. Ultrason. Ferroelectr. Freq. Control*, vol. 61, no. 2, pp. 251–265, 2014.
[143] K. W. Lin, T. Hall, R. McGough, Z. Xu, and C. Cain, “Synthesis of monopolar ultrasound pulses for therapy: The frequency-compounding transducer,” *IEEE Trans. Ultrason. Ferroelectr. Freq. Control*, vol. 61, no. 7, pp. 1123–1136, 2014.
[144] Z. Xu, J. B. Fowlkes, and C. a. Cain, “A new strategy to enhance cavitational tissue erosion using a high-intensity, initiating sequence,” *IEEE Trans. Ultrason. Ferroelectr. Freq. Control*, vol. 53, no. 8, pp. 1412–1424, 2006.
[145] G. T. Clement, J. White, and K. Hynynen, “Investigation of a large-area phased array for focused ultrasound surgery through the skull,” *Phys. Med. Biol.*, vol. 45, no. 4, pp. 1071–1083, 2000.
[146] G. T. Clement and K. Hynynen, “Micro-receiver guided transcranial beam steering,” *IEEE Trans. Ultrason. Ferroelectr. Freq. Control*, vol. 49, no. 4, pp. 447–453, 2002.

[147] N. McDannold, G. Clement, P. Black, F. Jolesz, and K. Hynynen, “Transcranial MRI-guided focused ultrasound surgery of brain tumors: Initial findings in three patients,” *Neurosurgery*, vol. 66, no. 2, pp. 323–332, 2010.
[148] M. Pernot, J.-F. F. Aubry, M. Tanter, J.-L. L. Thomas, and M. Fink, “High power transcranial beam steering for ultrasonic brain therapy,” *Phys. Med. Biol.*, vol. 48, no. 16, pp. 2577–2589, 2003.
[149] J. Tavakkoli, A. Birer, A. Arefiev, F. Prat, J. Y. Chapelon, and D. Cathignol, “A piezocomposite shock wave generator with electronic focusing capability: Application for producing cavitation-induced lesions in rabbit liver,” *Ultrasound Med. Biol.*, vol. 23, no. 1, pp. 107–115, 1997.
[150] A. Arefiev, F. Prat, J. Y. Chapelon, J. Tavakkoli, and D. Cathignol, “Ultrasound-induced tissue ablation: studies on isolated, perfused porcine liver,” *Ultrasound Med. Biol.*, vol. 24, no. 7, pp. 1033–1043, 1998.
[151] K.-W. Lin, Y. Kim, A. D. Maxwell, T.-Y. Wang, T. L. Hall, Z. Xu, J. B. Fowlkes, and C. A. Cain, “Histotripsy beyond the intrinsic cavitation threshold using very short ultrasound pulses: microtripsy,” *IEEE Trans. Ultrason. Ferroelectr. Freq. Control*, vol. 61, no. 2, pp. 251–265, Feb. 2014.
[152] E. Vlaisavljevich, K.-W. Lin, A. Maxwell, M. T. Warnez, L. Mancia, R. Singh, A. J. Putnam, B. Fowlkes, E. Johnsen, C. Cain, and Z. Xu, “Effects of Ultrasound Frequency and Tissue Stiffness on the Histotripsy Intrinsic Threshold for Cavitation,” *Ultrasound Med. Biol.*, vol. 41, no. 6, pp. 1651–1667, 2015.
[153] K. Bhunia, S. S. Sablani, J. Tang, and B. Rasco, “Non-invasive measurement of oxygen diffusion in model foods,” *Food Res. Int.*, vol. 89, pp. 161–168, 2016.
[154] D. E. Yount, “Skins of varying permeability: A stabilization mechanism for gas cavitation nuclei,” *J. Acoust. Soc. Am.*, vol. 65, no. 6, pp. 1429–1439, 1979.
[155] A. A. Atchley, “The Blake threshold of a cavitation nucleus having a radius-dependent surface tension,” *J. Acoust. Soc. Am.*, vol. 85, no. 1, pp. 152–157, 1989.
[156] E. newton Harvey, D. K. Barnes, W. D. McElroy, A. H. Whiteley, D. C. Pease, and K. W. Cooper, “Bubble formation in animals. I. Physical factors,” *J. Cell. Comp. Physiol.*, vol. 24, no. 1, pp. 1–22, Aug. 1944.
[157] N. F. Bunkin, A. V. Lobeev, O. I. Vinogradova, T. G. Movchan, and A. I. Kuklin, “Presence of submicroscopic air bubbles in water. Small-angle neutron scattering experiment,” *JETP Lett.*, vol. 62(8), pp. 685–688, 1995.
[158] D. L. Miller, O. D. Kripfgans, and P. L. Carson, “Cavitation nucleation agents for nonthermal ultrasound therapy.,” *J. Acoust. Soc. Am.*, vol. 107, no. 6, pp. 3480–3486, 2000.
[159] C. C. Coussios, C. H. Farny, G. ter Haar, and R. A. Roy, “Role of acoustic cavitation in the delivery and monitoring of cancer treatment by high-intensity focused ultrasound (HIFU),” *Int. J. Hyperth.*, vol. 23, no. 2, pp. 105–120, 2007.
[160] A. R. Williams, M. Delius, D. L. Miller, and W. Schwarze, “Investigation of cavitation in flowing media by lithotripter shock waves both in vitro and in vivo,” *Ultrasound Med. Biol.*, vol. 15, no. 1, pp. 53–60, 1989.
[161] D. E. Yount, “A microscopic investigation of bubble formation nuclei,” *J. Acoust. Soc. Am.*, vol. 76, no. 5, p. 1511, 1984.

[162] A. D. Maxwell, T. Y. Wang, L. Yuan, A. P. Duryea, Z. Xu, and C. a. Cain, “A tissue phantom for visualization and measurement of ultrasound-induced cavitation damage,” *Ultrasound Med. Biol.*, vol. 36, no. 12, pp. 2132–2143, 2010.
[163] A. D. Maxwell, C. a. Cain, T. L. Hall, J. B. Fowlkes, and Z. Xu, “Probability of Cavitation for Single Ultrasound Pulses Applied to Tissues and Tissue-Mimicking Materials,” *Ultrasound Med. Biol.*, vol. 39, no. 3, pp. 449–465, 2013.
[164] G. Kapodistrias and P. H. Dahl, “Scattering measurements from a dissolving bubble,” *J. Acoust. Soc. Am.*, vol. 131, no. 6, pp. 4243–4251, 2012.
[165] M. T. Lategola, “Measurement of total pressure of dissolved gas in mammalian tissue in vivo,” *J. Appl. Physiol.*, vol. 19, no. 2, pp. 322–324, 1964.
[166] Z. Xu, T. L. Hall, J. B. Fowlkes, and C. a Cain, “Effects of acoustic parameters on bubble cloud dynamics in ultrasound tissue erosion (histotripsy).,” *J. Acoust. Soc. Am.*, vol. 122, no. 1, pp. 229–236, 2007.
[167] E. Vlaisavljevich, T. Gerhardson, T. Hall, and Z. Xu, “Effects of f-number on the histotripsy intrinsic threshold and cavitation bubble cloud behavior,” *Phys. Med. Biol.*, vol. 62, no. 4, pp. 1269–1290, 2017.
[168] T. G. Muir and C. E.L., “Prediction of Nonlinear Acoustic Effects At Biomedical Frequencies and Intensities,” *Ultrasound Med. Biol.*, vol. 6, pp. 345–357, 1980.
[169] E. L. Carstensen, W. K. Law, N. D. McKay, and T. G. Muir, “Demonstration of nonlinear acoustical effects at biomedical frequencies and intensities,” *Ultrasound Med. Biol.*, vol. 6, no. 4, pp. 359–368, 1980.
[170] P. V Yuldashev, S. M. Shmeleva, S. a Ilyin, O. a Sapozhnikov, L. R. Gavrilov, and V. a Khokhlova, “The role of acoustic nonlinearity in tissue heating behind a rib cage using a high-intensity focused ultrasound phased array.,” *Phys. Med. Biol.*, vol. 58, no. 8, pp. 2537–59, 2013.
[171] W. Kreider, P. Yuldashev, O. A. Sapozhnikov, N. Farr, A. Partanen, M. Bailey, and V. A. Khokhlova, “Characterization of a multi-element clinical HIFU system using acoustic holography and nonlinear modeling,” *IEEE Trans. Ultrason. Ferroelectr. Freq. Control*, vol. 60, no. 8, pp. 1683–1698, 2013.
[172] B. Frost, D., Sturtevant, “Effects of ambient pressure on the instability of a liquid boiling explosively at the superheat limit,” *J. Heat Transfer*, vol. 108, no. 2, pp. 418–424, 1986.
[173] R. E. Apfel and C. K. Holland, “Gauging the likelihood of cavitation from short-pulse, low-duty cycle diagnostic ultrasound,” *Ultrasound Med. Biol.*, vol. 17, no. 2, pp. 179–185, 1991.
[174] D. Bradley and G. Roth, “Adaptive Thresholding using the Integral Image,” *J. Graph. Tools*, vol. 12, no. 2, pp. 13–21, 2007.
[175] L. A. Crum and G. M. Hansen, “Generalized equations for rectified diffusion,” *J. Acoust. Soc. Am.*, vol. 72, no. 5, pp. 1586–1592, 1982.
[176] W. Y. Yang, W. Cao, T.-S. Chung, and J. Morris, *Applied Numerical Methods Using MATLAB*. Hoboken, New Jersey: John Wiley & Sons, Inc., 2005.
[177] T. G. Leighton, “The Acoustic Bubble.” Academic Press, San Diego, 1994.
[178] D. E. Yount, “On the evolution, generation, and regeneration of gas cavitation nuclei,” *J. Acoust. Soc. Am.*, vol. 71, no. 6, pp. 1473–1481, 1982.
[179] B. D. Johnson and R. C. Cooke, “Generation of Stabilized Microbubbles in Seawater,”

Science (80-.)., vol. 213, no. 4504, pp. 209–211, 1981.
[180] J. Tavakkoli, A. Birer, A. Arefiev, F. Prat, J. Y. Chapelon, and D. Cathignol, "A piezocomposite shock wave generator with electronic focusing capability: Application for producing cavitation-induced lesions in rabbit liver," *Ultrasound Med. Biol.*, vol. 23, no. 1, pp. 107–115, 1997.
[181] S. P. Allen, E. Vlaisavljevich, J. Shi, L. Hernandez-Garcia, C. A. Cain, Z. Xu, and T. L. Hall, "The response of MRI contrast parameters in in vitro tissues and tissue mimicking phantoms to fractionation by histotripsy," *Phys. Med. Biol.*, 2017.
[182] J. J. Macoskey, S. W. Choi, T. L. Hall, E. Vlaisavljevich, J. E. Lundt, F. T. Lee, E. Johnsen, C. A. Cain, and Z. Xu, "Using the cavitation collapse time to indicate the extent of histotripsy-induced tissue fractionation," *Phys. Med. Biol.*, vol. 63, no. 5, 2018.
[183] K. R. Weninger, B. P. Barber, and S. J. Putterman, "Pulsed mie scattering measurements of the collapse of a sonoluminescing bubble," *Phys. Rev. Lett.*, vol. 78, no. 9, pp. 1799–1802, 1997.
[184] K. R. Weninger, P. G. Evans, and S. J. Putterman, "Time correlated single photon Mie scattering from a sonoluminescing bubble," *Phys. Rev. E - Stat. Physics, Plasmas, Fluids, Relat. Interdiscip. Top.*, vol. 61, no. 2, pp. R1020–R1023, 2000.
[185] R. Pecha and B. Gompf, "Microimplosions: Cavitation collapse and shock wave emission on a nanosecond time scale," *Phys. Rev. Lett.*, vol. 84, no. 6, pp. 1328–1330, 2000.
[186] O. Lindau and W. Lauterborn, "Cinematographic observation of the collapse and rebound of a laser-produced cavitation bubble near a wall," *J. Fluid Mech.*, vol. 479, no. 479, pp. 327–348, 2003.
[187] J. J. Macoskey, T. L. Hall, J. R. Sukovich, S. W. Choi, K. Ives, E. Johnsen, C. A. Cain, and Z. Xu, "Soft-Tissue Aberration Correction for Histotripsy," *IEEE Trans. Ultrason. Ferroelectr. Freq. Control*, vol. 65, no. 11, pp. 2073–2085, 2018.
[188] G. D. Kozak, "Measurement and calculation of the ideal detonation velocity for liquid nitrocompounds," *Combust. Explos. Shock Waves*, vol. 34, no. 5, pp. 581–586, 1998.
[189] A. D. Tete, A. Y. Deshmukh, and R. R. Yerpude, "Velocity of detonation (VOD) measurement techniques - practical approach," *Int. J. Eng. Technol.*, vol. 2, no. 3, pp. 259–265, 2013.
[190] O. Bolton, L. R. Simke, P. F. Pagoria, and A. J. Matzger, "High power explosive with good sensitivity: A 2:1 cocrystal of CL-20:HMX," *Cryst. Growth Des.*, vol. 12, no. 9, pp. 4311–4314, 2012.
[191] Y. a Pishchalnikov, O. a Sapozhnikov, M. R. Bailey, J. C. Williams, R. O. Cleveland, T. Colonius, L. a Crum, A. P. Evan, and J. a McAteer, "Cavitation bubble cluster activity in the breakage of kidney stones by lithotripter shockwaves.," *J. Endourol.*, vol. 17, no. 7, pp. 435–446, 2003.
[192] D. E. Yount and R. H. Strauss, "Bubble formation in gelatin: A model for decompression sickness," *J. Appl. Phys.*, vol. 47, no. 11, pp. 5081–5089, 1976.
[193] W. J. Galloway, "An Experimental Study of Acoustically Induced Cavitation in Liquids," *J. Acoust. Soc. Am.*, vol. 26, no. 5, pp. 849–857, 1954.
[194] M. Greenspan and C. E. Tschiegg, "Radiation-induced acoustic cavitation; Threshold versus temperature for some liquids," *Tech. Notes Res. Briefs, J. Acoust. Soc. Am.*, vol. 72, no. 1982, pp. 1327–1331, 1982.

[195] R. Apfel, *Acoustic Cavitation*, vol. 19. 1981.
[196] R. M. Miller, Xi Zhang, A. D. Maxwell, Tzu-Yin Wang, J. Brian Fowlkes, C. A. Cain, and Zhen Xu, "Investigation of the mechanism of ARFI-based Color Doppler feedback of histotripsy tissue fractionation," in *2013 IEEE International Ultrasonics Symposium (IUS)*, 2013, pp. 934–937.
[197] R. M. Miller, X. Zhang, A. D. Maxwell, C. A. Cain, and Z. Xu, "Bubble-Induced Color Doppler Feedback for Histotripsy Tissue Fractionation," *IEEE Trans. Ultrason. Ferroelectr. Freq. Control*, vol. 63, no. 3, pp. 408–419, Mar. 2016.
[198] C. F. Caskey, S. Qin, P. A. Dayton, and K. W. Ferrara, "Microbubble tunneling in gel phantoms," *J. Acoust. Soc. Am.*, vol. 125, no. 5, pp. EL183-EL189, 2009.
[199] A. R. Williams and D. L. Miller, "The use of transparent aqueous gels for observing and recording cavitation activity produced by high intensity focused ultrasound," *2003 IEEE Symp. Ultrason.*, vol. 2, no. 1, pp. 1455–1458, 2003.
[200] H. Alavi Tamaddoni, A. P. Duryea, E. Vlaisavljevich, Z. Xu, and T. L. Hall, "Acoustic Methods for Increasing the Cavitation Initiation Pressure Threshold," *IEEE Trans. Ultrason. Ferroelectr. Freq. Control*, vol. 65, no. 11, pp. 2012–2019, 2018.
[201] J. Macoskey, T. Hall, J. Sukovich, S. W. Choi, K. Ives, E. Johnsen, C. Cain, and Z. Xu, "Non-invasive Histotripsy Aberration Correction for Soft-Tissue using Cavitation-induced Shockwaves," *IEEE-IUS Conf.*, 2018.
[202] O. K. Baskurt, *Handbook of hemorheology and hemodynamics*, vol. 69, no. Sep. 2007.
[203] W. Hentchel and W. Lauterborn, "Acoustic emission of single laser-produced cavitation bubbles and their dynamics," *Appl. Sci. Res.*, vol. 38, pp. 225–230, 1982.
[204] G. W. Willard, "Ultrasonically Induced Cavitation in Water: A Step-by-Step Process," *J. Acoust. Soc. Am.*, vol. 25, no. 4, pp. 669–686, 1953.
[205] Y. Kim, C. G. Fifer, S. K. Gelehrter, G. E. Owens, D. R. Berman, E. Vlaisavljevich, S. P. Allen, M. F. Ladino-Torres, and Z. Xu, "Developmental Impact and Lesion Maturation of Histotripsy-Mediated Non-Invasive Tissue Ablation in a Fetal Sheep Model," *Ultrasound Med. Biol.*, vol. 39, no. 6, pp. 1047–1055, 2013.
[206] E. Vlaisavljevich, K.-W. Lin, M. T. Warnez, R. Singh, L. Mancia, A. J. Putnam, E. Johnsen, C. Cain, and Z. Xu, "Effects of tissue stiffness, ultrasound frequency, and pressure on histotripsy-induced cavitation bubble behavior," *Phys. Med. Biol.*, vol. 60, no. 6, pp. 2271–2292, 2015.
[207] R. Mettin, I. Akhatov, U. Parlitz, C. Ohl, and W. Lauterborn, "Bjerknes forces between small cavitation bubbles in a strong acoustic field," *Phys. Rev. E*, vol. 56, no. 3, pp. 2924–2931, 1997.
[208] E. A. Neppiras, "Subharmonic and Other Low-Frequency Emission from Bubbles in Sound-Irradiated Liquids," *J. Acoust. Soc. Am.*, vol. 46, no. 3B, pp. 587–601, 1969.
[209] L. A. Crum and A. I. Eller, "Motion of Bubbles in a Stationary Sound Field," *J. Acoust. Soc. Am.*, vol. 48, no. 1B, pp. 181–189, 1970.
[210] L. A. Crum and A. I. Eller, "Motion of Bubbles in a Stationary Sound Field," *J. Acoust. Soc. Am.*, vol. 46, p. 1411, 1969.
[211] P. A. Dayton, J. S. Allen, and K. W. Ferrara, "The magnitude of radiation force on ultrasound contrast agents," *J. Acoust. Soc. Am.*, vol. 112, no. 5, pp. 2183–2192, 2002.
[212] R. J. McGough, T. V. Samulski, and J. F. Kelly, "An efficient grid sectoring method for

calculations of the near-field pressure generated by a circular piston," *J. Acoust. Soc. Am.*, vol. 115, no. 5, pp. 1942–1954, 2004.
[213] J. F. Kelly and R. J. McGough, "A time-space decomposition method for calculating the nearfield pressure generated by a pulsed circular piston," *IEEE Trans. Ultrason. Ferroelectr. Freq. Control*, vol. 53, no. 6, pp. 1150–1159, 2006.
[214] D. Chen and R. J. McGough, "A 2D fast near-field method for calculating near-field pressures generated by apodized rectangular pistons," *J. Acoust. Soc. Am.*, vol. 124, no. 3, pp. 1526–1537, 2008.
[215] J. Lundt, T. Hall, A. Rao, J. B. Fowlkes, C. Cain, F. Lee, and Z. Xu, "Coalescence of residual histotripsy cavitation nuclei using low-gain regions of the therapy beam during electronic focal steering," *Phys. Med. Biol.*, vol. 63, no. 22, 2018.
[216] W. LAUTERBORN and A. PHILIPP, "Cavitation erosion by single laser-produced bubbles," *J. Fluid Mech.*, vol. 361, pp. 75–116, 1998.
[217] E. Vlaisavljevich, A. Maxwell, L. Mancia, E. Johnsen, C. Cain, and Z. Xu, "Visualizing the Histotripsy Process: Bubble Cloud–Cancer Cell Interactions in a Tissue-Mimicking Environment," *Ultrasound Med. Biol.*, vol. 42, no. 10, pp. 2466–2477, 2016.
[218] X. Chen, R. Q. Xu, Z. H. Shen, J. Lu, and X. W. Ni, "Optical investigation of cavitation erosion by laser-induced bubble collapse," *Opt. Laser Technol.*, vol. 36, no. 3, pp. 197–203, 2004.
[219] C. E. Shannon and W. Weaver, *The Mathematical Theory of Communication*. Urbana: The University of Illinois Press, 1964.
[220] M. J. E. Golay, "Notes on Digital Coding," *IEEE Proc.*, vol. 37, p. 657, 1949.
[221] R. W. Hamming, *Coding and Information Theory*. Englewood Cliffs, NJ: Prentice Hall, 1986.
[222] R. W. Hamming, "Error Detecting and Error Correcting Codes," *Bell Syst. Tech. J.*, vol. 24, no. 2, 1950.
[223] G. H. Norton and A. Sălăgean, "On the Hamming Distance of Linear Codes Over a Finite Chain Ring," *IEEE Trans. Inf. Theory*, vol. 46, no. 3, pp. 1060–1067, 2000.
[224] G. H. Norton and A. Sălăgean, "On the Structure of Linear and Cyclic Codes over a Finite Chain Ring," *Appl. Math. Sci.*, vol. 506, pp. 83–107, 2009.
[225] W. L. Nyborg and D. E. Hughes, "Bubble Annihilation in Cavitation Streamers," *J. Acoust. Soc. Am.*, vol. 42, pp. 891–894, 1967.
[226] D. F. Gaitan, L. A. Crum, C. C. Church, and R. A. Roy, "Sonoluminescence and bubble dynamics for a single, stable, cavitation bubble," *J. Acoust. Soc. Am.*, vol. 91, no. 6, pp. 3166–3183, 1992.
[227] R. Mettin, *From a single bubble to bubble structures in acoustic cavitation*. 2007.
[228] D. Krefting, "Untersuchung von Einzel- und Mehrblasensystemen in akustischen Resonatoren," 2003.
[229] L. A. Crum and D. A. Nordling, "Velocity of transient cavities in an acoustic stationary wave," *J. Acoust. Soc. Am.*, vol. 52, no. 1B, p. 294, 1972.
[230] A. J. Coleman, J. E. Saunders, L. A. Crum, and M. Dyson, "Acoustic cavitation generated by an extracorporeal shockwave lithotripter," *Ultrasound Med. Biol.*, vol. 13, no. 2, pp. 69–76, 1987.
[231] M. R. Bailey, V. A. Khokhlova, O. A. Sapozhnikov, S. G. Kargl, and L. A. Crum, "Physical

mechanisms of the therapeutic effect of ultrasound (a review)," *Acoust. Phys.*, vol. 49, no. 4, pp. 369–388, 2003.
[232] N. A. Pelekasis, A. Gaki, A. Doinikov, and J. A. Tsamopoulos, *Secondary Bjerknes forces between two bubbles and the phenomenon of acoustic streamers*, vol. 500, no. 500. 2004.
[233] L. A. Crum, "Bjerknes forces on bubbles in a stationary sound field," *J. Acoust. Soc. Am.*, vol. 57, no. 6, pp. 1363–1370, 1975.
[234] T. Barbat, N. Ashgriz, and C.-S. Liu, "Dynamics of two interacting bubbles in an acoustic field," *J. Fluid Mech.*, vol. 389, p. S0022112099004899, 1999.
[235] H. N. Oguz and A. Prosperetti, "A generalization of the impulse and virial theorems with an application to bubble oscillations," *J. Fluid Mech.*, vol. 218, pp. 143–162, 1990.
[236] A. A. Doinikov, "Acoustic radiation forces: Classical theory and recent advances," *Transw. Res. Netw. India Recent Res. Devel. Acoust.*, vol. 37661, no. 1, pp. 39–67, 2003.
[237] J. Jiao, Y. He, K. Yasui, S. E. Kentish, M. Ashokkumar, R. Manasseh, and J. Lee, "Influence of acoustic pressure and bubble sizes on the coalescence of two contacting bubbles in an acoustic field," *Ultrason. Sonochem.*, vol. 22, pp. 70–77, 2015.
[238] M. Minnaert, "XVI. *On musical air-bubbles and the sounds of running water*," *London, Edinburgh, Dublin Philos. Mag. J. Sci.*, vol. 16, no. 104, pp. 235–248, 1933.
[239] D. Psychoudakis, J. B. Fowlkes, J. L. Volakis, and P. L. Carson, "Potential of microbubbles for use as point targets in phase aberration correction," *IEEE Trans. Ultrason. Ferroelectr. Freq. Control*, vol. 51, no. 12, pp. 1639–1647, 2004.
[240] M. Pernot, G. Montaldo, M. Tanter, and M. Fink, "'Ultrasonic stars' for time-reversal focusing using induced cavitation bubbles," *Appl. Phys. Lett.*, vol. 88, no. 3, pp. 1–3, 2006.
[241] J. Gateau, J. F. Aubry, M. Pernot, M. Fink, and M. Tanter, "Combined passive detection and ultrafast active imaging of cavitation events induced by short pulses of high-intensity ultrasound," *IEEE Trans. Ultrason. Ferroelectr. Freq. Control*, vol. 58, no. 3, pp. 517–532, 2011.
[242] K. J. Haworth, J. B. Fowlkes, P. L. Carson, and O. D. Kripfgans, "Towards Aberration Correction of Transcranial Ultrasound Using Acoustic Droplet Vaporization," *Ultrasound Med. Biol.*, vol. 34, no. 3, pp. 435–445, 2008.
[243] S. Hilgenfeldt, D. Lohse, and M. P. Brenner, "Phase diagrams for sonoluminescing bubbles," *Phys. Fluids*, vol. 8, no. 11, pp. 2808–2826, 1996.
[244] S. I. Hatanaka, S. Hayashi, and P. K. Choi, "Sonoluminescence of alkali-metal atoms in sulfuric acid: Comparison with that in water," *Jpn. J. Appl. Phys.*, vol. 49, no. 7 PART 2, 2010.
[245] A. A. Doinikov, *Bjerkness forces and translational bubble dynamics*, vol. 661, no. 2. 2005.
[246] A. A. Doinikov, "Radiation forces between two bubbles in a compressible liquid," *J. Acoust. Soc. Am.*, vol. 102, no. 3, p. 1424, 1997.
[247] D.-Y. Hsieh and M. S. Plesset, "Theory of Rectified Diffusion of Mass into Gas Bubbles," *J. Acoust. Soc. Am.*, vol. 33, no. 2, pp. 206–215, 1961.
[248] A. Eller and H. G. Flynn, "Rectified Diffusion during Nonlinear Pulsations of Cavitation Bubbles," *J. Acoust. Soc. Am.*, vol. 37, no. 3, pp. 493–503, 1965.
[249] A. I. Eller, "Growth of Bubbles by Rectified Diffusion," *J. Acoust. Soc. Am.*, vol. 46, no. 5B, pp. 1246–1250, 1969.

[250] L. A. Crum, “Measurements of the growth of air bubbles by rectified diffusion,” *J. Acoust. Soc. Am.*, vol. 68, no. 203, pp. 203–211, 1980.
[251] J. B. Keller and M. Miksis, “Bubble oscillations of large amplitude,” *J. Acoust. Soc. Am.*, vol. 68, no. 628, p. 628, 1980.
[252] L. A. Crum, “Rectified diffusion,” *Ultrasonics*, no. September, pp. 215–223, 1984.
[253] Z. C. Feng and L. G. Leal, “Nonlinear Bubble Dynamics,” *Annu. Rev. Fluid Mech.*, vol. 29, no. 1, pp. 201–243, 1997.
[254] G. S. Gazelle, S. N. Goldberg, L. Solbiati, and T. Livraghi, “Tumor ablation with radio-frequency energy.,” *Radiology*, vol. 217, no. 3, pp. 633–46, 2000.
[255] S. Shiina, T. Teratani, S. Obi, S. Sato, R. Tateishi, T. Fujishima, T. Ishikawa, Y. Koike, H. Yoshida, T. Kawabe, and M. Omata, “A randomized controlled trial of radiofrequency ablation with ethanol injection for small hepatocellular carcinoma,” *Gastroenterology*, vol. 129, no. 1, pp. 122–130, 2005.
[256] T. D. Khokhlova, M. S. Canney, V. a. Khokhlova, O. a. Sapozhnikov, L. a. Crum, and M. R. Bailey, “Controlled tissue emulsification produced by high intensity focused ultrasound shock waves and millisecond boiling,” *J. Acoust. Soc. Am.*, vol. 130, no. 5, p. 3498, 2011.
[257] S. Park, A. D. Maxwell, G. E. Owens, H. S. Gurm, C. a. Cain, and Z. Xu, “Non-Invasive Embolus Trap Using Histotripsy-An Acoustic Parameter Study,” *Ultrasound Med. Biol.*, vol. 39, no. 4, pp. 611–619, 2013.
[258] J. C. Simon, O. A. Sapozhnikov, V. A. Khokhlova, Y. N. Wang, L. A. Crum, and M. R. Bailey, “Ultrasonic atomization of tissue and its role in tissue fractionation by high intensity focused ultrasound,” *Phys. Med. Biol.*, vol. 57, no. 23, pp. 8061–8078, 2012.
[259] R. M. Miller, A. D. Maxwell, T.-Y. Wang, J. B. Fowlkes, C. A. Cain, and Z. Xu, “Real-time elastography-based monitoring of histotripsy tissue fractionation using color Doppler,” in *2012 IEEE International Ultrasonics Symposium*, 2012, pp. 196–199.
[260] K. Hynynen, “The threshold for thermally significant cavitation in dog’s thigh muscle in vivo,” *Ultrasound Med. Biol.*, vol. 17, no. 2, pp. 157–169, Jan. 1991.
[261] C. H. Farny, “Identifying and Monitoring the Roles of Cavitation in Heating From High-Intensity Focused Ultrasound,” Boston University, 2007.
[262] C. H. Farny, R. G. Holt, and R. A. Roy, “The Correlation Between Bubble-Enhanced HIFU Heating and Cavitation Power,” *IEEE Trans. Biomed. Eng.*, vol. 57, no. 1, pp. 175–184, Jan. 2010.
[263] M. a L. Bell, B. C. Byram, E. J. Harris, P. M. Evans, and J. C. Bamber, “In vivo liver tracking with a high volume rate 4D ultrasound scanner and a 2D matrix array probe,” *Phys. Med. Biol.*, vol. 57, no. 5, pp. 1359–1374, Mar. 2012.
[264] A. Okada, T. Murakami, K. Mikami, H. Onishi, N. Tanigawa, T. Marukawa, and H. Nakamura, “A case of hepatocellular carcinoma treated by MR-guided focused ultrasound ablation with respiratory gating.,” *Magn. Reson. Med. Sci.*, vol. 5, no. 3, pp. 167–171, 2006.
[265] E. Rijkhorst, I. Rivens, G. Haar, D. Hawkes, and D. Barratt, “Effects of Respiratory Liver Motion on Heating for Gated and Model-Based Ultrasound Ablation,” *MICCAI (Medical Image Comput. Comput. Interv.*, pp. 605–612, 2011.
[266] G. Fichtinger, A. Martel, and T. Peters, *Medical Image Computing and Computer-Assisted Intervention – MICCAI 2011*, vol. 6891. Berlin, Heidelberg: Springer Berlin Heidelberg,

2011.
[267] V. Auboiroux, L. Petrusca, M. Viallon, A. Muller, S. Terraz, R. Breguet, X. Montet, C. D. Becker, and R. Salomir, “Respiratory-gated MRgHIFU in upper abdomen using an MR-compatible in-bore digital camera,” *Biomed Res. Int.*, vol. 2014, 2014.
[268] J. Wijlemans, J. van Breugel, M. de Greef, C. Moonen, M. van den Bosch, and M. Ries, “Spontaneous breathing vs. mechanical ventilation for respiratory-gated MR-HIFU ablation in the liver,” *J. Ther. Ultrasound*, vol. 3, no. Suppl 1, p. O87, 2015.
[269] D. Kopelman, Y. Inbar, A. Hanannel, D. Freundlich, D. Castel, A. Perel, A. Greenfeld, T. Salamon, M. Sareli, A. Valeanu, and M. Papa, “Magnetic resonance-guided focused ultrasound surgery (MRgFUS): Ablation of liver tissue in a porcine model,” *Eur. J. Radiol.*, vol. 59, no. 2, pp. 157–162, 2006.
[270] J. M. M. Van Breugel, J. W. Wijlemans, H. H. B. Vaessen, M. de Greef, C. T. W. Moonen, M. A. A. J. van den Bosch, and M. G. Ries, “Procedural sedation and analgesia for respiratory-gated MR-HIFU in the liver: A feasibility study,” *J. Ther. Ultrasound*, vol. 4, no. 1, pp. 1–12, 2016.
[271] C. Ozhasoglu and M. J. Murphy, “Issues in respiratory motion compensation during external-beam radiotherapy,” *Int. J. Radiat. Oncol. Biol. Phys.*, vol. 52, no. 5, pp. 1389–1399, 2002.
[272] S. S. Vedam, V. R. Kini, P. J. Keall, V. Ramakrishnan, H. Mostafavi, and R. Mohan, “Quantifying the predictability of diaphragm motion during respiration with a noninvasive external marker,” *Med. Phys.*, vol. 30, no. 4, pp. 505–513, 2003.
[273] H. Shirato, M. Oita, K. Fujita, Y. Watanabe, and K. Miyasaka, “Feasibility of synchronization of real-time tumor-tracking radiotherapy and intensity-modulated radiotherapy from viewpoint of excessive dose from fluoroscopy,” *Int. J. Radiat. Oncol. Biol. Phys.*, vol. 60, no. 1, pp. 335–341, 2004.
[274] T. Rohlfing, C. R. Maurer, W. G. O’Dell, and J. Zhong, “Modeling liver motion and deformation during the respiratory cycle using intensity-based nonrigid registration of gated MR images,” *Med. Phys.*, vol. 31, no. 3, pp. 427–432, 2004.
[275] A. Schweikard, G. Glosser, M. Bodduluri, M. J. Murphy, and J. R. Adler, “Robotic motion compensation for respiratory movement during radiosurgery,” *Comput. Aided Surg.*, vol. 5, no. 4, pp. 263–277, 2000.
[276] B. D. De Senneville, M. Ries, G. MacLair, and C. Moonen, “MR-guided thermotherapy of abdominal organs using a robust PCA-based motion descriptor,” *IEEE Trans. Med. Imaging*, vol. 30, no. 11, pp. 1987–1995, 2011.
[277] M. Von Siebenthal, G. Székely, U. Gamper, P. Boesiger, A. Lomax, and P. Cattin, “4D MR imaging of respiratory organ motion and its variability,” *Phys. Med. Biol.*, vol. 52, no. 6, pp. 1547–1564, 2007.
[278] M. Buehrer, J. Curcic, P. Boesiger, and S. Kozerke, “Prospective self-gating for simultaneous compensation of cardiac and respiratory motion,” *Magn. Reson. Med.*, vol. 60, no. 3, pp. 683–690, 2008.
[279] K. U. Köhrmann, M. S. Michel, J. Gaa, E. Marlinghaus, and P. Alken, “High intensity focused ultrasound as noninvasive therapy for multilocal renal cell carcinoma: Case study and review of the literature,” *J. Urol.*, vol. 167, no. 6, pp. 2397–2403, 2002.
[280] N. Sadatoh, H. Hatabu, M. Takahashi, K. Imanaka, and A. Sano, “Oxygen-assisted breath-

holding in computed tomography," *J. Comput. Assist. Tomogr.*, vol. 11, no. 4, pp. 742–744, 1987.
[281] C. J. Diederich and K. Hynynen, "Ultrasound technology for hyperthermia," *Ultrasound Med. Biol.*, vol. 25, no. 6, pp. 871–887, Jul. 1999.
[282] C. J. Diederich, "Thermal ablation and high-temperature thermal therapy: Overview of technology and clinical implementation," *Int. J. Hyperth.*, vol. 21, no. 8, pp. 745–753, Dec. 2005.
[283] C. C. Church, "Thermal dose and the probability of adverse effects from HIFU," *AIP Conf. Proc.*, vol. 911, no. June, pp. 131–137, 2007.
[284] W. A. N'Djin, N. R. Miller, J. C. Bamber, J. Y. Chapelon, and D. Melodelima, "Effects of respiratory motion on in-vivo HIFU treatments: A comparative study in the liver," *AIP Conf. Proc.*, vol. 1215, no. March, pp. 203–206, 2010.
[285] P. H. Breen, J. I. Sznajder, P. Morrison, D. Hatch, L. D. Wood, and D. B. Craig, "Constant flow ventilation in anesthetized patients: efficacy and safety," *Anesth. Analg.*, vol. 65, no. 11, pp. 1161–9, 1986.
[286] K. Galmén, P. Harbut, J. Freedman, and J. G. Jakobsson, "High frequency jet ventilation for motion management during ablation procedures, a narrative review," *Acta Anaesthesiol. Scand.*, vol. 61, no. 9, pp. 1066–1074, 2017.
[287] P. Biro, D. R. Spahn, and T. Pfammatter, "High-frequency jet ventilation for minimizing breathing-related liver motion during percutaneous radiofrequency ablation of multiple hepatic tumours," *Br. J. Anaesth.*, vol. 102, no. 5, pp. 650–653, 2009.
[288] J. Raiten, N. Elkassabany, and J. E. Mandel, "The use of high-frequency jet ventilation for out of operating room anesthesia," *Curr. Opin. Anaesthesiol.*, vol. 25, no. 4, pp. 482–485, 2012.
[289] A. Denys, Y. Lachenal, R. Duran, M. Chollet-Rivier, and P. Bize, "Use of High-Frequency Jet Ventilation for Percutaneous Tumor Ablation," *Cardiovasc. Intervent. Radiol.*, vol. 37, no. 1, pp. 140–146, Feb. 2014.
[290] J. H. Heinzerling, J. F. Anderson, L. Papiez, T. Boike, S. Chien, G. Zhang, R. Abdulrahman, and R. Timmerman, "Four-Dimensional Computed Tomography Scan Analysis of Tumor and Organ Motion at Varying Levels of Abdominal Compression During Stereotactic Treatment of Lung and Liver," *Int. J. Radiat. Oncol. Biol. Phys.*, vol. 70, no. 5, pp. 1571–1578, 2008.
[291] P. J. Keall, G. S. Mageras, J. M. Balter, R. S. Emery, K. M. Forster, S. B. Jiang, J. M. Kapatoes, D. A. Low, M. J. Murphy, B. R. Murray, C. R. Ramsey, M. B. Van Herk, S. S. Vedam, J. W. Wong, and E. Yorke, "The management of respiratory motion in radiation oncology report of AAPM Task Group 76," *Med. Phys.*, vol. 33, no. 10, pp. 3874–3900, 2006.
[292] C. L. Eccles, R. Patel, A. K. Simeonov, G. Lockwood, M. Haider, and L. A. Dawson, "Comparison of liver tumor motion with and without abdominal compression using cine-magnetic resonance imaging," *Int. J. Radiat. Oncol. Biol. Phys.*, vol. 79, no. 2, pp. 602–608, 2011.
[293] W. Wunderink, A. Méndez Romero, W. de Kruijf, H. de Boer, P. Levendag, and B. Heijmen, "Reduction of Respiratory Liver Tumor Motion by Abdominal Compression in Stereotactic Body Frame, Analyzed by Tracking Fiducial Markers Implanted in Liver," *Int.*

J. Radiat. Oncol. Biol. Phys., vol. 71, no. 3, pp. 907–915, 2008.
[294] Y. Negoro, Y. Nagata, T. Aoki, T. Mizowaki, N. Araki, K. Takayama, M. Kokubo, S. Yano, S. Koga, K. Sasai, Y. Shibamoto, and M. Hiraoka, "The effectiveness of an immobilization device in conformal radiotherapy for lung tumor: Reduction of respiratory tumor movement and evaluation of the daily setup accuracy," *Int. J. Radiat. Oncol. Biol. Phys.*, vol. 50, no. 4, pp. 889–898, 2001.
[295] A. M. Lake, T. L. Hall, K. Kieran, J. B. Fowlkes, C. a. Cain, and W. W. Roberts, "Histotripsy: Minimally Invasive Technology for Prostatic Tissue Ablation in an In Vivo Canine Model," *Urology*, vol. 72, no. 3, pp. 682–686, 2008.
[296] Y. Kim, S. K. Gelehrter, C. G. Fifer, J. C. Lu, G. E. Owens, D. R. Berman, J. Williams, J. E. Wilkinson, K. a. Ives, and Z. Xu, "Non-invasive pulsed cavitational ultrasound for fetal tissue ablation: Feasibility study in a fetal sheep model," *Ultrasound Obstet. Gynecol.*, vol. 37, no. 4, pp. 450–457, 2011.
[297] R. Devanagondi, X. Zhang, Z. Xu, K. Ives, A. Levin, H. Gurm, and G. E. Owens, "Hemodynamic and Hematologic Effects of Histotripsy of Free-Flowing Blood: Implications for Ultrasound-Mediated Thrombolysis," *J. Vasc. Interv. Radiol.*, vol. 26, no. 10, pp. 1559–1565, 2015.
[298] E. Vlaisavljevich, G. Owens, J. Lundt, D. Teofilovic, K. Ives, A. Duryea, J. Bertolina, T. H. Welling, and Z. Xu, "Non-invasive Liver Ablation Using Histotripsy: Preclinical Safety Study in an in Vivo Porcine Model," *Ultrasound Med. Biol.*, pp. 1–15, 2017.
[299] M. Ries, B. D. De Senneville, S. Roujol, S. Hey, G. Maclair, M. O. Köhler, B. Quesson, and C. T. W. Moonen, "Three dimensional motion compensation for real-time MRI guided focused ultrasound treatment of abdominal organs," *AIP Conf. Proc.*, vol. 1215, no. March, pp. 239–242, 2010.
[300] B. D. De Senneville, C. Mougenot, and C. T. W. Moonen, "Real-time adaptive methods for treatment of mobile organs by MRI-controlled high-intensity focused ultrasound," *Magn. Reson. Med.*, vol. 57, no. 2, pp. 319–330, 2007.
[301] B. Quesson, C. Laurent, G. Maclair, B. D. De Senneville, C. Mougenot, M. Ries, T. Carteret, A. Rullier, and C. T. W. Moonen, "Real-time volumetric MRI thermometry of focused ultrasound ablation in vivo: A feasibility study in pig liver and kidney," *NMR Biomed.*, vol. 24, no. 2, pp. 145–153, 2011.
[302] A. Hsu, N. R. Miller, P. M. Evans, J. C. Bamber, and S. Webb, "Feasibility of using ultrasound for real-time tracking during radiotherapy," *Med. Phys.*, vol. 32, no. 6, p. 1500, 2005.
[303] E. J. Harris, N. R. Miller, J. C. Bamber, P. M. Evans, and J. R. N. Symonds-Tayler, "Performance of ultrasound based measurement of 3D displacement using a curvilinear probe for organ motion tracking.," *Phys. Med. Biol.*, vol. 52, no. 18, pp. 5683–5703, 2007.
[304] K. K. Vigen, B. L. Daniel, J. M. Pauly, and K. Butts, "Triggered, Navigated, Multi-Baseline Method for Proton Resonance Frequency Temperature Mapping With Respiratory Motion," *Magn. Reson. Med.*, vol. 50, no. 5, pp. 1003–1010, 2003.
[305] S. Allen and T. Hall, "Real-time MRI feedback of cavitation ablation therapy (histotripsy)," *J. Ther. Ultrasound*, vol. 3, no. S1, p. O89, Dec. 2015.
[306] S. P. Allen, T. L. Hall, C. a. Cain, and L. Hernandez-Garcia, "Controlling cavitation-based image contrast in focused ultrasound histotripsy surgery," *Magn. Reson. Med.*, vol. 00,

no. November 2013, pp. 1–10, 2014.
[307] S. P. Allen, “Characterization of the in vivo Histotripsy Lesion Using High Field MRI,” *Differentiation*, vol. 20, p. 1582, 2012.
[308] S. P. Allen, E. Vlaisavljevich, J. Shi, L. Hernandez-Garcia, C. A. Cain, Z. Xu, and T. L. Hall, “The response of MRI contrast parameters in in vitro tissues and tissue mimicking phantoms to fractionation by histotripsy,” *Phys. Med. Biol.*, vol. 62, no. 17, pp. 7167–7180, 2017.
[309] L. A. Thompson and C. S. Gardner, “Experiments on laser guide stars at Mauna Kea Observatory for adaptive imaging in astronomy,” *Nature*, vol. 328, no. 6127, pp. 229–231, Jul. 2003.
[310] T. Gerhardson, J. R. Sukovich, A. S. Pandey, T. L. Hall, C. A. Cain, and Z. Xu, “Catheter Hydrophone Aberration Correction for Transcranial Histotripsy Treatment of Intracerebral Hemorrhage: Proof-of-Concept,” *IEEE Trans. Ultrason. Ferroelectr. Freq. Control*, vol. 64, no. 11, pp. 1684–1697, 2017.
[311] Haiyan Zhang, Xuerui Qi, Xiuli Sun, and Shixuan Fan, “Application of Hilbert-Huang transform to extract arrival time of ultrasonic lamb waves,” in *2008 International Conference on Audio, Language and Image Processing*, 2008, pp. 1–4.
[312] A. Norrdine, “An Algebraic Solution to the Multilateration Problem,” *2012 Int. Conf. Indoor Position. Indoor Navig.*, no. April, p. 2012, 2012.
[313] R. Kapoor, S. Ramasamy, A. Gardi, C. Bieber, L. Silverberg, and R. Sabatini, “A novel 3D multilateration sensor using distributed ultrasonic beacons for indoor navigation,” *Sensors (Switzerland)*, vol. 16, no. 10, pp. 1–13, 2016.
[314] T. L. Szabo, *Diagnostic Ultrasound Imaging: Inside Out*, 1st ed. Boston: Elsevier Academic Press, 2004.
[315] R. S. C. Cobbold, *Foundations of Biomedical Ultrasound*. Oxford: Oxford University Press, 2007.
[316] W. T. Shi, F. Forsberg, A. L. Hall, R. Y. Chiao, J.-B. Liu, S. Miller, K. E. Thomenius, M. A. Wheatley, and B. B. Goldberg, “Subharmonic Imaging with Microbubble Contrast Agents: Initial Results,” *Ultrason. Imaging*, vol. 21, no. 2, pp. 79–94, Apr. 1999.
[317] F. Forsberg, W. T. Shi, and B. B. Goldberg, “Subharmonic imaging of contrast agents,” *Ultrasonics*, vol. 38, no. 1–8, pp. 93–98, Mar. 2000.
[318] N. de Jong, M. Emmer, A. van Wamel, and M. Versluis, “Ultrasonic characterization of ultrasound contrast agents,” *Med. Biol. Eng. Comput.*, vol. 47, no. 8, pp. 861–873, 2009.
[319] J.-B. Liu, R. Y. Chiao, A. L. Hall, S. Miller, F. Forsberg, K. E. Thomenius, B. B. Goldberg, W. T. Shi, and M. A. Wheatley, “Subharmonic Imaging with Microbubble Contrast Agents: Initial Results,” *Ultrason. Imaging*, vol. 21, no. 2, pp. 79–94, 2013.
[320] F. Forsberg, W. T. Shi, R. Y. Chiao, A. L. Hall, S. D. Lucas, and B. B. Goldberg, “Implementation of subharmonic imaging,” in *1999 IEEE Ultrasonics Symposium. Proceedings. International Symposium (Cat. No.99CH37027)*, 2003, vol. 2, pp. 1673–1676.
[321] P. . Shankar, P. D. Krishna, and V. . Newhouse, “Advantages of Subharmonic Over Second Harmonic Backscatter for Contrast-To-Tissue Echo Enhancement,” *Ultrasound Med. Biol.*, vol. 24, no. 3, pp. 395–399, Mar. 1998.
[322] Peng Jiang, Zuhua Mao, and J. C. Lazenby, “A new tissue harmonic imaging scheme with better fundamental frequency cancellation and higher signal-to-noise ratio,” in *1998 IEEE*

Ultrasonics Symposium. Proceedings (Cat. No. 98CH36102), 2002, vol. 2, pp. 1589–1594.
[323] P. B. Rosnitskiy, B. A. Vysokanov, L. R. Gavrilov, O. A. Sapozhnikov, and V. A. Khokhlova, "Method for Designing Multielement Fully Populated Random Phased Arrays for Ultrasound Surgery Applications," *IEEE Trans. Ultrason. Ferroelectr. Freq. Control*, vol. 65, no. 4, pp. 630–637, 2018.
[324] T. L. Hall, C. R. Hempel, B. J. Sabb, and W. W. Roberts, "Acoustic access to the prostate for extracorporeal ultrasound ablation.," *J. Endourol.*, vol. 24, no. 11, pp. 1875–1881, 2010.
[325] F. J. Fry and J. E. Barger, "Acoustical properties of the human skull," *J. Acoust. Soc. Am.*, vol. 63, no. 5, pp. 1576–1590, May 1978.
[326] K. Hynynen and F. A. Jolesz, "Demonstration of potential noninvasive ultrasound brain therapy through an intact skull," *Ultrasound Med. Biol.*, vol. 24, no. 2, pp. 275–283, 1998.
[327] M. O'Donnell and S. W. Flax, "Phase Aberration Measurements in Medical Ultrasound: Human Studies," *Ultrason. Imaging*, vol. 10, no. 1, pp. 1–11, Jan. 1988.
[328] T. Long, V. Amin, R. Roberts, R. B. Thompson, S. McClure, and T. Ryken, "An experimental study of ffects of overlaying tissues on HIFU lesion," *AIP Conf. Proc.*, vol. 911, no. June, pp. 237–241, 2007.
[329] K. Vortman and S. Vitek, "TISSUE ABERRATION CORRECTIONS IN ULTRASOUND THERAPY," US 8,088,067 B2, 2012.
[330] Y. Han, G. Y. Hou, S. Wang, and E. Konofagou, "High intensity focused ultrasound (HIFU) focal spot localization using harmonic motion imaging (HMI)," *Phys. Med. Biol.*, vol. 60, no. 15, pp. 5911–5924, 2015.
[331] V. Suomi, J. Jaros, B. Treeby, and R. O. Cleveland, "Full modeling of high-intensity focused ultrasound and thermal heating in the kidney using realistic patient models," *IEEE Trans. Biomed. Eng.*, vol. 65, no. 5, pp. 969–979, 2018.
[332] H. Wang, E. S. Ebbini, M. O'Donnell, and C. a. Cain, "Phase aberration correction and motion compensation for ultrasonic hyperthermia phased arrays: experimental results," *IEEE Trans. Ultrason. Ferroelectr. Freq. Control*, vol. 41, no. 1, pp. 34–43, 1994.
[333] K. B. Bader, M. J. Crowe, J. L. Raymond, and C. K. Holland, "Effect of frequency-dependent attenuation on predicted histotripsy waveforms in tissue-mimicking phantoms," *Ultrasound Med. Biol.*, vol. 42, no. 7, pp. 1701–1705, 2016.
[334] J. C. Bamber and C. R. Hill, "Ultrasonic attenuation and propagation speed in mammalian tissues as a function of temperature," *Ultrasound Med. Biol.*, vol. 5, no. 2, pp. 149–157, Jan. 1979.
[335] Y. A. Pishchalnikov, O. A. Sapozhnikov, M. R. Bailey, I. V. Pishchalnikova, J. C. Williams, and J. A. McAteer, "Cavitation selectively reduces the negative-pressure phase of lithotripter shock pulses," *Acoust. Res. Lett. Online*, vol. 6, no. 4, pp. 280–286, 2005.
[336] Y. a Pishchalnikov, J. a McAteer, J. C. Williams, I. V Pishchalnikova, and R. J. Vonderhaar, "Why stones break better at slow shockwave rates than at fast rates: in vitro study with a research electrohydraulic lithotripter.," *J. Endourol.*, vol. 20, no. 8, pp. 537–541, 2006.
[337] S. Vaezy, M. Andrew, P. Kaczkowski, and L. Crum, "Image-Guided Acoustic Therapy," *Annu. Rev. Biomed. Eng.*, vol. 3, no. 1, pp. 375–390, Aug. 2001.
[338] B. Weigang, G. W. Moore, J. Gessert, W. H. Phillips, and M. Schafer, "The methods and effects of transducer degradation on image quality and the clinical efficacy of diagnostic

sonography," *J. Diagnostic Med. Sonogr.*, vol. 19, no. 1, pp. 3–13, 2003.
[339] M. Mårtensson, M. Olsson, B. Segall, A. G. Fraser, R. Winter, and L. Å. Brodin, "High incidence of defective ultrasound transducers in use in routine clinical practice," *Eur. J. Echocardiogr.*, vol. 10, no. 3, pp. 389–394, 2009.
[340] D. Welsh, S. Inglis, and S. D. Pye, "Detecting failed elements on phased array ultrasound transducers using the Edinburgh Pipe Phantom," *Ultrasound*, vol. 24, no. 2, pp. 68–73, 2016.
[341] N. J. Dudley and D. J. Woolley, "A multicentre survey of the condition of ultrasound probes," *Ultrasound*, vol. 24, no. 4, pp. 190–197, 2016.
[342] H. J. Lee, S. Zhang, Y. Bar-Cohen, and S. Sherrit, "High temperature, high power piezoelectric composite transducers," *Sensors (Switzerland)*, vol. 14, no. 8, pp. 14526–14552, 2014.
[343] J. P. Sferruzza, A. Birer, A. Matias, Y. Theillère, and D. Cathignol, "Experimental identification of a piezoelectric material for high impulse pressure wave applications," *Sensors Actuators, A Phys.*, vol. 88, no. 2, pp. 146–155, 2001.
[344] M. Michael Swindle and A. C. Smith, "Swine in Biomedical Research," in *Sourcebook of Models for Biomedical Research*, Totowa, NJ: Humana Press, 2008, pp. 233–239.
[345] M. M. Swindle, A. C. Smith, K. Laber-Laird, and L. Dungan, "Swine in Biomedical Research: Management and Models," *ILAR J.*, vol. 36, no. 1, pp. 1–5, Jan. 1994.
[346] A. S. Wright, L. A. Sampson, T. F. Warner, D. M. Mahvi, and F. T. Lee, Jr, "Radiofrequency versus Microwave Ablation in a Hepatic Porcine Model 1," *Radiology*, vol. 236, no. 1, pp. 132–139, 2005.
[347] T. Gerhardson, J. R. Sukovich, A. S. Pandey, T. L. Hall, C. A. Cain, and Z. Xu, "Effect of Frequency and Focal Spacing on Transcranial Histotripsy Clot Liquefaction, Using Electronic Focal Steering," *Ultrasound Med. Biol.*, vol. 43, no. 10, pp. 2302–2317, 2017.
[348] C. R. Hill, "Optimum acoustic frequency for focused ultrasound surgery," *Ultrasound Med. Biol.*, vol. 20, no. 3, pp. 271–277, 1994.
[349] H. T. O'Neil, "Theory of Focusing Radiators," *J. Acoust. Soc. Am.*, vol. 21, no. 5, pp. 516–526, 2005.
[350] A. D. Pierce, *Acoustics: An Introduction to Its Physical Principles and Applications*. Melville, NY: Acoustical Society of America, 1994.
[351] M. F. Hamilton and D. T. Blackstock, *Nonlinear Acoustics*, 1st ed. San Diego, CA: Academic Press, 1998.
[352] K. Lin, A. P. Duryea, Y. Kim, T. L. Hall, Z. Xu, and C. A. Cain, "Dual-Beam Histotripsy : A Low-Frequency Pump Enabling a High-Frequency Probe for Precise Lesion Formation," vol. 61, no. 2, 2014.
[353] K. W. Lin, T. L. Hall, Z. Xu, and C. A. Cain, "Histotripsy Lesion Formation Using an Ultrasound Imaging Probe Enabled by a Low-Frequency Pump Transducer," *Ultrasound Med. Biol.*, vol. 41, no. 8, pp. 2148–2160, 2014.
[354] K. B. Bader and C. K. Holland, "Predicting the growth of nanoscale nuclei by histotripsy pulses," *Phys. Med. Biol.*, vol. 61, no. 7, pp. 2947–2966, 2016.
[355] A. P. Evan, L. R. Willis, J. E. Lingeman, and J. A. McAteer, "Renal Trauma and the Risk of Long-Term Complications in Shock Wave Lithotripsy," *Nephron*, vol. 78, no. 1, pp. 1–8, 1998.

[356] M. R. Bailey, L. A. Crum, O. A. Sapozhnikov, A. P. Evan, J. A. McAteer, T. Colonius, and R. O. Cleveland, “Cavitation in shock wave lithotripsy,” *J. Acoust. Soc. Am.*, vol. 114, no. 4, pp. 2417–2418, Oct. 2003.
[357] A. P. EVAN, L. R. WILLIS, J. A. McATEER, M. R. BAILEY, B. A. CONNORS, Y. SHAO, J. E. LINGEMAN, J. C. WILLIAMS, N. S. FINEBERG, and L. A. CRUM, “Kidney Damage and Renal Functional Changes are Minimized by Waveform Control that Suppresses Cavitation in Shock Wave Lithotripsy,” *J. Urol.*, vol. 168, no. October, pp. 1556–1562, Oct. 2002.
[358] S. Z. Child, C. L. Hartman, L. a. Schery, and E. L. Carstensen, “Lung damage from exposure to pulsed ultrasound,” *Ultrasound Med. Biol.*, vol. 16, no. 8, pp. 817–825, 1990.
[359] Y. Pishchalnikov and J. McAteer, “Cavitation-induced streaming in shock wave lithotripsy,” *Proc. Meet. Acoust.*, vol. 19, 2013.
[360] X. Yin and K. Hynynen, “A numerical study of transcranial focused ultrasound beam propagation at low frequency,” *Phys. Med. Biol.*, vol. 50, no. 8, pp. 1821–1836, 2005.
[361] J. Sun and K. Hynynen, “Focusing of therapeutic ultrasound through a human skull: A numerical study,” *J. Acoust. Soc. Am.*, vol. 104, no. 3, pp. 1705–1715, 2002.
[362] G. T. Clement, J. Sun, T. Giesecke, and K. Hynynen, “A hemisphere array for non-invasive ultrasound brain therapy and surgery,” *Phys. Med. Biol.*, vol. 45, no. 12, pp. 3707–3719, Dec. 2000.
[363] R. E. Newnham, D. P. Skinner, and L. E. Cross, “Connectivity and piezoelectric-pyroelectric composites,” *Mater. Res. Bull.*, vol. 13, no. 5, pp. 525–536, May 1978.
[364] W. A. Smith and B. A. Auld, “Modeling 1–3 Composite Piezoelectrics: Thickness-Mode Oscillations,” *IEEE Trans. Ultrason. Ferroelectr. Freq. Control*, vol. 38, no. I, pp. 40–47, 1991.
[365] A. Safari, V. F. Janas, and A. Bandyopadhyay, “Development of fine-scale piezoelectric composites for transducers,” *AIChE J.*, vol. 43, no. S11, pp. 2849–2856, 1997.
[366] A. Bandyopadhyay, R. K. Panda, T. F. McNulty, F. Mohammadi, S. C. Danforth, and A. Safari, “Piezoelectric ceramics and composites via rapid prototyping techniques,” *Rapid Prototyp. J.*, vol. 4, no. 1, pp. 37–49, Mar. 1998.
[367] F. Foster and J. Hunt, “The design and characterization of short pulse ultrasound transducers,” *Ultrasonics*, vol. 16, no. 3, pp. 116–122, 1978.
[368] L. E. Kinsler, A. R. Frey, A. B. Coppens, and J. V. Sanders, *Fundamentals of Acoustics*, 4th ed. New York: John Wiley & Sons, Inc., 2000.
[369] J.-Y. Chapelon, D. Cathignol, C. Cain, E. Ebbini, J.-U. Kluiwstra, O. A. Sapozhnikov, G. Fleury, R. Berriet, L. Chupin, and J.-L. Guey, “New piezoelectric transducers for therapeutic ultrasound,” *Ultrasound Med. Biol.*, vol. 26, no. 1, pp. 153–159, Jan. 2000.
[370] G. S. Chen, H. C. Liu, and Y. L. Lin, “Comparison between 1-3 piezocomposite and PZT ceramic for high-intensity focused ultrasound transducer applications,” *AIP Conf. Proc.*, vol. 1481, no. October, pp. 47–52, 2012.
[371] S. H. Lee, S. H. Jun, H. E. Kim, and Y. H. Koh, “Fabrication of porous PZT-PZN piezoelectric ceramics with high hydrostatic figure of merits using camphene-based freeze casting,” *J. Am. Ceram. Soc.*, vol. 90, no. 9, pp. 2807–2813, 2007.
[372] M. L. Dunn and M. Taya, “Electromechanical Properties of Porous Piezoelectric Ceramics,” *J. Am. Ceram. Soc.*, vol. 76, no. 7, pp. 1697–1706, 1993.
[373] K. Takagi, M. Ono, W. Pan, J.-F. Li, M. Taya, A. Almajid, and R. Watanabe, “Fabrication

and Evaluation of Porous Piezoelectric Ceramics and Porosity-Graded Piezoelectric Actuators," *J. Am. Ceram. Soc.*, vol. 86, no. 7, pp. 1094–1098, 2009.
[374] C. Couinaud, "Liver anatomy: portal (and suprahepatic) or biliary segmentation.," *Dig. Surg.*, vol. 16, no. 6, pp. 459–467, 1999.
[375] S. Huang, B. Wang, M. Cheng, W. Wu, and X. Huang, "A Fast Method to Segment the Liver According to Couinaud ' s Classification," *Med. image Comput. Comput. Interv.*, pp. 270–276, 2008.
[376] Y. Kim, A. D. Maxwell, T. L. Hall, Z. Xu, K.-W. Lin, and C. Cain, "Rapid Prototyping Fabrication of Focused Ultrasound Transducers," *IEEE Trans. Ultrason.*, vol. 61, no. 9, pp. 1559–1574, 2014.
[377] J. R. Sukovich, J. J. Macoskey, J. E. Lundt, T. I. Gerhardson, T. L. Hall, and Z. Xu, "Real-time transcranial histotripsy treatment localization and mapping using acoustic cavitation emission feedback," *Manuscr. Prep.*, pp. 1–14, 2019.
[378] M. Annoni, F. Arleo, A. Trolli, A. Suarez, and A. Alberdi, "Fine abrasive water jet machining of piezoelectric ceramics: Cutting parameters optimization," *21st Int. Conf. Water Jet. Look. to Futur. Learn. from Past*, pp. 67–79, 2012.
[379] L. Chen, E. Siores, and W. C. K. Wong, "Optimising abrasive waterjet cutting of ceramic materials," *J. Mater. Process. Technol.*, vol. 74, no. 1–3, pp. 251–254, 1998.
[380] M. Hashish, "Visualization of the abrasive-waterjet cutting process," *Exp. Mech.*, vol. 28, no. 2, pp. 159–169, Jun. 1988.
[381] C. a. Cain and S. Umemura, "Concentric-Ring and Sector-Vortex Phased-Array Applicators for Ultrasound Hyperthermia," *IEEE Trans. Microw. Theory Tech.*, vol. 34, no. 5, pp. 542–551, May 1986.
[382] T. Fjield and K. Hynynen, "The combined concentric-ring and sector-vortex phased array for MRI guided ultrasound surgery," *IEEE Trans. Ultrason. Ferroelectr. Freq. Control*, vol. 44, no. 5, pp. 1157–1167, Sep. 1997.
[383] H. Jimbo, R. Takagi, K. Taguchi, S. Yoshizawa, and S. Umemura, "Advantage of annular focus generation by sector-vortex array in cavitation-enhanced high-intensity focused ultrasound treatment," *Jpn. J. Appl. Phys.*, vol. 55, no. 7S1, p. 07KF19, Jul. 2016.
[384] T. Yura, M. Lafond, S. Yoshizawa, and S. Umemura, "Effect of focal shape control on stone erosion rate using cavitation bubbles," 2017, vol. 020016, p. 020016.
[385] S. Yoshizawa, R. Takagi, and S. Umemura, "Enhancement of High-Intensity Focused Ultrasound Heating by Short-Pulse Generated Cavitation," *Appl. Sci.*, vol. 7, no. 3, p. 288, 2017.
[386] T. Yura, M. Lafond, S. Yoshizawa, and S. Umemura, "Effect of annular focusing of ultrasound on rate of stone erosion using cavitation bubbles," *Jpn. J. Appl. Phys.*, vol. 57, no. 7S1, p. 07LB18, Jul. 2018.
[387] J. J. Macoskey, S. W. Choi, T. L. Hall, E. Vlaisavljevich, J. E. Lundt, F. T. Lee, E. Johnsen, C. A. Cain, and Z. Xu, "Using the cavitation collapse time to indicate the extent of histotripsy-induced tissue fractionation," *Phys. Med. Biol.*, vol. 63, no. 5, 2018.
[388] J. J. Macoskey, X. Zhang, T. L. Hall, J. Shi, S. A. Beig, E. Johnsen, F. T. Lee, C. A. Cain, and Z. Xu, "Bubble-Induced Color Doppler Feedback Correlates with Histotripsy-Induced Destruction of Structural Components in Liver Tissue," *Ultrasound Med. Biol.*, vol. 44, no. 3, pp. 602–612, 2018.

[389] Q. L. Loh and C. Choong, “Three-Dimensional Scaffolds for Tissue Engineering Applications: Role of Porosity and Pore Size,” *Tissue Eng. Part B Rev.*, vol. 19, no. 6, pp. 485–502, 2013.
[390] A. A. Doinikov, “Bjerknes forces between two bubbles in a viscous fluid,” *J. Acoust. Soc. Am.*, vol. 106, no. 6, pp. 3305–3312, 1999.
[391] A. A. Doinikov, “Viscous effects on the interaction force between two small gas bubbles in a weak acoustic field,” *J. Acoust. Soc. Am.*, vol. 111, no. 4, pp. 1602–1609, 2002.
[392] P. Ariel, “A beginner’s guide to tissue clearing,” *Int. J. Biochem. Cell Biol.*, vol. 84, pp. 35–39, 2017.
[393] D. Jing, S. Zhang, W. Luo, X. Gao, Y. Men, C. Ma, X. Liu, Y. Yi, A. Bugde, B. O. Zhou, Z. Zhao, Q. Yuan, J. Q. Feng, L. Gao, W.-P. Ge, and H. Zhao, “Tissue clearing of both hard and soft tissue organs with the PEGASOS method,” *Cell Res.*, vol. 28, no. 8, pp. 803–818, Aug. 2018.